Faculty of Engineering and Science

The Experimental Analysis of Elastic Agitator Effects to Improve Turbulent Energy Transport

Yong Tshun Howe

This thesis is presented for the Degree of
Master of Philosophy (Mechanical Engineering)
of
Curtin University

November 2016

DECLARATION

To the best of my knowledge and belief this thesis contains no material previously published by any other person except where due acknowledgement has been made.

This thesis contains no material which has been accepted for the award of any other degree or diploma in any university.

Signature:

Date:

ABSTRACT

The conventional method to promote mass, momentum and energy transport between fluid particles is to introduce a disturbance to the flow. Conventionally, a rigid protruding surface (some may address it as agitator or vortex generation depending on application) is employed as the disturbance to create turbulence flow at the area of interest. However, they often dissipate more energy than to produce a satisfied turbulence production. This research aims to replace the rigid with a flexible protruding surface that has the potential to produce better turbulence generation ability than the rigid protruding surface.

An ultrasonic velocity profiler, UVP was used to study the mean and fluctuating flow properties in the near wake of the rigid and flexible protruding surface. Experiments were conducted in a water tunnel. The results from the rigid protruding surface (finite cylinder) is served as a validation to the published results and benchmark to the improvement of the turbulence generated by the flexible protruding surface.

In the current study, a circular finite cylinder (cantilever) was used as the geometry of the rigid and protruding surface. They were varied through the aspect ratio (*AR*) and materials. Also, a local Reynolds number within the subcritical flow range ($10^2<Re_D<10^5$) was considered. The aluminum rigid cylinder of *AR* = 10 and 16 at $Re_D = 4x10^3$, $6x10^3$ and $8x10^3$ was performed in this study. In the case of flexible cylinder, polymer based – Ethylene-vinyl acetate (EVA) of *AR* = 10, 12, 14, 16 and metal based – aluminium and carbon steel cylinder of *AR* = 50 and 54 were individually submerged in a flow at $Re_D = 4x10^3$, $6x10^3$ and $8x10^3$ and $Re_D = 2.5x10^3$.

The mean velocity distributions show that the wake region behind the flexible cylinder increases. The wake region of the flexible cylinders is generally 0.7 *D* ~ 1.7 *D* higher than the wake of the rigid flexible cylinders. The increment of the wake region is because of the weakening of the influence of downwash caused by the *x*-deflection of the flexible cylinder. The diminishing of the downwash is solely caused by the deflection only and is independent of the oscillation of the flexible cylinder.

As a means to quantify the turbulence generation ability, turbulence intensity, TI, production term from the Turbulent Kinetic Energy budget equation (***P*** term) and Reynolds stresses were studied. In general, the flexible cylinders show better capability in augmenting the turbulence than the rigid cylinder. The Reynolds stress shows a 4.5 % to 150.0 % increment compared to its respective rigid counterpart. The normalized amplitude response graph (y/D) which records the cross-flow oscillation of the flexible cylinder is studied. The motion of the cylinder alters the fluid flow significantly. The performance of turbulence enhancement depends heavily on the motion of the cylinder. An organized oscillating motion is in favor of a higher performance of turbulence enhancement. Under the same Re, the turbulence enhancement increases with the structural velocity.

Conclusively, a passively-oscillating flexible protruding surface has the ability in generating greater turbulence level compared to the conventional rigid protruding surface. Aside from that, it also increases the wake region, expanding the effectiveness of the wake region to a greater extend.

ACKNOWLEDGMENTS

First and foremost, I would like to express my deepest gratitude to my supervisor Associate Professor Dr. Sharul Sham Bin Dol for his guidance, patience, time and support; for he who guided me from my undergraduate final year project to the Mphil degree that I am currently undertaking. I would also like to thank my co-supervisor Dr Wee Siaw Khur and Associate Professor Dr Perumal Kumar. In addition, the input from Dr. Vincent Lee Chieng Chen is very valuable and appreciated.

I would also like to express my appreciation to my course mate Chan Hiang Bin, whom I worked so close with, constantly providing ideas and valuable help whenever needed, just as he always did during our undergraduate degree.

I wish to thank Siti at UTP for her hospitality during my visit to the lab and my stay at Tronoh. Without her, I could not have performed my experiments until late night. My heartfelt thanks to the lab technician Michael Ding, who so generously prioritized my materials order and guided me in the purchasing process; and lab technician Andyson Raymond Laman who so keen in helping with the equipment's fabrication.

On personal level, I would like to send my appreciation to my fellow HDR friends Alfred Tan, Hoe Chen Hou, Chan Hiang Bin and Room 2 colleagues, as they always add colors to my life whenever I feel demotivated.

Last, but not the least I owe thanks to my lovely parents and sister who continuously giving me full support and provide me with a comfortable environment and let me be able to focus on doing my thesis without unnecessary worriedness. I would not have made it this far without their love and encouragement. And finally, I would like to thank Melissa Siaw Yiin Ling, who was always there to congratulate, comfort, encourage, and motivate me.

This research project was fully supported and funded by Fundamental Research Grant Scheme from Ministry of Higher Education and no better word could express my gratitude towards them and Associate Professor Dr. Sharul for awarding the opportunity to me.

Table of Contents

List of Figures

List of Tables

NOMENCLATURE

Symbols

AR	Aspect Ratio	-
C_D	Drag Coefficient	-
C_P	Pressure Coefficient	-
c	Speed of sound	m/s
D:S	Distance to Spot ratio	-
D	Diameter	m
d	Deflection or Displacement	m
E	Elastic or Young Modulus	Pa
F_U	Fluid Force	N
f_o	Frequency Emitted by UVP Transducer	Hz
f_d	Doppler Shift Frequency	Hz
f_n	Cylinder Natural Frequency	Hz
f_s	Vortex Shedding Frequency	Hz
H_δ	Shape Factor	-
I	Second Moment of Inertia	m^4
K	Elastic Stiffness	N/m
L	Length	m
m	Mass	kg
*m**	Mass Ratio (m_{osc}/m_{disp})	-
m_{disp}	Mass of Displaced Fluid	kg
m_{osc}	Mass of Oscillating Object	kg
p	Production Term from Kinetic Energy Budget Equations	-
U	Freestream Velocity	m/s
$\bar{U}$	Time-Averaged Streamwise Velocity Component	m/s
u	*u* component velocity (velocity in *x* direction)	m/s
u'	Fluctuating Component of *u* Velocity	m/s
V_r	Reduced Velocity	-
$\bar{W}$	Time-Averaged Wall-normal Velocity Component	m/s

w	w component velocity (velocity in z direction)	m/s
w'	Fluctuating Component of w Velocity	m/s
Re	Reynolds Number	-
St	Strouhal Number	-
TI	Turbulence Intensity	%
x	Location in the x direction	m
y	Location in the y direction	m
y/D	Amplitude to Diameter Ratio	-
z	Location in the z direction	m

Greeks

δ	Boundary Layer Thickness	m
δ^*	Displacement Thickness	m
δ_θ	Momentum Thickness	m
μ	Dynamic Viscosity	-
ρ	Density	kg/m^3

Abbreviation

DoF	Degree of Freedom
DPIV	Digital Particle Image Velocimetry
EVA	Ethylene Vinyl Acetate
FIV	Forced Induced Vibration
FSI	Fluid-Structure Interaction
HD	High Density
PIV	Particle Image Velocimetry
RMS	Root-Mean-Square
RSS	Root-Sum-Square
SMA	Smart Memory Alloy
UVP	Ultrasonic Velocity Profiler
VIV	Vortex Induced Vibration

CHAPTER 1

INTRODUCTION

1.1. Background

Turbulence has always been and will always be a topic of interest in fluid dynamics ever since it was discovered. Many industries such as chemical, petrol-chemical, natural gas processing, semi-conductor, thermal power plants and food processes industries are benefiting from the concept of turbulence in part of their operations simply because the role of turbulent flow makes the mixing of fluids possible due to the features it possesses. The features include irregularity, diffusivity and rotationality, in which they work hand in hand to accelerate the mixing of fluids through the rate of momentum, mass and energy transports. Generally, the purpose of mixing, apart from homogenizing mixtures that are naturally not mixed, it is also to improve the heat transfer through the mixing of hot and cold fluids.

Basically, in order to achieve augmented turbulence, the devices can be done through active or passive control. Active control uses external energy such as propeller, turbine, pump, nozzle jet or lobed mixer (a type of lobed shape design which can fit on the nozzle jet or be in part of the design to induce turbulence) to generate vortex while passive control generally utilizes the geometry (e.g. protruding surface) (see Figure 1.1) to affect the flow field in a fixed manner (Mohan *et al.*, 2015). A very commonly found device such as heat exchangers in various industries which aim to enhance the mixing and heat transfer, falls under the category of passive control device as the efficiency of heat exchangers is often heavily dependent on the configurations and shapes of the internal tubes. Passive control method is popular amongst many industries as it is cheaper to run, simpler to maintain and easier to implement to suit their application needs. Despite that, the amount of turbulence generated is limited to the configurations of the geometry and the layout of the geometry.

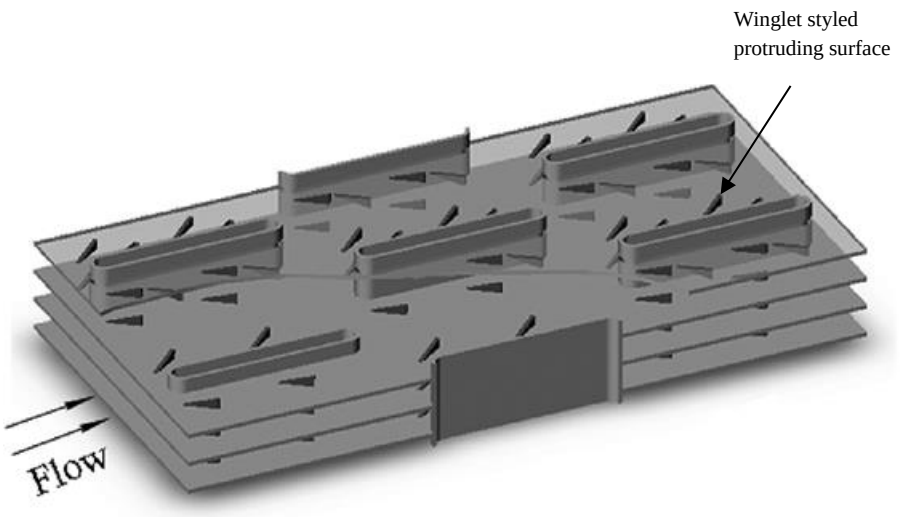

Figure 1.1: Winglet styled protruding surface mounted on a flat tube bank fin heat exchanger to further enhance heat transfer (Song & Wang, 2013)

Active control methods are more complex from the use and design point of view as energy, or auxiliary power, is introduced into the flow (Gupta & Uniyal, 2012). There have been studies on improving the rate of mixing through investigating the effect of the pumping direction of an axial flow (Aubin *et al.*, 2006), the different configurations of the lobe geometry (Waitz *et al.*, 1997; Qiu, 1992; Hu *et al.*, 2002) and others. Depending on the geometry of the lobe, Paterson (1984) found that the existence of large-scale streamwise vortices which were suggested to be responsible for the augmented mixing in lobed mixing flows induced by the geometry. Hu *et al.* (Hu *et al.*, 2002) had noticed the large-scale streamwise vortices broke down into smaller but not weaker vortices and concluded that this can be the reason that a lobed nozzle would enhance both large and small scale mixing. Therefore, it is understood that the augmented turbulence is primarily due to the stronger and coherent vortices. In spite of the turbulence improvement it would bring to the flow, it finds limited application in certain industries due to the need of external power in many practical applications (Gupta & Uniyal, 2012).

The biggest advantages of passive control over active control are mostly less complex from the use and design point of view, easier to implement in a lot of devices with limited space and does not require external source of energy. Since the passive control method solely depends on the geometries of the protruding surface, there exist many kinds of geometries such as vane type, wishbone type, doublet type, cylinder type,

groove type and many more (Lin, 2002). Besides, treated and rough surfaces of the geometry have also proven to promote turbulence in the flow field in the wall region (Gupta & Uniyal, 2012). Researchers tend to favour the concept of passive control in mixing enhancement because of the stronger vortices generated by the protruding surface under certain geometries (Carletti *et al.*, 1996).

However, there have been reports (Gupta & Uniyal, 2012; Lin, 2002; Lögdberg, 2006) on the considerably low pressure recovery behind the protruding surface and it is inversely proportional to the turbulence enhancement. It is inevitable that the pressure losses in turbulence due to flow separation. As a result, the fluid loses energy in subsequent locations, thus the mean velocity is slowing down. Therefore, as a means to overcome this shortcoming, pumps are installed to ensure high pressure recovery.

Although the protruding surface can indeed generate vortices, but the fact that it is essentially a rigid bluff body, it also inevitably dissipates energy of the flow. The energy can dissipate by viscous dissipation through the region where the boundary layer is formed. Apart from that, a portion of the kinetic energy in the oncoming flow can be "absorbed" by the protruding surface (the protruding surface which is like a rigid and stiff spring-like structure). The "absorbed" energy is then damped and wasted through a minute motion (usually negligible and can be neglected) of the structure. This type of interaction is called the Fluid-Structure Interaction, FSI. However, the protruding surface, in this case, only experiences a one-way interaction – that is part of the flow that is in contact with the structure is incapable to alter the structural dynamics in anyway and due to that reason the structure is unable to induce significant influences to the flow. As a result, the energy lost from the flow is wasted through a minute motion that could otherwise be salvaged if there were an interaction from the structure back to the flow.

1.2. Motivation

Since the low pressure recovery is inevitable, it is more important to increase the level of turbulence generated by the protruding surface. In addition, there is also a need to venture into innovative ideas to address the energy lost due to the rigid bluff body since the current approach of many researches is focusing on different configurations of rigid structures.

The biggest downside of a rigid structure is that the response to flow is not dynamic. A geometry with higher angle of attack (e.g. cylinder, flat plate, or blunt object of any shapes) is needed if higher level of turbulence is more favoured. Hence, compromising between the turbulence level and pressure loss is necessary when designing the geometry.

The recent research studies of the protruding surface have seen itself venturing into a new kind of material – smart memory alloy, SMA. While a fixed (rigid body) protruding surface can be configured to improve performance in one regime, it could potentially penalize the performance in other conditions. SMA based protruding surface has the ability to vary its angle of attack to enhance turbulence or minimize pressure loss through temperature change (Aris *et al.*, 2007; Aris *et al.*, 2011, Quackenbush *et al.*, 2010; Warsop, 2004). Since SMA is capable to return to its pre-deformed shape after it is deformed, the employment of SMA based protruding surface can orientate itself in accordance with the two pre-determined shapes. The SMA protruding surface can be activated at specified temperatures or deactivated at lower temperatures. Although it is undoubtedly an ingenious approach to the shortcomings, it cannot be installed on certain applications where the product of mixing (e.g. food, chemical or pharmaceutical industries) is not in sync with the operating temperature of the SMA as the phase transformation temperatures of the SMA protruding surface is commonly done at 70ºC to 90ºC (Aris *et al.*, 2007; Campbell, 2002).

It is without a doubt that the passive control method is more favourable in certain applications (e.g. heat sink) where the installation of pumps or any form of external energy is not possible. However, as this method does not require direct input of external energy, instead they use it from the system itself (moving flow) which would ultimately lead to pressure recovery problem though there might be some circumstances where the installation of pumps is permitted. The recent employment of SMA as the material of protruding surface was indeed an ingenious idea that has the ability to stow when augmented turbulence is not required, thus addressing pressure loss problem, and to deploy when augmented turbulence is needed. Its manipulating variables are not only limiting to the geometry but could extend to the selection of materials. Thus, the author

wishes to propose a protruding surface that could dynamically vary its angle of attack based on the flow condition.

1.3. Proposed Flexible Cylinder as Flexible Protruding Surface

There is a need to resolve the aforementioned problems associated to the passive control method (rigid bluff body) that is (i) to improve the turbulence generation without sacrificing too much of pressure loss and (ii) minimize the energy loss due to the rigid structure characteristics or viscous effects.

Inspired by the ingenious SMA based protruding surface, the present work proposes to replace a conventional rigid protruding surface with a flexible protruding surface that has the ability to oscillate passively based on the incoming flow. Through the oscillation of the protruding flexible, the wasted energy "absorbed" by the rigid protruding surface is able to return to the flow by altering the flow dynamics. Therefore, the adoption of flexible protruding surface could eliminate the probability of pairing with an external energy supply.

The oscillation motion of the flexible protruding surface is driven by the vortex-induced vibration, VIV. VIV is a very common phenomenon probably most intimated by wide discipline of engineering due to the potential failure it might bring to the structure. VIV can increase the strength of vortices shed through the vibration (Thulukkanam, 2013). Perhaps the most commonly known incident resulted from VIV is the Tacoma Narrows Bridge incident (Koughan, 1996) (see Figure 1.2) where the collapse of the bridge was deemed to be partially caused by vortex shedding. Since then, most research efforts have gone in to studying the structural dynamics to suppress the destructive phenomenon of VIV on any fluid-interacting structure in order to reduce the strain induced in the structures (Bailey *et al.* 2002; Keles, 2002; Dol *et al.* 2008) such as bridges, offshore structures, marine cables, towed cables and many more. As a result, the understanding and research on the fluid dynamics by VIV are also lacking.

Despite the discouragement, researchers have started to explore into the positive side of the VIV and incorporated into their invention. In the very recent discovery by a

remarkable Spanish company, Vortex Bladeless has developed an unprecedented method to harness the energy created by vortices through the VIV technique. Using a linear generator, the harnessed energy can be converted into electricity (see Figure 1.3) (Vortex Bladeless, 2015). It offers great inspiration to the mass public, including the present work. It has shown that VIV can be utilized for a better and useful purposes.

Figure 1.2: The fall of Tacoma Narrows Bridges (Koughan, 1996)

Figure 1.3: The vortex bladeless turbine in artist's impression (Vortex Bladeless, 2015)

To date, most of the VIV studies (Raghavan & Bernitsas, 2011; So et al., 2008; Lee & Bernitsas, 2011; Singh & Chatterjee, 2014) mainly focus on the structural aspect of VIV; the study on fluid dynamics behind a vortex-induced vibrating object, to the best of author's knowledge, receives relatively less attention.

1.4. Aim and Objectives

The aim of this research is to investigate the flow dynamics in relation to the flexible protruding surface. There is a need to understand how the structural mechanism affects the turbulence enhancement if the flexible protruding surface does indeed helps in augmenting the turbulence level. With the aim set and focused, two objectives are outlined to help in achieving the aim. These objectives are:

1. To experimentally investigate the turbulence enhancement of a single-phase flow by the flexible protruding surface, with the Re ranging within the subcritical flow regime ($10^2<Re_D<10^5$). The velocity field profile from the near wake, turbulence intensity, production term and Reynolds stress are studied to quantify the turbulence characteristics.
2. To understand the effect of governing parameters (aspect ratio, *AR*, Reynolds Number, Re and material type) of the protruding surface on the turbulence enhancement of the flow.

These objectives are achieved by conducting experimentally in an open channel water tunnel. In order to gain insights of the flow behaviour, Ultrasonic Velocity Profiler (UVP), capable of measuring velocity vector as a function of both space and time in an unidimensional Eulerian frame, was used to obtain the velocity vectors. To ensure success of the present study, the investigations were conducted in a systematic and organized manner. The tests were divided into two categories: rigid cylinder cantilever and flexible cylinder cantilever. External flow in the lower subcritical Reynolds number regime ~ $x10^3$ is selected as the regime of interest as it is the maximum flow velocity capably provided by the water tunnel. Given the height of the test section is only 20 cm, overall length of the structure to be less than 18 cm were conducted. Firstly, a series of tests was performed on a rigid cantilever in fluid. It served as an insight of flow behaviour influenced by the free end and can later be used to justify the change in flow behaviour caused by flexible cantilevers. Secondly, a series of tests was performed on a flexible cantilever in fluid where it provided a picture of the flow behaviour of the complex problems. The movement of the flexible cantilever was not limited by any means and was intended to vibrate freely

as the flow past through it. Two governing parameters, namely Reynolds numbers, and structural stiffness were varied throughout the tests. The variation of structural stiffness could be achieved by different material selections of different Young Modulus and also the geometry. Since the geometry was fixed in this research, different *AR* will be manipulated to achieve different stiffness for the same material.

1.5. Thesis Outline

The structure of this thesis consists of seven chapters where the main content starts from chapter 2.

Chapter 2 presents a brief information that is related to the work of this research. It contains fundamental theories that ease the understanding of this research. The governing parameters, the understanding of the phenomena of vortex shedding of bluff bodies (two-dimensional circular cylinder) and the Fluid structures interaction. At the end of this chapter, basic ideas on flow around a cantilever (three-dimensional finite circular cylinder) is presented as circular cantilever is chosen as the geometry in this research work.

Chapter 3 presents the literature review on flow dynamics of three-dimensional flow and the flow dynamics around a moving object. As there have been fewer research studies in the past regarding the velocity field downstream of the oscillating cantilever and turbulence characteristics of the oscillating cantilever, the literature review here are not intended to be a complete summary.

Chapter 4 discusses the experimental set-up employed in this study, including experimental equipment, flow facilities, and experimental techniques. Finally, the details of post-processing and uncertainty analysis are presented.

Chapter 5 provides the experiments results and discussions in between the rigid and flexible cylinders to highlight the differences made by the flexible cylinders. The rigid and flexible cylinders of the same conditions are put into comparisons by looking at their velocity profile, turbulence intensity distribution, production term and also Reynolds stresses.

Chapter 6 provides the experiments results of flexible cylinders with different material properties. It serves to unveil the structural mechanism behind the flexible cylinders that cause the changes to the turbulence enhancement.

Chapter 7 gives the concluding remarks of the findings and recommendations for future work.

CHAPTER 2

BACKGROUND THEORIES

This chapter brings together some fundamental theories about the governing parameters, the bluff body vortex shedding, the vortex-induced vibration, kinetic budget energy equations and the flow around the finite cylinder. These topics discussed here provide comprehensive knowledge to the readers and it is the fundamental key to helping the success of this research. This work focuses on the VIV of a flexible cylinder which comprises of the VIV of bluff body vortex shedding. On the other hand, Kinetic Budget Energy, as the name suggest, represents the 'strength' of the turbulence in the flow. The turbulence production element in the Kinetic Budget Energy is calculated in this work to quantify the 'strength' produced by both cylinders. Therefore, it is necessary to comprehend the underlying physics to fully appreciate the outcome of this research.

2.1. Governing Parameters

2.1.1. Reynolds number

Reynolds number is the most essential tool in characterizing the flow properties. As it is a dimensionless quantity, as proven by equation 2.1, it can be used on any fluid flow situations.

$$Re = \frac{\rho \mathrm{U} D}{\mu} \tag{2.1}$$

Where ρ is the density of the fluid, U is the flow velocity and D is the characteristic length of the object and μ is the dynamic viscosity of the fluid.

Equation 2.1 depicts the general expression for Reynolds Number. When referring to the Reynolds Number which describes the flow properties around the cylinder's surface, it is known as local Reynolds Number, $\mathrm{Re_D}$. In this case, the incoming fluid velocity, U and diameter of the cylinder, D are used as the characteristic length in the equation.

The Reynolds number generally increases with the velocity of the flow. At high Reynolds number, the inertia force is dominating the flow and the viscous force becomes less dominating. In general, different Reynolds number can have a different effect on the vortex pattern as shown in Table 2.1. The Reynolds number undertaken in this research is at subcritical regime – Re = 2.5, 4, 6 and 8 x 10^3.

Table 2.1: The effect of different Reynolds number on vortex pattern (Assessment of the vortex-Induced-Vibration prevention efficiency of a wave-energy-device, n.d.)

Reynolds Number Effects			
Creeping Flow	Re < 5	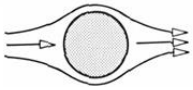	Creeping Flow (No separation)
Attached Eddies	5 < Re < 40	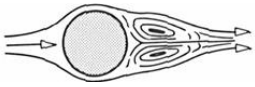	A pair of stable vortices in the wake
Laminar Vortex Shedding	40 < Re < 350	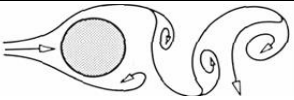	Laminar vortex street
Subcritical Regime	350 < Re < $3x10^5$	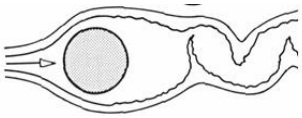	Wake is turbulent. Boundary layer is laminar until separation point
Critical Regime	$3x10^5$ < Re < 3.5 x 10^6	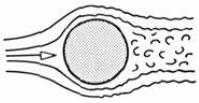	Transistion of laminar boundary to turbulent
Supercritical Regime	Re > 3.5 x 10^6	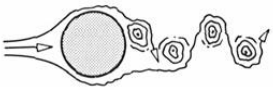	Turbulent vortex street but the separation is narrower than the laminar case

2.1.2. Structural stiffness

The main component that determines the flexibility or elasticity of the flexible cylinder is the structural stiffness. Stiffness relies on material properties and geometry. Therefore, it is the combination of the material's Young's modulus, *E* and the element's second moment of inertia, *I*.

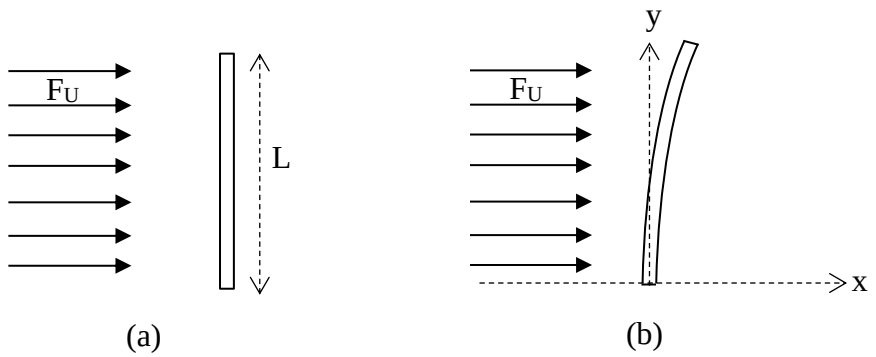

Figure 2.1: (a) A rigid cantilever cylinder subject to fluid force, F_U (b) A flexible cantilever cylinder subject to fluid force, F_U

$$d_x = \frac{F_U y^2}{6EI}(3L - y) \tag{2.2}$$

Considering the equation of motion that is only affected by the spring constant, the equation is as follows:

$$F(t) = m\ddot{x}(t) + c\dot{x}(t) + kx(t) \tag{2.3}$$

$$F_U = kx(t) \tag{2.4}$$

$$F_U = [\frac{6EI}{y^2(3L-y)}]\,\delta_x \tag{2.5}$$

Where *k*, which is the stiffness rating, is equal to the $[\frac{6EI}{y^2(3L-y)}]$ and *x*(t), which is the displacement as a function of time is equal to d_x.

The stiffness rating and the deflection is seen to be governed by the Young Modulus, *E*, second moment of inertia, *I*, overall length of the cantilever, *L*, and the spanwise location of the cantilever, *y*. It is collectively a function of material properties and the geometry as mentioned in Chapter 1.

In order to vary the Young Modulus, different materials of cantilever cylinder are adopted in this research – aluminium, carbon steel and Ethylene vinyl acetate (EVA). The variation of the geometry can be achieved by changing the length or shape of the object as it affects the second moment of inertia. To increase the flexibility of the cylinders, one could replace the material with high Young Modulus value with a lower Young Modulus

value – EVA. Other method is to adopt a very large length to diameter ratio (lower *I* and longer *L*) to compensate for the materials (aluminium and carbon steel) that have high Young Modulus value.

The instantaneous spanwise location of the cantilever, *y*, which will be referred to as local stiffness, is seen to experience lower local stiffness as it advances from the origin of the cylinder. Figure 2.1 shows the greatest deflection at the free end and reduces as it approaches the origin (ground) of the cylinder.

2.2. Bluff Body Vortex Shedding

Any object that is submerged in the fluid current and is not streamline in shape is classified as bluff body. It should cause the flow to separates and generates wake and turbulence behind the object. Circular-shaped cylinder has always been the shape to investigate for bluff body. There is a well-established information about the flow behaviour behind an infinite length circular cylinder by Chen (1987) and the review of Williamson (1996).

When oncoming uniform free stream of fluid meets a bluff body, such as circular cylinder, it is forced to separate itself and split around the cylinder. Viscous boundary layers are developed from the front stagnation point extend throughout the surface of the cylinder until separation occurs. Separation usually happens due to the strong adverse pressure gradient (positive) which occurs downstream of the cylinder, acting on the viscous profile of the boundary layer. To put into context, when the flow is presented to sharp corners, bluff bodies, or objects with high angles of attack, the drastic deceleration of the flow near the wall results in the loss of energy in the boundary layer. Thus, the boundary layers are forced to depart from the surface. In other words, it is the drastic deceleration that causes the adverse pressure gradient, $\frac{\partial P}{\partial y} > 0$ or $\frac{\partial P}{\partial y} < 0$ and the boundary layers are eventually separated as illustrated in Figure 2.2. In the case of flow past through circular-shaped cylinder, the flow initially decelerates on the upstream of the cylinder, while the local pressure increases to fulfil the Bernoulli's equation. At the edge of the cylinder, the local external pressure decreases and the flow, in ideal situation, should accelerate as the potential energy of the pressure field is converted to kinetic energy.

Nevertheless, not all the kinetic energy is recovered due to viscous losses and thus, the velocity of the flow remains very low, or even becoming reversed, leading to the inevitable separation. On the contrary, when the boundary layers are turbulent, it is less susceptible to flow separation due to the increased transport of momentum though it will still eventually separate.

Now the boundary layers are packed with high concentration of vorticity generated by shear velocity profile (the radical deceleration) close to the wall. So, when the boundary layers are separated, the vorticity within the boundary layers are also detached from the surface and convected into the near wake to form a free shear layer on each side of the body (in the case of cylinder) and this interaction is giving rise to the vortex shedding. The phenomenon is better comprehended in Figure 2.3. As depicted in Figure 2.3, the shear layer develops in between the free stream velocity and the very slow velocity located within the wake region. It is also in this region where the velocity gradient is large, giving the opportunity of the flow to circulate, forming a vortex. The vorticity within the boundary layers, at the separation points constantly feeds energy to the circulation in the free shear layer for the phenomenon to sustain. When the vortex is sufficiently fed, it begins to shed off and travels downstream and a new vortex is ready to be fed, only for the process to repeat.

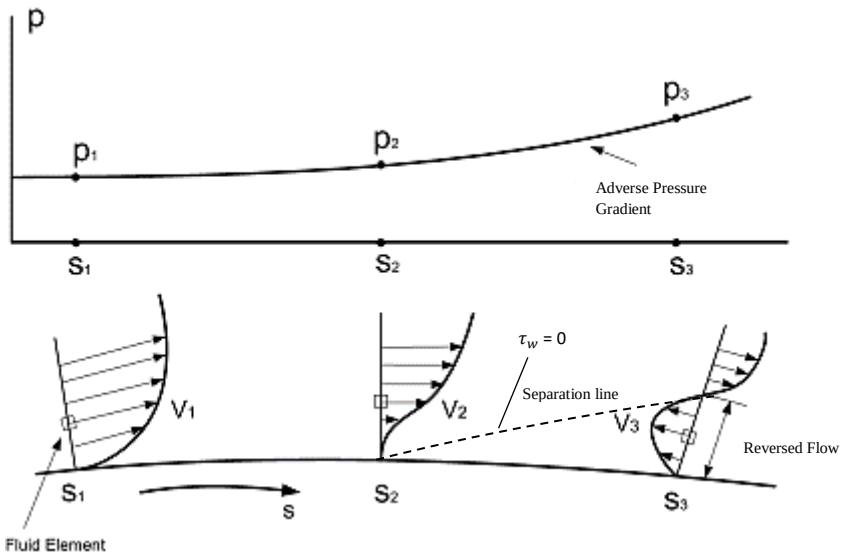

Figure 2.2: Reversed Flow by Adverse Pressure Gradient (Anderson Jr, 1985)

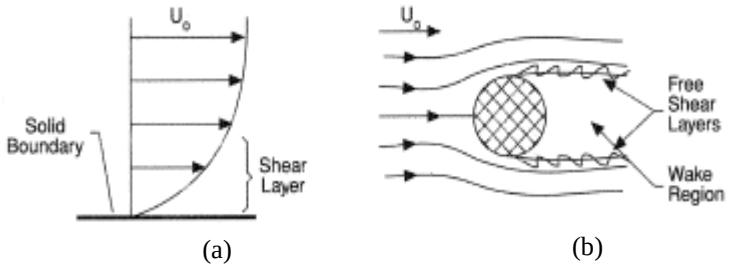

(a) (b)

Figure 2.3: (a) Shear layer can also be indicated through the velocity profile (b) Illustration of free shear layer and the wake region behind a cylinder (Swan, 2011)

Since a cylinder has two edges, there are also two shear layers from each side as indicated in Figure 2.3 (b). Vortices are formed from the two edges with an appearance of alternately opposite signed vortices. In the event that the vortices shed are asymmetric, the vortex from one edge which is fed sufficiently, is strong enough to draw the opposing shear layer (the second edge) across the wake, only to interrupts and terminates the feeding process of the second vortex from the second edge. This process is self-repeating and thus giving the appearance of alternately opposite signed vortices downstream. Bearman (1984) who so elegantly describes the mechanism of vortex shedding from bluff bodies as "A key factor in the formation of a vortex street wake is the mutual interaction between the two separating shear layers."

2.3. Fluid-Structure Interaction – A Brief Theory

In any case that the cylindrical structure, which has the ability to perform linear or angular movements, or even the combination of both, is put into interaction with fluid flow, the vortices shed from alternate sides create a periodic surface pressure fluctuation that can cause the cylindrical structure to vibrate. The cylinder structure can consist of a rigid structure that is elastically supported or a cylinder structure that has the properties of elasticity (low stiffness structure). Many studies on FSI however, were focused on elastically mounted configuration that simulates the mass-spring-damper model (Morse *et al.*, 2008; Klamo, 2007; Jauvtis & Williamson, 2004) and much less on the structure that has low stiffness values (Prastianto *et al.*, 2009). As a measure to understanding the impact that a flexible cylinder could have on the fluid flow, this sub-chapter would be revolving

around the intermediate interactions between structural body and external fluid flow rather than solely on the cylindrical structure and its FSI excitation mechanism.

2.3.1. Vortex-induced vibration

The sole mechanism that governs the oscillation of the proposed flexible cylinder in this research is VIV. VIV is the back and forth motion of the cylinder as a result of difference in pressure distribution of the flow near the cylinder. VIV is a phenomenon whereby vibrations are stable and self-limiting, resulting from large scale vortex shedding. VIV is a type of force-induced vibration, FIV. Other types of FIV are turbulence-induced vibration and vibration induced by tip vortex. Many renowned researchers in the field have published comprehensive reviews about the VIV mechanism (Gabbai & Benaroya, 2005).

Under general situations, there are two types of vortex shedding that can affect the oscillation mode of the VIV and one of which is perhaps more commonly known than the other – the Kármán vortex shedding. The Kármán vortex street consists of the alternately shed vortices due to the asymmetric vortex shedding behaviour. It is the asymmetric vortex shedding behaviour that alters the pressure distribution on the surface of each side of the cylinder, thus, leading to the vibration of the cylinder in transverse direction to the flow. This type of vibration is also widely known as cross-flow motion (see Figure 2.6). It is anticipated that the Kármán vortex shedding would be the dominant vortex shedding below the cylinder's span near the free end, therefore cross-flow vibration should happen during experiments. The second type of vortex shedding is the symmetric vortex shedding. As the name suggests, it consists of a pair of symmetrical vortices when shed in one cycle. The vibration mode of this shedding is in-line or parallel to the flow, hence the name of in-line VIV. Under certain conditions, in-line VIV accompanied by symmetric vortex shedding may occur at lower flow velocities than the Kármán vortex shedding (Nakamura *et al.*, 2013). Another type of shedding that would happen in addition to either the Kármán vortex shedding or symmetric vortex shedding, is the tip vortex shedding. It happens whenever the free end of the cylinder is exposed to the flow. These tip vortices are

generally shed at a frequency one-third the Kármán vortex shedding and may cause large amplitude vibrations (Nakamura *et al.*, 2013).

The back and forth motion, which are lift and drag, is due to vortex shedding at which the vortex shedding frequency, f_s was close to the cylinder natural frequency, f_n at the velocity. Figure 2.4 shows a schematic diagram of the pressure field around a circular cylinder when a vortex is being formed. U represents free stream velocity at the upstream of the cylinder. The resultant force, F, can be resolved into two components, drag component, F_x and lift component F_y, in relation to *x* and *y* axis.

The Strouhal number, St is the frequency of the excitation force in the lift direction whereas the frequency of the excitation force in the drag direction is normally two times the lift direction. The lift force can be explained as a group of vortices shed to one side of the cylinder once per cycle and the other side (see Figure 2.5). The lift force, which appears when the vortex shedding starts to occur, causes the cross-flow motion (perpendicular to the fluid flow direction). Similarly, the drag force appears as a result of vortex shedding but with all vortices shed downstream. In-line motion (in the same direction as the fluid flow) of the cylinder is caused by drag force. Since all the vortices are shed downstream of the cylinder in the drag direction, the drag force associated with vortex shedding occurs at twice the frequency of the lift force, as depicted in Figure 2.6 by Bai & Bai (2005).

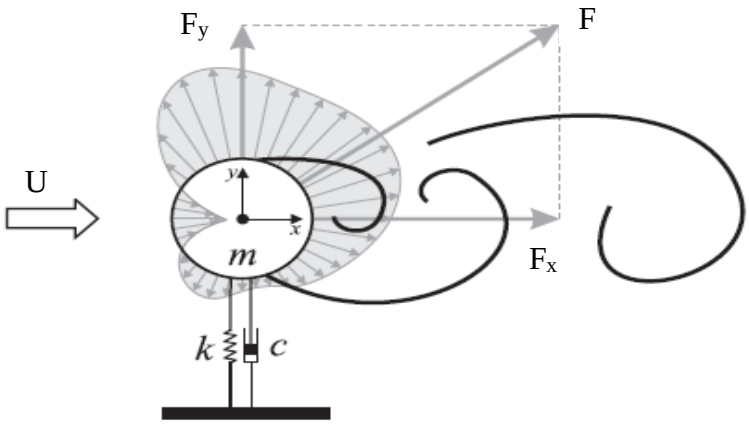

Figure 2.4: Harmonic oscillator model representing an elastically mounted cylinder. Adapted from (Drescher, 1956)

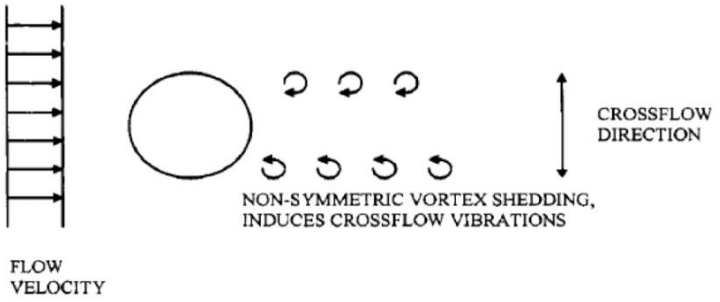

Figure 2.5: Cross-flow vortex-induced vibration by non-symmetric vortex shedding (Bai & Bai; 2005)

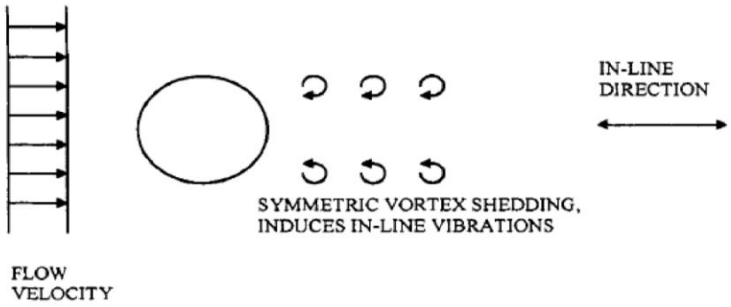

Figure 2.6: In-line vortex-induced vibration by symmetric vortex shedding (Bai & Bai; 2005)

Higher amplitudes of vibration in cross-flow direction have been documented by various experimental results in comprehensive review paper (Bai & Bai, 2005; King & Johns, 1976; Vandiver & Jong, 1987). King & Johns (1976) found that the in-line fundamental mode oscillations were excited at one quarter the velocity at which cross-flow oscillations were anticipated and the amplitudes in the in-line direction were lower than amplitudes recorded in cross-flow. Figure 2.7 shows a typical amplitude response as a function to reduced velocity. 'Hybrid' VIV can also happen when the in-line motion and cross-flow motion overlap. The cylinder is said to be vibrating in two degree of freedom, 2 DoF under this condition and is more common to happen in elastically mounted or a flexible cylinder. When the amplitude reaches its maximum, lock-in is said to happen.

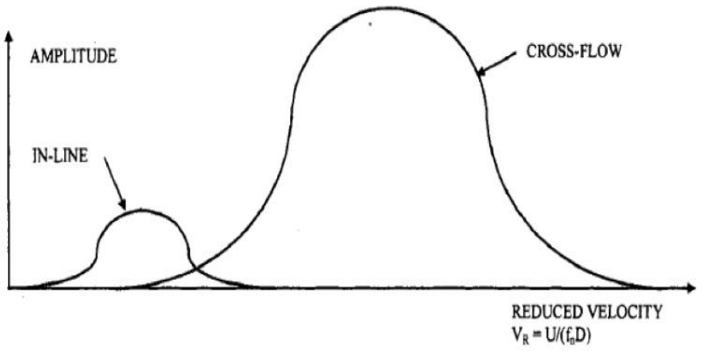

Figure 2.7: A typical amplitude response as a function to reduced velocity, V_r (Bai & Bai; 2005)

2.3.2 Lock-in

Faltinsen (1993), professor of Norwegian of Science and Technology, described the lock-in as resonant oscillations. Lock-in occurs when the natural frequency of the structure, f_n is in proximity with the vortex shedding, f_v, or in mathematical expression, $\frac{f_n}{f_v} = 1$. Both frequencies synchronise and large amplitude vortex induced structural vibration can occur. The vortices in lock-in condition can pack a colossal amount of energy. Besides the increase in vortex strength, consequences of lock-in also increase correlation length, in-line drag force, and lock-in bandwidth; all of which result in the increase of maximum amplitude. Lock-in has been observed in many laboratory experiments (Chen, 1987; Bernitsas et al., 2008; Blackburn & Henderson, 1996; Raghavan & Bernitsas, 2011). Figure 2.8 shows an experimental results produced by Blackburn and Henderson (1996). As seen in Figure 2.8, the amplitudes hit a record high when the ratio of natural frequency and the vortex shedding frequency are in vicinity to 1. It is predicted lock-in will commence starting at $V_r \approx 5$ and continue until $V_r \approx 7$ based on the St and V_r equations under the presumption of 0.2 St.

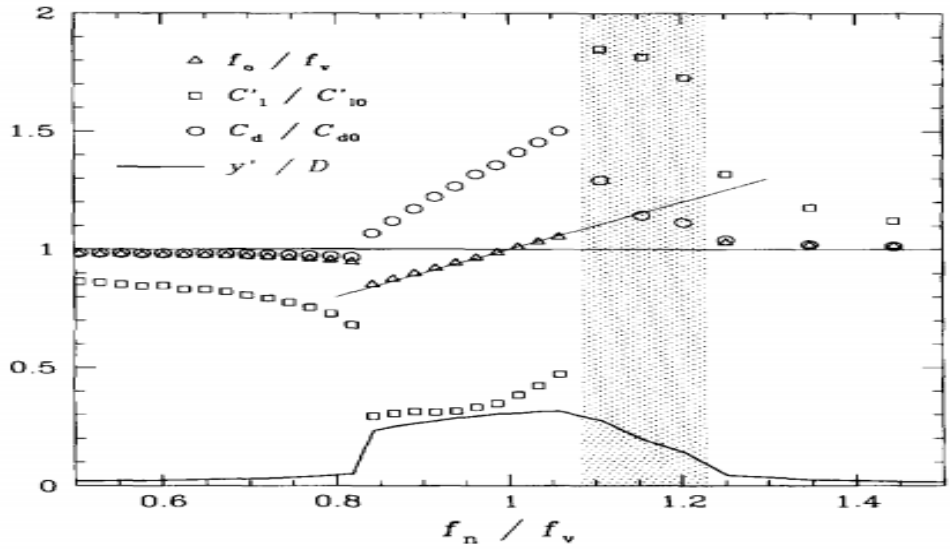

Figure 2.8: Cylinder response to the ratio of natural frequency and the vortex shedding frequency (Blackburn & Henderson, 1996)

Lock-in phenomenon is deemed dangerous and can bring catastrophic failure to the engineering structure as witnessed on the Tacoma Narrows Bridge and the cooling towers in Yorkshire (Ford, 1994). Therefore, as a means to fully understand the mechanism behind the lock-in condition, researchers have been focusing on the structural part of the cylinder and started with the simpler case of a classic spring-mounted rigid cylinders (Blackburn & Henderson, 1996; Khalak & Williamson, 1997; Khalak & Williamson, 1999). By using the spring-mounted rigid cylinders, it is easier to control the setup of the experiments with meticulously planned conditions. It was found that the mass ratio, m^* is critical in determining the lock-in bandwidth or the synchronization region. Bearman and Obasaju (1982) discovered that the low mass ratio cylinders have considerably larger lock-in bandwidth than their high mass ratio counterpart. As witnessed by them in their experimental results, the lock-in bandwith was found to increase with increasing response amplitude. It is easy to see that the lower mass ratio cylinders, require lesser energy to make vibration of the cylinder because it is lighter compared to higher mass ratio cylinders. Thus, it is able to achieve the maximum amplitude (lock-in) more effortlessly at a wider range of reduced velocity, as opposed to the higher mass ratio cylinders. The mass ratio is defined as the ratio of the cylinder's mass to the ratio of displaced fluid due to the solid cylinder and is given with the equation as below:

$$m^* = \frac{m}{\frac{1}{4}\pi\rho_{fluid}D^2} \tag{2.6}$$

2.4. Kinetic Budget Energy Equations

Though turbulent flow has often been described as "irregular" in time and space on a generic term, it actually contains vastly organized and near regular structures (Turbulence Handbook for Experimental Fluids Mechanics Professionals version 1.0, 2012). It is after all, these characteristics which promote molecular transport mechanisms make the turbulent flow capable of mixing and transferring mass much efficient than laminar flow.

Under mathematical term, turbulent flow can be described using a set of Navier-stokes equations coupled with a continuity equation. As it is impractical to provide solutions for instantaneous states, Reynolds formulated the 'Reynolds Decomposition Method', which accounts for the calculation of statistically mean states. Reynolds Decomposition Method describes the velocity, $u(x,t)$ as:

$$u(x,t) = \overline{U(x,t)} + u'(x,t) \tag{2.7}$$

Where $\overline{U(x,t)}$ is the mean flow and $u'(x,t)$ is the fluctuation component.

Apart from that, the Reynolds Decomposition Method can also be applied to pressure, p = $\bar{P} + p'$ or viscous tensor $\tau_{ij} = \bar{\tau}_{ij} + \tau'_{ij}$.

The behaviour of fluctuation quantities can be described by applying the Reynolds Decomposition Method to the Navier-Stokes equations and after a series of simplification, the Kinetic Energy Budget which describes the energy of turbulence is formed. Since Kinetic Energy Budget provides insight on how the turbulence is distributed after being produced from the mean flow, there exists the Kinetic Energy Budget for the mean flow and the Kinetic Energy Budget for the turbulent flow, both of which compliments each other in the process of examining the transfer of turbulence energy. The Kinetic Energy Budget of mean flow is:

$$\frac{D}{Dt}\left(\frac{1}{2}U_i^2\right) = \frac{\partial}{\partial x_j}\Big(\underbrace{-\frac{PU_j}{\rho_o}}_{\text{I}} + \underbrace{2\nu U_i E_{ij}}_{\text{II}} - \underbrace{\overline{u_i'u_j'}U_i}_{\text{III}}\Big) - \underbrace{2\nu E_{ij}E_{ij}}_{\text{IV}} + \underbrace{\overline{u_i'u_j'}\frac{\partial U_i}{\partial x_j}}_{\text{V}} - \underbrace{\frac{g}{\rho_o}\bar{\rho}U_3}_{\text{VI}} \tag{2.8}$$

The left-hand side describes the rate of change of the mean kinetic energy while the first three terms – I, II, III on the right-hand side represents the transport terms. They represent the transportation of energy by the pressure forces, viscous forces and the Reynolds stress forces respectively. In other words, they represent pure diffusion transfers. Therefore, the most important terms in this equation are term IV and term V which represents the viscous dissipation of the mean flow and the transfer between the mean flow and the fluctuating flow (loss of kinetic energy from the mean in this case) respectively. Term VI represents the loss of energy due to gravity in the vertical direction. However, term IV and VI are normally not important in the mean flow as its contribution to the losses are relatively small compared to term V.

One will notice the same set of equation 2.8 reappears in the Kinetic Energy Budget of turbulent flow except with the sign of the term V reversed.

$$\frac{D}{Dt}\left(\overline{\frac{1}{2}u_i'^2}\right) = -\frac{\partial}{\partial x_j}\Bigg(\underbrace{\overline{\frac{pu_j'}{\rho_o}}}_{\text{I}} - \underbrace{2\nu\overline{u_i' e_{ij}}}_{\text{II}} + \underbrace{\frac{1}{2}\overline{u_i' u_i' u_j'}}_{\text{III}}\Bigg) - \underbrace{2\nu\overline{e_{ij}e_{ij}}}_{\text{IV}} - \underbrace{\overline{u_i'u_j'}\frac{\partial U_i}{\partial x_j}}_{\text{V}} + \underbrace{g\alpha\overline{\omega T'}}_{\text{VI}} \qquad (2.9)$$

Again, the first three terms on the right-hand side represents the transport terms as is appeared in the Kinetic Energy Budget of mean flow. Term IV represents the viscous dissipation. As opposed to the case for the Kinetic Energy Budget of mean flow, the viscous terms, term IV, are important to the Kinetic Energy Budget of turbulence flow as it is not insignificant compared to the shear production (Term V) and it signifies a drain of turbulent energy. As mentioned in the preceding section, the shear production (Term V) also appears in the Kinetic Energy Budget of the mean flow, but with a positive sign. This being the $u_i'u_j'$ is normally negative in value due to the anisotropic character of turbulence. Therefore, the production term, $-\overline{u_i'u_j'}\frac{\partial U_i}{\partial x_j}$ is generally positive in the Kinetic Energy Budget of turbulent flow, signifying of an energy supply from the mean flow to the turbulent flow. When comparing the Equation 2.8 and 2.9, it can be understood that the transfer of energy between the mean and turbulent flow can only be done through the term V, and therefore is often labelled as the production term. Term VI is the buoyancy production from gravitational potential energy of the mean flow to the turbulent flow.

The Kinetic Energy Budget equations are useful in 'visualizing' the nature of turbulence and is especially useful in examining the level of turbulence energy produced by the rigid and flexible cylinders through evaluating the production term. In the current work, attention is given to the production term to understand the distribution of the energy by the rigid and flexible cylinders.

2.5. Flow Around Finite Circular Cylinder

As circular cylinder is chosen as the sole geometry of the flexible protruding surface, it is necessary to tackle on the phenomenon of flow past through a rigid finite circular cylinder as a reference to understanding flow past through a flexible finite circular cylinder. Research studies on flow around an infinitely long circular cylinder has always been abundant and has brought detailed knowledge to the mass people. However, a world with only problems and situations revolving around infinitely long cylinders is perhaps a bit too ignorant. With the development of high-speed computer, computational fluid dynamics software and highly sophisticated non-intrusive instrument, research studies on flow around finite cylinder was made possible.

In the current study, the cylinder is mounted perpendicular to the flow and its length extends through the boundary layer developing on the flat plate. The free end of the cylinder is exposed to the oncoming flow, making the flow effectively three-dimensional due to the significance of the end effects to the flow. While on the opposite site, the base of the cylinder is exposed to the boundary layer flow (see Figure 2.9). The *AR* of the cylinder is defined by its length over diameter ratio, $AR = L/D$.

The problem with finite cylinder is complicated as not only the free end conditions are hard to predict, the base of the cylinder, known as the cylinder wall junction, is also susceptible to the boundary layer of the oncoming flow. The flow in this particular region has been studied in Agui & Andreopoulos (1992) and Graf & Yulistiyanto (1998). The fluid near the wall, being obeyed by the no-slip condition at the wall, has a lower velocity flow inside of the boundary layers. This causes the fluid to recirculate at the leading edge of the cylinder, forming a type of vortex called horseshoe vortex. The rotating and rolling up actions can cause tendency of lifting away from the ground plane downstream as the

wall boundary layer separates in the presence of an adverse pressure gradient. Nevertheless, a nearly two-dimensional region at the mid-height span of the cylinder where the typical alternating Kármán vortices are formed will still exist if only the cylinder is long enough to have a mid-height region free from any end effects. Apelt and Fox (1992) regarded an infinitely long cylinder that has *AR* over 20 is free from any end effects. Okamoto and Yagita (1973), Park and Lee (2000), Roh and Park (2003) had studied the influence of end effects to the flow experimentally. They concluded that the central region that is free from the end effects starts to form at $AR > 3$. As the *AR* increases until $AR = 20$, the influence of end effects are so small to be considered to be two-dimensional (Apelt & Fox; 1992).

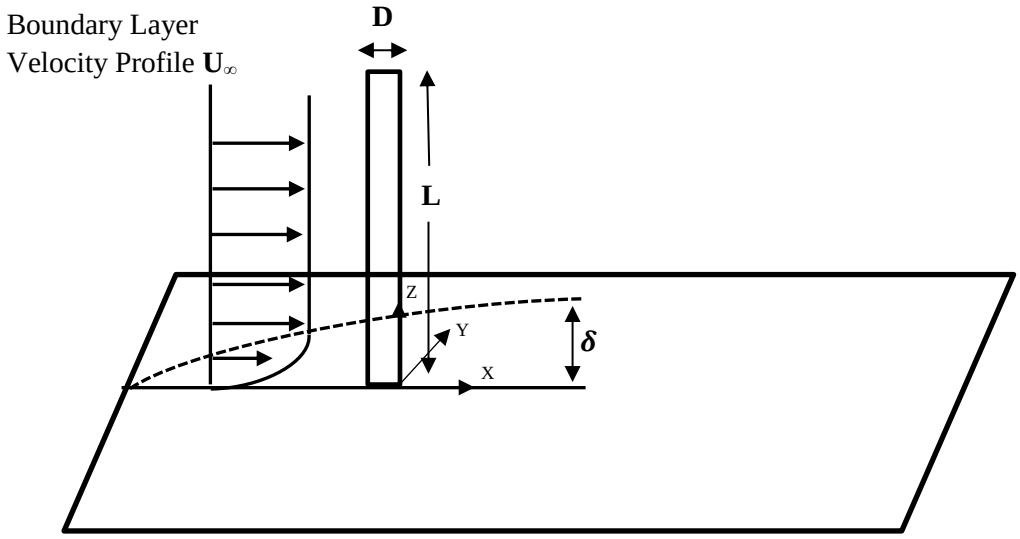

Figure 2.9: The boundary layer velocity profile of the flow and the finite circular cylinder (also known as cantilever)

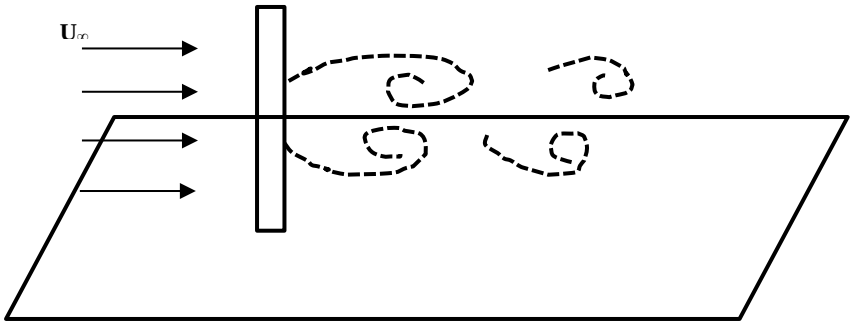

Figure 2.10: Kármán vortices at the central span of a finite cylinder

The end effects of a finite cylinder are highly dependent on the *AR* of the cylinder and the boundary layer thickness on the ground plane, δ/D as the reattachment of the separated flow can be influenced by those parameters. Though there are quite a few numbers of researchers actively involving in the research of end effects, the flow structure in this region remain speculative and need additional experiments or simulations to verify their existence or structure, particularly the origin of the side-tip or trailing vortices. Despite the inconclusive results for detailed flow structure, it showed that the tip vortices are much stronger than the base vortices (Rostamy, 2012). This further motivates the study of finite cylinder as the flexible structure to enhance the strength of the vortices as opposed to infinite cylinder.

When a free end of the finite cylinder, which has an *AR* greater than the critical *AR*, is exposed to the oncoming flow, there is a pair of counter-rotating trailing vortices exists near the tip. The formation of these vortices are due to a phenomenon called upwash, which the upstream flow is associated with a weak upward-directed local velocity field at the free end. Kawamura *et al.* (1984), one of the leading investigators in this field, investigated the flow around a finite circular cylinder with *AR* = 1, 2, 4, 6, and 8 in subcritical regime ($Re_D = 3.2x10^4$) in 1984 reported that part of the approach flow travels up to the cylinder tip with accelerated speed (upwash) and separates from the leading edge of the free end. As the flow passes over the free end, downwash happens when the flow is brought down into the low-pressure region, immediately behind the cylinder (see Figure 2.11). The combination of these upwash flow on the side and downwash flow at the centre interacts to form two counter-rotating trailing vortices (see Figure 2.12) (Kitagawa, 2002). Furthermore, Graf and Yulistiyanto (1998) reported that the part of the oncoming flow near the base moves downwards as it nears the cylinders and recirculates upstream of the cylinder-wall junction. It is there, where the horseshoe vortex is formed and loop around the cylinder in the downstream direction. Park and Lee (2000, 2004) also reported the similar flow pattern in their experimental results during their investigation on circular cylinders with *AR* = 6, 10 and 13 at $Re_D = 2x10^4$ and $7.5x10^3$.

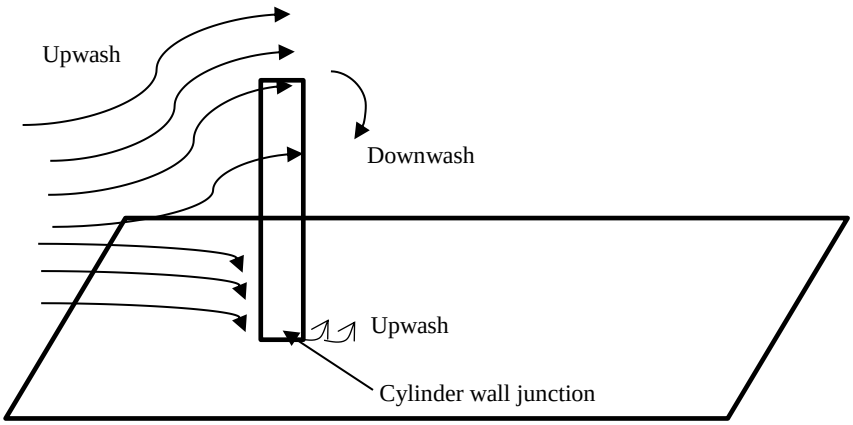

Figure 2.11: Upwash and Downwash formation of the flow near the free end

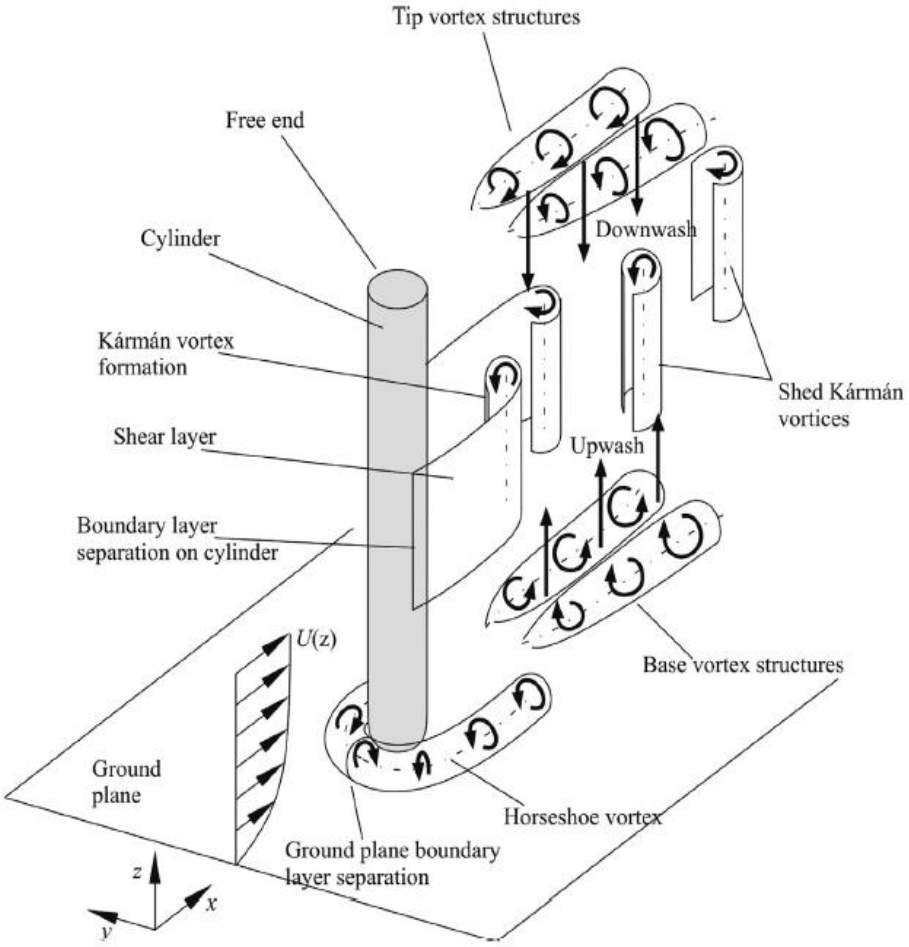

Figure 2.12: Schematic diagram of the flow field for finite circular cylinders greater than the critical aspect ratio (Sumner, 2013)

The flow structure for finite cylinder with lower *AR* on the other hand, shows a drastic change in the wake structure. Taniguchi *et al.* (1981) and Okamoto and Sunabashiri (1992), Okamoto and Yagita (1973) discovered a distinct wake structure in the near wake region for finite cylinder with *AR* lower than the critical *AR*. That distinct wake structure has been referred as arch vortex or mushroom vortex by some researchers (see Figure 2.13). As shown in the schematic (Figure 2.13) by Pattenden *et al.* (2005), the oncoming flow separates from the leading edge of the cylinder's free end and a recirculation zone forms on top of the free end surface. There is a reversed flow at the centreline of the free end surface. However, the results from Lee and Wang (1987) showed no trailing vortices and Kármán vortices associated with the arch vortex.

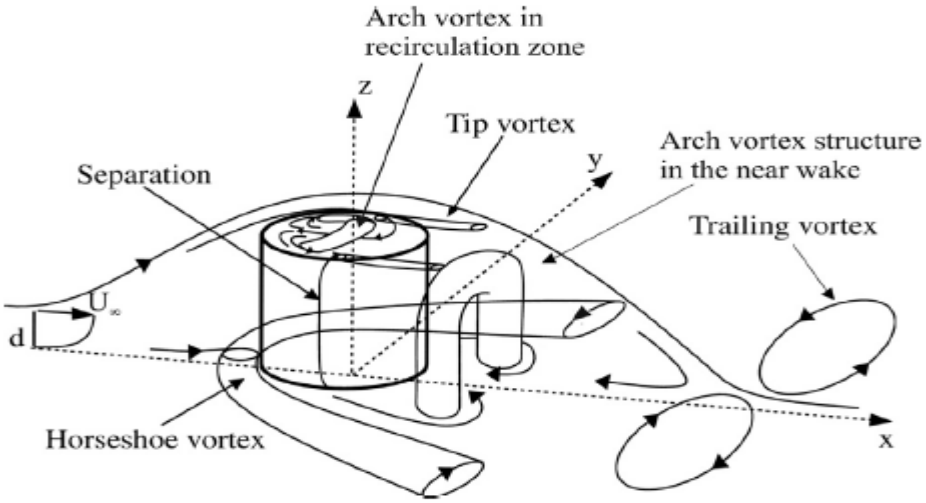

Figure 2.13: Schematic diagram of arch vortex formation for finite cylinders lower than the critical aspect ratio (Pattenden *et al.*, 2005)

2.6. Summary of Chapter

This chapter provides the necessary background theories to aid in understanding and comprehending the problem statement of the current research. The governing parameters available in this research problem are discussed. Next, a basic concept of bluff body vortex shedding is introduced. As one of the key aspects of flexible cylinder is to utilize the VIV phenomenon, a brief concept of fluid-structure interaction is also presented. It is then followed by introducing the Kinetic Budget Equations to discuss the fundamental

problems associated with the turbulent flow. The equations provide information that viscous loss is unavoidable. It is identified that it will be more useful to increase the turbulence production produced by the cylinder under the same flow condition.

The flexible protruding surface is introduced to potentially overcome the mentioned problems of the conventional rigid protruding surface. The turbulence production term from the Turbulence Budget Energy equations is focused to provide the 'strength' of the turbulence produced by flexible and rigid protruding surface. Lastly, it is followed by a brief concept of flow around a finite circular cylinder to understand the tip effects better before focusing onto the literature review, which will be presented in the next chapter.

CHAPTER 3

LITERATURE REVIEW

There has been considerably large amount of efforts in studying three-dimensional flow in the past decade, in particular to the flow near the free end of a circular cylinder. Efforts are put into the free end due to the exclusively distinctive free end effects only a finite cylinder possess. Intrigued by the free end effects, researchers have focused intensively on the flow structure around the finite cylinder. The changes affected by or related to the free end effects such as boundary layer thickness, aspect ratio, vortex shedding and surface pressure and drag reduction are presented in this following section. The turbulence characterises of the tip vortex behind the finite cylinder are reviewed, even though there are very less studies on the flow dynamics aspect. Furthermore, since this results also involve the presence of vibrating finite cylinder, the wake structure and its associated effects are reviewed as well. However, as there are too little literature or research that resemble the condition of current work/set-up, which is free-oscillating finite cylinder, the studies of the elastically mounted cylinder by VIV will be reviewed under this section as well. As this research mainly study the flow dynamics around a vibrating finite cylinder, the focus will be on the flow dynamics due to VIV; therefore, the wake structure and the turbulence characteristics are the primary aspects to be reviewed. Though there are numerous studies on the structural dynamics of the elastically mounted cylinder, they are not the aspect to be considered in this review.

3.1. Flow Field Behind a Finite Cylinder

As been presented in Chapter 2 the flow field around a finite cylinder, it is clear that the additional tip effects generated by the free end add a lot of complexity to the flow as it no longer consists of just Kármán vortices as witnessed by Sumner (2013). Near the cylinder's free end exists a vortex pair that is counter-rotating in nature and curved downwards at the symmetry line (Etzold & Fiedler, 1976). Below the free end region, the vortex is shed periodically, similarly to the classic Kármán vortex. In other words, the

wake becomes so complex that there exist two proposed models that describe the vortical structures at the free end. The complexity arises not because of the vortical structures near the free end itself; rather the interaction of these vortical structures that exist only in the three-dimensional flow.

Besides the trailing vortices model (see Figure 2.12) by Sumner *et al.* (2013) and Donnert *et al.* (2007) that explains the distinct wake structure at the free end, Okamoto and Yagita (1973), Lee and Wang (1987), Okamoto (1991) Sakamoto and Arie (1983), and Johnston *et al.* (1998) suggested the absence of trailing vortices. Instead, it is suggested that the Kármán vortices which is delayed near the free end, resulting in the delayed Kármán vortices to be inclined and attach to the cylinder near the free end region. Heseltine (2003) later supported their statement through his master's research on the flow around a circular cylinder with a free end which was conducted experimentally with seven-hole pressure probe. His speculation was based on the fact that the delayed Kármán vortices that is shed later at the free end must be linked to the ordinary Kármán vortex since a vortex filament cannot end in a fluid. Moreover, the simulation results of vorticity iso-surface visualization in Figure 3.1 by Afgan *et al.* (2007) showed agreement with the latter model. Despite several new findings which are in agreement to the model without the trailing vortices, there are few researchers who continue to adopt the model by Sumner *et al.* (2013) in their literature review including Sumner itself. Nevertheless, the vortical structures at the free end remains a task for researchers to describe.

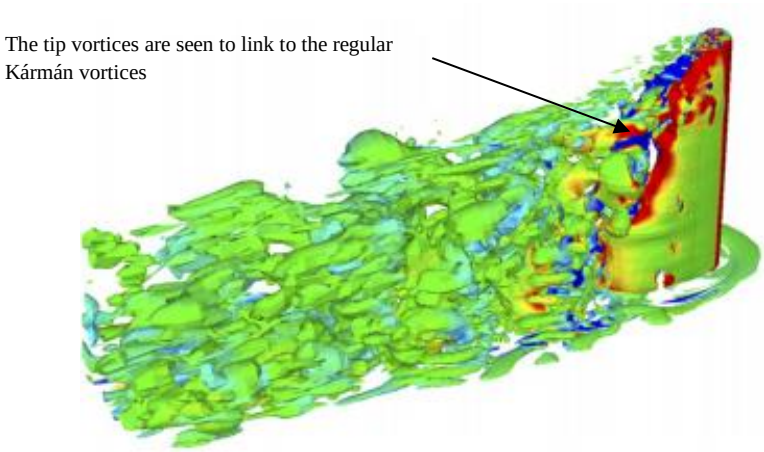

Figure 3.1: Vorticity iso-surface via LES for cylinder of *AR* = 10. (Afgan *et al.*, 2007)

3.1.1. Boundary layer thickness

The wake of the finite circular cylinder is heavily dependent on many parameters. Apart from the Reynolds number, cylinder aspect ratio, and the velocity profile of the oncoming flow, the relativity to the boundary layer thickness of the oncoming flow also has a significant role in determining the reattachment. Inside a boundary layer viscous effects are important as the tangential shear stress at the wall, $\tau_w = \mu\delta u/\delta y$, depends on the velocity gradient, $\delta u/\delta y$. The existence of a boundary layer is after all the reason to flow separation. The sensitivity of the boundary layer thickness that reacts to different values of δ/H and δ/D amplifies in the case of finite cylinders. Kawamura *et al.* (1984) noticed in his experimental results that the ratio of boundary layer height to span, δ/H determines the aspect ratio where vortex shedding is suppressed. Sumner *et al.* (2004) reported that larger δ/H values may influence the formation of vortex cells along the cylinder's span.

Porteous *et al.* (2014) investigated the wake dynamics of a circular finite cylinder (AR = 18.2) influenced different boundary layers. In his studies, two conditions – low thickness turbulent boundary layer (δ/H = 0.1 and $\delta/D = 1.4$) and high thickness turbulent boundary layer (δ/H = 0.26 and $\delta/D = 4.4$) were performed in a wind tunnel. The author concluded that the junction region for the high thickness turbulent boundary layer experienced higher overall turbulent intensity and lower frequency shedding. Surprisingly, it was interesting that the results showed that the free end region experienced a higher mean velocity and less overall turbulent intensity despite being far away from the boundary layer. The midspan of the cylinder remained unchanged.

This could largely be due to the reattachment of the separated flow at the free end. Kawamura *et al.* (1984) found that the reattachment occurred for the highest *AR* (AR = 8, δ/H = 0.125) and the lowest *AR* (AR =1, δ/L = 1) but not for the intermediate cylinder (AR = 4, δ/H = 0.25) in their flow visualization results. Table 3.1 compiles some of the experimental studies of finite circular cylinder in relation to the influence of boundary layer thickness.

Table 3.1: Experiments on finite cylinder by various authors

Authors	*AR*	δ/*H*		δ/*D*		Re	Measurement techniques	Findings
Kawamura *et al.* (1984)	1	1.01	0.53	1.01	0.53	$3.2x10^4$	Dye visualization and hot wire anemometer and surface pressure	Critical aspect ratio happens at $AR \geq 6$
	2	0.51	0.26					
	4	0.25	0.13					
	6	0.17	0.09					
	8	0.13	0.07					
Hain *et al.* (2008)	1	0.25		0.25		$1x10^5$	Tomographic and time resolved PIV in the free-end region	Low-aspect ratio shows high unsteadiness of separation on the free end's surface of cylinder
Rödiger *et al.* (2007)	2	0.184		0.092		$2x10^5$	Oil film visualization and surface pressure	Horse-shoe vortex on the ground
Donnert *et al.* (2007)	2.5	0.1		0.25		$4.4 x10^4$	Dye visualization and tracer concentration measurements	Significant upward motion (horse-shoe) exists for $AR = 2.5$ and vice versa for $AR = 5$
	5			0.5		$2.2x10^4$		
Rostamy *et al.* (2012)	3	0.54		1.6		$4.2 x10^4$	PIV	Span of free end effect is 3*D* from free end. Below critical aspect ratio ($AR \leq 5$) does not apply.
	5	0.32						
	7	0.23						
	9	0.18						

3.1.2. Critical aspect ratio

The wake structure differs according to below and above the critical aspect ratio. From the various studies by several authors, the value of critical aspect ratio seems to be sensitive to experimental conditions, especially the relative thickness of the boundary layer (Sumner *et al.*, 2004; Luo, 1993). The critical aspect ratio varied from AR = 1-7 in many literatures, which is a wide range. Fox and West (1993) showed for a small δ/D and δ/H, the disturbance of the end plate can extend to a distance of 3.5D along the span of the cylinder. For large δ/D and δ/H, the critical aspect ratio increases with δ/D and the Strouhal number increases to near infinite cylinder (two-dimensional) value when δ/H decreases. When a cylinder at a very low AR is immersed in an atmospheric boundary layer, the vortex formation length, the width of the near wake and the value of Strouhal number at mid-height are reduced, comparable to the case of small δ/D and δ/H (Taniguchi *et al.*, 1981; Park & Lee, 2002). Liu *et al.* (2005) supported that a two-

dimensional region exists when the *AR* is greater than the critical aspect ratio but the area of the two-dimensional region decreases when the Re increases. It should however be noted that the range of critical aspect ratio is only loosely defined based on the observation of the wake structure.

It can be seen that the critical aspect ratio is sensitive and scales with the boundary layer thickness and Re because the *AR* has to be large enough in order to sustain the two-dimensional region. A lower *AR* or *AR* lower than the critical aspect ratio that is put in a higher Re and a thicker boundary layer signify that the region of free end effects will engulf the whole span of the cylinder, supressing the two-dimensional region

3.1.3. Vortex shedding

It has been established in various studies in literature that the highly three-dimensional tip vortices interrupt Kármán vortex shedding in the three-dimensional effective region (near free end). Lee and Wang (1987) reported that for circular cylinders of $AR > 7$, there is a dominant frequency at mid-height location which lies unchanged with *AR*. The dominant frequency is weak and less obvious for $AR < 7$. They found that the vortex shedding is supressed near the free end as no dominant frequency within 3.5*D* is detected. The result is consistent with result from Okamoto and Yagita (1973), which in their paper, they explained that the region where tip effects are present may extend about 2*D* from the free end, and the region of lower Strouhal number may range between 2*D* and 4*D* from the free end. Farivar (1981), Kawamura *et al.* (1984), Lee and Wang (1987) and Luo (1993) regarded that the suppression of alternate Kármán vortex shedding is due to the interference of tip vortices and the associated downwash flow with the separated shear layers which formed along the sides of the cylinder. As a result, the shear layers are unable to roll-up. As the location moves away from free end (more than 2*D* to 4*D*), the Strouhal number increases to $St \approx 0.14$. Lee and Wang (1987) also reported that no vortex shedding is detected for $AR < 3$ in their experimental results. Sumner *et al.* (2004) however, found the Strouhal number to be at $St \approx 0.16$ (though at a very vague vortex shedding peak signal in power spectra graph for $AR = 3$) at mid-height for $AR = 3, 5, 7, 9$ in their experimental results collected using constant-temperature anemometer. The existence of

Kármán vortex shedding from the vague and weak peak power spectra is debatable in the literature.

At the free end, some researchers have identified an additional, lower constant frequency component which they attributed to suppression of regular vortex shedding by the tip vortices (Lee & Wang, 1987; Park & Lee, 2002). Park and Lee (2000) found that though the vortex shedding frequency and power spectra peak decrease near the free end, there exists a dominant 24 Hz signal which remain unchanged with *AR* in their experiments on circular cylinder of *AR* = 6, 10, 13. They suggested that the trailing vortices contribute to the dominant frequency. Apart from that, they also noticed that the shedding frequency decreases with decreasing *AR*.

There are basically four regions that single out the characteristic of the flow based on the Strouhal number collected by Budair *et al.* (1991). (i) Existence of tip effects within 2*D to 3D* of the free end where vortex shedding is suppressed. (ii) A non-shedding region where the frequency components are in-phase with each other at symmetrical positions across the wake centre-plane. (iii) A region 3*D* to 4*D* away from free end that has a vortex shedding near consistent with a Strouhal number, St ≈ 0.14. (iv) A region greater than 20*D* from the free end that behaves nearly like two-dimensional flow where the vortex shedding frequency is consistent to that of a two-dimensional flow.

3.1.4. Surface pressure and drag reduction

The surface pressure distribution of the cylinder has been studied extensively by Fox and West (1993), Park and Lee (2000), Luo (1993), and Afgan et al. (2006). Their results showed general agreement. Fox and West measured the pressure using Betz-type micro-manometer at various circumferential and one diameter intervals along the spanwise positions for cylinders of *AR* in the range 4 to 30 (see Figure 3.1(a) for the pressure coefficient, C_p of finite cylinder of *AR* = 10). Fox and West (1993) found that the pressure along the back of the cylinder decreases with an increase height of the cylinder. He stated that the pressure is seen less negative (lesser) at the free end region than that of two-dimensional region due to the presence of downwash from the free end. In addition, he also attributed the irregularities in the rear surface pressure are caused by the trailing

vortices. The results also showed that the C_P along the front of the cylinder increases to a positive pressure (see Figure 3.2 (a) and (b)). This might be attributed to the approaching flow that is perpendicular to the cylinder so that the dynamic pressure is converted to a static pressure along the front of the cylinder.

The same phenomenon is also discovered by Park and Lee (2000) where the rear end pressure is less negative in the free end region (see Figure 3.2 (b)). He reported that the less negative pressure resulting from the separated shear flow declining towards the downward direction and hence the suppression of regular Kármán vortex shedding. Luo (1993) supported the statement by stating that the shear layer separated from the free end can delay the flow separation along the spanwise direction of the cylinder and hence less negative wake pressure.

Afgan *et al.* (2006) performed a Large Eddy Simulation, LES on flow over a vertically mounted finite cylinder on a flat plate. His findings on the pressure distribution behind the cylinder do not differ much with the experimental values of Park and Lee (2000).

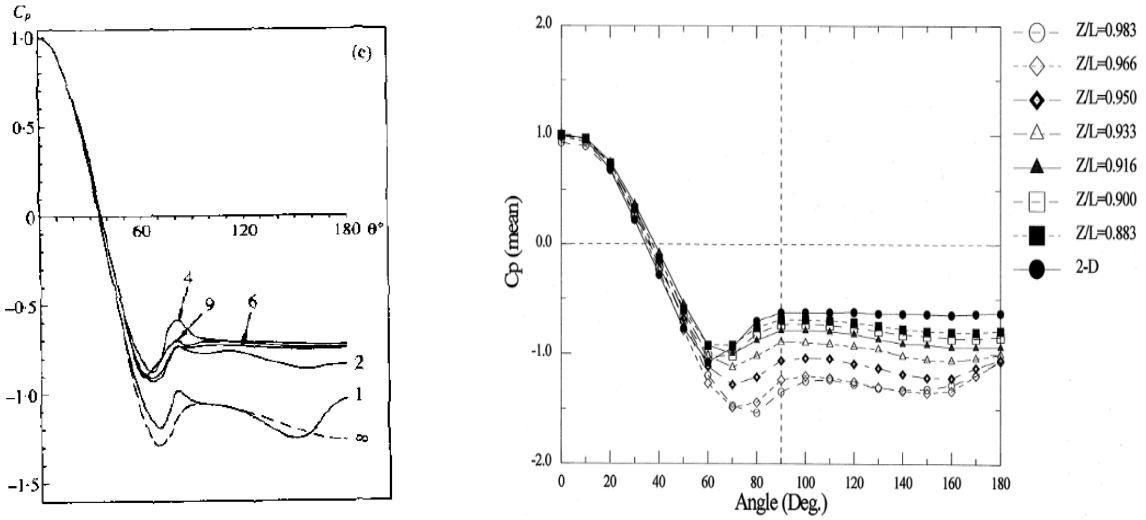

(a) (b)

Figure 3.2: (a) Circumferential distributions of the mean pressure coefficient measured at spanwise locationon the cylinder with *AR* = 10 (Fox & West, 1993) (b) Comparison of mean pressure coefficient distributions around the cylinder of *AR* = 10 (Park & Lee, 2000)

As always, drag is associated with the pressure drop because the existence of drag is due to the pressure drop. When flow separation occurs, the pressure losses in the wake due to eddy formation. As a result of the pressure loss, drag is formed due to the pressure difference. Interestingly, it has been reported by many researchers that the drag coefficient, C_D near the free end is normally at a lower value than the region regarded as infinite cylinder. Table 3.2 shows that the drag coefficient of the finite cylinder is lower than the infinite cylinder.

Fox and West (1993) found that the local drag at few distance from the free end is dependent to the *AR* for cylinders of $AR < 13$ and is relatively independent for cylinders of $AR > 13$. Maximum local drag value occurs near the free end and decreases dramatically along the span until in the vicinity of 4*D* from free end, after which it becomes nearly constant. The local drag begins with maximum and decreases rapidly along the span until near 4*D* from free end but starts to increase thereafter for cylinders of $AR > 13$, until the value of infinite cylinder, which is at ~1.2 for *Z/D* more than 20.

Sumner *et al.* (2004) noticed that the C_D is nearly the same (0.74, 0.78, 0.81) for $AR = 5, 7, 9$ expect a relatively lower C_D value at 0.61 for $AR = 3$. He postulated that the lower C_D value indicates a distinctly wake structure, which also corresponds to where the critical *AR* lies. It is speculated that the pressure can recover more completely after the separation due to the stronger downwash effect over the entire span at smaller *AR*. Thus, the lower C_D at lower *AR*.

Table 3.2: Drag coefficient for circular cylinder of different *AR* (Drag and Lift, 2015)

Body	Dimensional ratio	Datum area, *A*	Drag coefficient, C_D
Cylinder (right angles to flow) 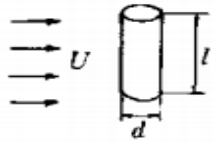	$l/d = 1$	dl	0.63
	2		0.68
	5		0.74
	10		0.82
	40		0.98
	∞		1.20

Kawamura *et al.* (1984) took investigation of the reduction in local drag near the free end and he relates the reduction of C_D to the decrease in flow separation at the side wall in the free end region. The delay of separation resulting from the decrease in separation velocity helps the recovery of pressure. Afgan *et al.* (2007) attributed the lower C_D at the free end to the better pressure recovery due to the stronger downwash effect.

3.1.5. Turbulence characteristics and flow visualization behind a finite cylinder

Despite the two different proposed models which describe how the tip vortex interacts, the tip vortices are known to have more turbulent energy than the regular Kármán vortices. The turbulence intensity has also been reported to increase considerably at the free end of the cylinder. In the recent work of Rostamy *et al.* (2012), they demonstrated that the streamwise turbulence intensity (u'/U) and wall-normal turbulence intensity (w'/U) are indeed higher at the free end and within the recirculation region on the wake centreline (y/D = 0). On the other hand, Park and Lee (2004) also showed in their results, that the turbulent kinetic energy is at its highest level at the free end for cylinder of AR = 6 at Re_D = 7500. Rostamy *et al.* (2012) noticed that the elevated turbulence intensity extends into the downwash region. One noticeable distinct pattern that separates the cylinder of AR = 3 from the rest is that the location of the highest wall-normal turbulence intensity moves downward and further away to a distance of x/D = 2. The location of the highest wall-normal turbulence intensity appears to remain at x/D < 2 as the AR of the cylinder increases.

Similarly, the Reynolds shear stress ($-\overline{u'w'}/U^2$) are also reported to be at a higher value in the experimental work from Rostamy *et al.* (2012). They noticed a region of positive shear stress and a region of negative shear stress at an evaluated value near the wake region. However, the region of positive shear stress is absent below the free end, leaving only the region of negative shear stress for cylinder of AR = 3. On the contrary, the positive shear stress is dominating the region just below the free end for AR = 9 but slowly decreasing in size and level as the AR decreases until it disappears at AR = 3. In their results, the Reynolds shear stress are found be at highest for cylinder of AR = 9 with the peak at 0.018. However, the Reynolds shear stress decreases as AR decreases. Besides,

according to Figure 3.3, Sumner *et al*. (2004) also showed in their experimental results that the vorticity contour is immensely elevated near the free end. Thus, the tip vortices can greatly improve the quality of mixing. However, due to the downwash phenomenon that is always present at the free end, the tip vortices are always brought downwards to the ground plane. Therefore, its influence could only impinge on fluid in the very near wake. The mean velocity, turbulence intensity and Reynolds shear stress distributions are similar for cylinders above the critical aspect ratio but dissimilar for cylinders below the critical aspect ratio (Sumner *et al.*, 2004; Adaramola, 2008).

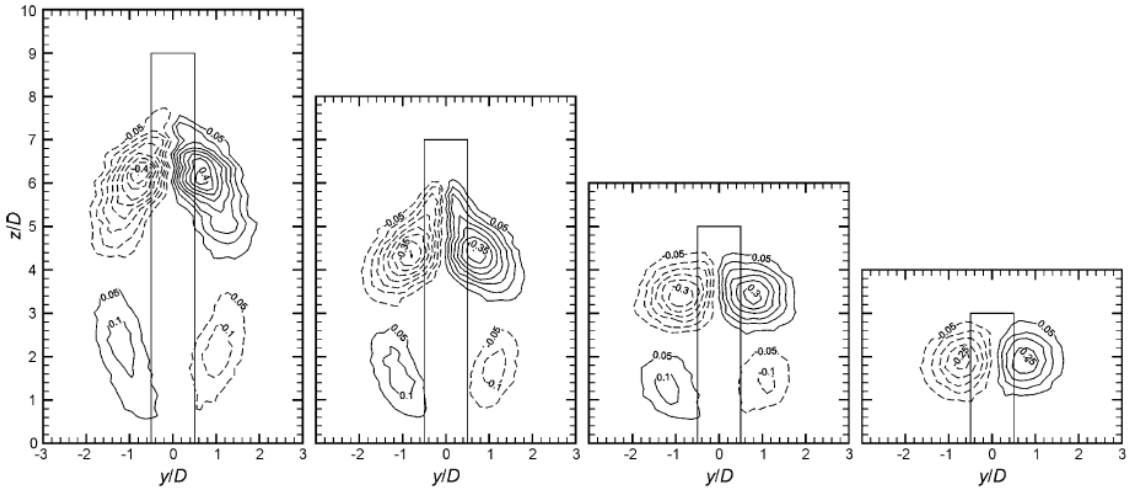

Figure 3.3: The non-dimensional, time-averaged, streamwise vorticity field at *x*/*D* = 6 (a) *AR* = 9, (b) *AR* = 7, (c) *AR* = 5 and (d) *AR* = 3. Vorticity contour increment is 0.05 and minimum vorticity contour is ± 0.05, solid lines represent positive counter-clockwise (Adaramola, 2008)

Being intrigued with the numerical results collected, some researchers started to performing qualitative research on the flow past cantilever cylinder. Park and Lee (2004) studied the flow visualization on cylinder with *AR* = 6 using a particle tracer method in a circulating water tunnel. They noticed that the trailing tip vortices are nearly symmetrical across the central plane in the near wake and have a similar size (see Figure 3.4 (a)). It is noticeable that the separated shear layer moves towards the central region, forming large recirculating flow rotating in a clockwise direction (see Figure 3.4 (b) and Figure 3.5). They attributed the downwash to the cause of trailing vortices. The irrotational flow at the downwash region affects vortex formation behind the cylinder and increases the vortex

formation length. The vortices increase in size and shift downwards as they travel further downstream.

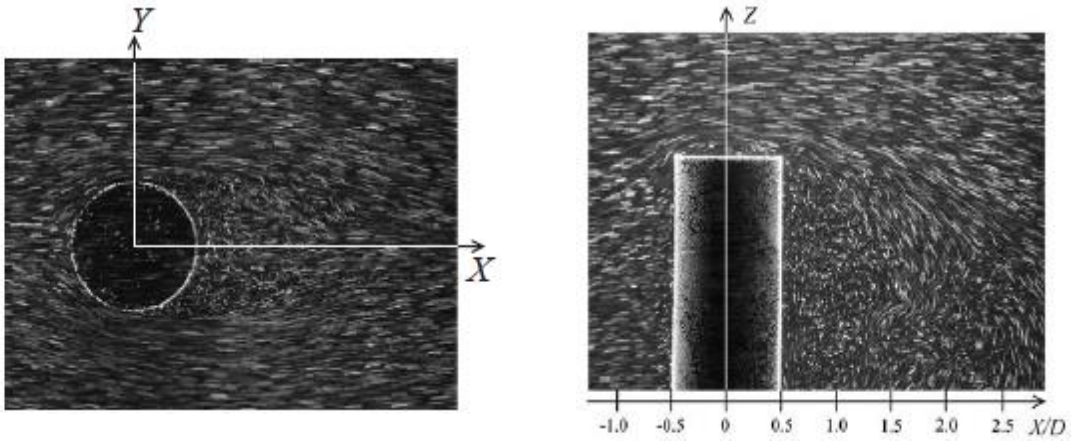

(a) (b)

Figure 3.4: (a) Top view of visualized flow in *x-y* plane (b) flow around finite cylinder at symmetrical plane. Adapted from Park and Lee (2004)

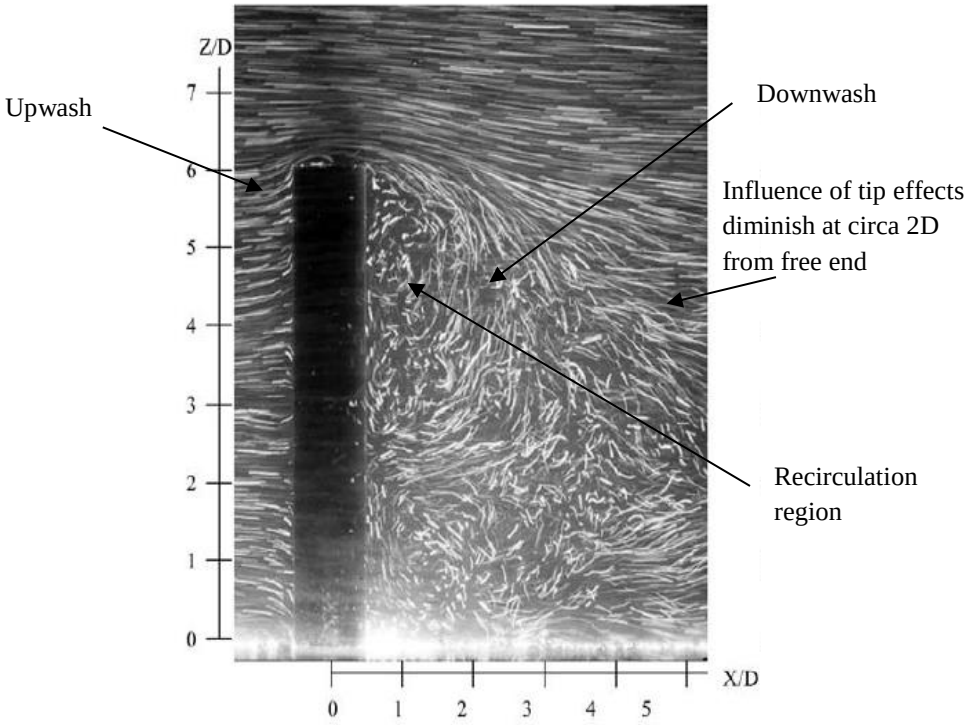

Figure 3.5: Flow visualization around the finite cylinder of *AR* = 6 (Park & Lee, 2002)

It has been well-documented that the wake structure of the flow around the finite cylinder is different for *AR* below and above the critical aspect ratio. The most notable change was the wake patterns where the downwash from the free end is dominant (the influence of downwash extends to the whole span of the finite cylinder until the base, leaving no room for upwash flow near the cylinder wall junction) for *AR* below the critical aspect ratio. Due to the strong downwash, the antisymmetric Kármán vortex shedding are also being suppressed. Okamoto (1991) referred this to the size of the recirculation region. The flow at the free end will reattach to the ground plane for small *AR* cylinders, resulting in the absence of upwash flow, if not very weak. When the upwash do exist for cylinder of *AR* above the critical aspect ratio, they originate near the ground plane and travel upwards towards the mid-height of the wake. When the tip effects seize at 3*D* to 4*D* from the tip (usually for cylinder of *AR* above the critical aspect ratio), the influence of downwash slowly decrease in strength from the free end to the base of the cylinder and reattachment of the end flow seize to occur. This observation is also consistent with the results from Rostamy *et al.* (2012). Sumner *et al.* (2004) also noticed the existence of an upwash flow originates from the base of the cylinder, allowing the making of a second pair of counter-rotating vortices (also known as base vortex structures) within the wall boundary layer in addition to the counter-rotating pair of tip vortex structures near the free end for *AR* = 5, 7, and 9 (see Figure 3.3). Apart from that, a strong Kármán vortex shedding signal is detected, further confirms the existence of the antisymmetric Kármán vortex shedding for *AR* = 5, 7, and 9 and vice versa for *AR* = 3.

3.2. Flow Field Behind a Vibrating Finite Cylinder

To date, there are less emphasis on the flow field behind a freely vibrating finite cylinder. This is especially true for experimental studies due to the feasibility and cost to investigate the flow properties. There are quite a few remarkable research studies (Raghavan & Bernitsas, 2011; Dahl *et al.*, 2006; Jeon & Gharib, 2001; Kang & Jia, 2013; Khalak & Williamson, 2004) on forced vibrating cylinders with either 1 DoF (either in-line or transverse to the flow only) or 2 DoF (both) on elastic supports and the focus was on the vortex structures in relation to the cylinder's structural properties. Though not as

comprehensive, some of the authors did briefly discuss the flow structures caused by the vibrating cylinder.

The wake of a cylinder that is oscillating in the direction transverse to the freestream direction can be significantly different than the wake of a non-oscillating cylinder depending on the oscillating amplitude. Williamson and Roshko (1988) analytically studied the structure of wakes produced under different oscillation conditions. The cylinder was forced to oscillate up to a desired amplitude so that the influence of the oscillating cylinder to the wake can be investigated in a more controlled condition. They identified several distinct distributions of vortices in the wake, which they referred to as wake modes and are shown in Figure 3.6. As introduced by them, the terminology of 2S, as depicted in Figure 3.6, refers to two single vortices per cycle, just like the classic Kármán street; whereas 2P refers to two vortex pairs formed in each cycle of body motion. They discovered that the wake modes are determined by non-dimensional parameters such as amplitude ratio, A/D and wavelength ratio, λ/D. The non-dimensional parameters that correspond to the wake modes region is indicated in Figure 3.7. The map was put together by them through experiments conducted over a range of 300 Re to 1000 Re. As can be seen from the map, higher amplitude of oscillation could yield a P+S vortex structure. Of course, it is subjected to the reduced velocity condition as well. Willamson and Govardham (2004) later continued the work started by William and Roshko (1988), also supported the findings and the map scribed by William and Roshko (1988). They identified the vortex structures in the wake of an oscillating cylinder to the reduced velocity and amplitude ratio and is shown in Figure 3.8.

Jeon and Gharib (2004) investigated the mechanism by which the oscillation of the cylinder determines the wake structure through a 2 DoF forced oscillations experiments. They learned that the wake vortex pinches off from the separated shear layer that supplies it with vorticity when the non-dimensional kinetic energy of the shear layer is lower than that of the forming vortex. It shows insight of the vortex pinch off timing. Therefore, they concluded that the resulting wake modes are determined by the flux of mass, momentum, energy and vorticity in the separated shear layers, which in turn is affected by the cylinder oscillations.

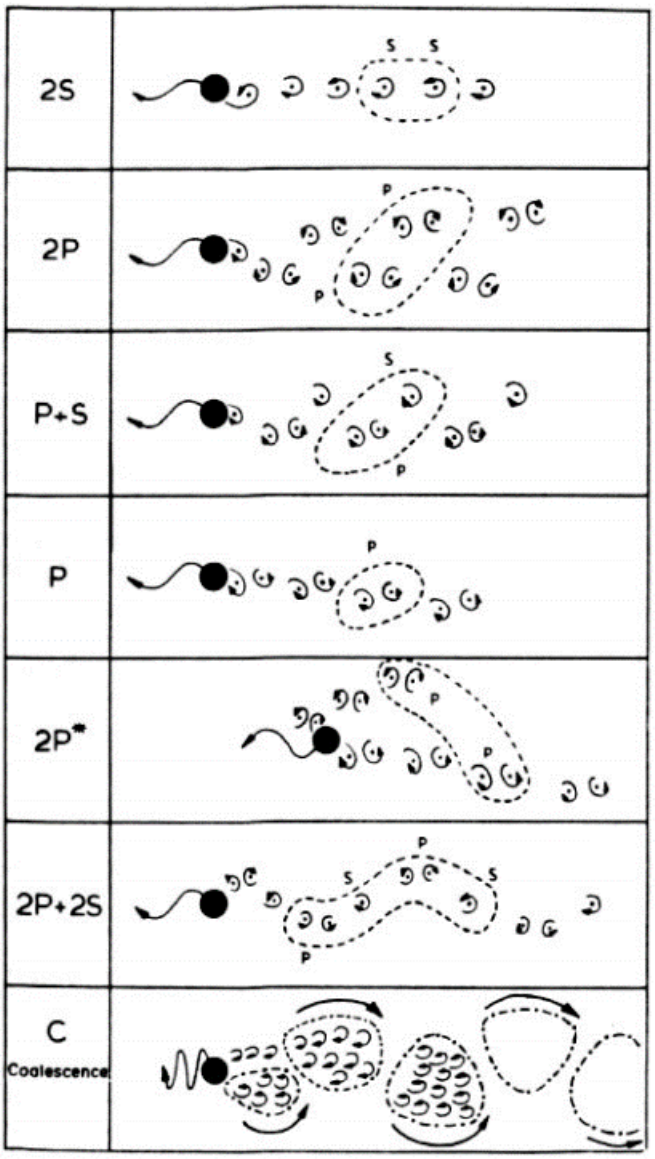

Figure 3.6: Sketches of the vortex shedding patterns for better illustration. S refers to a single vortex while P refers to a vortex pairs formed in each cycle (Williamson & Roshko, 1988)

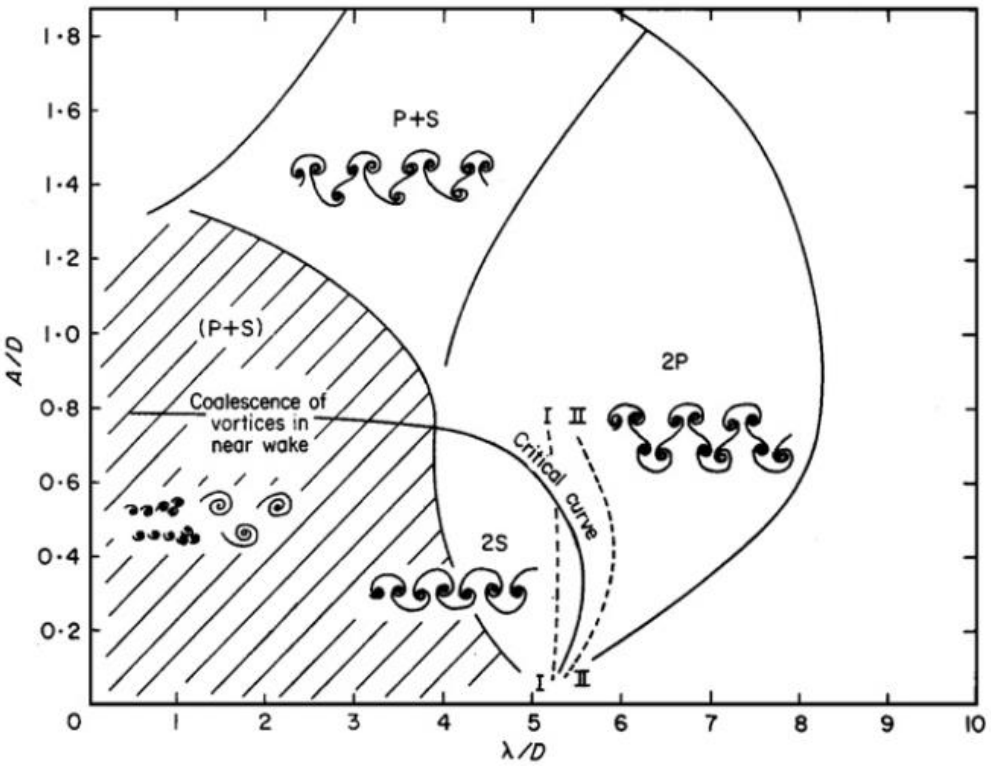

Figure 3.7: The map of regimes for vortex wake modes by William and Roshko (1988)

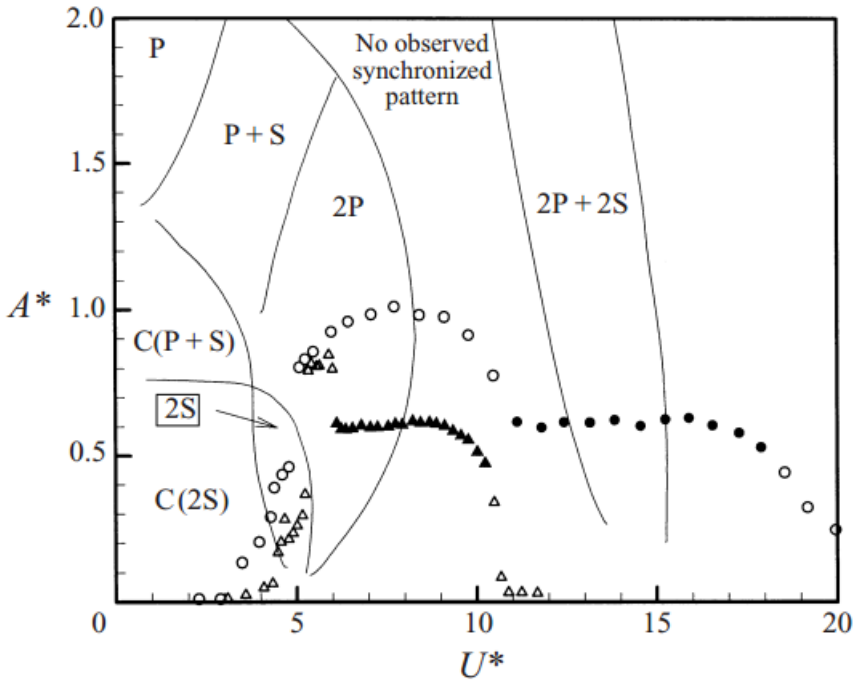

Figure 3.8: Vortex patterns as a function of amplitude ratio and reduced velocity (Williamson & Govardhan, 2004)

Govardhan and Williamson (2000 & 2001) studied the modes of vortex formation and frequency response of an elastically mounted rigid cylinder in a fluid flow using Digital Particle Image Velocimetry, DPIV. He found that a 2S vortex structure is formed at lower amplitude. At a larger amplitude, there exists a 2P vortex structure. The oscillating amplitude corresponds to 3 branches of oscillating mode – Initial branch, Upper branch and Lower branch. The initial branch represents the initial oscillation (therefore its amplitude is always low) while the upper branch represents the fully excited oscillating condition. The lower branch represents the condition when the oscillation starts to subside. It is worth mentioning that the branches of oscillating mode rely on the mass-damping parameter ($m^*\zeta$) and the Upper branch only appears in low mass-damping parameter. However, as this is on the structural part so the mass-damping parameter is not considered in this research, it will not be reviewed. Morever, similar phenomena are also observed by Lam *et al.* (2010) in his experiments using the Particle Image Velocimetry, PIV equipment. Besides the aforementioned phenomena observed by Govardhan and Williamson (2000 & 2001), they also noticed the P + S vortex structure exists at high amplitude, though this phenomenon only happens at lower reduced velocity.

Griffin (1971) found that the formation length, which is the location along the wake centreline where velocity fluctuations reach a maximum, on the velocity field of the forced vibration of a cylinder at low Re ≈ 200 reduce to half the value found for a rigid cylinder in his investigation through hot-wire anemometer. Besides that, he also observed that the velocity fluctuation was generally greater than a rigid cylinder.

Despite the major findings by some renowned researchers, they are all related to the elastically mounted cylinders which their both ends are fixed to the system's fixture, therefore no free end is exposed to the flow. This is because most of their work was motivated by the potential failure of marine engineering applications by VIV. As the experimental setup in this research work concerns flow past cantilever, the literature review might not be able to justify the condition of this research work in more exact manner. Moreover, the vibration of the flexible cylinder in this research work is not being restricted in any way, unlike the ones reviewed above. Nevertheless, there exists a few researchers who like to perform their investigations in a different approach.

Large amplitude tip vibration at around 1.5 to 1.6 *D* has been reported by Vickery and Watkins (1964) and King (1974) in one of their earliest studies. It was later supported by Pesce and Fujarra (2000), showing comparable tip amplitudes of around 1.7 *D.* In the case of flexible cantilever where it comprises of one fixed end and one open end, it cannot be thought equivalent to the elastically mounted rigid cylinder as the oscillating amplitude varies along the span (Fujarra *et al.*, 2001). Fujarra *et al.* (2001) conducted an experiment of flow past a flexible cantilever, which he restricted the vibrations of the cantilever to primarily transverse motion. They found that the transverse amplitude response of the cantilever has surprisingly modest similarity with the transverse vibrations of an elastically mounted rigid cylinder.

Prastianto *et al.* (2009) investigated the flow dynamics of a flexible free-hanging circular cantilever under VIV. Their results suggested the vortex structures are different along the span of the cantilever. They observed near the fixed end of the cantilever (cylinder-wall junction), 2S vortex structure is shed; whereas a 2P vortex structure is found near the free end. Since the amplitude varies along the span, it is thought to be logical as the vortex structures in the wake are dependent on the mode of cylinder oscillation (not solely).

The Reynolds normal ($\overline{u'u'}/U^2$) and shear ($\overline{u'v'}/U^2$) stress of a flexible cylinder has also been reported by Govardhan and Williamson (2001) to increase significantly compared to that of rigid cylinder. They first investigated the Reynolds shear stress of a rigid cylinder and compared with the results from Cantwell and Coles (1983). The periodic part of Reynolds normal and shear stress of both authors are a near match though the experiment conducted by Cantwell and Coles (1983) was much higher at Re = 140000. The peak total Reynolds stress is however much higher for the higher Re experiments. Govardhan and Williamson (2001) therefore concluded that the periodic part of Reynolds stress, which is generated from the repeatable large-scale coherent structures, holds true over the range of Re = 3900 to 140000. As the other component of total Reynolds stress – random part of Reynolds stress, gain strength from the increasing strength of the Kelvin-Helmholtz instability of the separating shear layer as Re increases, the total Reynolds stress value increases. They also compared the Reynolds normal and shear stress value of

vibrating cylinder to that of rigid cylinder and found that the largest increase in periodic part of Reynolds stress $(\overline{\tilde{u}\tilde{u}}/U^2)_{max}$ increases by 485%, $(\overline{\tilde{v}\tilde{v}}/U^2)_{max}$ increases by 100% and $(\overline{\tilde{u}\tilde{v}}/U^2)_{max}$ increases by 125% in the Lower branch.

3.3. Critical Thoughts and Identified Gap

The flow fields and the flow dynamics of the finite rigid and oscillating cylinders have provided essential and in-depth understanding towards this research project. Throughout the studies of relevant literature paper, it can be understood that the efforts that have gone into the three-dimensionality of the flow are critically in need. Though the research on flow past finite cylinder has started approximately thirty years ago, it has only been constantly active for the near two decades. The flow structures and the free end effects are clearly identified and supported with substantial evidence. In summary, the tip effects are the most distinctive feature to differentiate the finite (three-dimensional flow) and infinite (two-dimensional) cylinder.

The flow past a vibrating finite cylinder on the other hand, has also received equivalent attention after the catastrophe incident of the famous Tacoma Narrows Bridge. However, more attention was given to the structural dynamics as a means to suppress the VIV and hence the oscillation of the structure. Later, the underwater pipe which also creates VIV, sparked the interest of researchers to the field. Despite that, most of the published work are on two-dimensional – elastically mounted rigid circular cylinder where the oscillation response is uniform for the entire span.

In this current work, it involves a finite vibrating cylinder which has the free end exposed and different oscillating amplitude throughout the entire length from the highest amplitude at the free end and decrease gradually until static at the fixed end (the cylinder is not spring mounted). Though there have only been a few papers published regarding the wake structure behind the vibrating cylinder, their results and findings are reported to be consistent; thus, the findings on the wake structure could be considered established.

The research on the velocity field and on the aspect of turbulence characteristics are suffering from the attention of researchers in the field. To the best of the author's

knowledge, there are only two papers that were investigating the velocity field and its fluctuating velocity (turbulence) of the vibrating cylinder. The lack of attention to these aspects are appalling as Govardhan and Williamson (2001) themselves described the event – quote "The only detailed investigation of the velocity field (in the form of a set of velocity profiles) to our knowledge, was conducted by Griffin (1971), for the forced vibration of a cylinder at low Re ≈ 200." The time between the two published is remarkably long and no paper related to these aspects have been reported since (to the best of the author's knowledge). Nevertheless, it was fortunate that these papers have reported an escalation in the fluctuating velocity by vibrating cylinder. However, the values of the augmented turbulence are different for various conditions and it lacks the link between the structural mechanism and the augmented turbulence production. It is therefore existing the urge to bridge the gap between the structural mechanism to the augmented turbulence production to get further insight and control of the condition to gain desired turbulence. The current work is designed to lay a foundation and gain insight of the factors which influence the turbulence of vibrating cylinder.

CHAPTER 4

EXPERIMENTAL DESIGN AND METHODOLOGY

This chapter explains a detailed description of the experimental rig and apparatus used to perform the experiments. A description of the water tunnel and its flow quality are described in this chapter. Detailed information on the UVP and the transducer, which were the velocity measurement techniques used are presented in subchapter 4.3. The cylinder models and its specification related to the freestream conditions are described in this subchapter 4.4. Associated instrumentation such as the traverse, infrared thermometer and camera are described in subchapter 4.5 to 4.7. A detailed set-up of the experiments with schematic diagram are discussed in subchapter 4.8, followed by the post-processing procedure, which is the Reynolds stresses method, is explained in subchapter 4.9. Finally, a detailed uncertainty analysis of measurements and results parameters are presented in subchapter 4.10.

4.1. Water Tunnel

Experiments in the present study were conducted in circulating open channel water tunnel located at the Turbo Machine Laboratory of the Department of Mechanical at Universiti Teknologi PETRONAS (see Figure 4.2). The water tunnel was measured at 1.2 m (*W*) x 1.2 m (*H*) x 3 m (*L*) and has a test section of 0.2 m (*W*) x 0.2 m (*H*) x 0.75 m (*L*) (see Figure 4.1 for schematic diagram). The test section was fitted with tempered glass on one of the side wall, allowing complete view of the models for visualization purpose as well as visual inspection of the probe position (see Figure 4.3). The water tunnel, equipped with a 1200 l/m end suction pump of 7.5 hp 440 VAC 3 phase capacity pump that was coupled with a Toshiba Inverter velocity controller, capable of providing a freestream velocity of U = 0 to 1 m/s in the test section. A maximum speed of 0.75 m/s was chosen for only a small part of the experiments as higher pump speed could lead to a more vigorous vibration and increase the water temperature significantly. A poly-tube hexagonal honeycomb section was fitted upstream of the test section to straighten the flow

reduce the turbulence intensity to no more than 7 % at the region of interest of the test section depending on freestream velocity (see Figure 4.6, Figure 4.8 and Figure 4.10).

A high-density fibre board, which was laminated with a layer of melamine for water proofing reason, was used as an end plate. The end plate had a dimension of 0.2 m (*W*) x 0.01 m (*H*) x 0.6 m (*L*) (see Figure 4.4 for schematic diagram and Figure A2 for actual end plate). The end plate was marked with guidelines around the point of origin at 5 mm apart to serve as an indication for the displacement by the oscillating cylinder. The purpose of the end plate was to secure the placement of the cylinders. A 30° chamfer was made on the leading edge of the end plate to enhance the development of zero pressure gradient boundary layer (see A2 in Appendix A). This design was also employed by Park and Lee (2000) in their experimental work to investigate the free end effects on the near wake flow structure behind a finite circular cylinder. A circular hole was drilled on the end plate at roughly 0.35 m from the leading edge so that the cylinder can be securely fitted with bolts. Thirteen weighted plates made from stainless steel were attached to the bottom of the end plate in order for it to stay submerged in the water. The end plate was designed according to Stansby (1974).

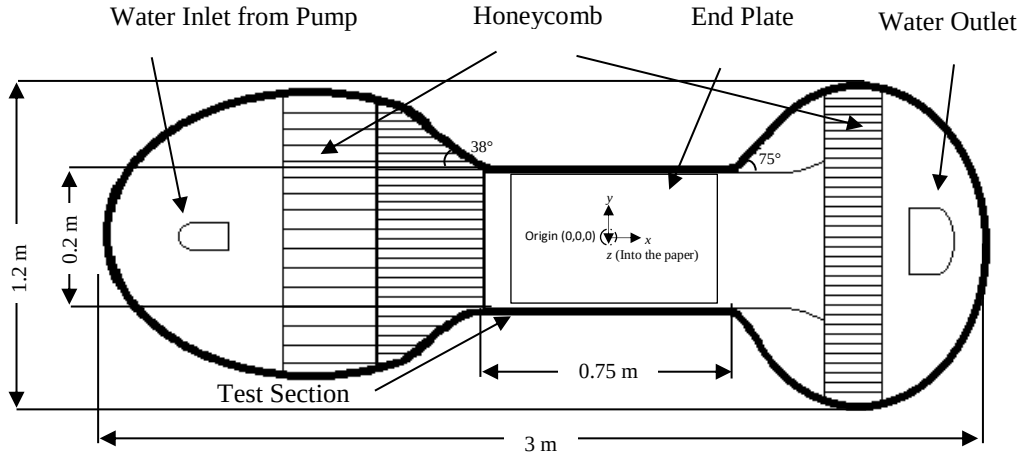

Figure 4.1: Schematic diagram of the water tunnel with the end plate installed in the test section when viewed from top

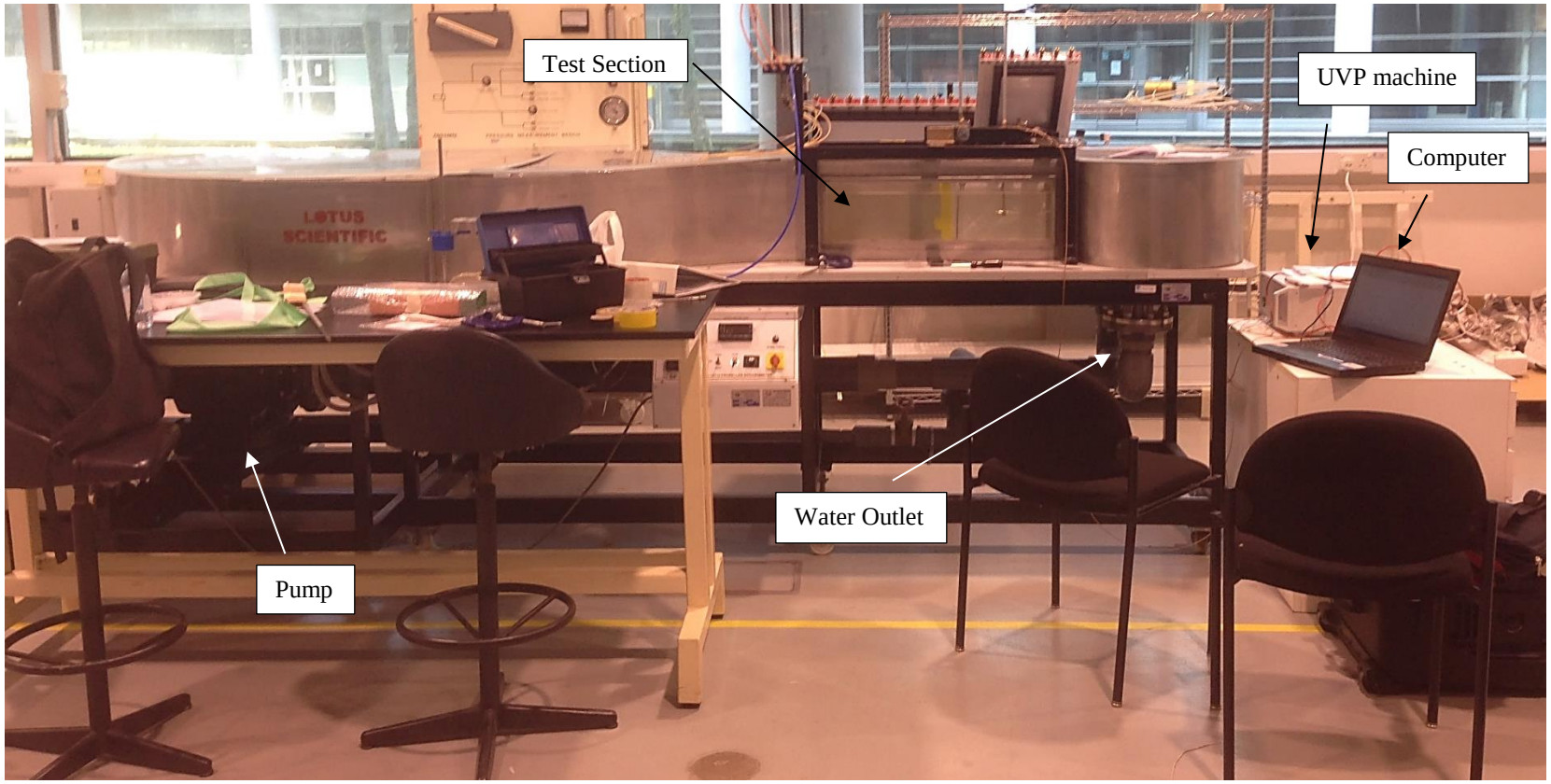

Figure 4.2: Recirculating water channel at Universiti Teknologi PETRONAS

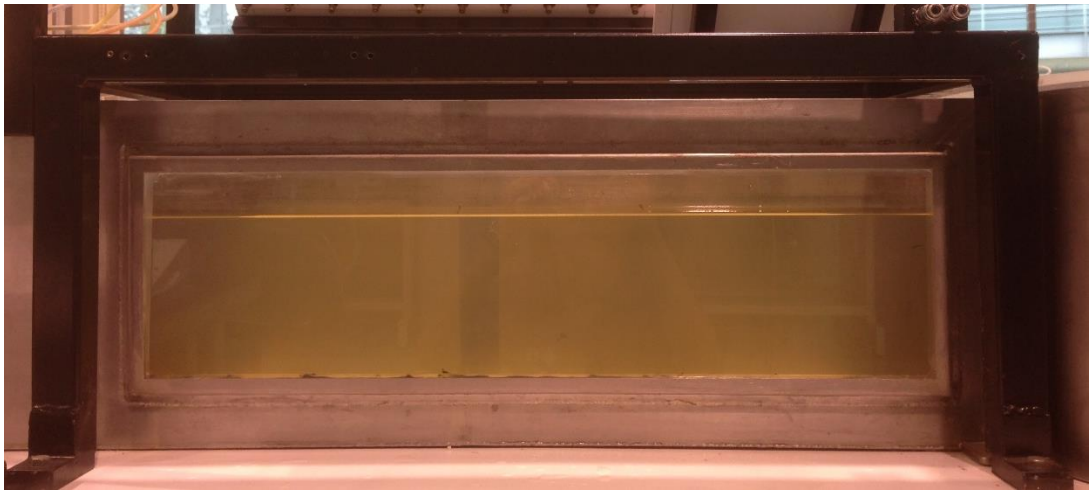

Figure 4.3: Close up view of the test section which was made from tempered glass on one side for visualizing purpose

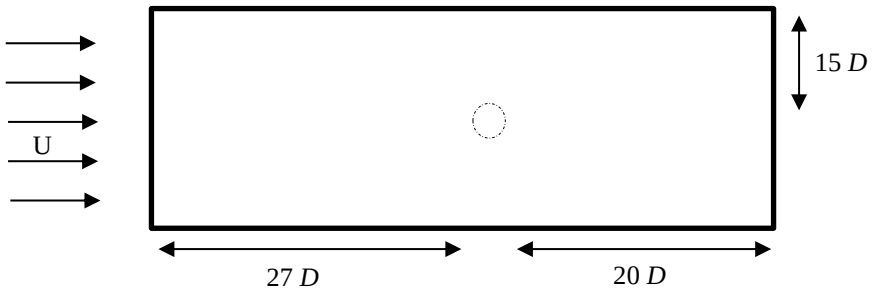

Figure 4.4: Schematic diagram of end plate used in the experiments when viewed from top

4.2. Flow Quality

All experiments conducted were at the middle of the test section where the boundary layers were expected to be fully developed. Therefore, a set of experiments was performed to investigate the boundary layer and properties of the flow prior to the finite and flexible cylinder experiments. The boundary layer thickness, δ was defined as the point where the local mean velocity was 99% of the freestream velocity while the displacement thickness, δ^* was defined as the boundary layer displacement thickness. The momentum thickness, δ_θ on the other hand, was defined as the distance by which the boundary should be displaced to compensate for the reduction in momentum of the flowing fluid because of

boundary layer formation. The shape factor, H_δ which is the ratio of the displacement thickness over the momentum thickness provides information on the nature of the flow.

The velocity profile across the testing section was taken using a UVP (Ultrasonic Velocity Profiler) which was manufactured by MET-FLOW. These experiments were carried out with a flat plate on the ground and the finite cylinder removed. Profiles of the *x*-component were taken at the symmetry plane and at the three different locations – i) -10*D* denotes 10 diameters before where the cylinder is located ii) 0 denotes the exact location where the cylinder is located iii) +10*D* denotes 10 diameters after where the cylinder is located. The time-average freestream velocity profile and turbulence intensity of U = 0.33 m/s, 0.49 m/s and 0.65 m/s at three different locations are shown in Figure 4.5 to Figure 4.10. These time-average freestream velocity profile are averaged from 3000 samples. An incident angle of 30º of the transducer was projected into the water from the surface (Details will be discussed in subchapter 4.3).

According to Figure 4.5, Figure 4.7 and Figure 4.9, the mean velocity profiles collapse onto a common point indicating a fully developed boundary layer was attained. Tables below show a summary of the boundary layer measurements on the ground plane at different freestream velocity. $x/D = 0$ (350 mm from the leading edge of the flat plate) indicates the location of the cylinder. The Re_L is based on the distance across the leading edge to the location of interest. The specifications of the boundary layer of U = 0.33 m/s, 0.49 m/s and 0.65 m/s are shown in Table 4.1 to Table 4.3 while the boundary layer to the cylinder thickness ratio, δ/D and the boundary layer to the cylinder length ratio, δ/H can be found in Table 4.4 and Table 4.5 under subchapter 4.7.1 and 4.7.2. The cylinders were partially immersed in the boundary layer (δ/H ranged from 0.3 to 0.5) for both rigid and flexible cylinder under all Re. As mentioned in subchapter 3.2 and 3.3 where the ratio of the boundary layer thickness to cylinder's span, δ/H would greatly alter the critical aspect ratio where the vortex shedding at the free end is suppressed. Therefore, it is with great care in making sure the boundary layer is small enough such that the free end of the cylinder does not submerge in the boundary layer. As shown in Table 4.4 and Table 4.5, all the cylinders were only partially immersed in the boundary layer, ensuring the free end was free from the boundary layer effect.

Figure 4.5, Figure 4.7 and Figure 4.9 show lower velocities from the 2/3 height towards the surface. This feature is well known to happen in open flow water channel. There are a few techniques known to artificially accelerate the surface flow, but none was employed in this study (SNAJ, 1986). The time-average free stream turbulence intensity, $\overline{TI}$ was also calculated to be of 9.04%, 13.53% and 10.77 % for U = 0.33 m/s, 0.49 m/s and 0.65 m/s respectively. The two main regions of higher free stream turbulence were located at the surface and at the bottom of the test section.

Table 4.1: Boundary layer measurements on the ground plane at U = 0.33 m/s

Location *x*/*D*	δ (mm)	δ* (mm)	δ_θ (mm)	H_δ	Re_L x 10^5
-10	50	11.6	8.9	1.30	0.80
0	54	11.9	9.9	1.20	1.28
+10	61	12.0	10.0	1.20	1.76

Table 4.2: Boundary layer measurements on the ground plane at U = 0.49 m/s

Location *x*/*D*	δ (mm)	δ* (mm)	δ_θ (mm)	H_δ	Re_L x 10^5
-10	52	11.7	10.1	1.15	1.19
0	58	11.9	9.9	1.20	1.90
+10	67	12.3	10.2	1.20	2.61

Table 4.3: Boundary layer measurements on the ground plane at U = 0.65 m/s

Location *x*/*D*	δ (mm)	δ* (mm)	δ_θ (mm)	H_δ	Re_L x 10^5
-10	54	11.9	9.0	1.30	1.58
0	56	11.9	9.3	1.30	2.52
+10	60	12.0	9.4	1.30	3.45

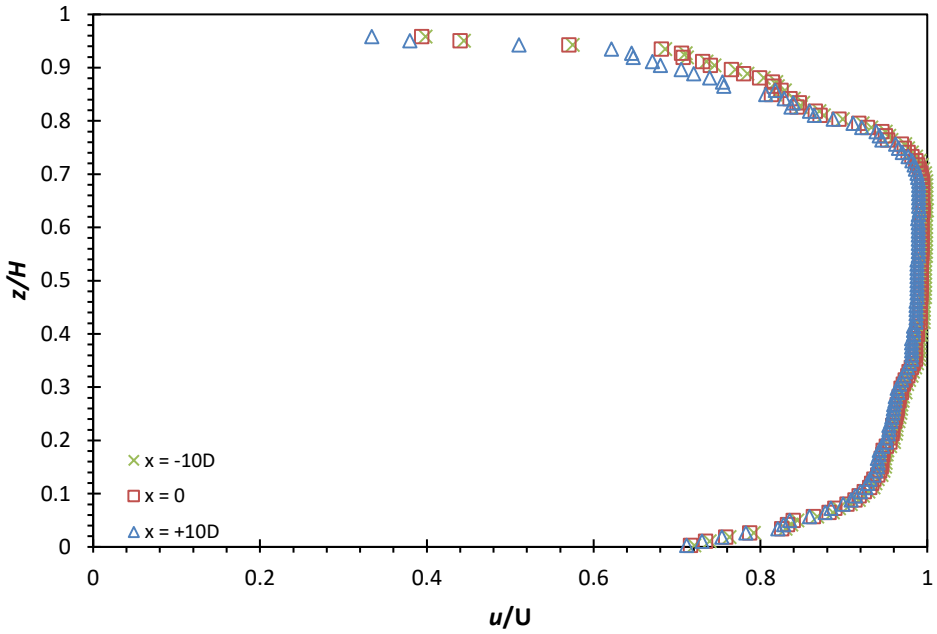

Figure 4.5: The mean velocity profiles at three different locations at a freestream velocity of U = 0.33 m/s. *z* represents height at any given location which *H* represents the overall height of the water tunnel what is filled with water

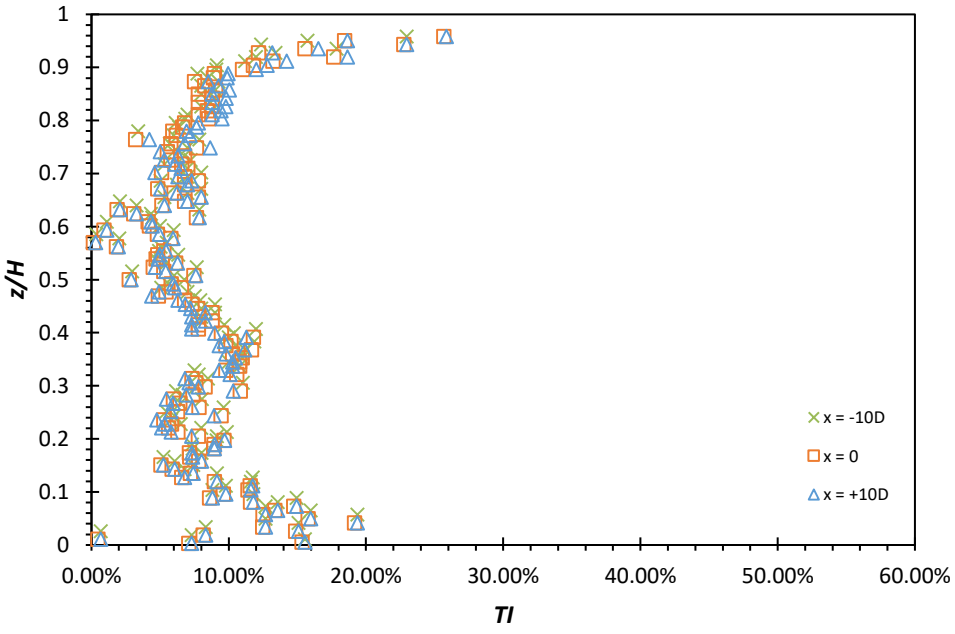

Figure 4.6: Turbulence intensity at three different locations at a freestream velocity of U = 0.33 m/s

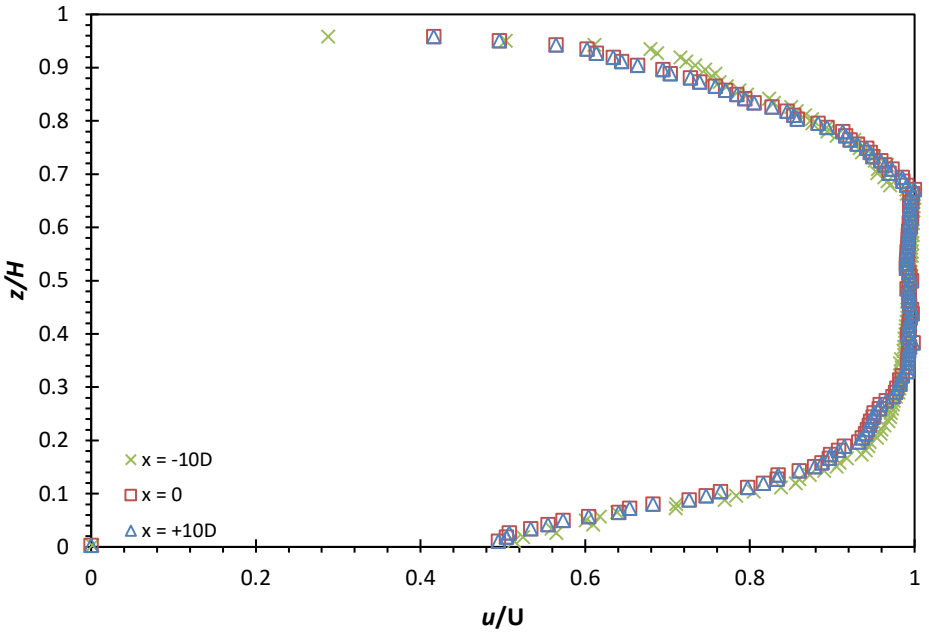

Figure 4.7: The mean velocity profiles at three different locations at a freestream velocity of U = 0.49 m/s

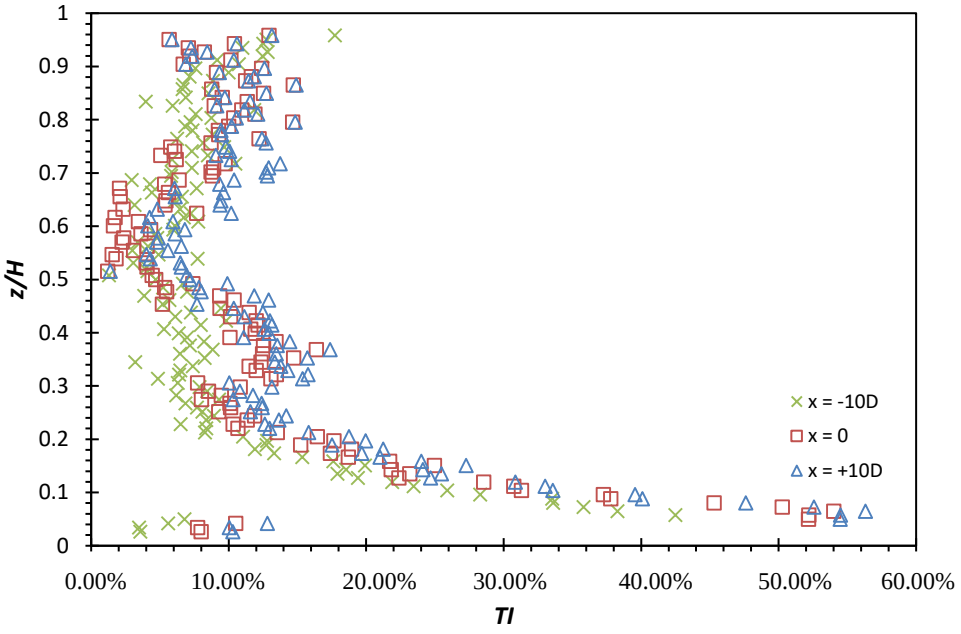

Figure 4.8: Turbulence intensity at three different locations at a freestream velocity of U = 0.49 m/s

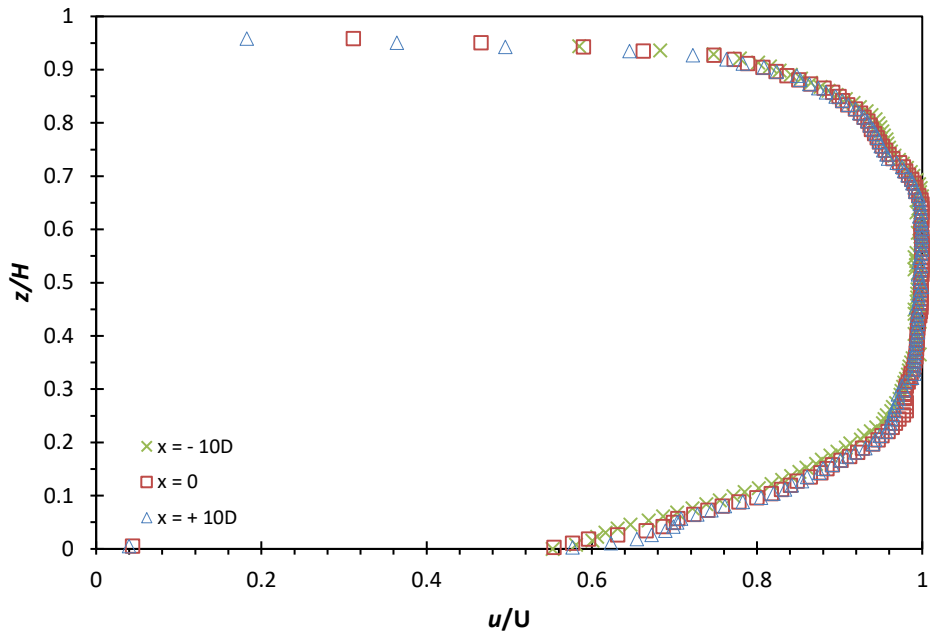

Figure 4.9: The mean velocity profiles at three different locations at a freestream velocity of U = 0.65 m/s

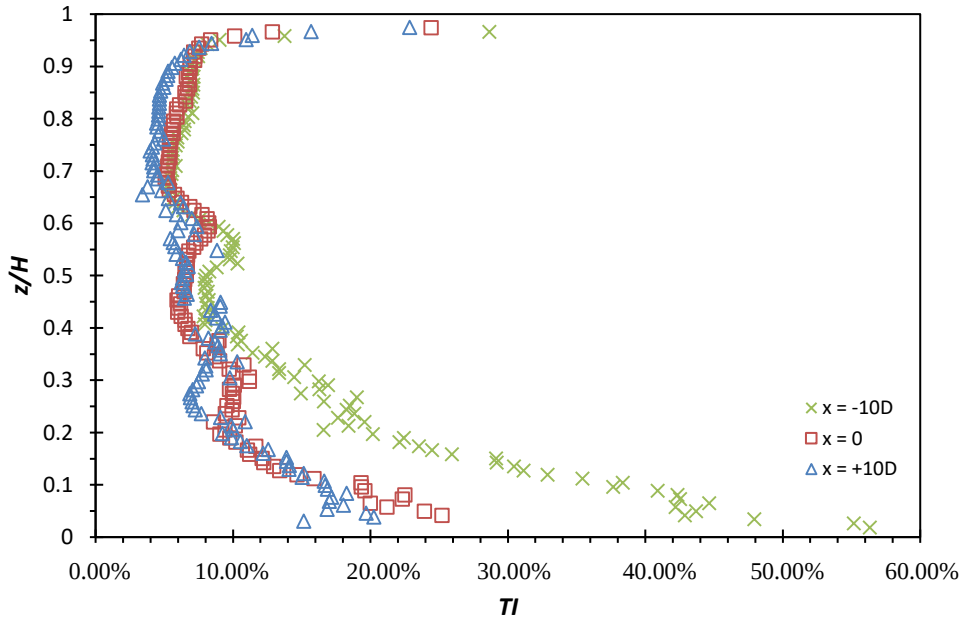

Figure 4.10: Turbulence intensity at three different locations at a freestream velocity of U = 0.65 m/s

4.3. Ultrasonic Velocity Profiler

The UVP used in these experiments were manufactured by MET-FLOW (see Figure A4). It is non-intrusive equipment that measures velocity as a function of both space and time in an one-dimensional Eulerian frame. A low frequency transducer, 2 MHz (see Figure 4.11), was used owing to its ability to measuring long distance and large velocity. The 2 MHz transducer has a spatial resolution of 1.48 mm and depending on the parameters configuration; the velocity resolution can be as minimum as 0.36 mm/s and 193 mm/s at its maximum. The sampling period which it is capable to capture is 130 msec at its minimum and 0.2 msec at its maximum depending on parameters such as measured depth, velocity range, repetition and many more. The 2 MHz transducer is made of stainless steel casing and has an outer diameter of 13 mm.

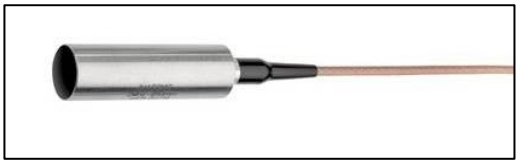

Figure 4.11: Picture of the 2 MHz transducer

The UVP uses pulsed ultrasonic Doppler Effect together with the echography relationship. The UVP transducer emits an ultrasound pulse into the liquid and the echoes are received by the same transducer. The time duration between the pulse emission and the instant of echo reception enable the transducer to calculate each position information of the fluid particle. The velocity information, on the other hand, is derived from the instantaneous Doppler shift frequency at that instant. The final form of equation which is based on the Doppler shift frequency method can be written as below:

$$v = \frac{cf_d}{2f_0} \tag{4.1}$$

Where *v* is the speed of the particle, *c* is the speed of sound in propagation medium, f_d is the detected Doppler shift frequency, and f_0 is the frequency emitted by the transducer.

However, when used in conjunction with the transducer, one must account for the trajectory angle, α called the Doppler angle as the transducer is always placed into the experimental system at an angle. The velocity of the particle can then be expressed as:

$$v = \frac{cf_d}{2f_0 cos\alpha} \tag{4.2}$$

Where α is the Doppler angle and other parameters are as stated in equation 4.1.

The detailed working principle of the method is described in (Takeda, 1995). The UVP is capable in measuring either one velocity component or two and three velocity components. During the event of one velocity component measurement, one transducer is sufficient owing to its linewise measuring capability. However, when measuring two or three velocity components, more than one transducers are needed (Yokoyama *et al.*, 2004). Yokoyama *et al.* (2004) investigated the reliability of UVP in measuring one-dimensional and two-dimensional flow in an open channel. He tested the accuracy of a single transducer in one-dimensional flow and also two-dimensional flow. He concluded that in the test of one-dimensional flow, the error was estimated to be 2.5 % to about 7 % depending on the incident angle of the transducer. The results show that smaller incident angle give a higher error. Nevertheless, it shows high accuracy of a single transducer in measuring one-dimensional flow. However, the results of two-dimensional flow measured by a single transducer deviate significantly. This indicates that in order to perform a highly precise measurement in two-dimensional and three-dimensional flow, velocity vector must be measured using at least two or three transducers. Furthermore, this related experiments are also performed in (Leal *et al.*, 2010; Ohkubo *et al.*, 2004; Ihara *et al.* 2013) and their results are in good agreement. The use of UVP in measuring complex flow field (Kantoush *et al.*, 2008) and also the coherent structures in the near filed of an axisymmetric jet (Inoue *et al.*, 1999) further proved the capability of UVP in handling complex flow with confidence.

The Doppler angle has a crucial role in calculating the particle velocity. With reference to Equation 4.2, the dependence on the Doppler angle is in the form of a cosine. The cosine of the Doppler angle provides the component of the true flow velocity vector projected onto the line of the measurement. Therefore, changing the trajectory angle of the transducer with reference to the direction of the main flow will inherently change the true value of the velocity vector by a little. Since the transducer were in contact directly with the water, the sound wave is transmitted directly from the transducer to the water

through the same medium. Therefore, no refraction angle was calculated using Snell's Law for correction.

Speed calculations based on Doppler shift measurements are only possible if the Doppler angle is specified. Since the flow direction of the freestream is known (thereby assumed that the flow is fully one-dimensional), the Doppler angle can be predicted easily with only one transducer. The calibration of the 2MHz transducer was carried by positioning it at a trajectory angle that has the minimum Doppler angle error possible which is used in speed calculations. The Doppler angle at large angles is more critical than it is at small angles in error estimation because the frequency shift becomes very small at large angles and the system sensitivity is reduced (Knoblauch, 2002). Nevertheless, three sets of measurements with different trajectory angle of 20° 30° and 40° were conducted in the investigation of the freestream quality and each set of trajectory angle was repeated three times. It was found from the mean velocity profiles that the differences of the profiles measured from the trajectory angle of 20° and 30° were negligible, though the repeatability of trajectory angle of 30° was better. As a result of that, trajectory angle of 30° was used. A 256 pulse of repetitions was selected throughout the experiments (one velocity profile is determined after 256 repetitions whereby the repetition represents the number of samples the echo signals reflected which the system uses it to reconstruct the Doppler frequency correctly). A sampling rate of 1 kHz was used in obtaining 3000 samples of the profiles. The spatial resolution is 1.47 mm.

Much can be said the same for two or three-dimensional flow measurements except more than one transducer is needed in determining the velocity components accurately. As stated by Yokoyama *et al.* (2004), at least two transducers are needed in measuring two-dimensional flow and three transducers for three-dimensional flow. This is because each transducer is needed to measure each velocity component at one spatial point in order to form a vector. The vector is therefore obtained from any two non-parallel measured components. As the vector component is an orthogonal projection of a true vector into a measuring line (see Figure 4.12), therefore, a large projection angle in between the two transducers is encouraged to avoid large inaccuracy in direction estimation. In other words, a two-dimensional flow or three-dimensional flow measurements, unlike the

technique of one-dimensional flow measurements, relies solely on the orthogonal composition technique which in turn can only be achieved at their respective intersection points.

With that in mind, the projection angle between two transducers is orthogonal (90° in between the two transducers) when measuring the *u* and *w* velocity components behind the finite cylinder (see Figure 4.13). For each of the measurements, 4069 samples were taken at a sampling rate of 100 Hz. Though proven mathematically that the sampling rate must be twice the highest frequency contained in the analogue signal, researchers normally would opt for a sampling rate more than twice the highest frequency contained in the analogue signal if plausible, to be safer, the 100 Hz sampling rate chosen in this experimental work was the highest sampling rate that could be selected after sacrificing the repetition to only 64 pulse. When considering the St for a cantilever, the St is approximately 0.14 ~ 0.18 (Sumner, 2004). Based on the Strouhal number equation, $St = \frac{fD}{U}$, selecting the maximum St, freestream velocity and the minimum diameter give the opportunity in accounting for the maximum vortex shedding frequency available in this research project. Taking into consideration, the sampling rate chosen is twice as big than the maximum vortex shedding frequency calculated – ~ 40 Hz.

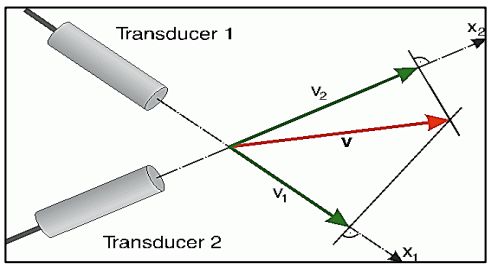

Figure 4.12: Vector orthogonal composition technique

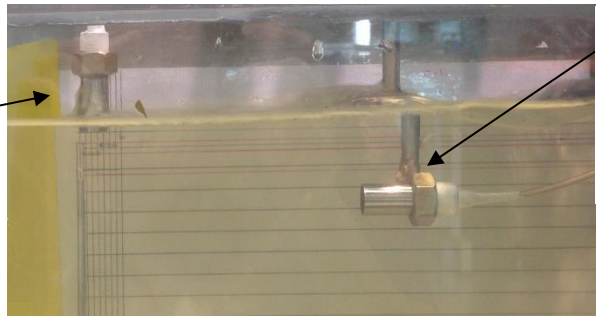

Figure 4.13: Actual transducers set-up at 90° to each other

4.4. Experimental Models

4.4.1. Finite rigid circular models

Two smooth aluminium circular models with a diameter D = 13.0 ± 0.5mm and 11.0 ± 0.5 mm and AR = 10 and 16 (see Figure 4.14) were used. Each cylinder has a flat and sharp edge. The surface of all the experimental models was assumed to be smooth and no surface roughness manipulation was treated as skin friction in the laminar boundary layer is insignificant. A threaded hole was drilled at the bottom of the cylinder so that it can be mounted onto the flat plate located at 350 mm from the leading edge using a bolt. The cylinder was partially immersed in the boundary layer on the ground plane. The blockage ratio was at most 4.8 %, which is still well acceptable within the prescribed range for cylinder flows (West & Apelt, 1982). West and Apelt (1982) had conducted a series of experiments and concluded that the effects of blockage ratio that is less than 6 % are insignificant. Frohlich and Rodi (2004) used a blockage ratio of 7.1% for their simulations and still achieving a near match results to their experiments that had a blockage ratio of 7.1%. Thus, no wall interference corrections were made. The blockage ratio is defined as the frontal area of the model over the cross-sectional area of test section of the water tunnel. The freestream velocity, U_∞ conducted on these models were at U_∞ = 0.28 m/s, 0.33 m/s, 0.42 m/s, 0.49 m/s, 0.55 m/s, and 0.65m/s, giving a Re_D (cylinder diameter) = 4 $x10^3$, 6 $x10^3$ and 8 $x10^3$. Table 4.4 shows the specifications of the models used in the experiments.

Figure 4.14: Two aluminium cylinders with *AR* = 10 and 16

Table 4.4: Summary of the specifications of finite rigid circular models

AR	10	16
D (mm)	13.0 ± 0.5	11.0 ± 0.5
L (mm)	130.0 ± 1	176.0 ± 1
δ/*D*	4.15, 4.46, 4.30	4.90, 5.27, 5.09
δ/*H*	0.41, 0.44, 0.43	0.30, 0.32, 0.31
Blockage ratio (%)	4.2	4.8
Re_D	4 x10^3, 6 x10^3, 8 x10^3	4 x10^3, 6 x10^3, 8 x10^3
Material	Aluminium	Aluminium
Young Modulus (GPa)	65	65

4.4.2. Finite flexible circular models

As for the experiments of finite flexible circular cylinders, it is separated into two categories by the choice of materials – metal and polymer. Under the category of metal, aluminium cylinder and carbon steel cylinder were used, whereas Ethylene vinyl acetate, EVA cylinder was chosen for the category of polymer.

The diameter of the aluminium and carbon steel cylinder was D = 3.0 ± 0.5 mm (see Figure 4.15). Two AR = 50 and 54 of the aluminium and carbon steel cylinder were investigated in these experiments. The intentionally large AR was chosen for two reasons. First, the stiffness of metal is significantly higher than that of polymer. Thus, in order for the cylinder to experience vibration induced by the different pressures caused by the vortex shedding, the diameter and the length must be kept small and long, as suggested by the equation of second moment of inertia, $I = \frac{\pi r^4}{4}$ and the equation of deflection of cantilever beams, $P = y\left[\frac{6EI}{x^2(3L-x)}\right]$. Second, the height was physically limited by the water tunnel dimensions. On the other hand, four EVA cylinders with diameter D = 11.0 ± 0.5 mm and AR = 10, 12, 14, and 16 (see Figure 4.16) were used in these experiments. The cylinder was located at the same position as the finite rigid circular cylinder (350 mm from the leading edge). The blockage ratio was at most 1.2 % for metal group models and 4.8 % for polymer group models. The freestream velocity, U_∞ conducted on these models were at U_∞ = 0.33 m/s, 0.49 m/s, 0.65 m/s and 0.75m/s giving a Re_D (cylinder diameter) = 2.5 x10^3 for metal group models and 4 x10^3, 6 x10^3, 8 x10^3 for polymer group models. A Reynolds number of Re_D = 2.5 x10^3 was selected for the metal group flexible cylinder because it was limited by the maximum freestream velocity available due to a very high U that was needed to achieve the same Re as the polymer group cylinder. Table 4.5 shows the specifications of the models used in the experiments.

Figure 4.15: Aluminium and carbon steel cylinders with *AR* = 50 and 54

Figure 4.16: Four EVA cylinders with *AR* = 10, 12, 14 and 16

Table 4.5: Summary of the specifications of finite flexible circular models

Group	Metal	Polymer
AR	50 and 54	10, 12, 14 and16
D (mm)	3.0 ± 0.5	11.0 ± 0.5
L (mm)	150.0 ± 1, 160.2 ± 1	110.0 ± 1, 132.0 ± 1, 154.0 ± 1, 176.0 ± 1
δ/D	25.0, 26.0	4.90, 5.27, 5.09
δ/H	0.46 – 0.52	0.30 – 0.52
Blockage ratio (%)	1.1 and 1.2	3.0, 3.6, 4.2, 4.8
Re_D	2.5 x10^3	4 x10^3, 6 x10^3, 8 x10^3
Material	Aluminium and AISI 12L14 carbon steel	EVA
Young Modulus (GPa)	65 and 200	0.0015

4.5. Traverse

A traverse is important as it guides the UVP accurately. The basic design of traverse can be seen in Figure 4.17 and Figure 4.18. It can be extended in *x* and *z* directions. The main body of the traverse was taken from a drawer slides as it can be extended with minimum friction and the extension was perfectly guided so it could travel in a straight line. The extension can be made up to 25 cm long. The extension had a resolution of a ruler, which is 1 mm, as a 50 cm long ruler was fitter on the guiding rail. The drawer slides were made to sit on a steel frame that provide stability to the traverse. All the joints were bolted using hexagonal nuts and bolts to ensure the sturdiness of the structure. In order to account for the ability to move in the z direction, 4 hollow bars were welded onto the 2 inch flat bars. The UVP transducer was attached to the holder that were moved and guided by the square hollow bar. When the transducer reaches a desired location, the holder was jammed by the bolts so that it would stay in place. The UVP probe emits sound waves in *z* direction (top

to bottom) and *x*-direction (streamwise). They are free to move in *x* and *z* direction to collect the velocity around the cylinder upstream and downstream.

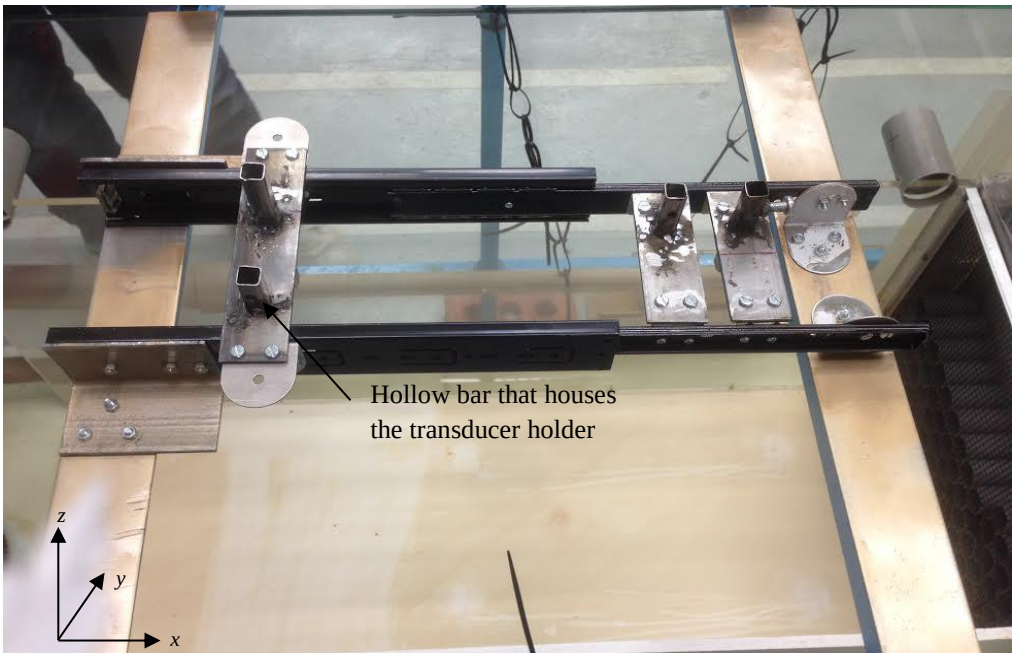

Figure 4.17: Picture of the transverse

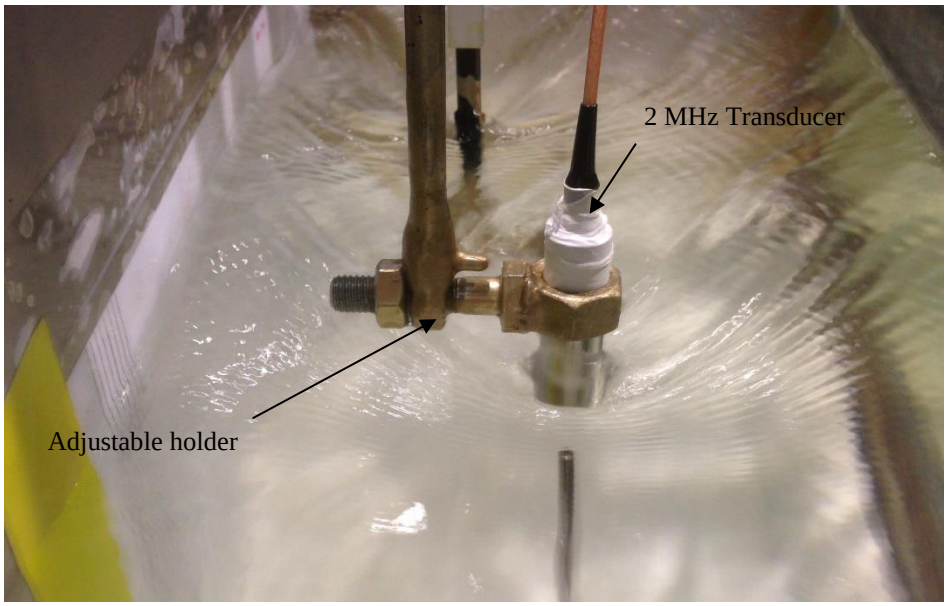

Figure 4.18: Diagram of the traverse that holds the transducer during measurement

4.6. Temperature Measurements

The temperature of the water is very critical in achieving accurate results. As the UVP emits sound waves and the temperature has influence on sound velocity, it is important to be aware of the temperature when the experiments are performed. Although water was used throughout the whole experiments, the sound speed emitted by the sound waves varies a little based on the temperature it is operating in. Thus, as a measure to keep the upmost accuracy of the measurements and calculations, great efforts were invested to ensure the operating water temperature was maintained within a tolerable temperature fluctuation. The heat generated from the pump can gradually increase the temperature of the water as time passes by. Therefore, to ensure the experiments were performed at a water condition with a stable temperature, a EDISON Infrared Thermometer was used to measure the temperature of the water before and during the experiments. The temperature of the surface at which the laser landed on was recorded as the trigger mechanism was deployed. The infrared thermometer had an emissivity of 0.95, which meant it had a 95 % efficiency of absorbing the incident energy. The accuracy of an infrared thermometer is primarily determined by the Distance-to-spot, D:S ratio. The larger the D:S ratio, the better resolution and the smaller area that can be measured. The infrared thermometer was always measured in a distance within 12-inches from the targeted object as it has a 12:1 ratio. This meant that the maximum distance it can be to accurately measuring a 1-inch object size is 12 inches away.

As the water tunnel was located in a temperature controlled air-conditioned laboratory, the water temperature was maintained at 25°C ± 1°C for most of the time before the heat from the pump starts to disseminate to the water. The temperature of the water in the test section was measured every half an hour. As a means of data accuracy, a conventional thermometer was used to countercheck the measurements from the infrared thermometer. During these measurements, it was found that the temperature only started to rise at the 5^{th} hour into the experiments to roughly 27°C. The water inside the water tunnel was fully discharged and was replaced with filtered water from water pipe inside the laboratory in order to keep the water temperature in between 25°C ± 1°C.

4.7. Camera and Image Processing

In order to visualize the oscillations by flexible cylinder inside the recirculating water tunnel, a Canon Eos 60D camera was used. The camera is capable of recording 60 fps at 1280 x 720 pixels. The camera lens was mounted directly above the flexible cylinder where the oscillating motions were recorded and the distance between the lens and the cylinder's free end were kept constant. It is important that the lens was perfectly aligned to the cylinder's free end so that the light wave is approaching the water in a direction which is perpendicular to the water surface since theoretically the light does not refract at the normal line. A 5 mm grid that was true to scale was marked on the end plate at the location where the cylinder was installed.

As a means to ensure that the deflection of the cylinder recorded by the camera is within the safe range unaffected by the possible refraction, a simple test was conducted. According to the Snell's Law, only the greatest deflection away from the normal line or a deep immersion of the cylinder would there be greater influence of the refraction. The setup is as shown in Figure 4.19, which the ruler on the right was placed outside of water, serving as a reference point. The ruler on the left was positioned on the same height as the cylinder's free end, replicating the height of the cylinder's free end. The setup was strictly kept untouched and unchanged. Figure 4.19 (a) shows the condition where the cylinder/ruler was submerged in the water while Figure 4.19 (b) shows the condition where the water was released to below the height of the cylinder's free end. The distance difference between the ruler which was submerged and not was compared to see if refraction does indeed affect the distance viewed through the camera. The results show that the effect of refraction only took place approximately 4 cm away from the centre line, at approximately 0.1 mm of difference. The greatest deflection of the cylinder recorded was approximately 2 cm, which is within 4 cm. So, it is still acceptable.

The video was analysed by using a motion analysis software, Photon FASTCAM Analysis version 1.3.2.0. The motion software has an automatic tracking feature which identifies the pixel of the point of interest. Users can input the actual dimension of any objects in the video and the software will automatically calculate the distance corresponded to a single pixel.

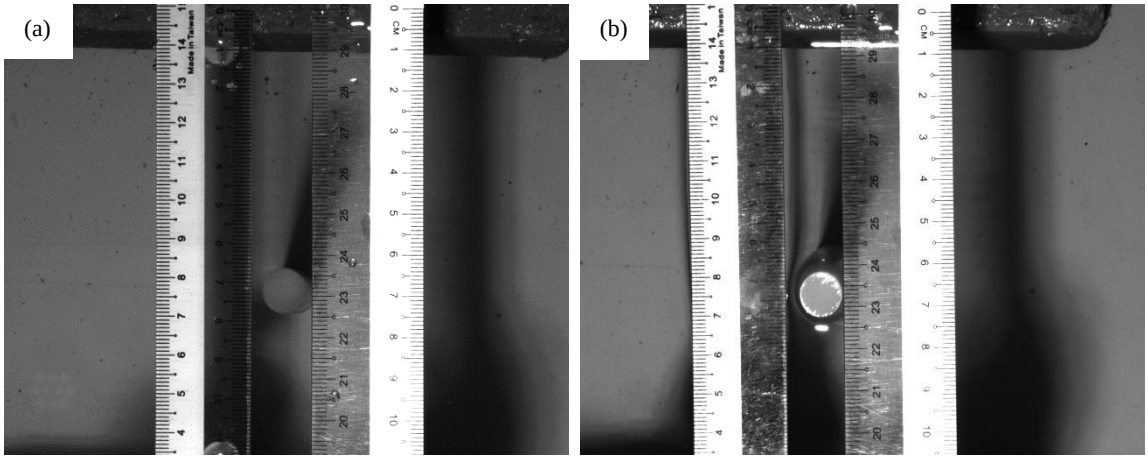

Figure 4.19: (a) Cylinder's free end/left ruler submerged in water (b) Cylinder's free end/left ruler exposed outside the water surface

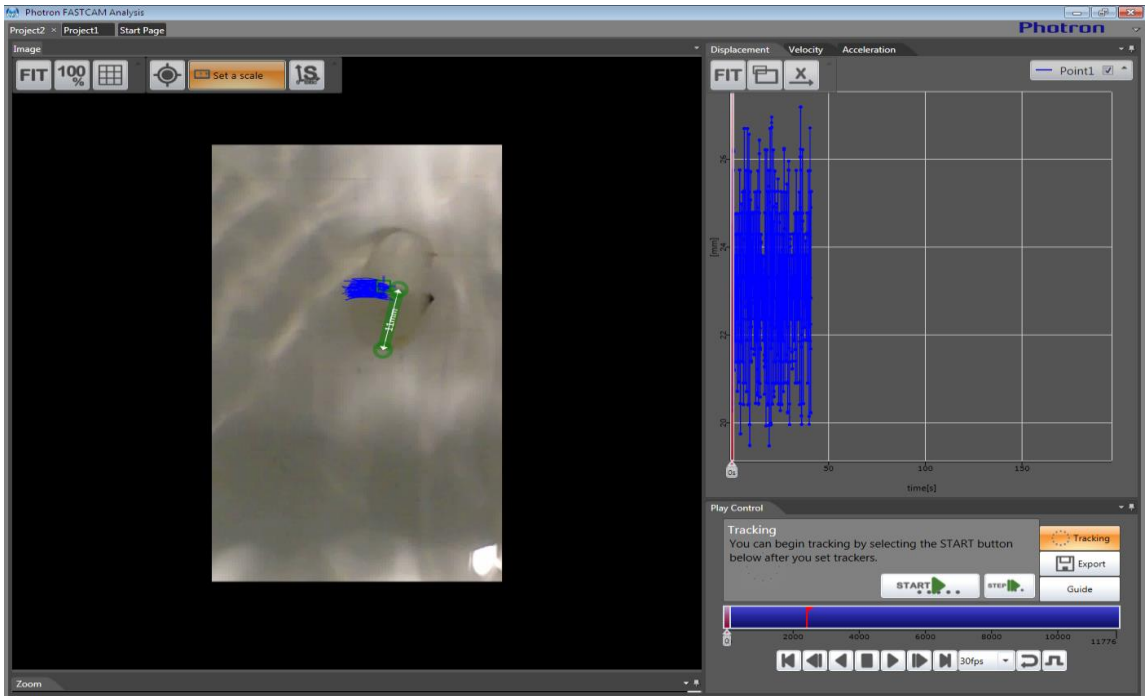

Figure 4.20: The distance of the point of interest was pint-pointed to enable the software to calculate the pixels across the motion of the cylinder

4.8. Description of Experiments

In these series of experiments, two phase of experiments; Phase I and Phase II, were conducted. Phase I focused on the flow passing through a finite rigid circular cylinder. Although the finite rigid circular cylinder was not the main focus in this studies, it served as a basis for comparison with the finite flexible circular cylinder results, which was in Phase II. Apart from that, the results from Phase I can also be used to verify the measuring techniques and confidence of the UVP by comparing it with renowned published results of finite rigid circular cylinder.

They were a total of 22 sets of experiments performed in this studies (see Table 4.6 for the experimental matrix); 6 sets of experiments in Phase I and 16 sets of experiments in Phase II. Different *AR*, Re and materials were varied in these experiments. The material selected for the finite rigid circular cylinder in Phase I was aluminium with different *AR* (*AR* = 10 and 16); while aluminium, carbon steel and EVA were chosen as the material for finite flexible circular cylinder at different *AR* (*AR* = 10, 12, 14, 16, 50, 54).

Table 4.6: Experimental matrix of the experiments performed

	Materials	*AR*	Re	Diameter (mm)	Number of Sets
Rigid	Aluminium	10 and 16	4k, 6k and 8k	13 and 11	6
Flexible	EVA	10, 12, 14 and 16	4k, 6k and 8k	11	12
	Aluminium	50 and 54	2.5k	3	2
	Carbon Steel	50 and 54	2.5k	3	2

Figure 4.21 shows the schematic diagram of experimental set-up within the test section of the water tunnel. For each cylinder, the time-averaged velocity field ($\overline{U}, \overline{W}$) in the downstream (*x*-*z* plane) of the cylinder was measured over a 5 mm uniform grid over the top 5*D* span of the cylinder at streamwise locations of *x*/*D* = 1 to *x*/*D* = 5 (see Figure 4.22). The measurement point in the wall-normal direction (*z* plane) increased to a 10 mm uniform grid after 5*D* span of the cylinder until 10 mm from the ground. As the tip effects are generally extended up to 3*D* to 4*D* from the free end (Okamoto & Yagita, 1973; Park & Lee, 2000; Roh & Park, 2003), more attention was given to the free end until 5*D* along

the cylinder span so that the tip effects can be captured. The measurement zone was free from the influence of the ground plane boundary layer for all cylinders. All the measurements were made at the *y*-*z* plane of symmetry. No measurements were made for $x/D > 6$ because the high turbulence flow in the downwash flow field close to the cylinder free end was more significant at $x/D < 5$. Figure 4.16 illustrates the configurations of measurement. The intersection points correspond to the point of measurements of $\overline{U}, \overline{W}$ velocity components.

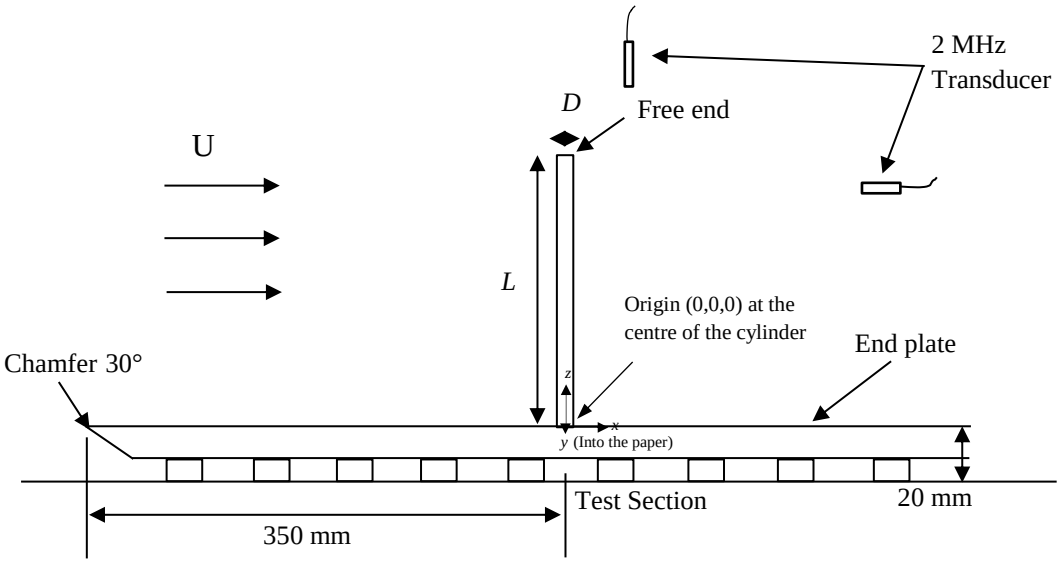

Figure 4.21: Schematic diagram of experimental set-up in the water tunnel

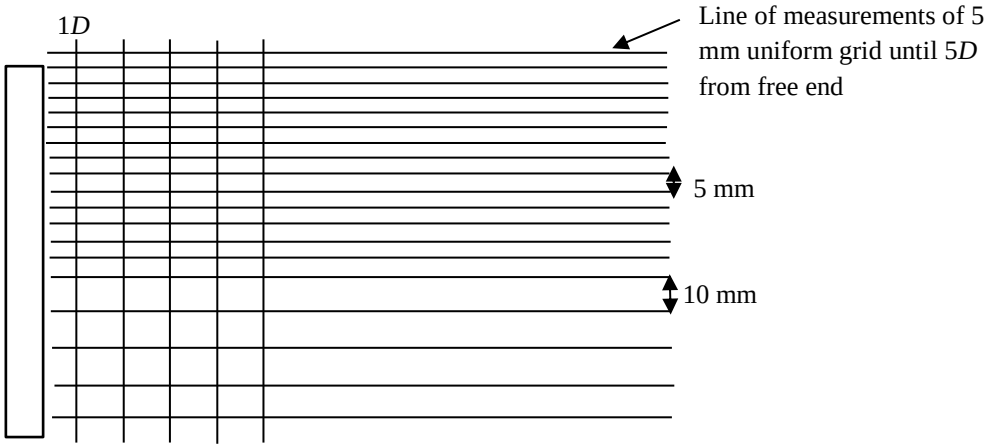

Figure 4.22: The measurement points behind the cylinder

For the Phase II experiments where flexible cylinders were involved, the measurements at very near wake (i.e. $x/D = 1$) cannot be measured because the oncoming freestream caused the flexible cylinder to bend in the streamwise direction.

The two 2 MHz transducers used in these experiments have a diameter of $D = 13$ mm. An incident angle between the transducers was chosen to be perpendicular to each other as shown in Figure 4.13. The sampling period was chosen to be 10 msec for each profile and a total of 4096 profiles for each component was taken. Based on the extreme maximum St, the calculated maximum vortex shedding frequency available in this research project was ~ 40 Hz (the case of flexible metal cylinder). There were over ~ 1600 cycle of vortex shedding over the period of measurement.

4.9. Post Processing

In order to examine the strength of the turbulence, the Reynolds averaged statistics, which is important as it gives insight on the transport of momentum within the flow because velocity fluctuations give turbulent flow extra kinetic energy and hence generate extra momentum transfer. Reynolds stress is used to account for turbulent fluctuations in fluid momentum. Hence, the fluctuating components of the instantaneous flow was determined from each velocity field in the *x*–*z* plane.

Since the Reynolds stress is the component of the total stress tensor in a fluid obtained from the averaging operation over the Navier-Stokes equations, the Reynolds averaged Navier-Stokes equation can be written as:

$$\frac{\partial \overline{u}_i}{\partial t} + \overline{u}_j \frac{\partial \overline{u}_i}{\partial x_j} = \frac{1}{\rho} \frac{\partial}{\partial x_j} [\overline{\tau_{ij}} - \overline{\rho u'_i u'_j}] \tag{4.1}$$

Where $\overline{\rho u'_i u'_j}$ is the Reynolds stress tensor.

The instantaneous and mean velocity can be extracted directly from the Met-Flow Software Version 3 except the fluctuation velocity, so the fluctuation velocities of 4096 data points at one location were calculated by subtracting the mean from instantaneous. The *u* component fluctuation velocities were then multiplied by each other before

averaging was performed in order to calculate the normal stress, $\overline{u^2}$ contributed by *u* component. The same procedure is valid for *w* component. To calculate the Reynolds shear stress, $\overline{uw}$, the *u* fluctuation velocities were multiplied with the *w* component before averaging.

4.10. Uncertainty Analysis

As this project is fully based on experimental work, the results have to be assured to be of high integrity. The uncertainty analysis is performed to give a quantitative estimation of the reliability of the measured value generated from a series of experiments. In the series of results, a 90 % confidence interval was used to estimate the true value of the results.

In general, all the instrumentations, data acquisitions, and the test environment influence the experimental results because errors are always present in all measurements. Though they cannot be eliminated, their effects on particular results can be minimized. In most of experimental situations, the final result is not taken directly. Instead, multiple individual measurements are obtained to achieve the final result. Each of the individual measurement contains individual errors that will have a cumulative effect on the result. Errors can be classified into bias and precision errors. The bias error is a fixed error that is associated with the instrument and can be reduced to a certain limit by calibration. On the other hand, the precision error is a random error that causes the result to be fluctuating around the true value of the result. It can be reduced by obtaining multiple measurements.

The Coleman and Steele method (1999) gives the uncertainty analysis of the measured variables using data reduction equation. R is a variable that depends on *n* independent measured variables X as follow:

$$R = R\ (X_1, X_2, \ldots, Xn). \tag{4.1}$$

It is assumed that this relation is continuous and has continuous derivatives in the domain of interest. Therefore, the uncertainty in R due to the uncertainties can be calculated by performing the partial derivatives.

$$\delta R = \frac{\delta R}{\delta X}\delta X \tag{4.2}$$

The equation can be normalized by dividing both sides by R.

$$\frac{\delta R}{R} = \frac{X}{R}\frac{\delta R}{\delta X}\frac{\delta X}{X} \tag{4.3}$$

δR and δX are the uncertainties in R and X_1. For the ease of expressing, δR and δX can be substituted to W_R and W_1 respectively. Thus, the overall uncertainty in R can be written:

$$\left(\frac{W_R}{R}\right)^2 = \left(\frac{1}{R}\frac{\delta R}{\delta X_1}W_1\right)^2 + \left(\frac{1}{R}\frac{\delta R}{\delta X_2}W_2\right)^2 + \ldots + \left(\frac{1}{R}\frac{\delta R}{\delta X_n}W_n\right)^2 \tag{4.4}$$

The above equation, $\left(\frac{W_R}{R}\right)^2$ is valid for bias error analysis. To determine the overall uncertainty of the experimental result, the bias and precision limits, W_R and P_R must be combined. The precision error accounted with confidence level can be expressed as follow:

$$P_R = {t\sigma_R}/{\sqrt{n}} \tag{4.5}$$

Where t is the t factor from t-distribution table, σ is the precision index and *n* is the number of samples.

The overall precision error is identical to the one used for determination of the bias limit of the results except to substitute the bias error $\left(\frac{W_R}{R}\right)^2$ with the precision error $\left(\frac{P_R}{R}\right)^2$ accounted with confidence level.

The combination of bias and precision limits can be done through the root-sum-square (RSS) method.

$$U_R = \left(W_R{}^2 + P_R{}^2\right)^{0.5} \tag{4.6}$$

Where *W* and *P* are the bias and precision uncertainties respectively.

The uncertainty estimation for the different parameters are calculated based on the Coleman and Steele (1999) approach at a 90 % confidence level. Based on the approach, the summary of the uncertainty estimation in the freestream parameters and experimental model dimensions are presented in Table 4.6. The uncertainty estimation for the results parameters are presented in Table 4.7.

Table 4.7: Summary of uncertainty estimation in the freestream parameters and experimental model dimensions

Parameter	Uncertainty (%)
Freestream Density, ρ	± 1.17
Freestream Kinematic Viscosity, V	± 1.16
Freestream Velocity, U	± 3.64
Cylinder Diameter, D	± 0.38
Cylinder Length, L	± 0.76
Reynolds Number, Re	± 4.41

Since the temperature of water is at absolute constant and the density of water is a function of the water temperature, the water temperature and density table give the bias error. As a constant averaged density will be used throughout the experiments so no precision error is accounted for. The same applies to the freestream kinematic viscosity. However, in the calculation of the uncertainty error of freestream density, the precision error approach was used as the variation in temperature give the water density precision error. The measured temperature of the water was used to find its corresponded water density and the data was used to feed into the calculation of σ_R, which is $\sigma_R = \left[\frac{\sum(x_i-\bar{x})^2}{n-1}\right]^{1/2}$. A t value from the t-distribution table at a 90 % confidence level was chosen in the process.

The diameter of the cylinder was measured by a vernier caliper with a resolution of ± 0.05 mm and the same approach of precision error (see equation 4.5) was taken to calculate the bias error. The length of the cylinder on the other hand, was measured using a tape measure with a resolution of ± 1 mm. They are being presented as bias error because a constant dimension will be used throughout the Phase I and II experimental phases.

As for the freestream velocity uncertainty, it comprises of the bias and precision error of the equipment and randomness respectively. Therefore, equation 4.6 was adopted in estimating the uncertainty presented in Table 4.7. The bias error of the freestream

velocity can be calculated from the resolution of the 2MHz transducer, which was given by the manufacturer at 0.4% of velocity range; while the precision error can be calculated based on equation 4.5. At last, RSS method is used in combining the bias and precision errors of the freestream through equation 4.6.

While the uncertainty of the Reynolds number, which is dependent from the bias and precision errors combined of its parameters (from the equation $\mathrm{Re} = \frac{\rho UD}{v}$), a RSS method is used (equation 4.6). However, before reaching the RSS method, a bias error of each parameters in the Reynolds number equation must be combined through the data reduction equation (see equation 4.4) by performing the partial derivatives of the Reynolds number equation as follow:

$$\mathrm{Re} = \rho \mathrm{U} D v^{-1}$$

$$\left[\frac{\mathrm{W_{Re}}}{\mathrm{Re}}\right]^2 = \left(\frac{1}{\mathrm{Re}}\frac{\partial \mathrm{Re}}{\partial \rho}\mathrm{w}_\rho\right)^2 + \left(\frac{1}{\mathrm{Re}}\frac{\partial \mathrm{Re}}{\partial \mathrm{U}}\mathrm{w}_\mathrm{U}\right)^2 + \left(\frac{1}{\mathrm{Re}}\frac{\partial \mathrm{Re}}{\partial D}\mathrm{w}_D\right)^2 + \left(\frac{1}{\mathrm{Re}}\frac{\partial \mathrm{Re}}{\partial v}\mathrm{w}_U\right)^2$$

By computing the derivatives (as shown here is example for the first parameter, ρ):

$$\frac{1}{\mathrm{Re}}\frac{\partial \mathrm{Re}}{\partial \rho}\mathrm{w}_\rho = \left(\frac{1}{\rho \mathrm{U} D v^{-1}}\right)(\mathrm{U} D v^{-1})\mathrm{W}_\rho = \frac{\mathrm{W}_\rho}{\rho}$$

Substituting all the parameters into the uncertainty expression for $\mathrm{W_{Re}}$:

$$\left(\frac{\mathrm{W_{Re}}}{\mathrm{Re}}\right)^2 = \left(\frac{\mathrm{W}_\rho}{\rho}\right)^2 + \left(\frac{\mathrm{W_U}}{\mathrm{U}}\right)^2 + \left(\frac{\mathrm{W}_D}{D}\right)^2 + \left(\frac{-\mathrm{W}_v}{v}\right)^2$$

Where W is the bias error estimated and ρ is the nominal value. Same applies to the subsequent parameters.

Substituting the bias uncertainty of the related parameters from table 4.17:

$$\left(\frac{\mathrm{W_{Re}}}{\mathrm{Re}}\right)^2 = 0.0117^2 + 0.0040^2 + 0.0038^2 + 0.0116^2$$

$$\left(\frac{\mathrm{W_{Re}}}{\mathrm{Re}}\right)^2 = 3.0189x10^{-4}$$

$$\left(\frac{\mathrm{W_{Re}}}{\mathrm{Re}}\right) = 0.01737 \text{ or } 1.737\%$$

Same procedure is also applied for the precision error and can be written as:

$$\left(\frac{\mathrm{P_{Re}}}{\mathrm{Re}}\right)^2 = \left(\frac{\mathrm{P_U}}{\mathrm{U}}\right)^2$$

Substituting the precision uncertainty of the freestream velocity:

$$\left(\frac{P_{Re}}{Re}\right)^2 = 1.3032x10^{-3}$$

$$\left(\frac{P_{Re}}{Re}\right) = 0.0361 \text{ or } 3.61\%$$

Combining both bias and precision uncertainty:

$$\left(\frac{U_{Re}}{Re}\right) = \left[\left(\frac{W_{Re}}{Re}\right)^2 + \left(\frac{P_{Re}}{Re}\right)^2\right]^{\frac{1}{2}}$$

$$\left(\frac{U_{Re}}{Re}\right) = \ [3.0189x10^{-4} + 1.3032x10^{-3}]^{\frac{1}{2}}$$

$$\left(\frac{U_{Re}}{Re}\right) = 0.0441 \text{ or } 4.41\%$$

There is only one parameter – the freestream velocity, U that is in consideration because the density, kinematic viscosity and also diameter do not have precision error. Once the combined bias and precision errors of parameters are determined, RSS method can be used to calculate its overall uncertainty, which is presented in Table 4.7. The same procedure is applied to the streamwise and wall-normal velocity component, streamwise and wall-normal turbulence intensity and also Reynolds shear stress are they are presented in Table 4.8.

The accuracy of the UVP is fairly adequate, with an associated velocity resolution of 0.4 % of velocity range. Therefore, a ± 0.4 % of value obtained by the MET-FLOW UVP is accounted for and is treated as a bias error that are always present in all the values obtained by MET-FLOW UVP throughout the experiments. The uncertainty estimation of the digital recording is only made based on the bias error of the image resolution and therefore the estimated error presented in Table 4.7 for the distance of oscillation acquired from digital recording is likely to be under-estimated.

Table 4.8: Summary of uncertainty estimation for results parameters

Parameter	Uncertainty (%)
Angle of the Probe	± 0.50
Streamwise Velocity Component, u	± 4.67
Wall-normal Velocity Component, w	± 4.82
Streamwise Turbulence Intensity, u'	± 6.24
Wall-normal Turbulence Intensity, w'	± 6.81
Reynolds shear stress, $\overline{u'w'}$	± 8.36
Distance of Oscillation Acquired from Digital Recording	± 3.37

4.11. Summary of Chapter

This chapter mainly discuss the experimental rig and methodology. As the experiments took place in a water tunnel, the specifications of the water tunnel and its flow quality are investigated. The freestream profile at three different positions collapsed onto a common point, signifying its developed flow. Furthermore, the boundary layer thickness was calculated to ensure that the free end is free from the boundary layer effect. The experimental models and its conditions in the water tunnel are presented. Apart from that, the steps and methods of conducting the experiments are listed. The Reynolds stress calculation is presented to reveal the method of post processing the data once required. Finally, a set of uncertainty analysis is calculated to ensure the integrity of the results. The findings and discoveries between the rigid and flexible cylinders will be revealed in the next chapter.

CHAPTER 5

TURBULENT WAKES AND CHARACTERISTICS OF THE RIGID AND FLEXIBLE FINITE CIRCULAR CYLINDERS

This chapter presents the results of the rigid finite circular cylinders and flexible finite circular cylinders investigated under Reynolds number of 4000, 6000 and 8000. The local flow field in the near wake was investigated in order to gain insight of the changes of the wake structure that flexible finite circular cylinders could bring. As this chapter mainly aims to identify the difference in the wake structure between rigid and flexible finite circular cylinders, only cylinders of *AR* = 10 and 16 will be discussed in this section. As all of the turbulence characteristics such as separated shear layer profiles, vortices and vorticity are packed in the wake, it would be ideal to first examine the wake of these two cylinders produced. As mentioned in Chapter 3, there is also limited information in the literature about the characteristics of the turbulence quantities in the wake of a rigid and flexible finite circular cylinder. Each of the velocity graph below is measured at the wake centreline ($y/D = 0$) in the plane of symmetry (x-z plane). The velocity vectors have been normalized by the freestream velocity ($\overline{u}/\mathrm{U}$,$\overline{w}/\mathrm{U}$). As there are three Reynolds number conducted in these experiments and thereby resulting in three different freestream velocity, it is important to normalize the velocity by the freestream velocity in order to bring the different values to a notionally common scale for comparison.

5.1. Time-Averaged Velocity Distribution

The study of velocity profiles might be the easiest way to comprehend the size of the wake region between the rigid and flexible cylinders. It tells information such as the direction the mean flow is travelling and also the wake region. The information on where the mean flow is traveling is extremely important as the vortices generated from the free end of the cylinder will follow the path of the mean flow. Rostamy *et al.* (2012) studied the flow field behind the rigid cylinder and showed that the turbulence structure (turbulence intensity and Reynolds stress) follows the path of the mean flow. Therefore, understanding

the path of the flow, effectively means that the region where the vortical structures travel is known. Aside from that, the wake region, which is the common phenomenon behind any bluff body objects, is regarded as the region where turbulence structures take place. As a result of that, a bigger wake region signifies a more effective region of "mixing" behind the protruding surface.

5.1.1. Velocity profiles along the wake centreline

The time-averaged streamwise ($\overline{u}/\mathrm{U}$) and wall-normal ($\overline{w}/\mathrm{U}$) velocity profile of rigid and flexible finite cylinders of *AR* = 10 and 16 at Re = 4000, 6000 and 8000 are shown in Figures 5.1 to Figure 5.12. The distance measured of each velocity profile behind the cylinder are one diameter apart at x/D = 1, 2, 3, 4 and 5.

The profiles of the rigid cylinder (see Figure 5.1 to Figure 5.6) spot a very steep velocity gradient at the region near the free end behind the cylinders for both *AR*. These changes are believed to cause by the tip effects, a region where tip vortex plays a role. However, below the free end region, this phenomenon quickly disappears and slowly achieving a more consistent profile and is likely to be where the regular Kármán vortex is. The strong influence of tip effects which are influential up to approximately 3*D* from the free end (e.g. wake region is $z/D \approx 7$ for *AR* = 10 and $z/D \approx 13$ for *AR* = 16) have been consistently reported in several journal papers (Rostamy, 2012; Park & Lee, 2000; Roh & Park, 2003; Okamoto & Yagita, 1973). A strong velocity defect occurs at $z/D \approx 7$ for *AR* = 10 and $z/D \approx 13$ for *AR* = 16 (as indicated by a long dash double dot arrow at Figure 5.1 (e)) downstream of the cylinder. The strong velocity gradient marks the boundary between the wake region and the flow outside of the wake region as the flow within the wake region is much slower than outside. In other words, the region within the velocity defect can serve as the 'body' of the wake region. Chan *et al.* (2016) explained that the velocity defect is a direct consequence of the presence of vortical motion in the flow field because energy from the mean flow is extracted for the formation of the vortical structures. It is supported in their simulation results of cantilever of *AR* = 3, 5, and 7 that the Turbulent Kinetic Energy (TKE) contours are higher with larger velocity defect and vice versa.

The wake region is circa 3*D* shorter than the *AR* due to the tip effects from the free end. The ($\overline{u}$/U) and ($\overline{w}$/U) velocity profile must be examined simultaneously for the investigation. According to Figure 5.1 to 5.12 (a) to (c) for rigid cylinder only, it can be seen that the localised negative $\overline{w}$ component velocity of both *AR* at circa $x/D < 3$ at all Re are much higher than that of localised $\overline{u}$ component velocity. In other words, the influence of $\overline{w}$ component velocity (compare Figure 5.1 and Figure 5.7 (a) to (c) for example) is so dominant that it diminishes the movement in streamwise direction. As a result of that, the flow behind the rigid cylinder at $x/D \leq 3$ is brought downwards to the floor along the wake centreline. The $\overline{u}$ component velocity slowly gain velocity until it finally dominates the $\overline{w}$ component velocity at circa $x/D \geq 3$. The phenomenon of the flow convected downwards is called downwash. Since the vortex mainly follows the path of the mean flow, in the case of the rigid cylinder, most of the vortices generated are transported downwards along the cylinder span rather than transported downstream due to the influence of the downwash flow that cause the tip effects.

Fox and West (1993) had showed that large pressure drop across the rigid cylinder for *AR* = 4 to 30. He showed that there is a local minimum C_p at the free end behind the cylinder and it is gradually rose to $z/D \approx 3$ from the free end before it slowly falls again. Therefore, the flow at the free end that is immediately brought downwards is due to the low pressure wake behind the cylinder. The results obtained in this research work show that at the span below $z/D \approx 7$ for *AR* = 10 and $z/D \approx 13$ for *AR* = 16, the profiles appear to be taking a more consistent form as compared to the span above $z/D \approx 7$ and $z/D \approx 13$ for *AR* = 10 and 16 respectively. This indicates that the strong influence of tip effects begins to diminish at 3*D* below the free end, consistent with what was reported in (Rostamy 2012; Park & Lee, 2000; Roh & Park, 2003; Okamoto & Yagita, 1973) for a finite cylinder. Since the influence of tip effects are consistent for both *AR* at all Re, it is logical to suggest that the wake structure is indeed independent to Re and *AR* once it has exceeded the critical aspect ratio.

The profiles of the flexible cylinders on the other hand are different. It is noticed that the flexible cylinder of *AR* =16 only exists in the first three locations in Figure 5.2 for Re = 4000 and first two locations in Figure 5.4 and Figure 5.6 for Re = 6000 and 8000 is

because the flexible cylinder took a huge deflection to $x/D \approx 2$ and 3 respectively due to the force from the oncoming freestream (see Figure B1 and Figure B2 in Appendix B). This prevents the measurements at any locations at $x/D < 3$. Thus, only profiles starting from the original $x/D = 3$ to $x/D = 5$ were measured. However, as top priority was given to the tip, profiles of flexible cylinder of $AR = 16$ at $x/D = 3$ was put into comparison with rigid cylinder at $x/D = 1$ and subsequently the latter locations. Figure 5.1 illustrates the comparison of the free end position shift of flexible cylinder to the rigid cylinder.

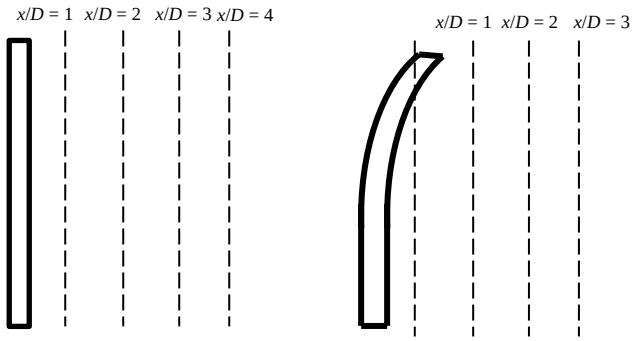

Figure 5.1: Schematic diagram of the measurements concerning the position shift due to the hindrance of flexible cylinder.

The profiles of the flexible cylinders of $AR = 10$ at Re = 4000 and 6000 (see Figure 5.2 and 5.4 (a) (b)) behave similarly to that of rigid cylinders; that is, it has approximately the same velocity profile at $x/D = 1$ and 2 in terms of the wake region and flow velocity value. Despite the similar wake profile of the flexible cylinder of $AR = 10$ at Re = 4000 and 6000 at $x/D \leq 2$, the slight deflection ($x/D < 1$) of flexible cylinder of $AR = 10$ at Re = 6000 (see Figure B4) appears to cause the negative $\bar{u}$ component velocity to shift to positive at $x/D = 3$. A very dominant $\bar{w}$ component velocity as compared to the weak $\bar{u}$ component velocity at $x/D \leq 3$ (see Figure 5.2 and Figure 5.8 (a) to (c) for comparison) of the flexible cylinders of $AR = 10$ at Re = 4000 indicate the influence of downwash is very strong at $x/D \leq 3$, very much alike with the rigid cylinder case. The flexible cylinder of $AR = 10$ at Re = 6000 has the strong influence of downwash happens at $x/D \leq 2$, as seen by the weaker $\bar{w}$ component velocity compared to $\bar{u}$ component velocity at $x/D = 3$ (see Figure 5.4 and Figure 5.10 (a) to (c) for comparison).

Though the flexible cylinder of $AR = 10$ at Re = 4000 and 6000 do not have much impact on the velocity profile, it does at Re = 8000. It appears from Figure 5.6 (a) to (e)

that the wake region is increased slightly to around $z/D \approx 8$ as opposed to the wake region at $z/D \approx 7$ for Re = 4000 and 6000. Besides that, the lower value of the $\overline{w}$ component velocity as opposed to the relatively higher value of the $\overline{u}$ component velocity signifies the influence of downwash is weaken (see Figure 5.6 and Figure 5.12 (a) to (c) for comparison). The deflection of the flexible cylinder of $AR = 10$ at Re = 8000 is at $x/D < 2$ (see Figure B5).

On the other hand, it can be seen from Figure 5.3, Figure 5.5 and Figure 5.7 (a), (b) and (c) that the influence of tip effects for flexible cylinder of $AR = 16$ is only up to $2D$ from the free end as indicated by the strong velocity deflect which attenuates at $z/D \approx 14$ (see the long dashed double dot arrow that marks the boundary of the wake region in approximate estimation). This means that the wake region is increased to $z/D \approx AR - 2$ from the free end for the flexible cylinder. However, since the flexible cylinder was deflecting/bending in the x-direction, the height of the cylinder was shorten by a little to compensate for the bending. Therefore, the wake region should increase more than only $2D$ from the free end. In fact, it can be seen that the flexible cylinder of $AR = 16$ at Re = 6000 and 8000 from Figure B2, where the bend (fluctuates at $x/D = 3$) is the most significant amongst all. Their respective velocity profiles show the velocity at the intended AR is close to the freestream velocity (as indicated by the circle in Figure 5.5 and 5.7 (a) for flexible cylinder only). The near freestream velocity within the circle shows that the cylinder is deflected/bent so that the region is not affected by the bluff body object. Additionally, see Figure 5.15 and 5.16 of the flow visualization of both rigid and flexible cylinders for better illustration. As the cylinder of $AR = 16$ was deflecting gradually from ground position to $x/D \approx 2$ at the free end, the free end was closest to the point of measurements and gradually increase in distance along the span of the cylinder (see Figure B1 for visualization). Due to that reason, the $\overline{u}$ component velocity near free end is much slower than that of the region below the free end (see Figure 5.2 to Figure 5.7 (a)).

Conclusively, it can be seen that the diminishing/weakening of downwash has resulted in the increased height of the wake region. Thus, most of the vortices generated can be transported downstream instead of downwards in the case of the rigid cylinder. As most of the vortices generated are immediately transported downwards for rigid cylinder,

the wake region is smaller. As all the turbulent activities happen within the wake, the region of wake can serve as a preliminary indication to the amount of turbulence present behind an object.

As discussed above, the influence of the tip effects for a rigid and flexible cylinder is up to 3*D* and insignificant diameters from the free end respectively. This translates to different sizes of wake behind the rigid and flexible cylinders. The size of the wake behind a flexible cylinder is greater than that of a rigid cylinder by circa 2*D* for the same *AR*. As the influence of downwash phenomena is very negligible behind a flexible cylinder, the tip vortex generated can be transported downstream more effectively without being downwashed towards the ground. Thus, the effective area of which the turbulent activities happen improves considerably. The average wake region in accordance to the rigid and flexible cylinders in different *AR* and Re are presented in Table 5.1. In addition, the average wake region increment produced by the flexible cylinders is calculated and shown in Table 5.1. It is with substantial evidence that the wake region increment is achieved using flexible cylinder. However, there are two additional phenomena that is associated with the flexible cylinder – deflection in the *x*-direction and oscillation traverse to the flow. Therefore, the roles of these phenomena are examined in the subchapter 5.13.

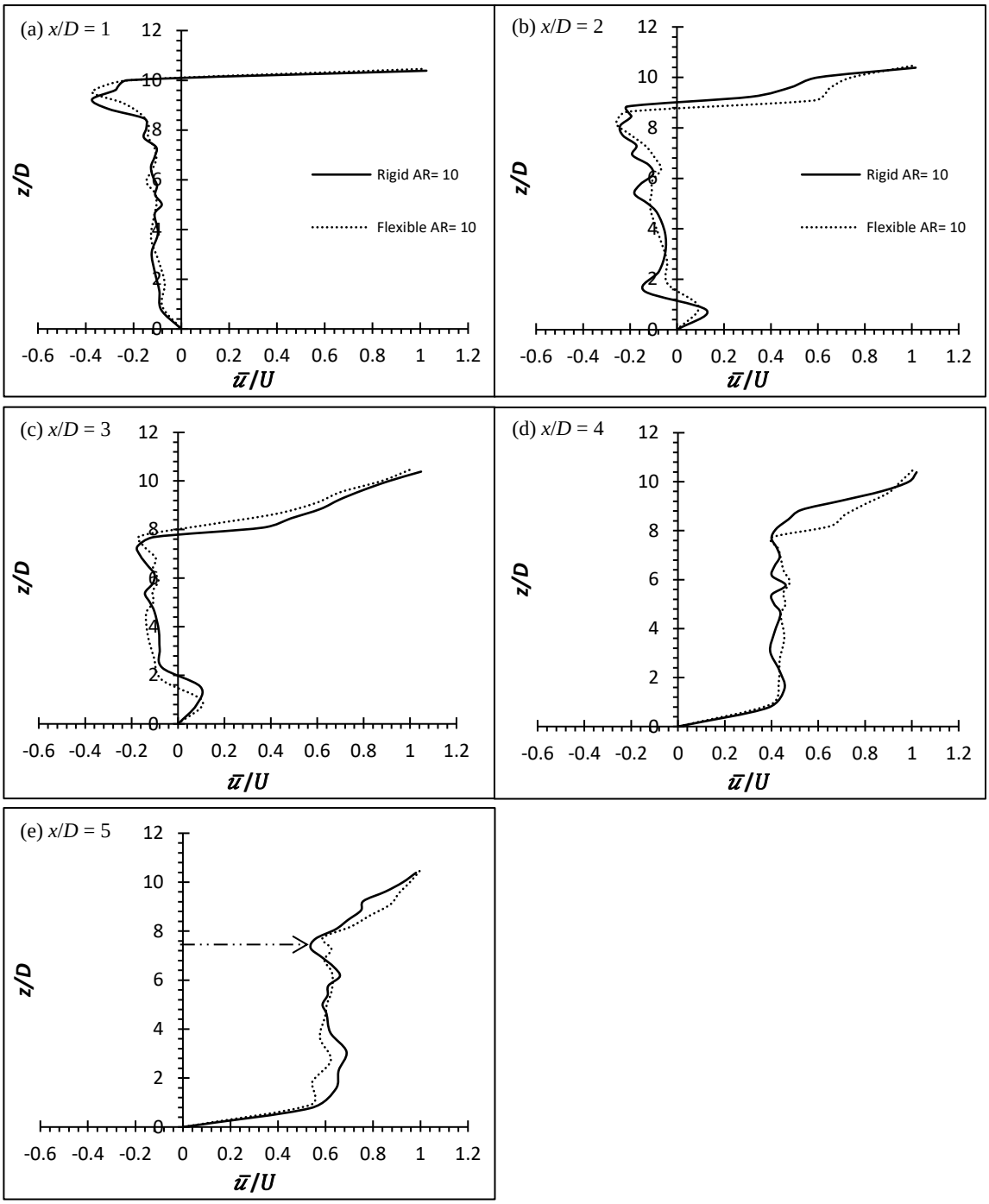

Figure 5.2: Time-average streamwise velocity profile of rigid and flexible finite cylinder of *AR* = 10 at wake centreline (*y*/*D* = 0) for Re = 4000

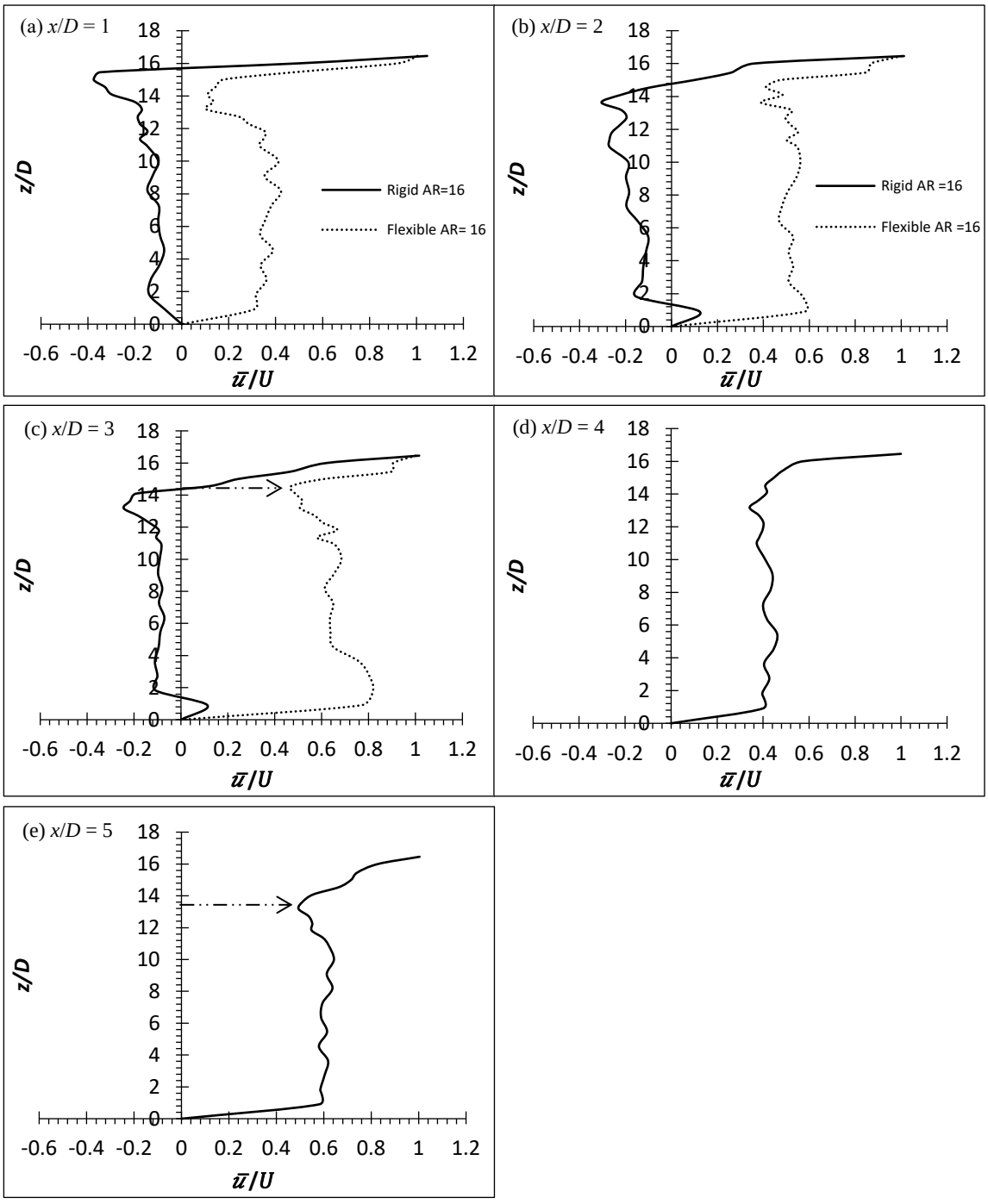

Figure 5.3: Time-average streamwise velocity profile of rigid and flexible finite cylinder of *AR* = 16 at wake centreline (*y*/*D* = 0) for Re = 4000

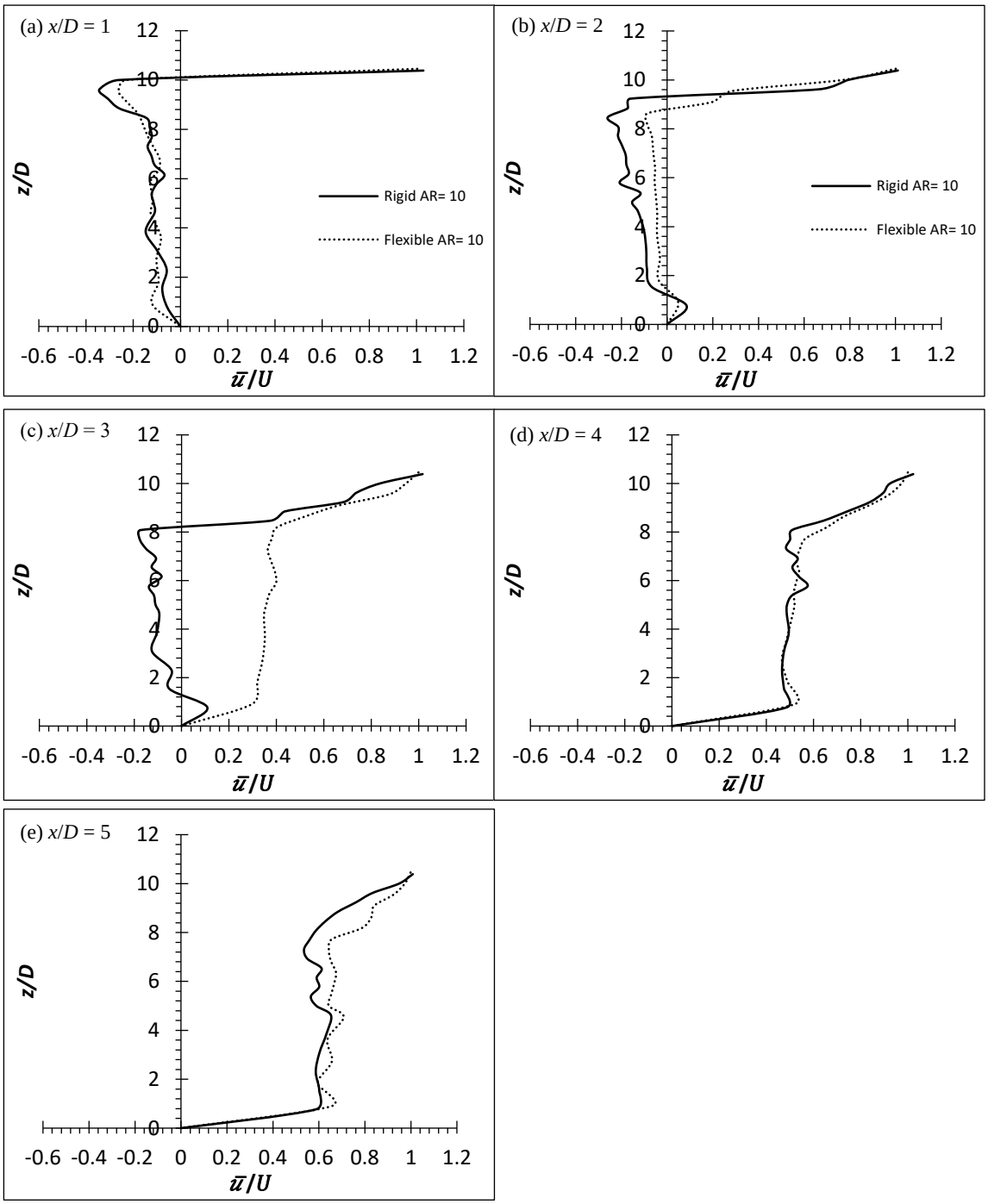

Figure 5.4: Time-average streamwise velocity profile of rigid and flexible finite cylinder of *AR* = 10 at wake centreline (*y*/*D* = 0) for Re = 6000

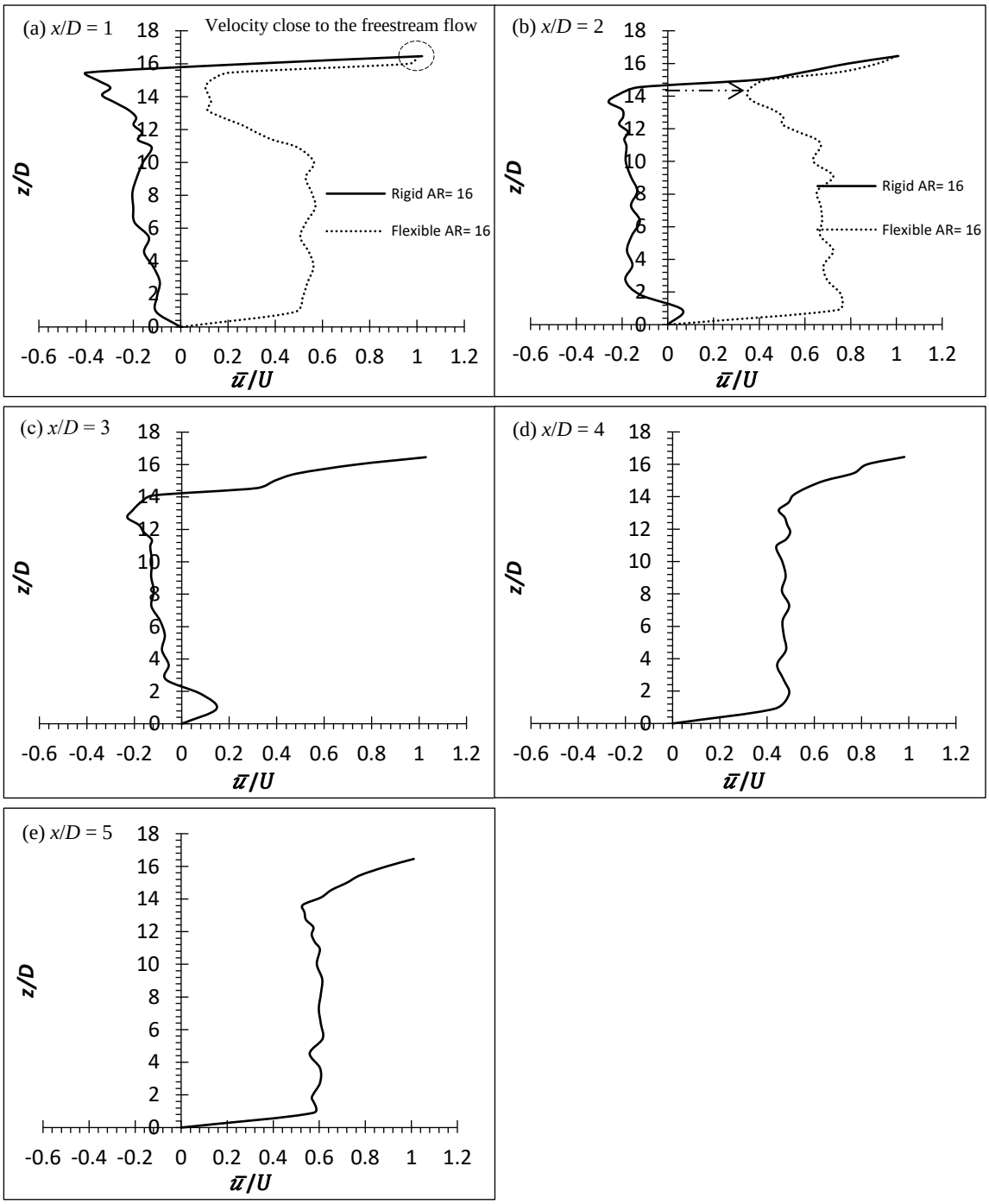

Figure 5.5: Time-average streamwise velocity profile of rigid and flexible finite cylinder of *AR* = 16 at wake centreline (*y*/*D* = 0) for Re = 6000

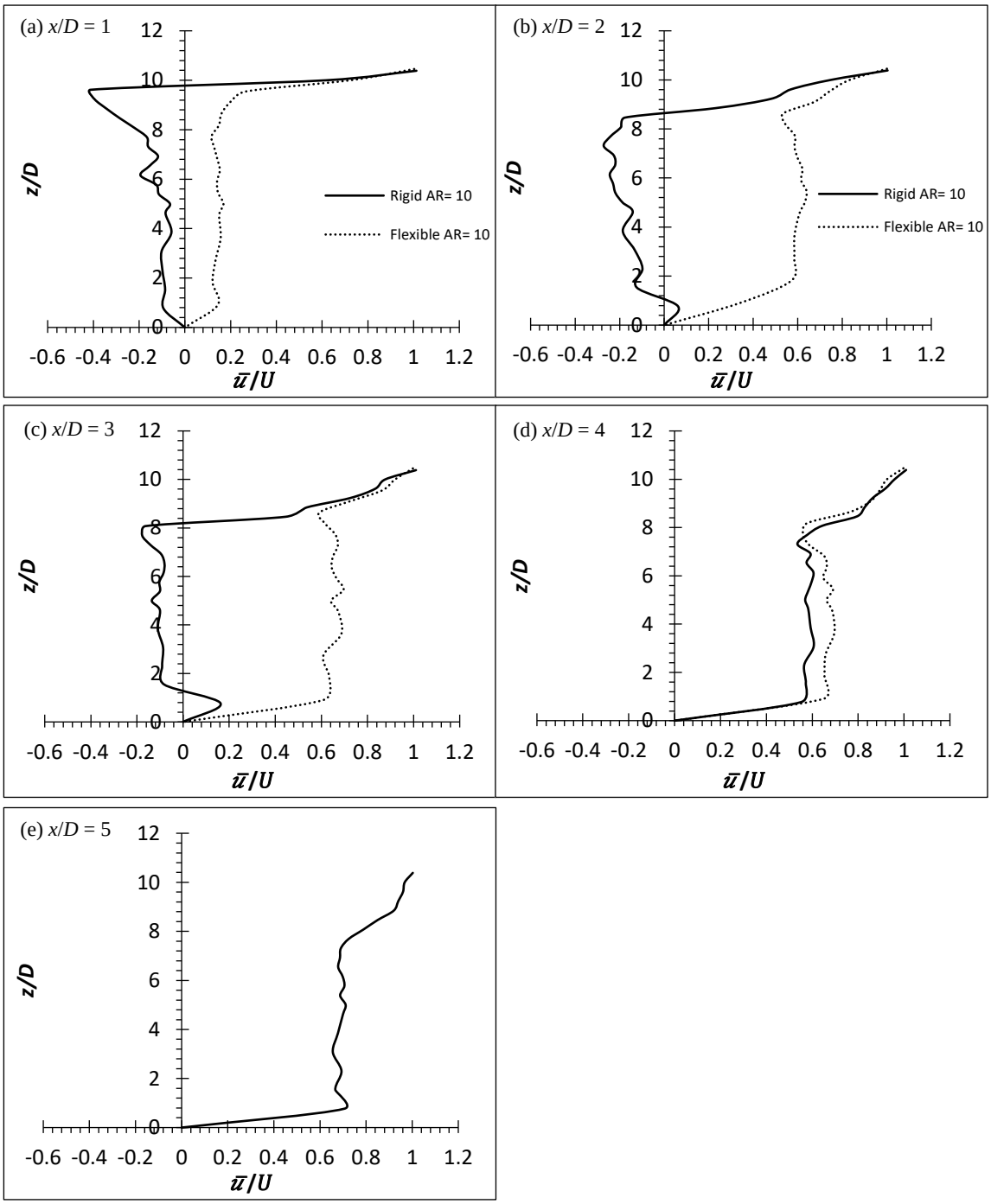

Figure 5.6: Time-average streamwise velocity profile of rigid and flexible finite cylinder of *AR* = 10 at wake centreline (*y*/*D* = 0) for Re = 8000

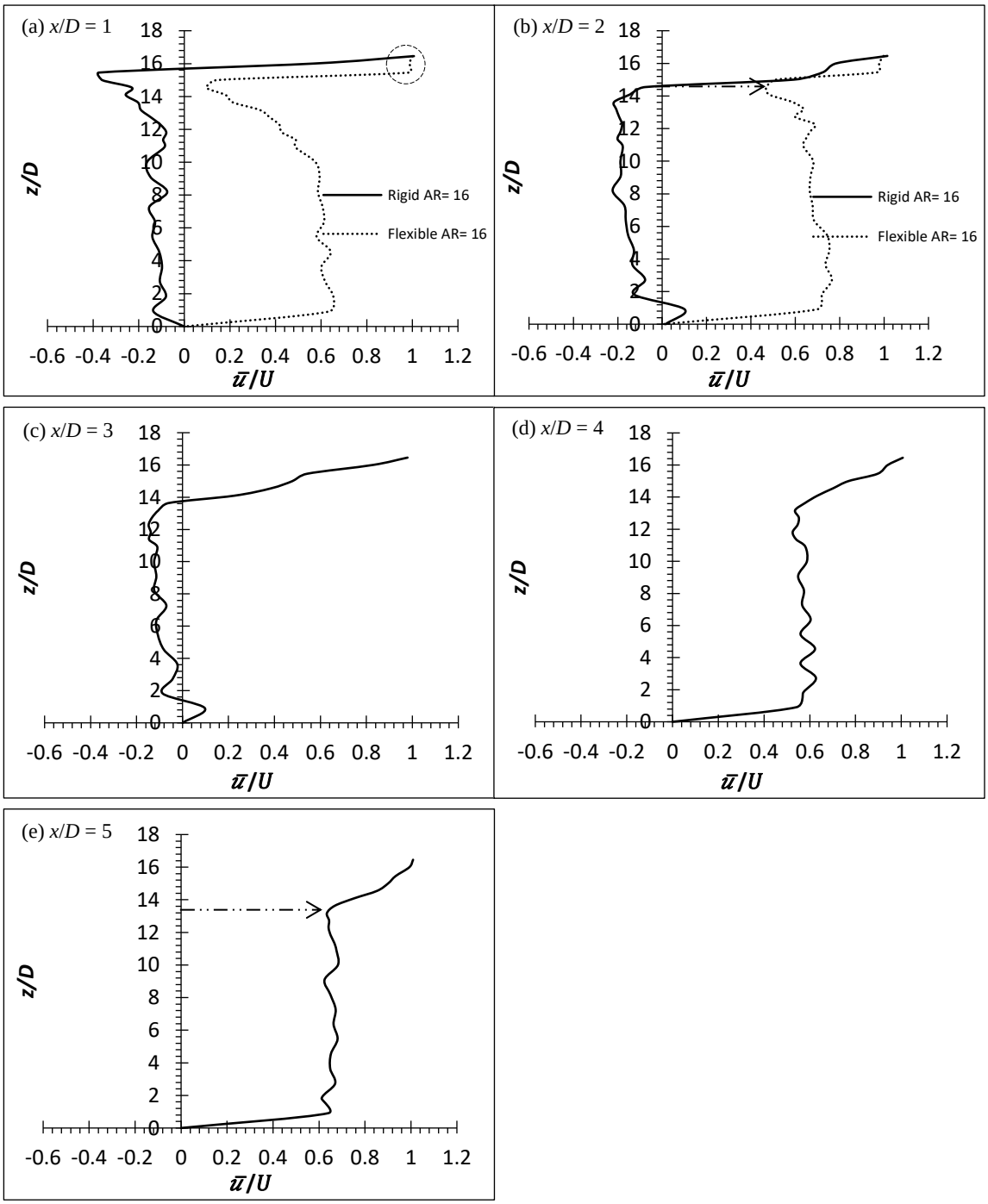

Figure 5.7: Time-average streamwise velocity profile of rigid and flexible finite cylinder of *AR* = 16 at wake centreline (*y*/*D* = 0) for Re = 8000

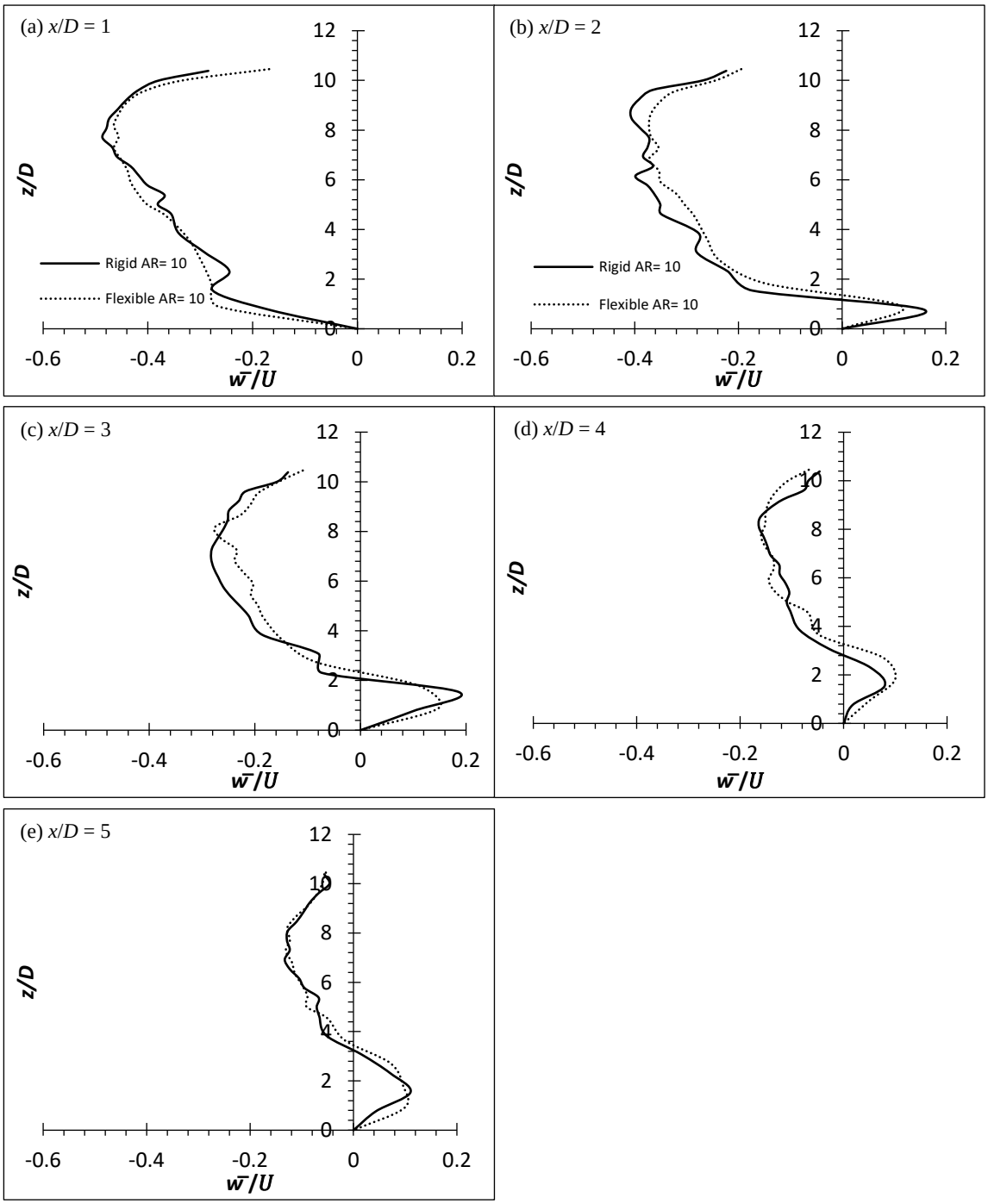

Figure 5.8: Time-average wall-normal velocity profile of rigid and flexible finite cylinder of *AR* = 10 at wake centreline (*y*/*D* = 0) for Re = 4000

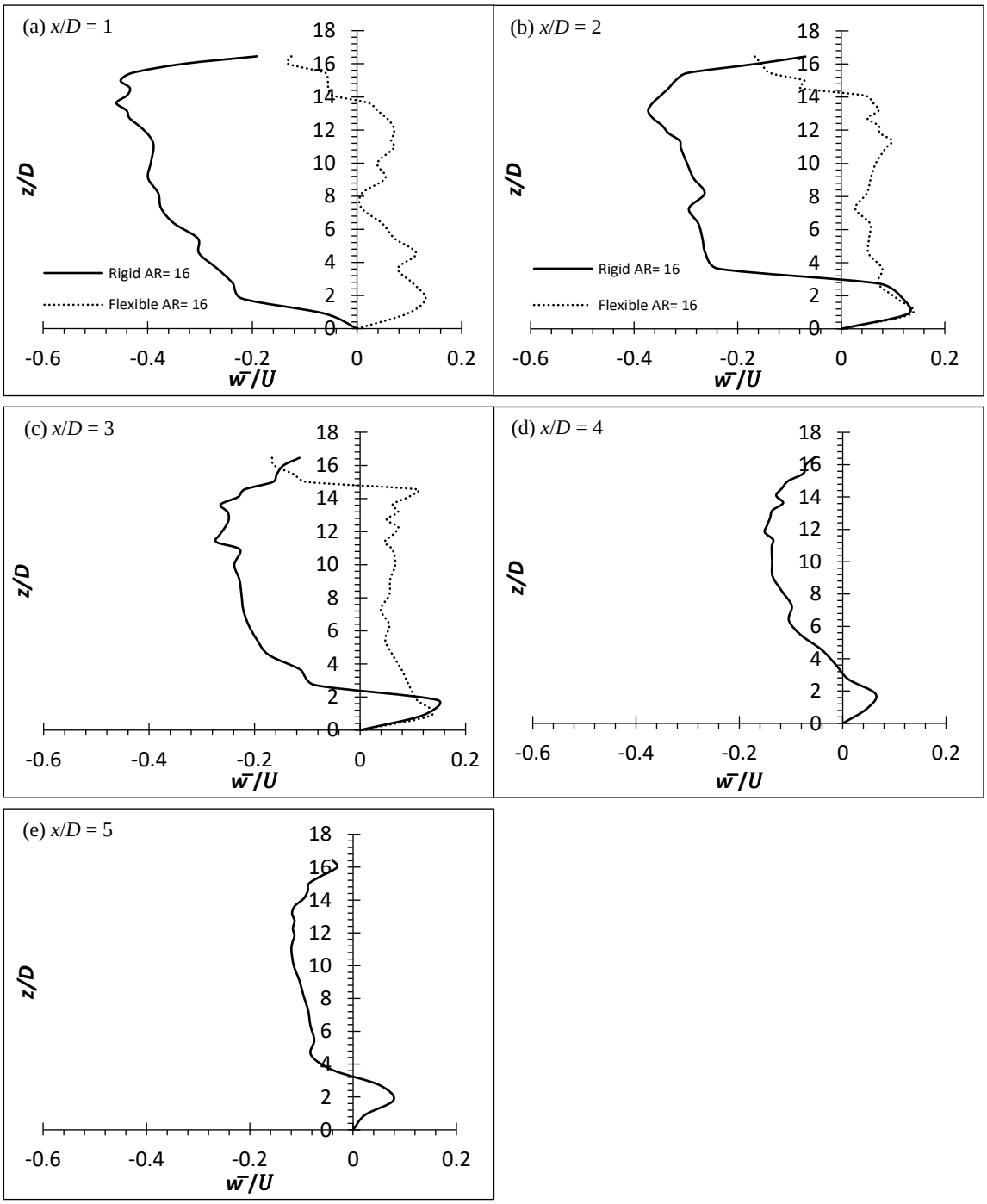

Figure 5.9: Time-average wall-normal velocity profile of rigid and flexible finite cylinder of *AR* = 16 at wake centreline (*y*/*D* = 0) for Re = 4000

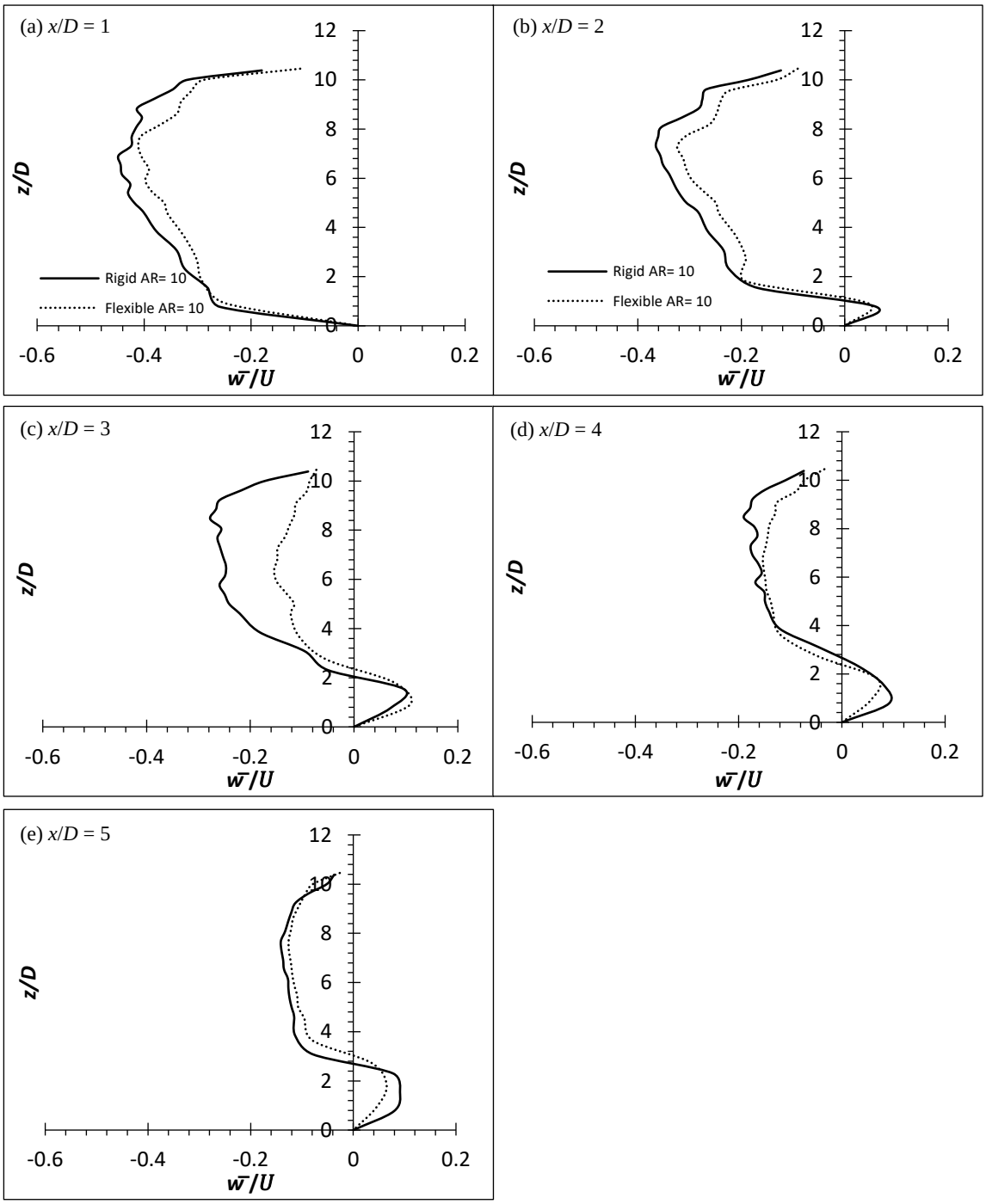

Figure 5.10: Time-average wall-normal velocity profile of rigid and flexible finite cylinder of AR = 10 at wake centreline (y/D = 0) for Re = 6000

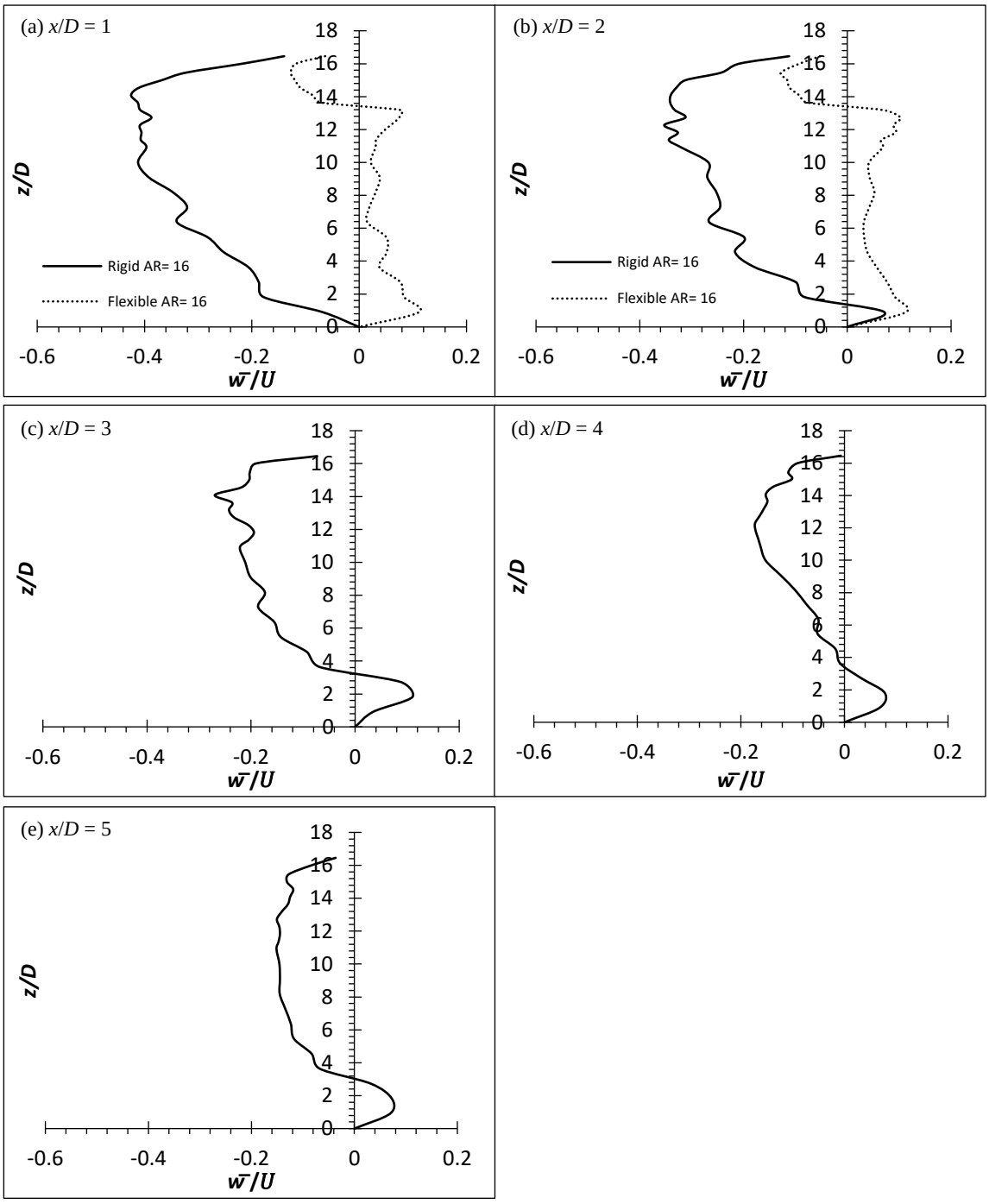

Figure 5.11: Time-average wall-normal velocity profile of rigid and flexible finite cylinder of *AR* = 16 at wake centreline (*y*/*D* = 0) for Re = 6000

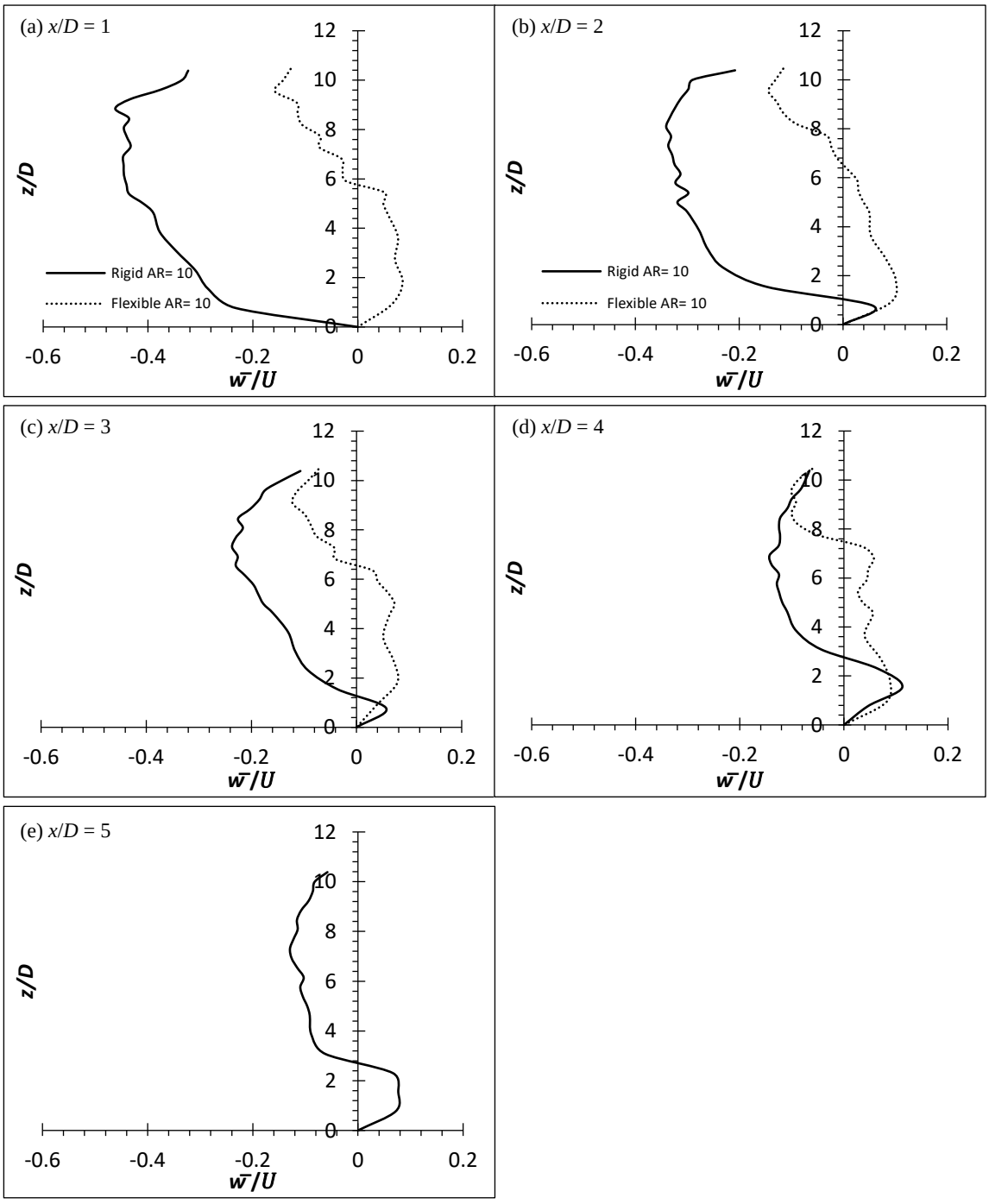

Figure 5.12: Time-average wall-normal velocity profile of rigid and flexible finite cylinder of *AR* = 10 at wake centreline (*y*/*D* = 0) for Re = 8000

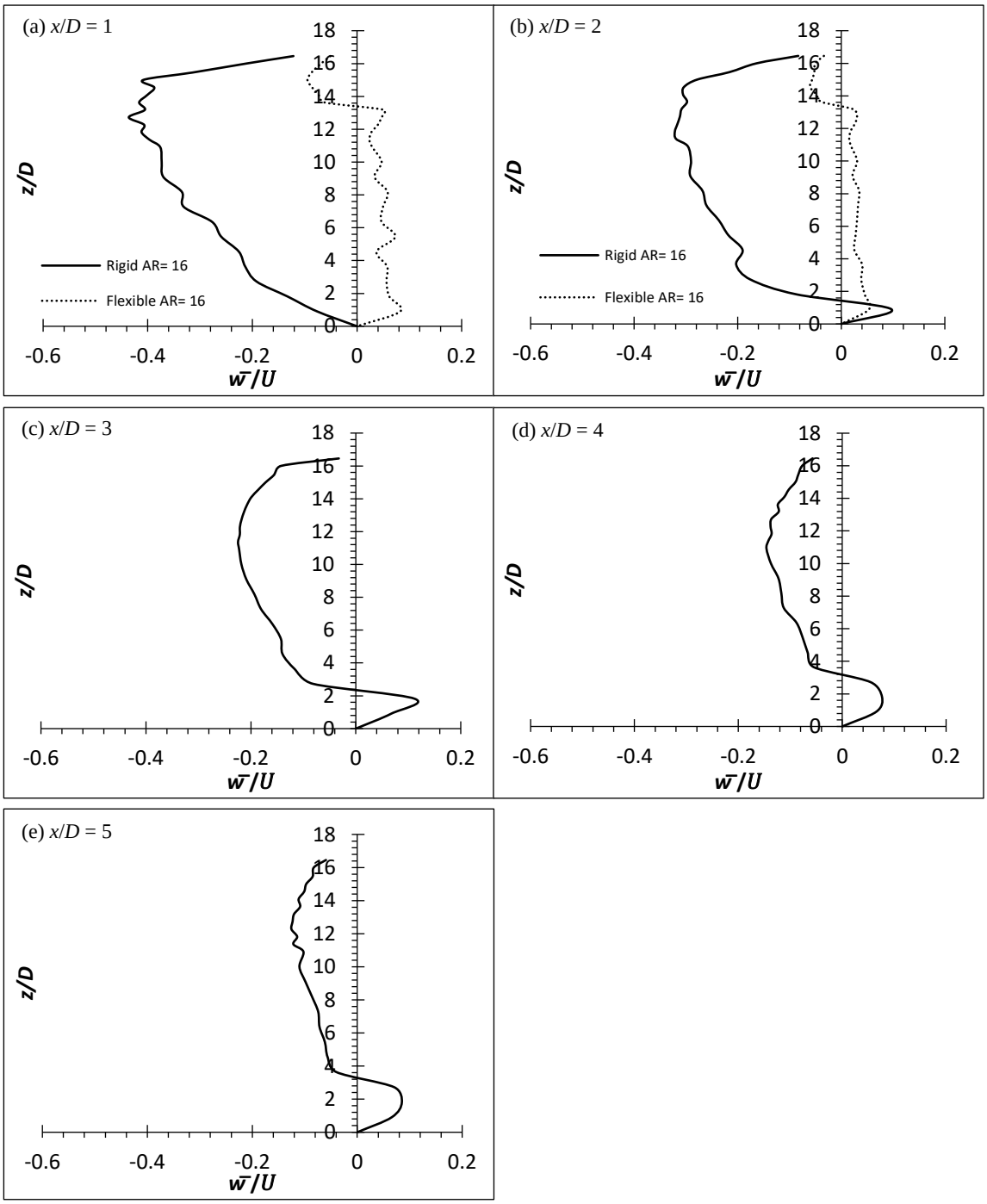

Figure 5.13: Time-average wall-normal velocity profile of rigid and flexible finite cylinder of *AR* = 16 at wake centreline (*y*/*D* = 0) for Re = 8000

Table 5.1: The average wake region (in approximation) behind the rigid and flexible cylinders at different conditions

		Average wake region		
AR	Re	Rigid Cylinder	Flexible Cylinder	Increment (%)
10	4000	~ 7.0 D	~ 7.0 D	0
	6000	~ 7.0 D	~ 7.7 D	~ 10.00
	8000	~ 7.2 D	~ 8.0 D	~ 11.10
16	4000	~ 13.0 D	~ 14.4 D	~ 10.77
	6000	~ 13.1 D	~ 14.2 D	~ 8.40
	8000	~ 13.0 D	~ 14.4 D	~ 10.77

5.1.2. Flow visualization around the finite rigid and flexible cylinders

As an effort to provide substantial evidence that shows the different wake region by the rigid and flexible cylinder, a separate set of experiment that utilizes the high-speed camera capability to capture the flow pattern behind the rigid and flexible cylinders. A rigid cylinder of *AR* = 10 and a flexible EVA cylinder of *AR* = 16 which were operating at Re = 3500 were being recorded by a Photron FASTCAM Mini UX 100 compact high-speed camera. It is a monochrome camera which is capable to shoot 4000 fps at full HD resolution, 1,280 x 1,024 pixel. A tracer which has roughly the same density as water is used in order to ensure the tracer follows the flow field, without interrupting the nature of the path of the flow field.

As can be seen from Figure 5.14, the wake behind the rigid cylinder of *AR* = 10 shows strong influence of the downwash, especially below the free end. A circular region below the free end is spotted (see indicator in Figure 5.14), which brings the flow downwards to the ground, as visualized by Park and Lee (2000) (see Figure 3.5) and also agrees with the interpretation from the velocity distribution profile as discussed above. As the result of the downwash, most of the vortices generated are downwashed to the ground as they follow the path of the flow field (as indicated by the darker colour of the tracer before x/D = 3).

On the other hand, the most notable feature of the flow behind the flexible cylinder which has deflected (take note of the flexible cylinder of *AR* = 10 at Re = 4000 and 6000

which barely reflected) is the absence of downwash and tip effects, as shown in Figure 5.15. Due to the absence of the downwash flow, no strong influence of downwash can be seen in the near wake of the cylinder. The tracer is transported downstream instead of downwards. Hence, the vortices associated with the flow can be transported and prolonged downstream, expanding the effectiveness of turbulence region. The wake region is seen on the same height as the free end of the cylinder, proving the effectiveness of the flexible cylinder in increasing the wake region.

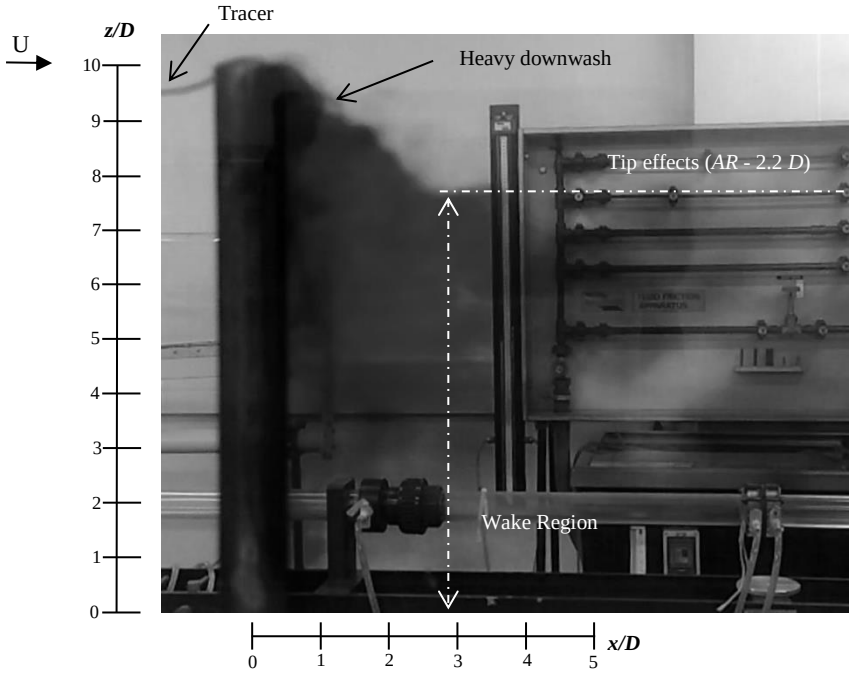

Figure 5.14: Flow visualization of rigid cylinder of *AR* = 10 at Re = 3500

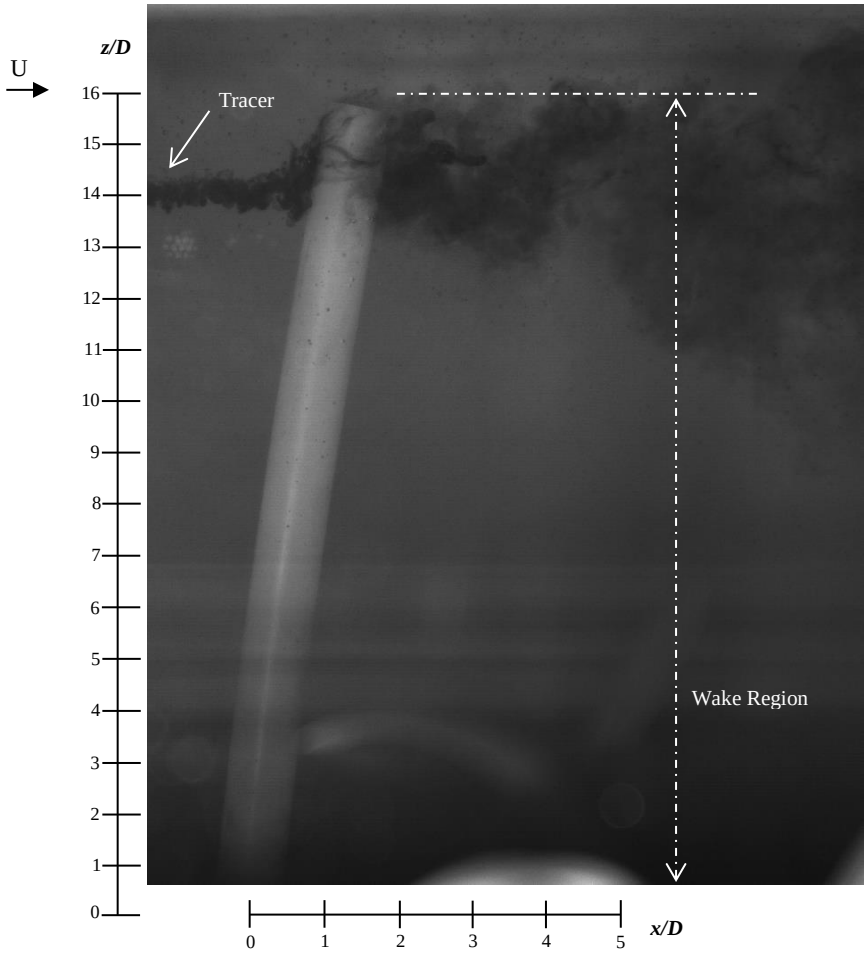

Figure 5.15: Flow visualization of rigid cylinder of *AR* = 10 at Re = 3500

5.1.3. Roles of deflection and oscillation of the flexible cylinder on the wake region

It has seen that the wake region of the rigid cylinder is circa 3*D* from the free end. Okomoto and Yagita (1973), Park and Lee (2000) and Roh and Park (2003) had discovered the same phenomenon in their experimental results and concluded the downwash effect is the main contributor to this phenomenon. The vortex generated is therefore drawn to the floor instead of transported downstream, making the wake size smaller in the case of rigid cylinders, regardless of *AR*. This can also be confirmed through the study of $\overline{u}$ and $\overline{w}$ component velocity profiles because vortices travel in the same path as the mean velocity. The absence of downwash for the flexible cylinders on the other hand, suggests that the vortices generated at the free end can be transported downstream once it has received enough energy and detach itself from the boundary layer or under circumstances that it is forced to detach due to the interference of the structural motion that is vibrating. As a result of that, the wake region can be larger than that behind the rigid cylinders.

It is because of the elastic property of the flexible cylinders possess, the additional two phenomena emerge – a) deflection and b) oscillation. With reference to the Figure C1, the oscillation of flexible cylinders comprises the oscillating motion, oscillating frequency and the oscillating amplitude. When put into comparison of the wake structure and its respective cylinder's oscillation response, it can be observed that the wake structure from the velocity profiles of the flexible cylinders under any condition are irrelevant of the oscillation response because the oscillating motion, frequency and amplitude are distinctive at each Re; while the wake region behind the flexible cylinders under all Re behaves quite similar.

The *x*-deflection on the other hand though, has its effect on the downwash and subsequently the wake region behind the cylinder. The degree of deflection, as can be seen from Figure B1 to B5, are different. In comparison to its respective velocity profiles, presence of downwash can be discerned from the static cylinders (no deflection) associated with it. Apart from that, the increase in wake region is also seen associate with higher *x*-deflection. From Table 5.1, there is no increment in the wake region because the flexible EVA cylinder of *AR* = 10 at Re = 4000 was not deflected at all (see Figure B3).

As the Re is increased, the deflection of the flexible EVA cylinder of *AR* = 10 increases; hence, the increment in the wake region as well. The deflection is not a function directly of Re but of oncoming freestream velocity as greater velocity induces greater force on the cylinder. With reference to Table 5.1, the wake region behind the flexible EVA cylinder of *AR* = 16 compared to the rigid cylinder of *AR* = 16 does not seem to be a huge increment because the height of the cylinder decreases as it is deflected (as proven by the local streamwise velocity at $z/D \approx 15.4$ to be nearly identical as freestream velocity (see Figure 5.4 (b)), so the wake region is almost at the same height as the free end.

It would seem that the greater in deflection of the cylinder, the effect of downwash is less pronounced and therefore the velocity of $\bar{u}$ component flow behind the cylinder at the same location as cylinders with less deflection is recovering quicker towards the freestream velocity. It has been demonstrated by Kawamura *et al.* (1984) and Taniguchi *et al.* (1981) that there exists a large pressure drop (higher pressure in front of the cylinder and lower pressure behind the cylinder) for the rigid finite cylinder that leads to the downwash behind the cylinder. Since the velocity profile distributions of the flexible cylinder show that downwash is weaken or diminished, the pressure drop behaviour could have been altered for the flexible cylinder. The pressure drop could have been lessen for the downwash phenomenon to be weaken or the pressure distribution around the deflected cylinder could be have been altered. The extremely high localized $\bar{w}$ component velocity against the same significantly low localized $\bar{u}$ component velocity can be seen from any rigid cylinder regardless of *AR* and Re. On the other hand, the difference between the extremely high localized $\bar{w}$ component velocity against the same significantly low localized $\bar{u}$ component velocity becomes closer until where the $\bar{u}$ component velocity becomes more dominant than the $\bar{w}$ component velocity can be observed for the cylinder in the order of the magnitude of deflection/bending. In other words, the cylinder with less deflection spots a higher influence of downwash and the influence is slowly being weaken for the cylinder with higher degree of deflection, signifying that the deflection of the cylinder is capable of weakening the downwash. (e.g. see flexible cylinder of *AR* = 10 at Re = 8000 and its deflection at Appendix B and see flexible cylinder of *AR* = 16 at Re = 6000 and its deflection at Appendix B). Nevertheless, in order to further confirm the above

speculation, a future work is recommended to study the effect of deflection only in relation to the pressure drop and downwash.

The turbulence characteristics of the flexible cylinder will be examined and discussed through the turbulence intensity and Reynolds stresses of the flow field to further solidify the improvement brought by the flexible cylinder over rigid cylinder.

5.2. Turbulence Intensity

Turbulence intensity is perhaps the most direct indication in evaluating the level of turbulence in the flow. Turbulence intensity is a part of turbulence statically analysis that examines the fluctuations about the mean. As the turbulent motions associated with the eddies are random, the study of turbulence intensity is able to characterize how a random variable is distributed about the mean flow. The equation of the turbulence intensity can be written as:

$$\mathrm{TI} = \frac{u'}{\mathrm{U}} \tag{5.1}$$

Where u' is the RMS of the turbulent velocity fluctuations and U is the averaged mean velocity.

A higher turbulence intensity would indicate a higher level of turbulence in the flow. Therefore, by examining the localized turbulence intensity in the near wake of the rigid and flexible cylinder of *AR* = 10 and 16 in accordance with its deflection and oscillation motions, it is hoped that the reason behind the changes in the localized turbulence intensity between the rigid and flexible cylinder could be answered.

5.2.1. Turbulence intensity distribution of rigid cylinders

The distributions of the streamwise turbulence intensity (u'/U) and the wall-normal turbulence intensity (w'/U) of rigid cylinder of *AR* = 10 at Re = 4000 in the wake centreline (y/D = 0) are shown in Figure 5.16.

As seen from Figure 5.16 (a), the localized maximum turbulence intensity (u'_{max}/U) ≈ 26.14 % can be seen located at $z/D \approx 8$ of the cylinder at x/D = 2; consistent

with the existence of the tip vortex where it has a greater strength as witnessed by Park and Lee (2004) and Rostamy *et al.* (2012) in their experiments where the higher turbulence intensity coincides with the tip vortex. The tip vortex at $x/D = 1$, slightly at a smaller value is extended into the region of the downwash flow within the near wake and hence, the local (u'_{max}/U) is found to be at $z/D \approx 7$ and 8 (see the long dashed double dot arrow marked at Figure 5.16 (a) for $x/D = 3$). Below the region, the influence of tip vortex is becoming weaker that it can no longer suppress the formation of Kármán vortex, therefore, the regular Kármán vortex is present below the tip vortex and can be represented by the considerable weaker turbulence intensity value (Rostamy *et al*., 2012). It is however important to note that the freestream turbulence intensity was at circa 11 %, so the increment of the turbulence intensity at the tip is only a mere approximate 15 %. The phenomenon of (u'_{max}/U) near the mid-height span can also be seen through findings from (Park & Lee, 2000; Park & Lee, 2004; Sumner *et al.*, 2004; Afgan *et al.*, 2006) which Sumner *et al.* (2004) regarded that as the region that are bounded on the four corners by the tip and base vortices. As this region is the focal point where the vortex structures, vortex street, downwash and upwash meet, it is highly interactive.

The (w'/U) also show a concentrated region at the near mid-height at $x/D \approx 3$ which also corresponds to the interaction of upwash and downwash. As the higher turbulence intensities region for both components move downwards as x/D increases, it can be said that vortex generated does indeed being downwashed.

Apart from that, the turbulence intensity distributions for rigid cylinder of $AR = 10$ at Re = 6000 and 8000 (not shown) are also in the same fashion as Re = 4000, except that the values of turbulence intensity do increase by marginally as Re increases. The (u'_{max}/U) of Re = 6000 and 8000 are approximately 28.82 % and 30.25 %.

Figure 5.17 shows the distributions of the (u'/U) and the (w'/U) of rigid cylinder of $AR = 16$ at Re = 4000 in the wake centreline ($y/D = 0$). Similar to what is found in cylinder of $AR = 10$ at Re = 4000, the (u'_{max}/U) of $AR = 16$ at circa 29.15 % can be seen located at $z/D \approx 13$ where the tip vortex is being downwashed and transported downwards. It shows that at the span roughly below 4D from the free end, the regular Kármán vortex shedding becomes dominant. There is an overall increment of turbulence intensity as the

AR increases (as shown in Figure 5.16 and 5.17). Again, the turbulence distributions of cylinder of *AR* = 16 at Re = 6000 and 8000 are not shown as they show similar fashion to that of Re = 4000 except the values increase marginally at approximately 29.72 % and 31.35 % respectively.

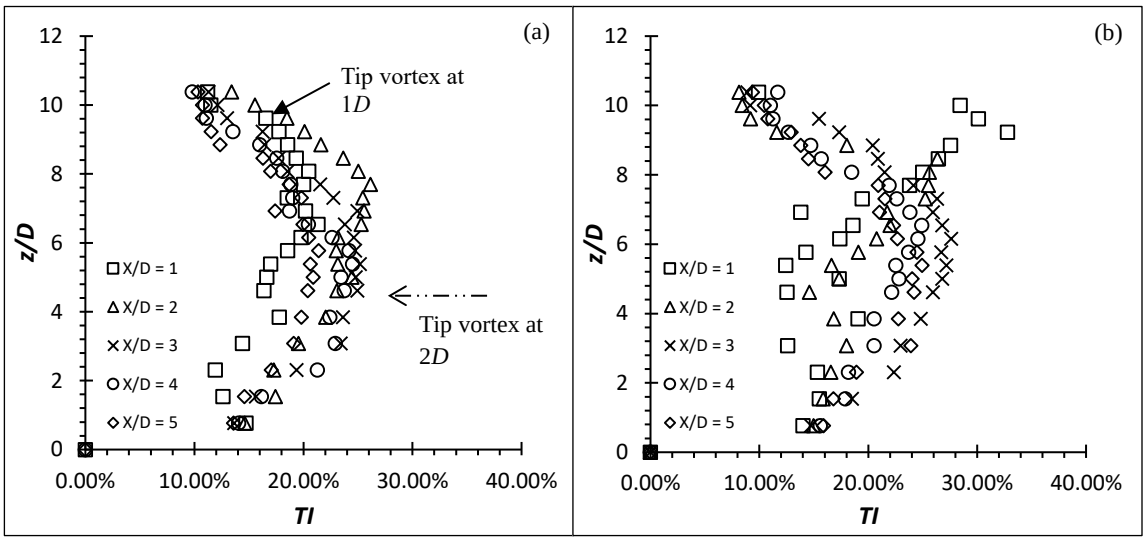

Figure 5.16: Turbulence intensity distribution for rigid cylinder of *AR* = 10 at Re = 4000: (a) Streamwise turbulence intensity (b) wall-normal turbulence intensity

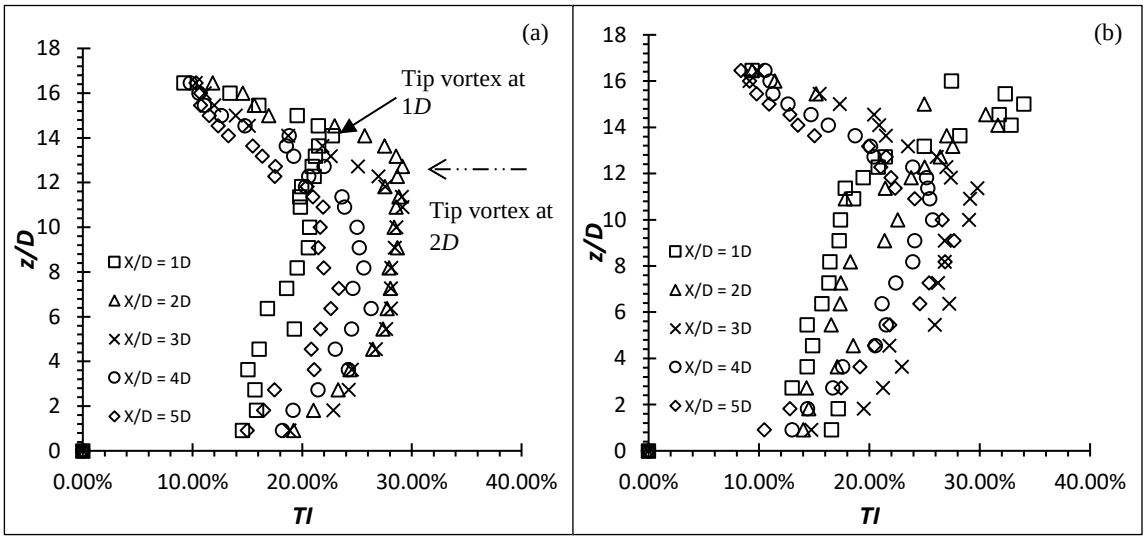

Figure 5.17: Turbulence intensity distribution for rigid cylinder of *AR* = 16 at Re = 4000: (a) Streamwise turbulence intensity (b) wall-normal turbulence intensity

5.2.2. Turbulence intensity distribution of flexible cylinders

The distributions of the streamwise turbulence intensity (u'/U) and the wall-normal turbulence intensity (w'/U) of flexible cylinder of AR = 10 and 16 at Re = 4000, 6000 and 8000 in the wake centreline (y/D = 0) are shown in Figure 5.18 to Figure 5.23. With reference to the (u'/U) distribution of the rigid cylinders, which shows no major changes at different AR; the (u'/U) distribution of flexible cylinders (see Figure 5.20 (a) to Figure 5.23 (a)) shows the upwards shifting of the local (u'_{max}/U) compared to the rigid cylinder. While the rigid cylinder has roughly (u'_{max}/U) at $z/D \approx AR$ - 3D to 4D, the flexible cylinder has approximately (u'_{max}/U) at $z/D \approx AR$ - 1D to 2D at x/D = 3, 4, and 5 subjecting to the order of the magnitude of deflection; roughly equivalent to the deflected height of flexible cylinder. This indicates that the tip vortex generated is not being downwashed as the vortex follow the path of the bulk flow.

The cylinder of AR = 10 at Re = 4000 and 6000 do not experience major increment as it behaves nearly the same as the rigid cylinder of the same condition. This could be due to the fact that the cylinder at Re = 4000 and 6000 do not oscillate and deflect, which acts like a rigid cylinder. The cylinder at Re = 8000 has spotted a slight increment.

It is important to remind the readers that as the cylinders were deflected during the measurements, the measurement point could only be made after the deflection of the cylinder. In light of that, the distance of the free end will be much closer to the measurement point than that of the span below the free end. According to the (u'/U) distribution of the rigid and flexible cylinders, increase in magnitude of the (u'/U) of flexible cylinders can also be discerned. It is the increment in the magnitude that shows the potential of flexible cylinders in enhancing turbulence in the flow. The (u'_{max}/U) of the flexible cylinder of AR = 10 and 16, which is approximately at $z/D \approx AR$ - 2D, ranged from 36.67 % to 97.35 % (in approximation) from AR = 10 at Re = 8000 to AR = 16 at Re = 8000. It is a huge increment over the rigid cylinders which is at a mere 26.14 % of AR = 10 at Re = 4000.

Surprisingly, according to Figure 5.22 (a) and Figure 5.23 (a), the local (u'_{max}/U) for Re = 8000 is lower than that of 6000. However, this could be attributed to the disorganized oscillating motion and also the oscillation that happens off-axis (see Figure

C1 (c)) for Re = 8000. The word “disorganized” in this context means that the oscillation of the cylinder does not follow the typical sinusoidal wave where the frequency and amplitude become slow/low at few cycles and the existence of double or triple crests and troughs (see Figure C1 (b) and (c) for illustration and comparison). Nevertheless, the overall turbulence intensity distribution of the flexible cylinders shows considerable improvement over the rigid cylinders in promoting turbulent activities in the flow.

The (w’/U) on the other hand, shows a general reduction in the magnitude at the mid-span of the flexible cylinders. The turbulence intensity near the free end of the flexible cylinders shows decrease in the magnitude from circa 32 % for the rigid cylinders to 13 % at the lowest for the flexible cylinders. The fluid particle is therefore not active in the w component. The reason could be because it has no downwash flow behind the cylinder and thus the fluctuation in w component is not active. Nevertheless, the (u’/U) of the flexible cylinder has seen increasing so significantly (in the range of 36 % to 97 %) over the rigid cylinder, though a slight reduction in the (w’/U), it still shows vast improvement over the rigid cylinder.

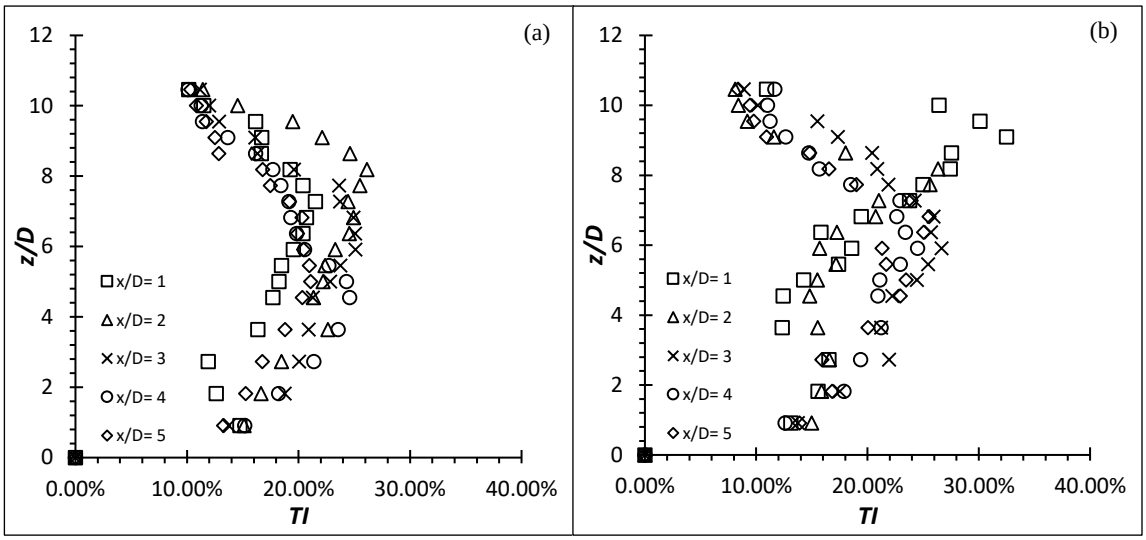

Figure 5.19: Turbulence intensity distribution for flexible cylinder of *AR* = 10 at Re = 4000: (a) Streamwise turbulence intensity (b) wall-normal turbulence intensity

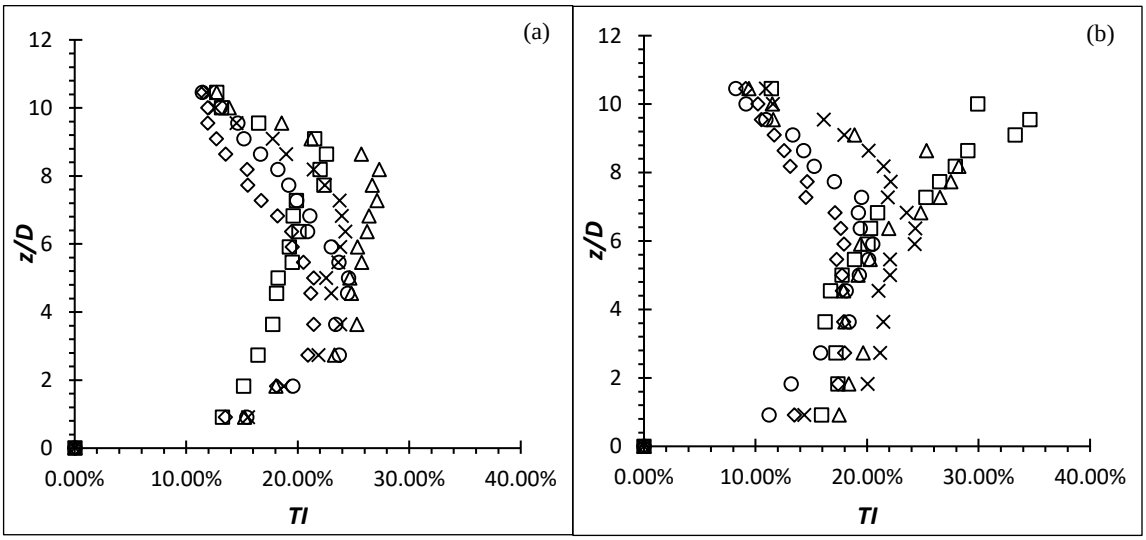

Figure 5.18: Turbulence intensity distribution for flexible cylinder of *AR* = 10 at Re = 6000: (a) Streamwise turbulence intensity (b) wall-normal turbulence intensity

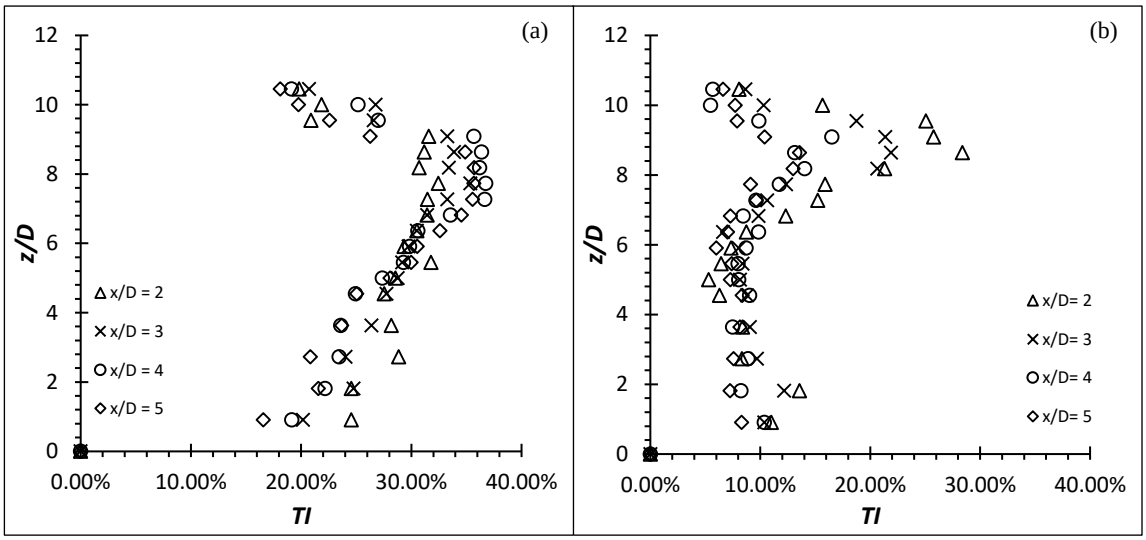

Figure 5.21: Turbulence intensity distribution for flexible cylinder of *AR* = 10 at Re = 8000: (a) Streamwise turbulence intensity (b) wall-normal turbulence intensity

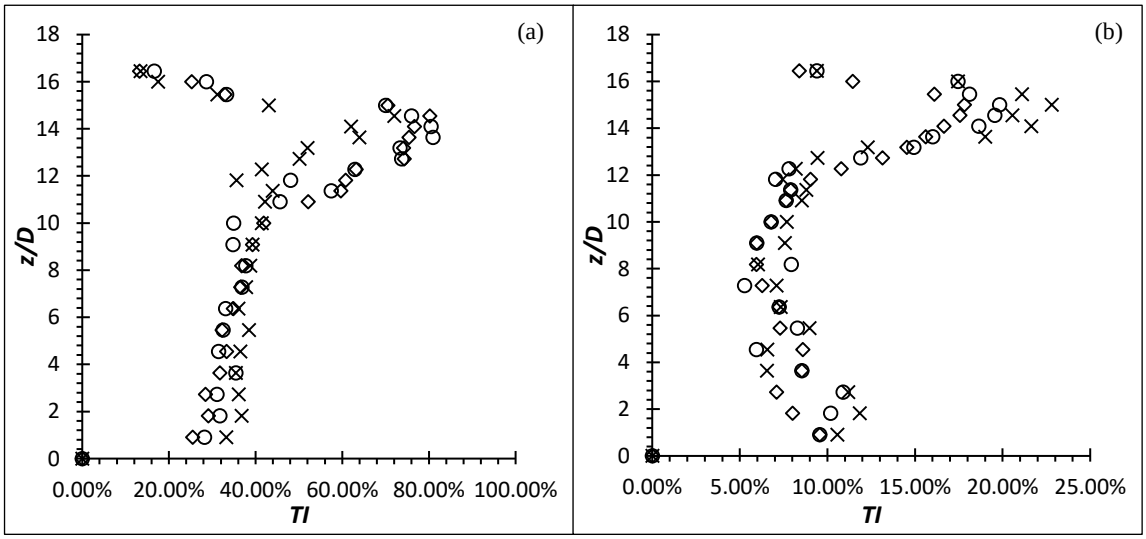

Figure 5.20: Turbulence intensity distribution for flexible cylinder of *AR* = 16 at Re = 4000: (a) Streamwise turbulence intensity (b) wall-normal turbulence intensity

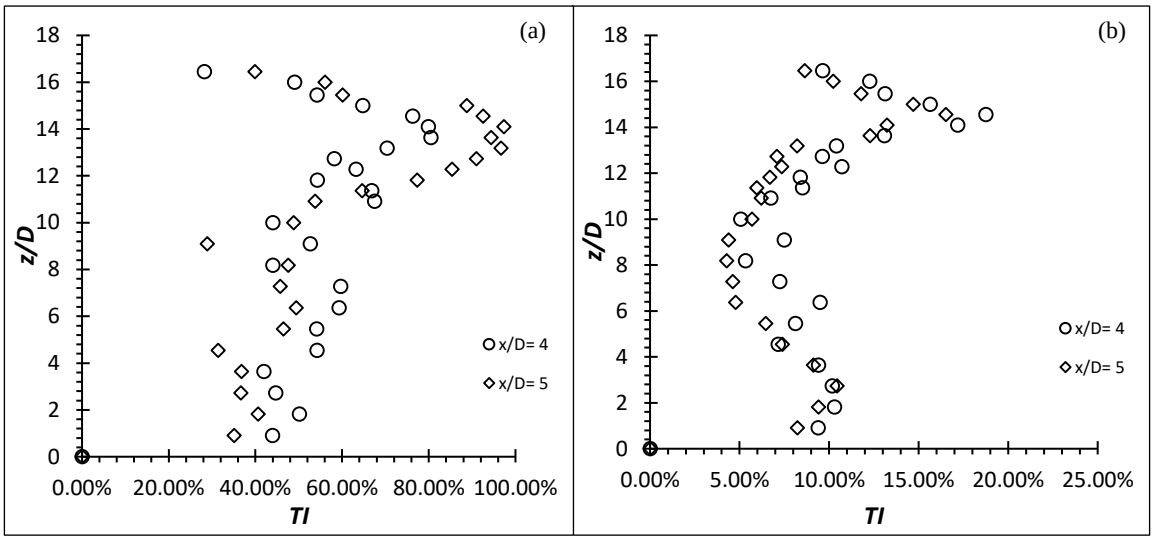

Figure 5.23: Turbulence intensity distribution for flexible cylinder of *AR* = 16 at Re = 6000: (a) Streamwise turbulence intensity (b) wall-normal turbulence intensity

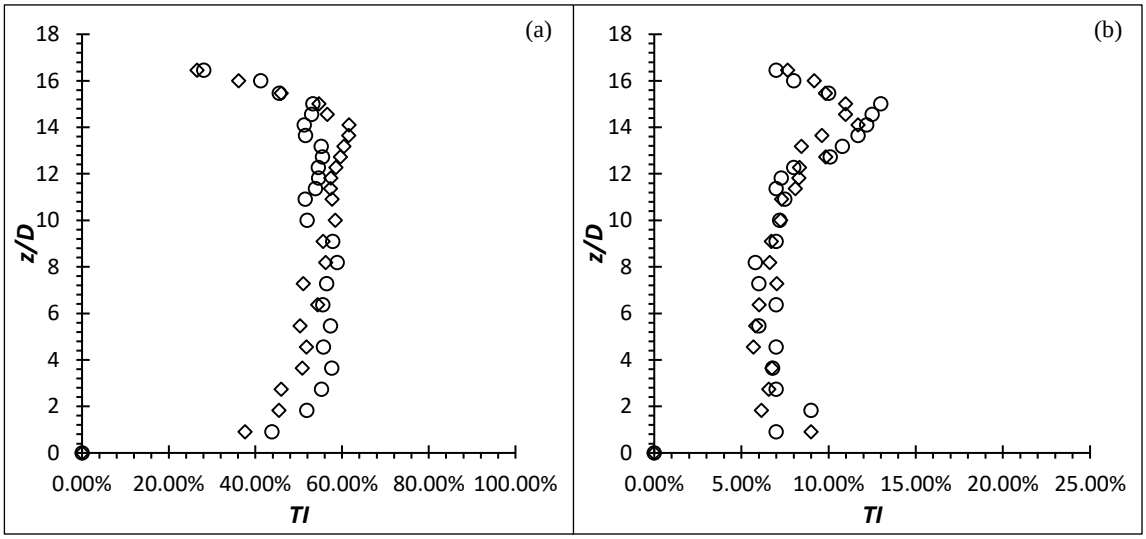

Figure 5.22: Turbulence intensity distribution for flexible cylinder of *AR* = 16 at Re = 8000: (a) Streamwise turbulence intensity (b) wall-normal turbulence intensity

5.3. Turbulent Kinetic Energy

It is seen that from Chapter 5.2 that the turbulence intensity of flexible cylinder has a significant increment over the rigid cylinder. It gives a direct 'picture' of how turbulent the flow is in vicinity and over the span of the cylinder. However, the turbulence intensity could only give details on one directional, which is the *u* component and *w* component separately.

Turbulent kinetic energy, (that is labelled as *k* throughout the context), which is the transport term in the turbulence quantities, accounts for all three components. The turbulent kinetic energy, $\frac{1}{2}(\overline{u'u'}+\overline{v'v'}+\overline{w'w'})$ is calculated by half of the added Reynolds normal stresses together. It is worth to note that only the *u* and *w* component is taken into calculation in this study so the *k* is accounted for the two components only.

5.3.1. Turbulent kinetic energy of rigid cylinders

The normalized (k/U^2) graph downstream of the rigid cylinders of AR = 10 at Re = 4000, 6000 and 8000 are presented in Figure 5.24. The graph shows the local maximum k (k_{max}) being consistently near the free end of the rigid cylinders at x/D = 2. The localized k_{max} value of the rigid cylinders are approximately 0.083, 0.085 and 0.086 for Re = 4000, 6000 and 8000 respectively. There is a slight increment of turbulent kinetic energy for increased Re but the increment is too minute to confirm the relationship. The *k* value attenuates considerably quickly after x/D = 3 but concentrate more in the midspan, which is consistent with the downwash phenomena where it transports most of the vortices downwards.

The profiles of the turbulent kinetic energy for rigid cylinder of AR = 16 (see Figure 5.25) is seen with similar pattern with that of AR = 10. The localized maximum *k* value is concentrated at the free end region at x/D = 2. This is also the region where the shear layer instability happens due to the free end effect where the layers are separated between above the free end and below the free end. The localized k_{max} value of the rigid cylinders are approximately 0.084, 0.083 and 0.087. Similar observations can be for AR = 10 and 16 at three different Re.

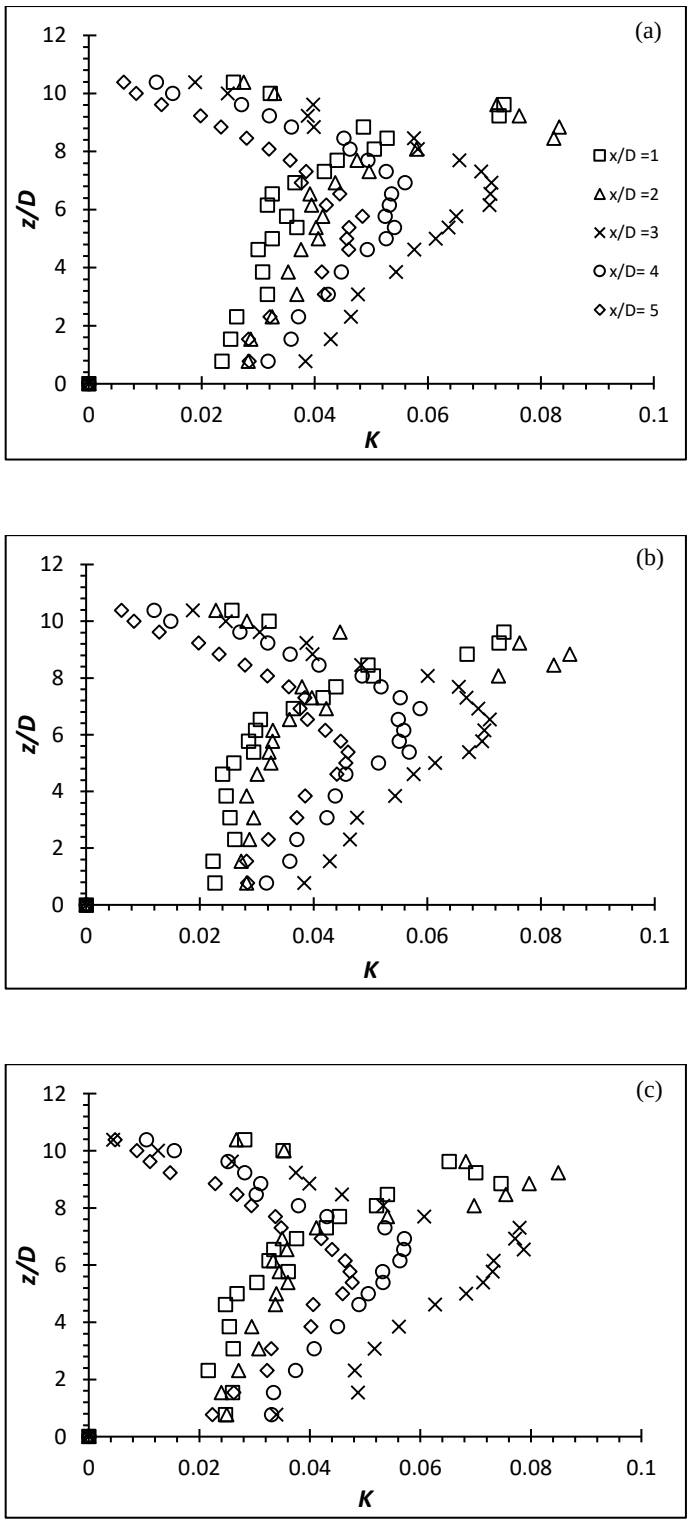

Figure 5.24: Turbulent kinetic energy, *k* for rigid cylinder of *AR* = 10 at (a) Re = 4000 (b) Re = 6000 (c) Re = 8000

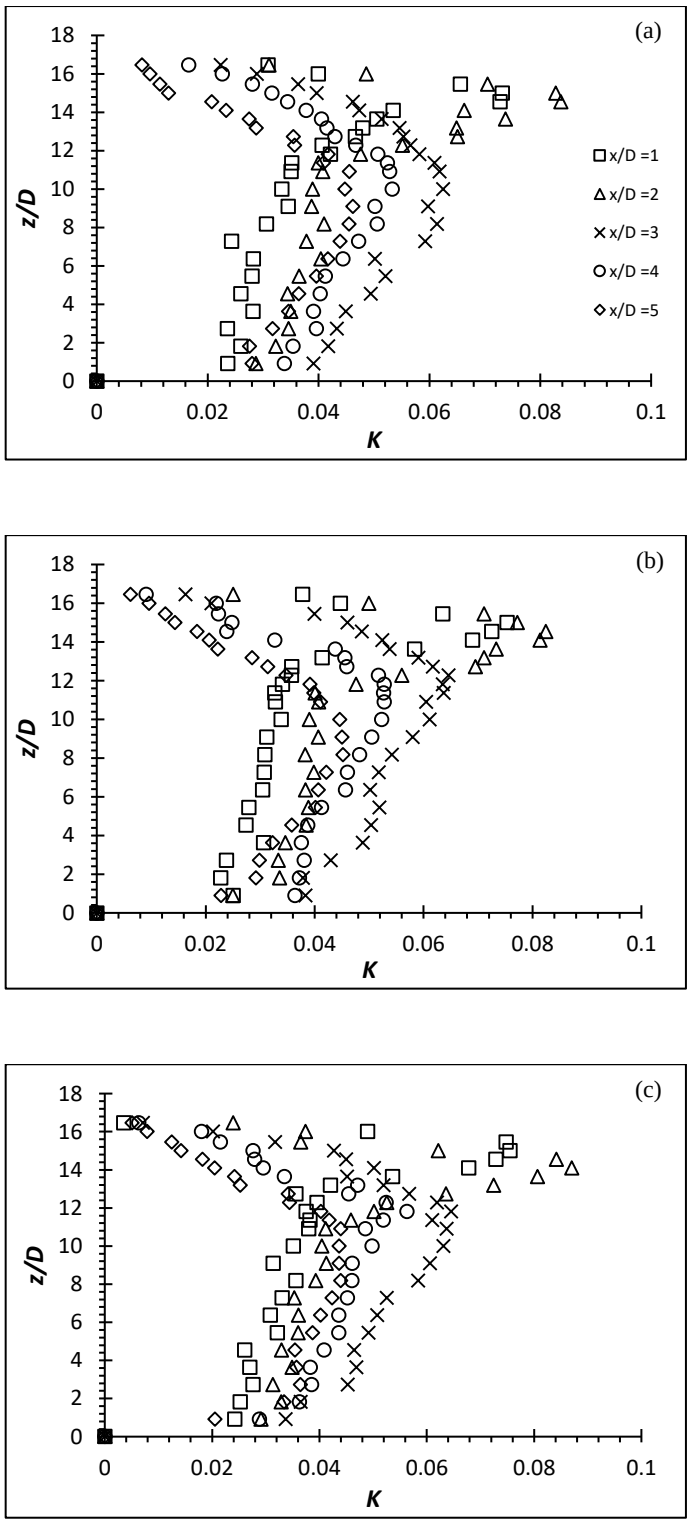

Figure 5.25: Turbulent kinetic energy, *k* for rigid cylinder of *AR* = 16 at (a) Re = 4000 (b) Re = 6000 (c) Re = 8000

5.3.2. Turbulent kinetic energy of flexible cylinders

Figure 5.26 shows the normalized k graph of the flexible cylinders of AR = 10 at Re = 4000, 6000 and 8000. Similar observations of the rigid counterpart can be seen on the flexible cylinders of AR = 10 at Re = 4000 and 6000. The flexible cylinder at Re = 8000 on the other hand has spotted a slight increment of the localized k_{max} at 0.090 over its rigid counterpart at the same Re. Similarly, the maximum turbulent kinetic is generated near the free end where a large amount of shear happens. The cylinder did oscillate but the oscillation was too minute to be registered.

The normalized k graph of the flexible cylinders of AR = 16 at Re = 4000, 6000 and 8000 are presented in Figure 5.27. It is important to remind the readers again that due to the deflection of the flexible cylinders during the experiments, no measurement can be made in the near wake where the deflection interfered with the measurement points. In general, the localized k_{max} occurs at near the free end, very much like its rigid counterpart. This is the region where it is most active with high turbulent kinetic energy. The localized k_{max} of the flexible cylinders are 0.223, 0.236 and 0.166 for Re = 4000, 6000 and 8000 respectively.

Like the turbulence intensity, the midspan region of the cylinder at x/D = 3 and 4 has seen improvement over its rigid counterpart. As the turbulence activities follow the main flow, it is suggested that the phenomenon of downwash might be absent from the flexible cylinder which its main affect is to transport the flow downwards instead of downstream.

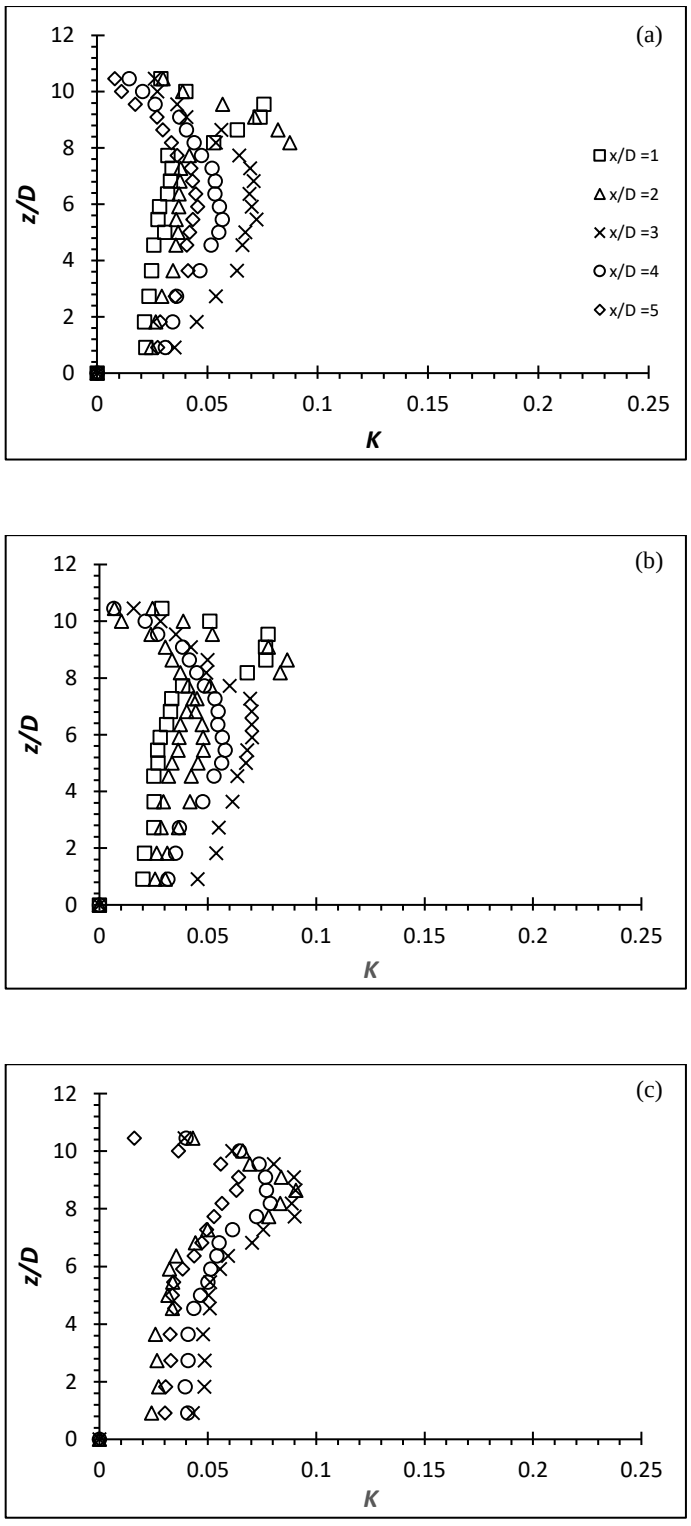

Figure 5.26: Turbulent kinetic energy, *k* for flexible cylinder of *AR* = 10 at (a) Re = 4000 (b) Re = 6000 (c) Re = 8000

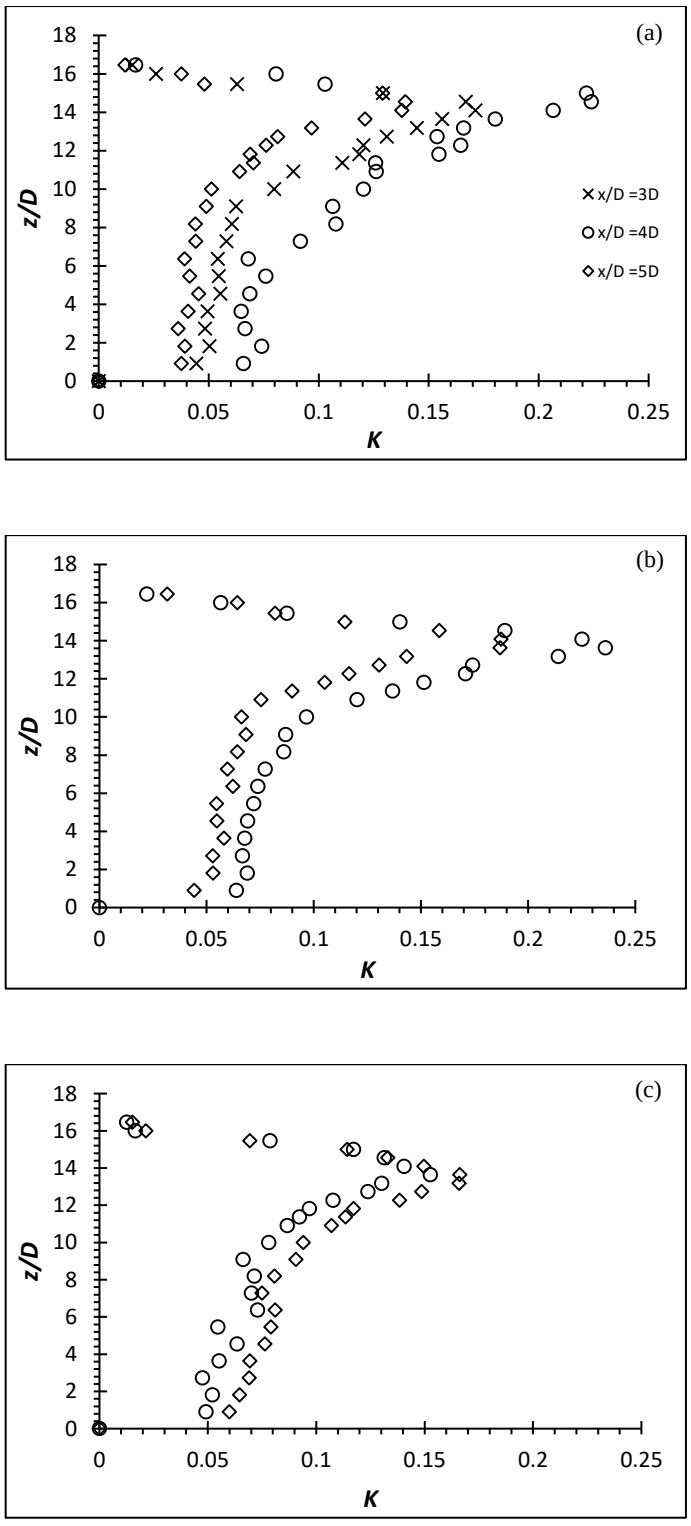

Figure 5.27: Turbulent kinetic energy, *k* for flexible cylinder of *AR* = 16 at (a) Re = 4000 (b) Re = 6000 (c) Re = 8000

5.4. Turbulence Kinetic Energy Budget

It was discussed in Chapter 2.4 that the kinetic energy budget equations provide 'visualization' on how turbulence is spatially distributed after being produced in the mean flow. It is particularly useful to analyse the production term, $-\overline{u_i'u_j'}\frac{\partial U_i}{\partial x_j}$, (for convenience, it is thereby labelled as ***P*** throughout the context) to examine how much energy is contributed to the turbulence formation. Therefore, attention is put on this term as its relationships with the coherent structures present in the flow (Haase *et al.*, 2009) and its evolution along the downstream location can provide adequate information as when the turbulence energy starts to attenuate.

The expression in ***P*** term is nothing more than the shear in the flow. The expression shows that the production term consists of second moment of fluctuating velocity (a.k.a. Reynolds stresses), $\overline{u_i'u_j'}$ and the shear rate, $\frac{\partial U_i}{\partial x_j}$. It can be observed that the Reynolds stresses, which comprises of the fluctuation component, u', is the shear produced in the fluctuation regime; while the shear rate, which comprises of the mean component, *U*, illustrates the shear produced in the main flow regime. The shear rate can be examined in a rather straightforward way as, $\frac{\partial U_i}{\partial x_j}$ describes the change in velocity along the direction that is perpendicular to its flowing direction. Therefore, it should be clear that a higher velocity gradient of the flow should ideally give a higher shear production in the main flow which would also contribute to a higher generation of velocity fluctuations in the wake. The Reynolds stresses on the other hand, describes the flux of momentum in different components and directions caused by the fluctuating flow. Therefore, the product of these two aspects would give the total kinetic energy or the source of turbulence formation.

Since $-\overline{u_i'u_j'}\frac{\partial U_i}{\partial x_j}$ is in the Einstein notation form, naturally as being a vector, there are two components, *i* and *j*. However, with the current study, the terms containing the transverse derivatives are neglected as they were not measured. The ***P*** term being evaluated in here is:

$$\boldsymbol{P} = -\left[\overline{u'u'}\frac{\partial U}{\partial x} + \overline{u'w'}\frac{\partial U}{\partial z} + \overline{u'w'}\frac{\partial W}{\partial x} + \overline{w'w'}\frac{\partial W}{\partial z}\right] \quad (5.1)$$

The $\boldsymbol{P}$ value calculated from the production term serve as a measure to quantify the turbulence enhancement generated by the rigid and flexible cylinders.

Figure 5.28 provides a simple illustration of how the energy is transferred from the mean flow to the turbulent flow. Clearly, the loss of kinetic energy from the mean flow in the form of shear flow is then transferred to the turbulent regime where the turbulent regime gains its energy and slowly dissipate through viscous effect as heat (internal energy of the fluid). However, since the viscous dissipation is unavoidable and it happens at the smallest scale of turbulence, it is not of importance in this study.

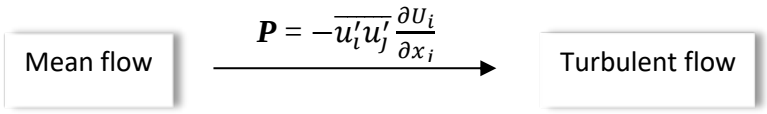

Figure 5.28: Simplified diagram of energy transfers between the mean and turbulent flow

5.4.1. Production term of rigid cylinders

The normalized ($\boldsymbol{P}$/(U^3/D) graph downstream of the rigid cylinders of AR = 10 at Re = 4000, 6000 and 8000 are presented in Figure 5.29. As shown in the figures, the local maximum $\boldsymbol{P}$ ($\boldsymbol{P}_{max}$) in the vicinity of the free end of the rigid cylinders at x/D = 2. The localized $\boldsymbol{P}_{max}$ value of the rigid cylinders are approximately 0.035, 0.035 and 0.037 for Re = 4000, 6000 and 8000 respectively. There is a slight increment of turbulent energy production for rigid cylinder at Re = 8000. The $\boldsymbol{P}$ value attenuates considerably quickly after x/D = 3, which is consistent with the downwash phenomena where it transports most of the vortices downwards.

The rigid cylinders of AR = 16 (see Figure 5.30) on the other hand, also spot a similar observation where the $\boldsymbol{P}_{max}$ occurs near the free end of the rigid cylinders at x/D = 2. The localized $\boldsymbol{P}_{max}$ value is observed at 0.035, 0.036 and 0.039 for Re = 4000, 6000 and 8000. Similar to AR = 10, the $\boldsymbol{P}$ value at circa $z/D = AR$ - 2 is significantly lower than the

span below due to the tip effects which is up to 3*D* from the free end (see Figure 5.13), limiting the wake region to approximately 2*D* - 3*D* below the free end of the cylinder.

As turbulence is an instability generated by shear, the stronger the shear would ideally indicate a stronger turbulence. This is also evident from the shear production term equation, ***P***, of Turbulent Kinetic Budget equations where the term is governed partly by the shear rate. Additionally, the localized $\boldsymbol{P}_{max}$ occurs in the vicinity of the free end of the rigid cylinders because that is the region where shear layer instability happens most dramatically, which then induces the roll-up phenomenon and later transfer the kinetic energy from the mean flow to the primary vortices. As the flow accelerates over the free end, the accelerated layer and the layer below it creates a strong shear region.

It would also seem that the *AR* plays no significant role in enhancing the turbulence production in the rigid cylinder case as both *AR* = 10 and 16 have similar ***P*** value at the same Re. It is therefore suggested that the geometrical factor does not contribution to the turbulence enhancement.

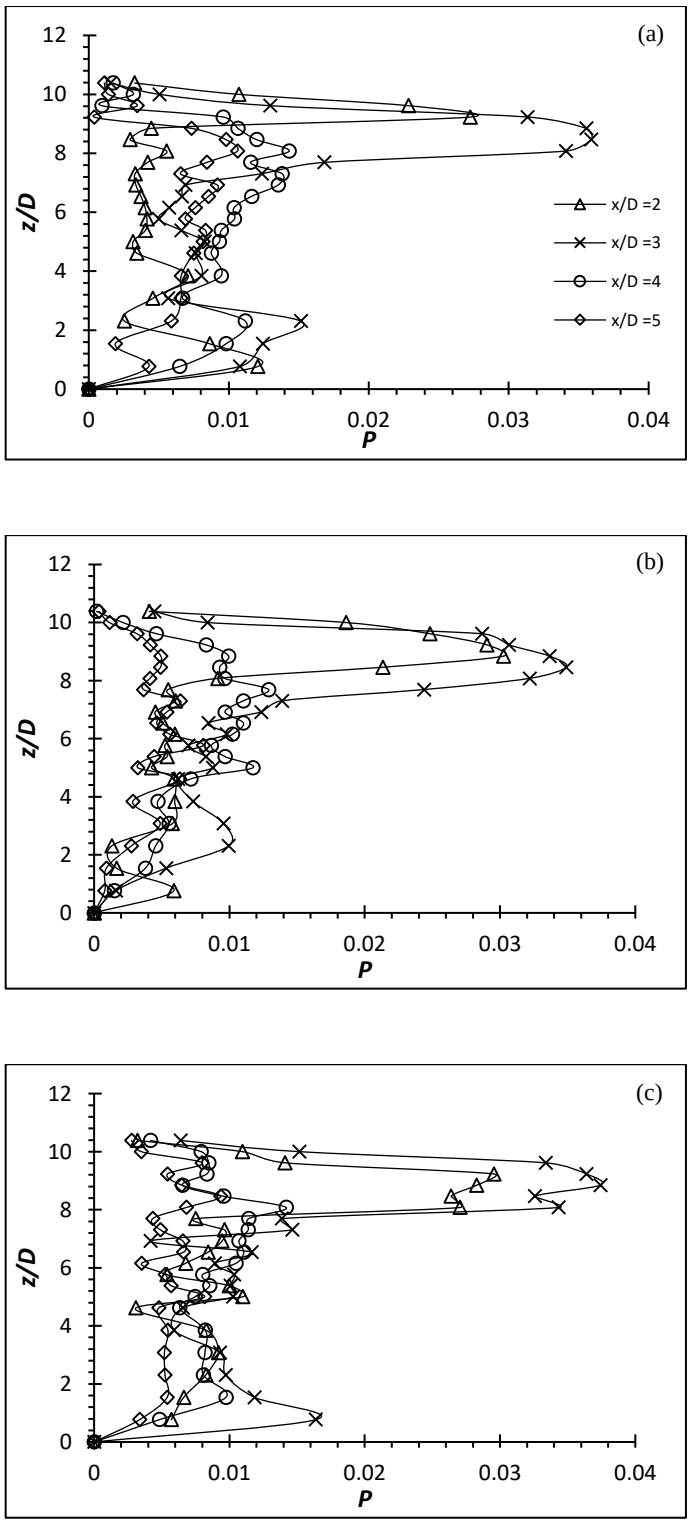

Figure 5.29: Production term, $-\overline{u_i' u_j'} \frac{\partial U_i}{\partial x_j}$ for rigid cylinder of *AR* = 10 at (a) Re = 4000 (b) Re = 6000 (c) Re = 8000

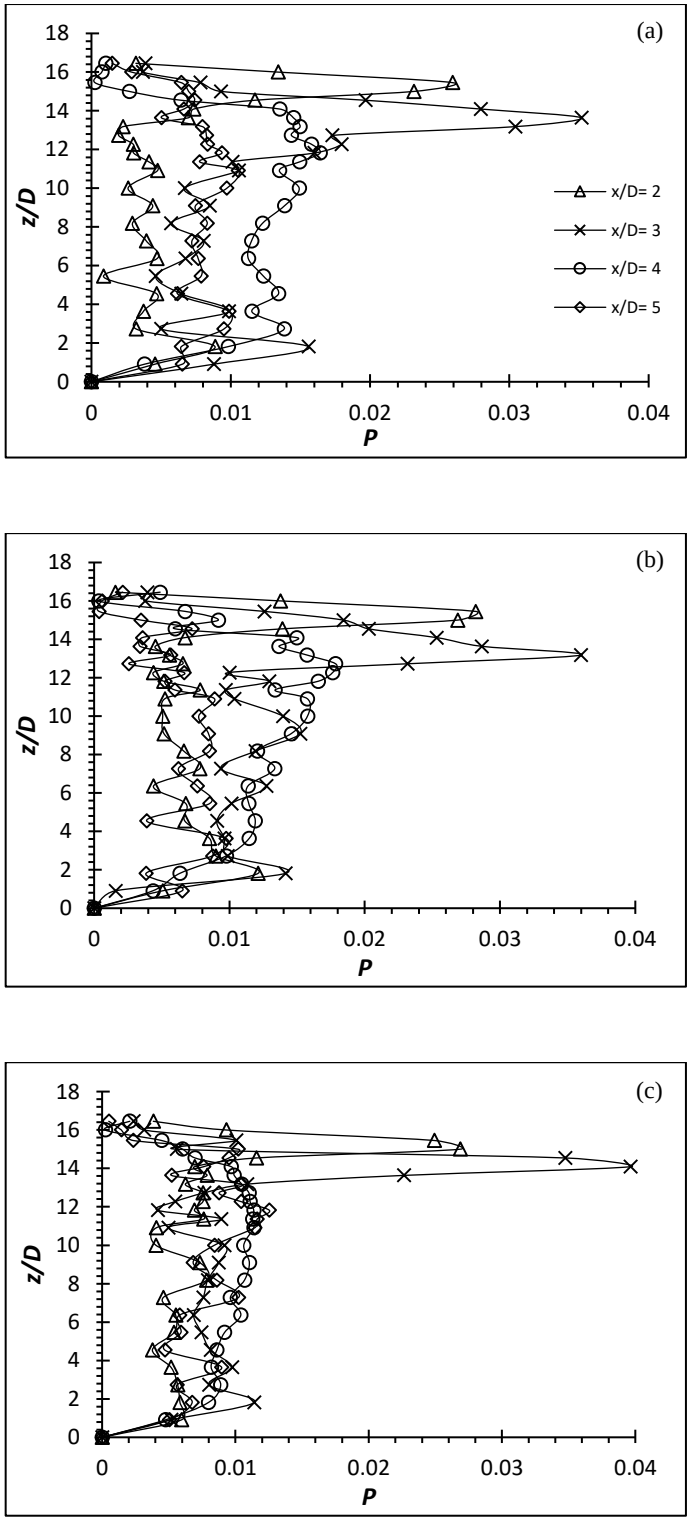

Figure 5.30: Production term, $-\overline{u_i' u_j'} \frac{\partial U_i}{\partial x_j}$ for rigid cylinder of *AR* = 16 at (a) Re = 4000 (b) Re = 6000 (c) Re = 8000

5.4.2. Production term of flexible cylinders

Figure 5.31 shows the normalized $\boldsymbol{P}$ graph of the flexible cylinders of AR = 10 at Re = 4000, 6000 and 8000. Similar observations of the rigid counterpart can be seen on the flexible cylinders of AR = 10 at Re = 4000 and 6000 as it has been established in the previous sub-chapter that the cylinders under these two Re conditions behave like a rigid cylinder. Thus, it is expected to have a similar turbulence performance as the rigid counterpart. The flexible cylinder at Re = 8000 on the other hand has spotted a slight increment of the localized $\boldsymbol{P}_{max}$ at 0.041 over its rigid counterpart at the same Re. Similarly, it also happens in the vicinity of the free end, where a large amount of shear happens. The cylinder did oscillate but the oscillation was too minute to be registered.

The normalized $\boldsymbol{P}$ graph of the flexible cylinders of AR = 16 at Re = 4000, 6000 and 8000 are presented in Figure 5.32. It is important to remind the readers again that due to the deflection of the flexible cylinders during the experiments, no measurement can be made in the near wake where the deflection interfered with the measurement points. In general, the localized $\boldsymbol{P}_{max}$ occurs at near the free end, very much similar to its rigid counterpart as it is where the region shear happens most. This indicates that the energy from the mean flow is transferred to the fluctuating flow through the mechanism of shear. The localized $\boldsymbol{P}_{max}$ of the flexible cylinders are 0.081, 0.109 and 0.076 for Re = 4000, 6000 and 8000 respectively. The localized $\boldsymbol{P}_{max}$ value have increased significantly from 131 %, 203 % and 94 % against its rigid counterpart of AR = 16 at the same condition of Re respectively.

Apart from the obvious increment of localized $\boldsymbol{P}_{max}$ near the free end, it can also be discerned that the region below the free end has increased as well, compared to its rigid counterpart at the same localized region. The $\boldsymbol{P}$ value at the midspan of the cylinder at x/D = 3 and 4 has a modest improvement over its rigid counterpart. This suggests that the production of turbulent energy is slightly stronger than its rigid counterpart probably due to the absence of downwash which limits most of the turbulence activities within the near wake.

The turbulent performance is seen increased significantly at three different Re for the flexible cylinders. Since it is suggested by the results of the rigid cylinder that the

geometry factor (increasing *AR*) does not contribute to the turbulent performance, the major value difference generated by the flexible cylinders at three different Re is believed to be caused by the structural dynamics factors (e.g. degree of deflection, oscillation frequency), which are heavily dependent on the *AR*. It is after all, the increase in *AR* results in the reduction of structural stiffness (provided the geometry and material used are consistent). Therefore, the increase in *AR* should make the cantilever experiences a larger deflection and oscillation. Conclusively, it is believed that the turbulent performance should be closely linked to the structural dynamics caused by different *AR* rather than the *AR* itself.

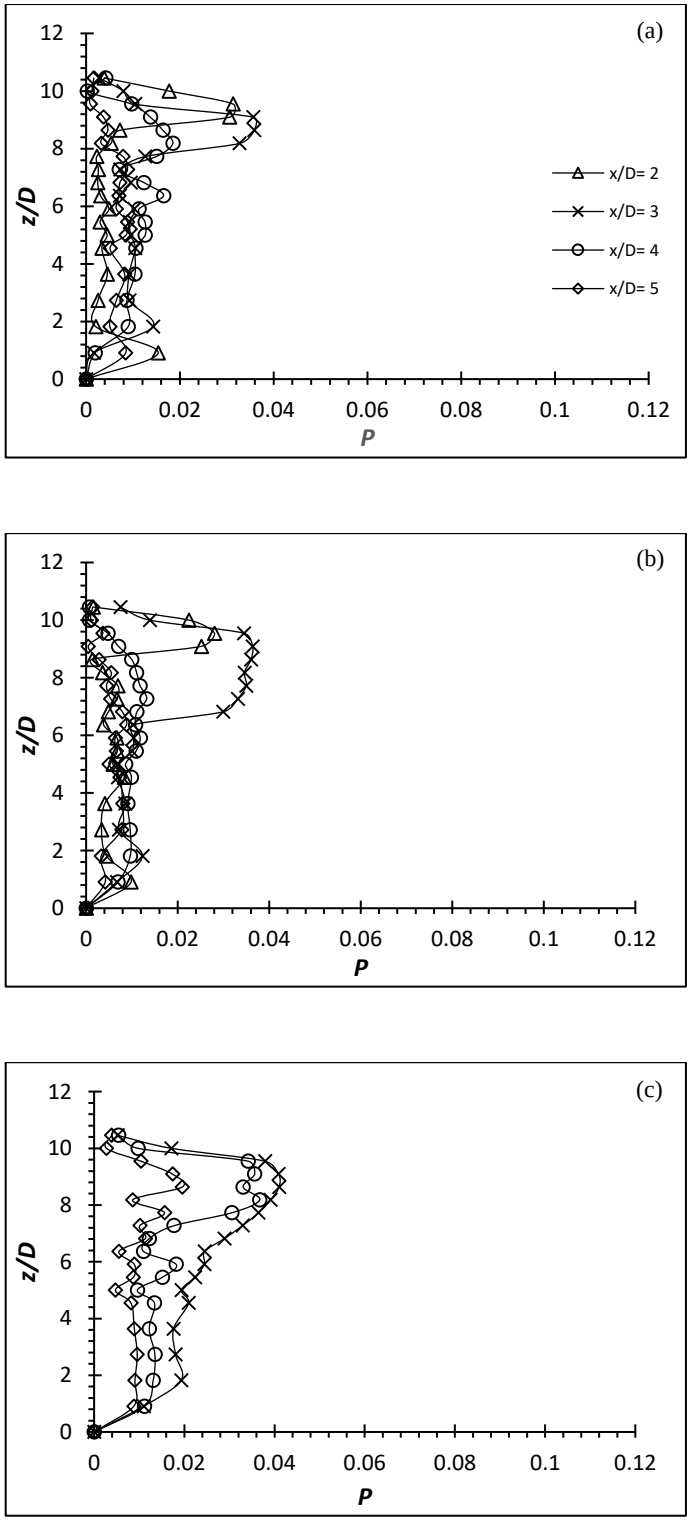

Figure 5.31: Production term, $-\overline{u_i' u_j'} \frac{\partial U_i}{\partial x_j}$ for flexible cylinder of AR = 10 at (a) Re = 4000 (b) Re = 6000 (c) Re = 8000

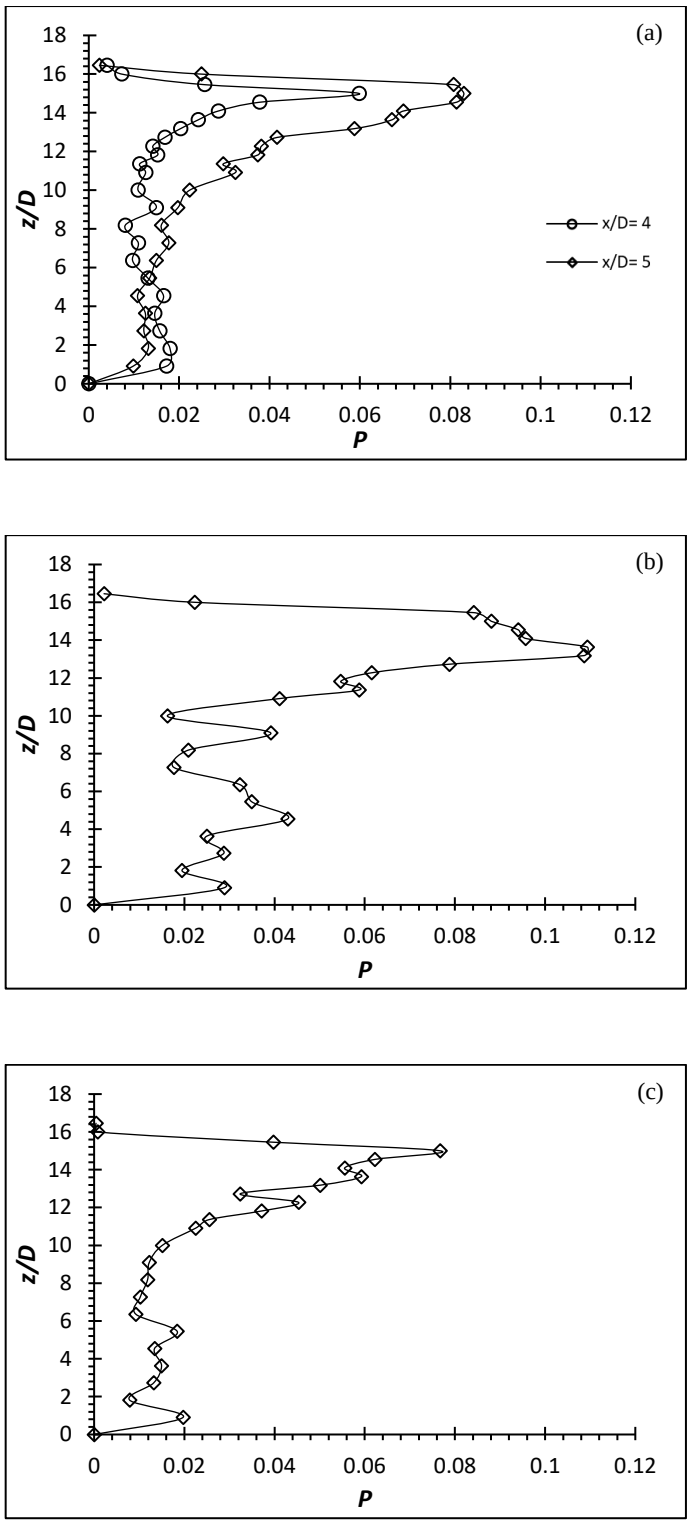

Figure 5.32: Production term, $-\overline{u_i' u_j'} \frac{\partial U_i}{\partial x_j}$ for flexible cylinder of AR = 16 at (a) Re = 4000 (b) Re = 6000 (c) Re = 8000

5.5. Reynolds stresses

It is seen that the flexible cylinders indeed bring turbulence enhancement in the wake of the flow via the production term of the Kinetic Energy Budget equations. However, in order to further quantify the turbulent activities, it is necessary to examine the Reynolds stresses produced in the wake. As shear is one of the most important source components in producing turbulence, it would signify that the higher shear production results in higher turbulence energy content in the wake. With reference to the kinetic budget energy for turbulence flow, the $-\overline{u'_\iota u'_J}$ term, which is the shear generated at the fluctuation component, clearly express the importance of Reynolds stresses in contributing to the production and transfer of turbulence energy in the wake flow. In turbulence flow, as it involves the transferring of fluctuating fluid particle not only in horizontal plane but also across vertical plane, it exists a difference in U in between these two planes; hence, shear stress happens. It has exactly the same physical effect as an actual frictional force exerted directly between the two layers of fluid on either side of the plane: the faster-moving fluid above the plane exerts an accelerating force on the slower-moving fluid below the plane, and conversely the fluid below exerts an equal and opposite retarding force on the fluid above. To put it into context, it can be interpreted as a mechanism for momentum exchange between the mean flow and the turbulence; therefore, turbulence can be interpreted as to produce additional stress in the fluid. Physically, Reynolds stress relates to the transport of momentum due to the turbulent fluctuations in the flow. One of the characteristics of turbulent flow is to enhance the transport of mass momentum and energy. As the presence of Reynolds stress tensor results in the turbulent diffusivity, it makes a large contribution to the overall momentum transport than the viscous stress tensor in the case of momentum transport. Bernard *et al.* (1993) has concluded that the Reynolds stress production is inseparable from the dynamics of organized coherent vortical structures.

5.5.1. Reynolds averaged statistics of rigid cylinders

The normalized Reynolds stresses, $\frac{\overline{u'^2}}{U^2}$, $\frac{\overline{w'^2}}{U^2}$ and $\frac{\overline{u'w'}}{U^2}$, along the span of the rigid cylinder of *AR* = 10 and 16 at the wake centreline (y/D = 0) are presented under this section. The

Reynolds stresses, $\frac{\overline{u'^2}}{U^2}$, $\frac{\overline{w'^2}}{U^2}$ and $\frac{\overline{u'w'}}{U^2}$, of the rigid cylinder are presented to provide a benchmark, that will later be used to compare with the increment gained by the flexible cylinder.

The Reynolds stresses, $\frac{\overline{u'^2}}{U^2}$, $\frac{\overline{w'^2}}{U^2}$ shows great increment of values at $x/D = 2$. A peak $\frac{\overline{u'^2}}{U^2}$ is evident at 3D from the free end at $x/D = 2$, could be associated to the free end shear layers. The $\frac{\overline{u'^2}}{U^2}$ starts to attenuate as it goes down the span of the cylinder, giving an overall 'picture' related to the vortex shedding strength at each particular depth. The $\frac{\overline{w'^2}}{U^2}$ displays a visible peak at above the midspan ($z/D \approx AR$ - 3) of the cylinder at $x/D \leq 3$ and this could be attributed to the strong downwash as the vortex follows the path of the bulk flow. In the near wake, $x/D \leq 2$, the w' are more energetic than the u', hence the magnitude of $\frac{\overline{w'^2}}{U^2}$ component is much larger than the $\frac{\overline{u'^2}}{U^2}$ component. In general, the Reynolds shear stress is negative at $x/D \leq 3$ at roughly above the midspan of the cylinder. The location of elevated Reynolds stress at $x/D = 2$ can be said to stem from the w', $\frac{\overline{w'^2}}{U^2}$ since the $\frac{\overline{w'^2}}{U^2}$ are more energetic than the $\frac{\overline{u'^2}}{U^2}$ in that region.

Based on Figure 5.33 (c), there is a local maximum of $\frac{\overline{u'w'}}{U^2}_{\max} \approx$ - 0.042 at $x/D = 2$ which is located at $z/D \approx 8$ of cylinder of $AR = 10$ at Re = 4000. Since the most important aspect of the turbulent flow is to enhance transport of mass momentum and energy, it can be seen that in this case of momentum transport, the turbulent diffusivity results from the presence of the Reynolds stress tensor, which generally is the contributor to the overall momentum transport. The Reynolds shear stress for the rigid cylinder of $AR = 16$ at Re = 4000 on the other hand has local maximum of $\frac{\overline{u'w'}}{U^2}_{\max} \approx$ - 0.043 at $x/D = 2$ which is located $z/D \approx 14$. Both the cylinder of $AR = 10$ and 16 spot a similar pattern and similar location of $\frac{\overline{u'w'}}{U^2}_{\max}$. Besides, there is not much gain in magnitude of both AR suggesting the AR has no apparent effect on enhancing the turbulence production for a rigid cylinder.

As anticipated from the (u'/U) results which see slight increment at Re = 6000 and 8000 over 4000, increase in the magnitude of Reynolds stresses at the higher Re (Re = 6000 and 8000) is apparent as well at $\frac{\overline{u'w'}}{U^2}_{\max} \approx$ - 0.043 and -0.044 for *AR* = 10 and $\frac{\overline{u'w'}}{U^2}_{\max}$ ≈ -0.044 and -0.045 for *AR* = 16 (not shown), though they are only by marginally. The Reynolds stresses pattern also spotted to be similar, further confirming the physics of vortex feeding process and vortex shedding are similar for rigid cylinder.

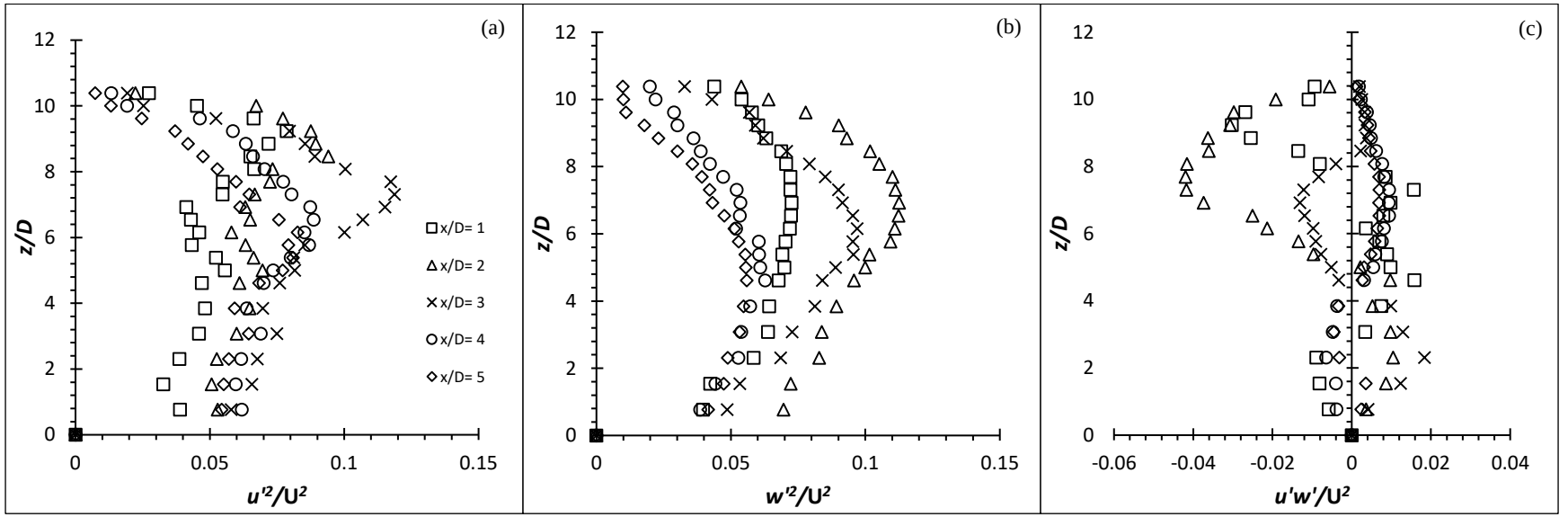

Figure 5.33: Reynolds stress profiles for rigid cylinder of AR = 10 at Re = 4000: (a) $\frac{\overline{u'^2}}{U^2}$ (b) $\frac{\overline{w'^2}}{U^2}$ (c) $\frac{\overline{u'w'}}{U^2}$

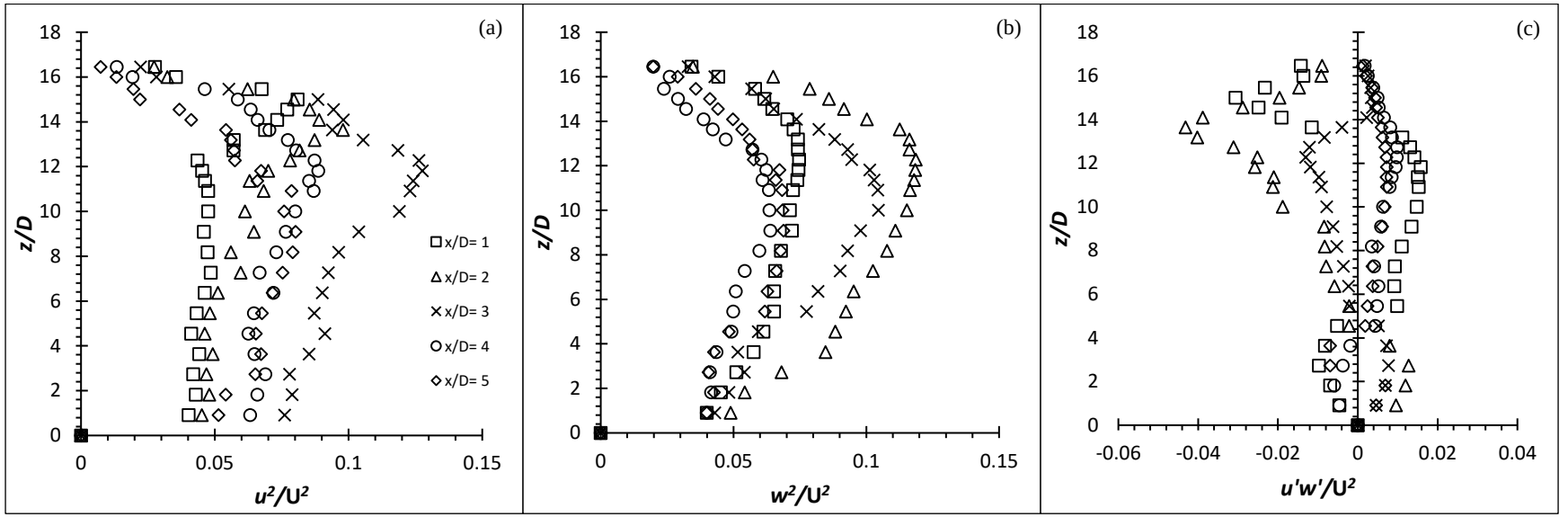

Figure 5.34: Reynolds stress profiles for rigid cylinder of *AR* = 16 at Re = 4000: (a) $\frac{\overline{u'^2}}{U^2}$ (b) $\frac{\overline{w'^2}}{U^2}$ (c) $\frac{\overline{u'w'}}{U^2}$

5.5.2. Reynolds averaged statistics of flexible cylinders

The Reynolds stresses, $\frac{\overline{u'^2}}{U^2}$, $\frac{\overline{w'^2}}{U^2}$ and $\frac{\overline{u'w'}}{U^2}$, along the span of the cylinder of *AR* = 10 and 16 at Re = 4000, 6000 and 8000 at the wake centreline (*y*/*D* = 0) are presented under this section. In general, it can be seen that the Reynolds shear stress for the vibrating cylinders have increased dramatically in magnitude.

Similarly, as expected from the ***P*** terms of the flexible cylinders of *AR* = 10 at Re = 4000 and 6000, the $\frac{\overline{u'^2}}{U^2}$, $\frac{\overline{w'^2}}{U^2}$ and $\frac{\overline{u'w'}}{U^2}$ are similar to that of the rigid counterpart. The flexible cylinders at Re = 8000, and *AR* = 16 at Re = 4000, 6000 and 8000 on the other hand do see increment in the Reynolds stresses.

From Figure 5.35 to Figure 5.37, in general, it can be concluded that the Reynolds shear stress stems from the $\frac{\overline{u'^2}}{U^2}$ component as $\frac{\overline{u'^2}}{U^2}$ is more energetic than the $\frac{\overline{w'^2}}{U^2}$ component. The decreased $\frac{\overline{w'^2}}{U^2}$ suggests that the *w*' component is not as active as its rigid counterpart. The could be due to the diminishing influence of downwash flow by the flexible cylinder as evident by the very low $\overline{w}$ and hence, the slightly weaker level of fluctuations in *w*'.

The Reynolds shear stress for flexible cylinder of *AR* = 10 at Re = 8000 shows a marginal increase in magnitude of the local peak Reynolds shear stress at $\frac{\overline{u'w'}}{U^2}_{\max} \approx$ - 0.046, a 4.5 % increment over the rigid cylinder case of the same condition.

The Reynolds shear stress for flexible cylinder of *AR* = 16 has a huge increment of local peak Reynolds shear stress at $\frac{\overline{u'w'}}{U^2}_{\max} \approx$ - 0.090, - 0.113 and - 0.071 for Re = 4000, 6000 and 8000 respectively, a 109.30 %, 150.00 % and 61.36 % increment over the rigid cylinder of the same condition. The increment of $\frac{\overline{u'w'}}{U^2}$ for the flexible cylinder is related to the fluctuating kinetic energy contents in the vortex structures as $\overline{u'w'}$ is the turbulent vortical advection of streamwise turbulent momentum. As an example, a fluid particle which is transferred vertically (*z* direction) on the plane that is having a positive or negative *w*' will transport the *u*' as well. It is this turbulent motion of the fluid particle that

accounts for a more effective mass, energy and momentum transport. As discussed in subchapter 5.2.2, the lower magnitude of $\frac{\overline{u'w'}}{U^2}$ for flexible cylinder of *AR* = 16 at Re = 8000 is due to the oscillation of the flexible which happened off axis so it is suspected that the vortex is not fully captured. The off-axis oscillation at Re = 8000 could be due to the extremely high incoming fluid force exerted on the polymer based cylinder which has a comparatively low structure stiffness compared to the high incoming force and hence, it would succumb to the force and not have enough resistance to go back to its original position.

The local peak region of Reynolds stress at approximately $z/D = 2 \sim 3$ from the free end is also corresponding to the tip vortex generated by the free end. The intensity of the tip vortices is related to the oscillation at the free end because only higher magnitude of Reynolds shear stress is seen for cylinders that oscillate (All of flexible cylinders except flexible cylinder of *AR* = 10 at Re = 4000 and 6000 that behave nearly identical as rigid cylinder). Below that region, the regular Kármán vortices become dominant (indicated by the lower magnitude of Reynolds stress along the span of the cylinder) as the strength of the tip effect diminishes and could no longer supresses the formation of the regular Kármán vortices. There is also a slight increase of Reynolds stress for flexible cylinders when compared to rigid cylinders at $x/D \approx 4$ and 5, below mid-span of the cylinder, suggesting that the vortices are prolonged downstream of the cylinder.

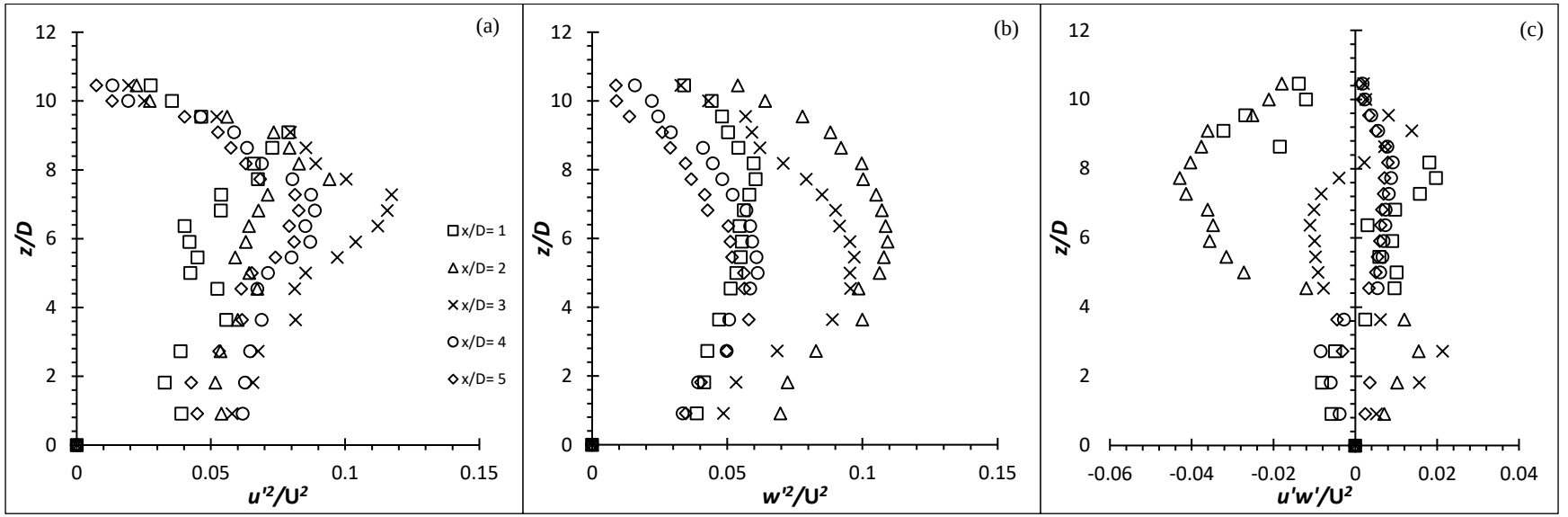

Figure 5.35: Reynolds stress profiles for flexible cylinder of *AR* = 10 at Re = 4000: a) $\frac{\overline{u'^2}}{U^2}$ (b) $\frac{\overline{w'^2}}{U^2}$ (c) $\frac{\overline{u'w'}}{U^2}$

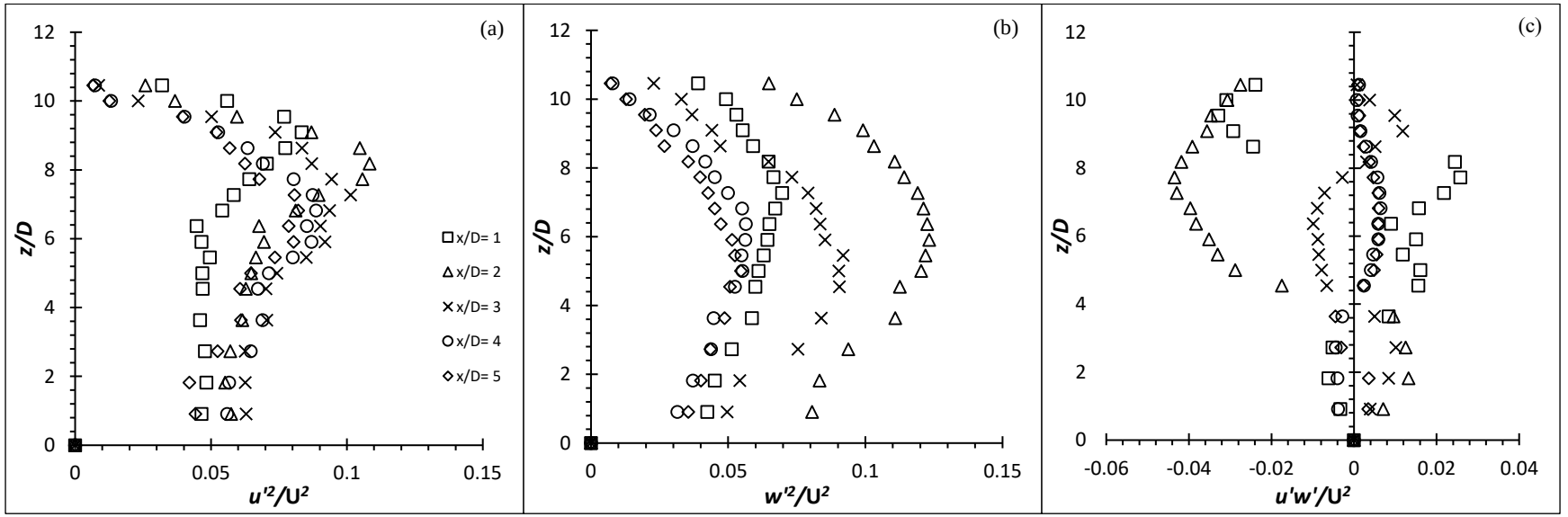

Figure 5.36: Reynolds stress profiles for flexible cylinder of *AR* = 10 at Re = 6000: a) $\frac{\overline{u'^2}}{U^2}$ (b) $\frac{\overline{w'^2}}{U^2}$ (c) $\frac{\overline{u'w'}}{U^2}$

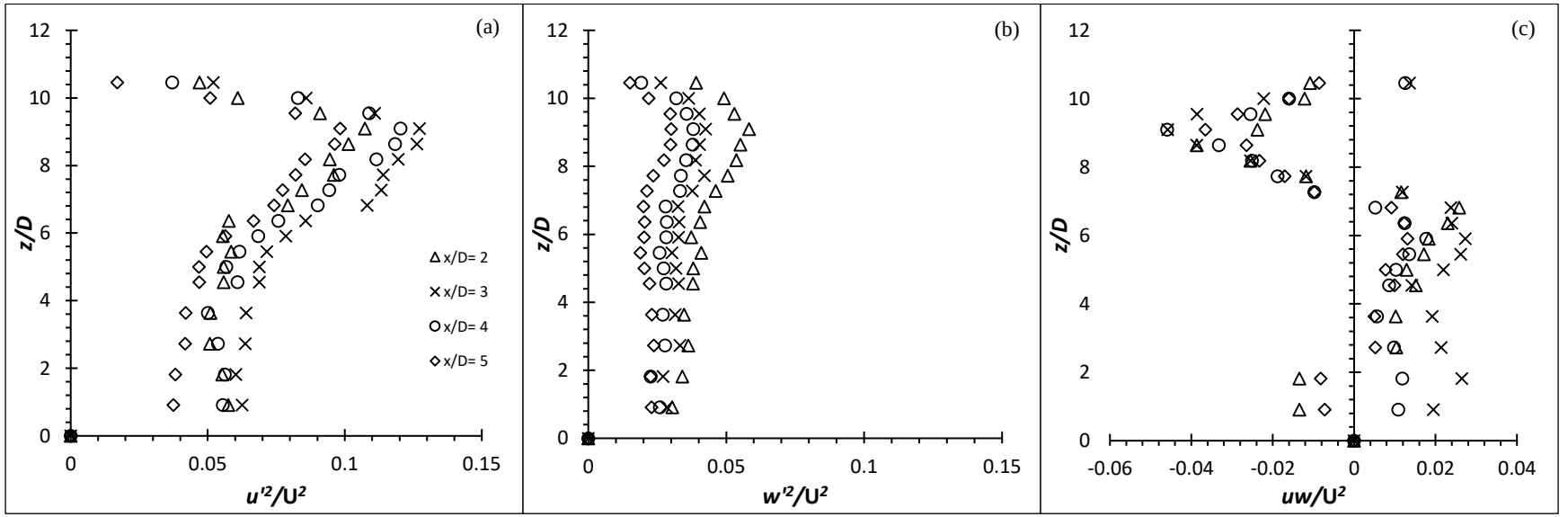

Figure 5.37: Reynolds stress profiles for flexible cylinder of *AR* = 10 at Re = 8000: a) $\frac{\overline{u'^2}}{U^2}$ (b) $\frac{\overline{w'^2}}{U^2}$ (c) $\frac{\overline{u'w'}}{U^2}$

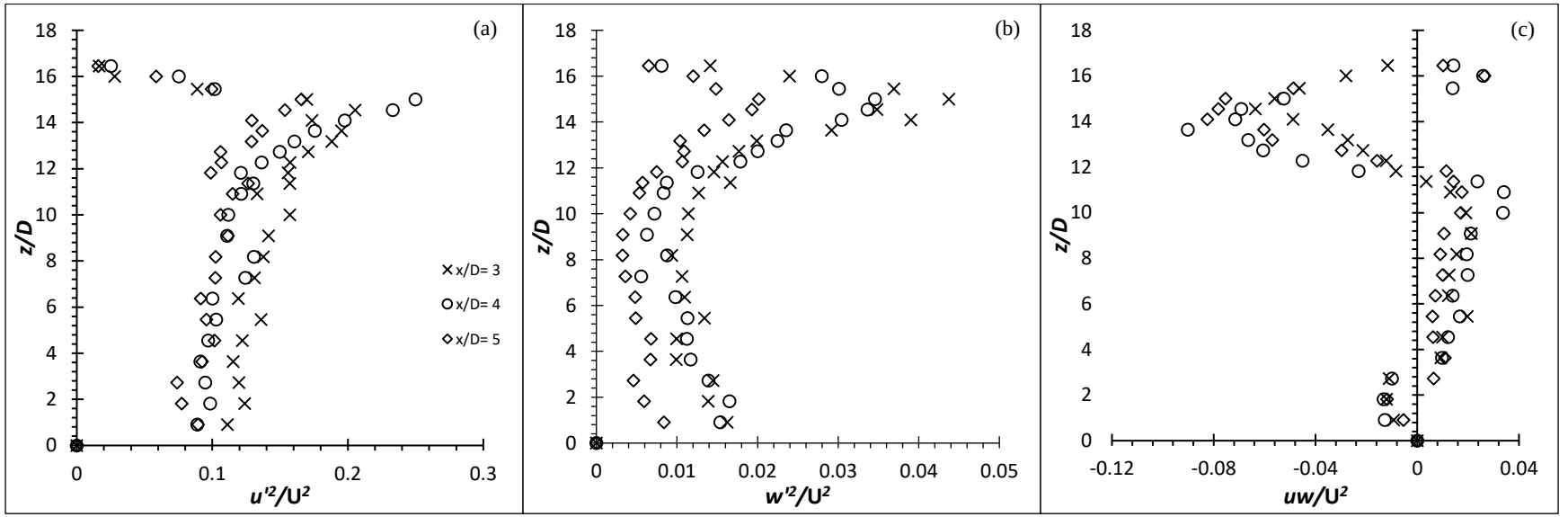

Figure 5.38: Reynolds stress profiles for flexible cylinder of *AR* = 16 at Re = 4000: a) $\frac{\overline{u'^2}}{U^2}$ (b) $\frac{\overline{w'^2}}{U^2}$ (c) $\frac{\overline{u'w'}}{U^2}$

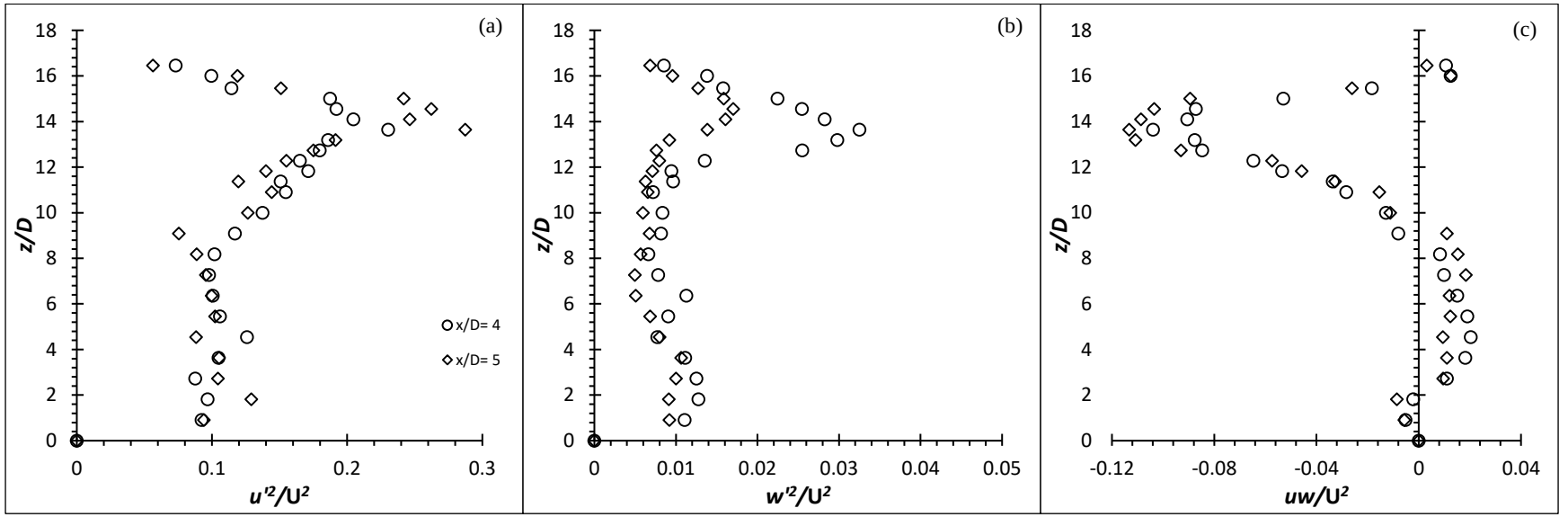

Figure 5.39: Reynolds stress profiles for flexible cylinder of *AR* = 16 at Re = 6000: a) $\frac{\overline{u'^2}}{U^2}$ (b) $\frac{\overline{w'^2}}{U^2}$ (c) $\frac{\overline{u'w'}}{U^2}$

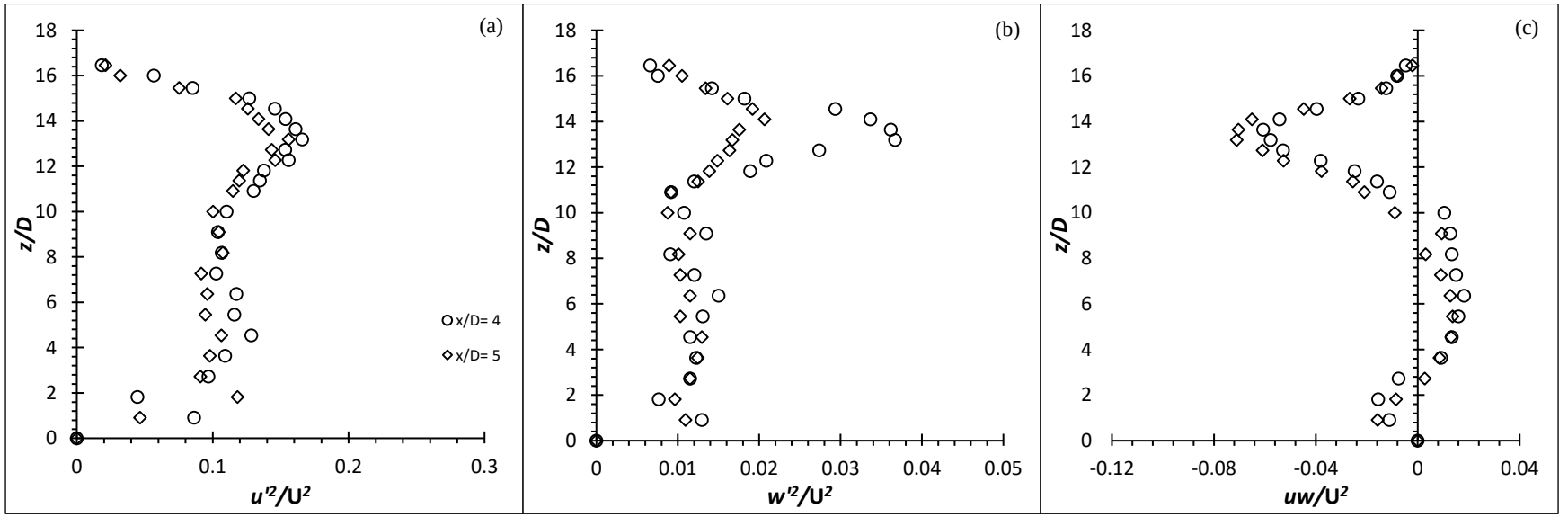

Figure 5.40: Reynolds stress profiles for flexible cylinder of *AR* = 16 at Re = 8000: a) $\frac{\overline{u'^2}}{U^2}$ (b) $\frac{\overline{w'^2}}{U^2}$ (c) $\frac{\overline{u'w'}}{U^2}$

5.5.3. Roles of deflection and oscillation of the flexible cylinder on the turbulence enhancement

The above results have shown the augmented turbulence intensity, production term and Reynolds stresses of the flexible cylinders over the rigid cylinders. However, the cause of this improvement has not been identified yet. It is known that the geometrical factor has no input in the turbulence enhancement; instead, the structural dynamics factors are identified to be the possible cause. Therefore, the time series normalized amplitude response (*y*-direction, transverse to the freestream) of the flexible cylinders is studied with the hope that it could provide valuable insight into the cause of the improvement. Since packing the total amplitude response of 40.96 s at 60 Hz in one graph will only give coarse details on the oscillating behaviour, all normalized amplitude response graphs, (*y*/*D*) of the flexible cylinders (see Figure C1) shown are presented at t = 31 s to 34 s from a total period of 40.96 s for one experiment for the purpose of examining the oscillating behaviour. However, the RMS oscillating amplitude presented in the next chapter accounts for the whole period. Unfortunately, no amplitude response graphs for flexible cylinders of *AR* = 10 at all Re could be produced as the oscillation is too minute to be detected accurately.

With reference to the figures of deflected flexible cylinders (see Figure B1, B2, B4 and B5) and their respective turbulence intensity distribution graphs and Reynolds stresses, it is evident that the role of the deflected flexible cylinders further substantiate the diminishing of downwash of the vortex as seen by the upshift of (u'_{max}/U) and $\frac{\overline{u'w'}}{U^2}_{\max}$ at *x*/*D* = 3, 4 and 5 for flexible cylinders that deflect/bend. Besides, it has also ruled out the possibility of the deflection in enhancing the turbulence. As can be seen with cylinder of *AR* = 16 at all Re, they have nearly the same degree of deflection/bending, yet the turbulence characteristics are all different. As a result of that, it can be concluded that the deflection of the cylinder has no effect on the turbulence enhancement ability.

The (*y*/*D*) graphs for *AR* = 16 at all Re tells information related to oscillating amplitude, oscillating frequency and oscillating motion. In general, the flexible cylinder of *AR* = 16 at Re = 6000 produces a higher oscillating amplitude, consistent oscillating frequency and also a more organized oscillating motion; all of which, correspond to the

highest increment in the turbulence energy production. On the other hand, the turbulence energy production of the flexible cylinder of AR = 16 at Re = 4000 which only gain relatively modest increment in magnitude, correspond to the (y/D) graph that produces relatively moderate oscillating amplitude and a less organized oscillating motion. Lastly, the turbulence energy production of the flexible cylinder of AR = 16 at Re = 8000 appears to be the lowest amongst all because the cylinder was oscillating off-axis (as seen from Figure C1 (c)), so the vortex was not fully captured. Nevertheless, the localized $\boldsymbol{P}_{\max}$ still sees a major improvement over its rigid counterparts. The (y/D) graph shows a large amplitude and a disorganized oscillating motion.

Conclusively, the above results suggest that the increment of the turbulence energy production is caused by the structural motion or oscillation of the flexible cylinder and not the deflection. The deflection of the flexible cylinder starting to take place at AR = 10 at Re = 8000 and subsequently to AR = 16 at Re = 8000 with the increasing of degree of deflection (due to lower structural stiffness, k when AR is higher and higher fluid force at higher Re since ρ, D and μ are kept constant) though the degree of deflection for flexible cylinder of AR = 16 for all Re are roughly similar. Therefore, if the increment of the turbulence intensity is in fact caused by the deflection, the turbulence energy production for flexible cylinder of AR = 16 at all Re should have an approximately similar performance. Despite that, with the current comparison, conclusion cannot be drawn to which parameters of structural motion (oscillating amplitude, oscillating frequency, oscillating motion) contribute to the increment. Therefore, a further analysis which cover the same EVA material with different AR is conducted. In order to encourage organized oscillating motion (which cuts down one parameter so the contributor can be easily identified), a flexible cylinder of different material properties is used and its results are revealed in Chapter 6.

5.6. Summary of Chapter

In this chapter, the flow dynamics behind the rigid and flexible cylinder are presented. The main objective is to discern the turbulent wakes and characteristics contributed by the rigid and flexible cylinder. The major conclusion that can be made is that size difference between the wake of the rigid and flexible cylinder. Based on the analysis, it can be discerned that the wake region of the flexible cylinder is generally larger than that of the rigid cylinder. A larger wake region translates to a larger region where turbulence activities can happen effectively. Therefore, the increase of wake region can be denoted as a direct evidence of turbulence enhancement, in terms of the effectiveness of the region where turbulence activities take place. In addition, it is speculated that the increase of wake region is caused by the bending of flexible cylinder. On the other hand, the turbulence intensity, $\boldsymbol{P}$ term and Reynolds stress have also seen huge increment in flexible cylinder. It is speculated that the increment is not caused by the bending but oscillating motion. However, this speculation can only be confirmed in the next chapter.

CHAPTER 6

THE INFLUENCE OF THE PROPERTIES OF FLEXIBLE CYLINDERS TO THE TURBULENCE WAKE AND CHARACERISTICS

It was shown in the previous chapter that the flexible cylinders bring significant changes to the turbulence in the near wake – the *x*-deflection of the flexible cylinders increases the turbulence wake region, which effectively increase the region of turbulent activities; and the aspects of the structural motion such as oscillating amplitude, oscillating frequency and the oscillating motion are able to enhance the turbulence energy production as demonstrated by the ***P*** term and the Reynolds stresses. Despite the remarkable findings, it is unable to confirm which parameter(s) of the structural motion could bring effects to the enhancement of turbulence energy in the near wake. It is therefore, this chapter mainly investigates the influence of different properties of the flexible cylinders to bridge the gap left in Chapter 5. As an effort to encourage an organized oscillating motion, material properties such as aluminium and carbon steel with moderately high stiffness and low damping coefficient are employed in this studies. The metal group flexible cylinders are performed at Reynolds number of 2500 due to the limitation of the highest possible freestream velocity the water tunnel could provide. Nevertheless, the results that will be revealed below show that the Re_D used is enough to initiate the vibration of cylinder. Apart from that, *AR* = 12 and 14 of polymer based EVA flexible cylinders at Reynolds number of 4000, 6000 and 8000 will also be investigated in this chapter.

6.1. Time-Averaged Velocity Distribution

6.1.1. Velocity profiles along the wake centreline

Since the *AR* for metal group flexible cylinders (*AR* = 50 and 54) is immensely bigger compared to polymer group flexible cylinders (*AR* = 12 and 14), the comparisons will be made within the material group. Figure 6.1, 6.2 and 6.3 and Figure 6.6, 6.7 and 6.8 show

the time-averaged streamwise velocity profile ($\overline{u}/\mathrm{U}$) and wall-normal velocity profile ($\overline{w}/\mathrm{U}$) of flexible cylinders of *AR* = 12 and 14 on the wake centreline (*y*/*D* = 0) at Re = 4000, 6000 and 8000. The distance measured of each velocity profile behind the cylinder are one diameter apart at *x*/*D* = 1, 2, 3, 4 and 5.

It is important to remind the readers that the flexible cylinder of *AR* = 14 at Re = 6000 are deflected to *x*/*D* = 3 (see Figure B6), therefore only profiles at *x*/*D* = 4 and 5 can be measured and they are presented together with *x*/*D* = 3 (see Figure 6.2 (a)) for flexible cylinder of *AR* = 12 so that the free end can be compared. Generally, the ($\overline{u}/\mathrm{U}$) profiles of EVA flexible cylinders of *AR* = 12 and 14 do not differ a lot from *AR* = 16 as anticipated. This is because the flexible cylinders are deflected during the experiments (See Figure B6 and B7 for flexible cylinders of *AR* = 12 and 14 at Re = 6000 for one Reynolds case example). The deflection downstream of the flexible cylinders have resulted in the increment of wake region nearly identical as the cylinder's height as indicated by the point where strong velocity gradient happens. The tip effects for both flexible cylinders of *AR* = 12 and 14 at all Re can be seen only influential to *z*/*D* ≈ *AR* - 1, consistent with the postulation of wake region increment due to cylinder's deflection.

The time-averaged ($\overline{u}/\mathrm{U}$) and ($\overline{w}/\mathrm{U}$) of flexible cylinders of *AR* = 50 and 54 on the wake centreline (*y*/*D* = 0) at Re = 2500 are shown at Figure 6.4, 6.5 and Figure 6.9, 6.10 respectively. The ($\overline{u}/\mathrm{U}$) and ($\overline{w}/\mathrm{U}$) for both materials at *AR* = 50 and 54 have hinted the influence of downwash, as indicated by the higher localize negative *w* component velocity than the *u* component at very near wake at *x*/*D* = 1 and 2 (compare Figure 6.4 and Figure 6.9 for aluminium and carbon steel cylinder of *AR* = 50 example). Due to the extremely long *AR* (*AR* = 50 and 54), the influence of downwash is only affected from the free end to circa 7*D* from the free end at the near wake of *x*/*D* = 1 and 2 for both materials and *AR* while the span below that region is considered to be of two-dimensional flow region which is free from the tip vortex.

It is observed that all the cylinders did not succumb to the incoming force exerted on it by the oncoming fluid and deflect due to the relatively higher stiffness properties of both materials (see Figure B8 – Aluminium flexible cylinder of *AR* = 50 for one example case). Though the aluminium cylinders of both *AR* are not deflected in the *x*-direction (too

negligible), they do however, oscillate/vibrate transversely. Downwash phenomenon is seen associated with all the metal group cylinders – carbon steel which acts like a rigid cylinder and aluminium which barely has any deflection but oscillates. As a result, it can be confirmed that the downwash phenomenon is caused by the deflection of the cylinder alone and not by the oscillation. Table 6.1 shows the average wake region based on the point of the greatest velocity gradient from the ($\bar{u}$/U) profiles of EVA, aluminium and carbon steel cylinders. It is apparent to see from the Table 6.1 that there is an increase in the wake region of the deflected cylinders; roughly equivalent to the deflected height of the cylinder.

In general, the ($\bar{u}$/U) velocity profile might look similar for all the cylinders. However, the localized velocity for aluminium cylinders of both *AR* near the free end is slightly slower than that of carbon steel cylinders (see Figure 6.4 and 6.5). The lower velocities of the aluminium cylinders could be due to the transverse oscillation of the cylinders (see Figure C4 and C5). As the cylinder is oscillating transverse to the flow, more energy from the mean flow is needed to account for the higher fluctuation velocities due to the higher shear rate and hence, the lower velocities. On the contrary, throughout the experiment, it is observed that no oscillation phenomenon occurs for the carbon steel cylinders of both *AR*. As a result, the carbon steel cylinder is behaved in the same manner as the rigid cylinder.

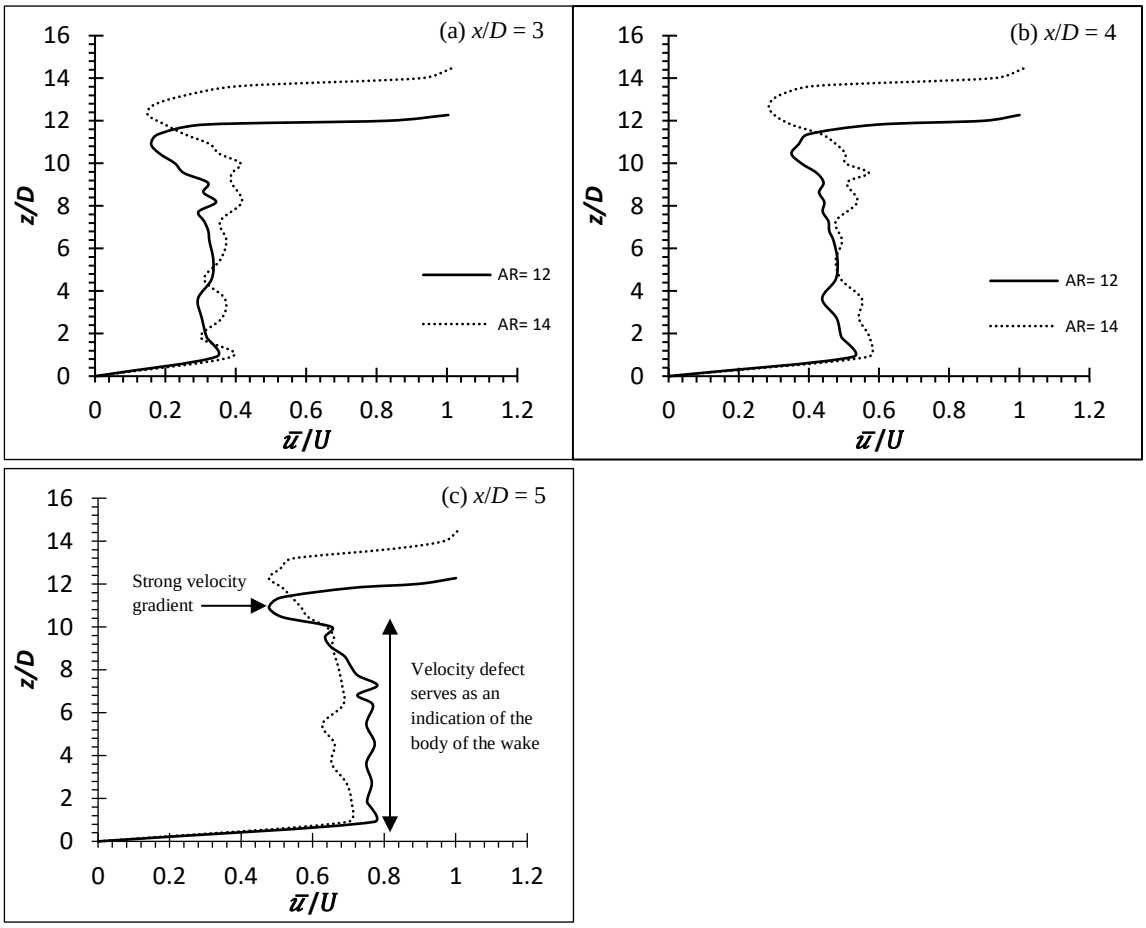

Figure 6.1: Time-average streamwise velocity profile of flexible finite cylinder of *AR* = 12 and 14 at wake centreline (*y*/*D* = 0) for Re = 4000

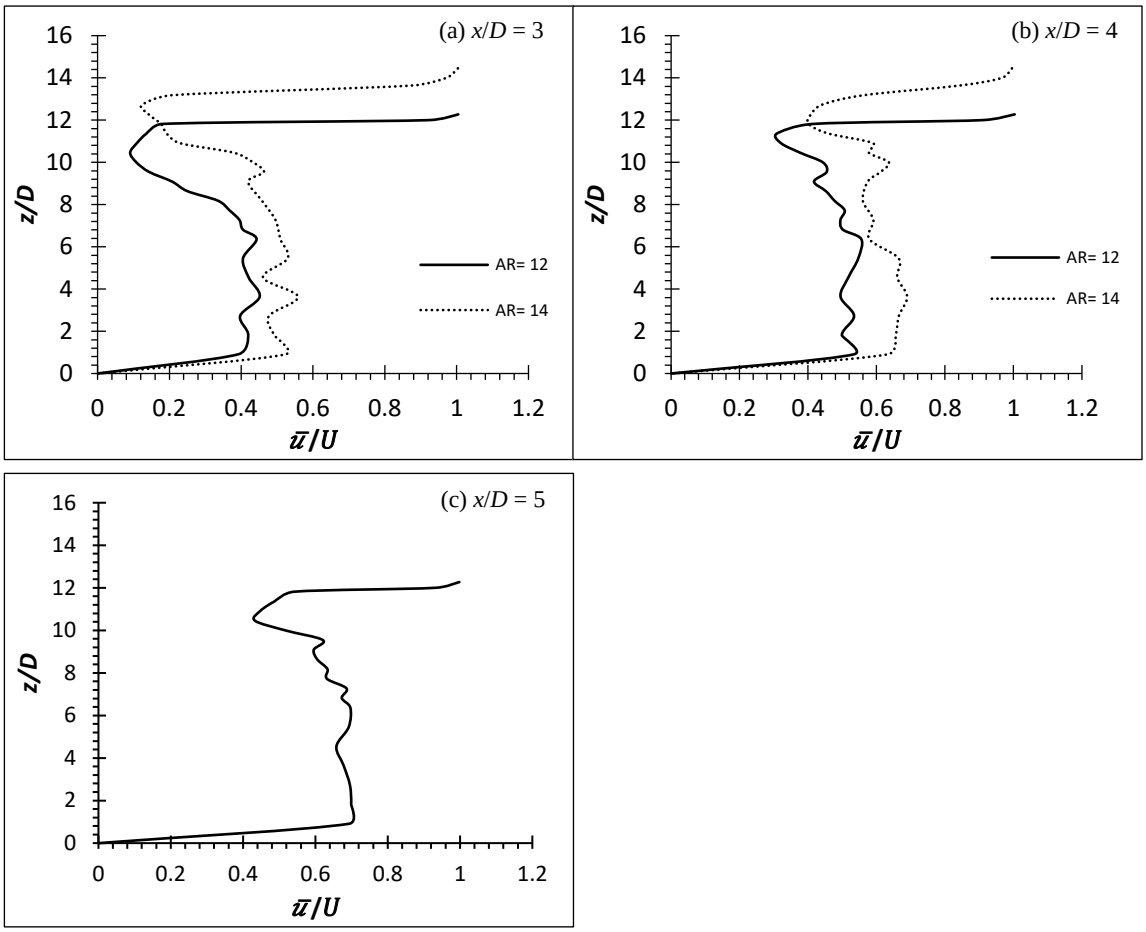

Figure 6.2: Time-average streamwise velocity profile of flexible finite cylinder of *AR* = 12 and 14 at wake centreline (*y*/*D* = 0) for Re = 6000

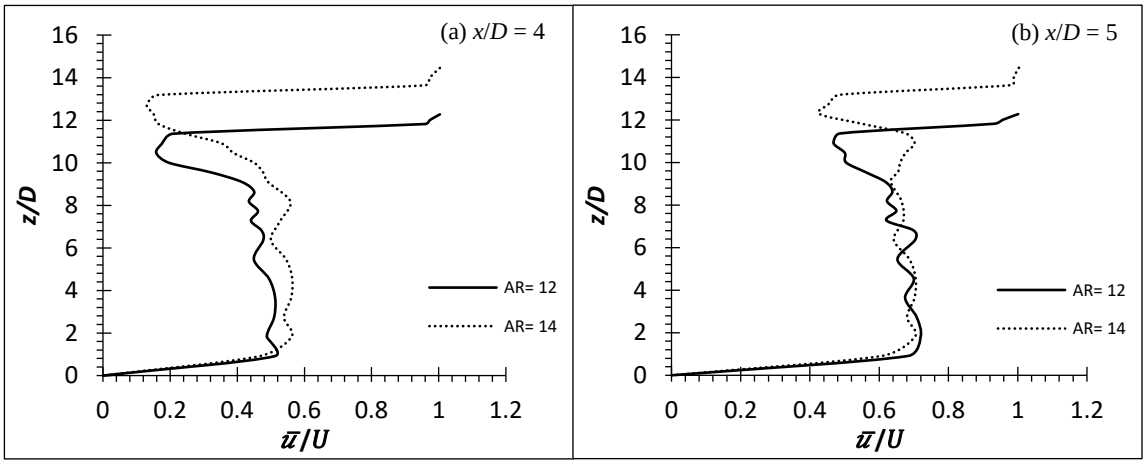

Figure 6.3: Time-average streamwise velocity profile of flexible finite cylinder of *AR* = 12 and 14 at wake centreline (*y*/*D* = 0) for Re = 8000

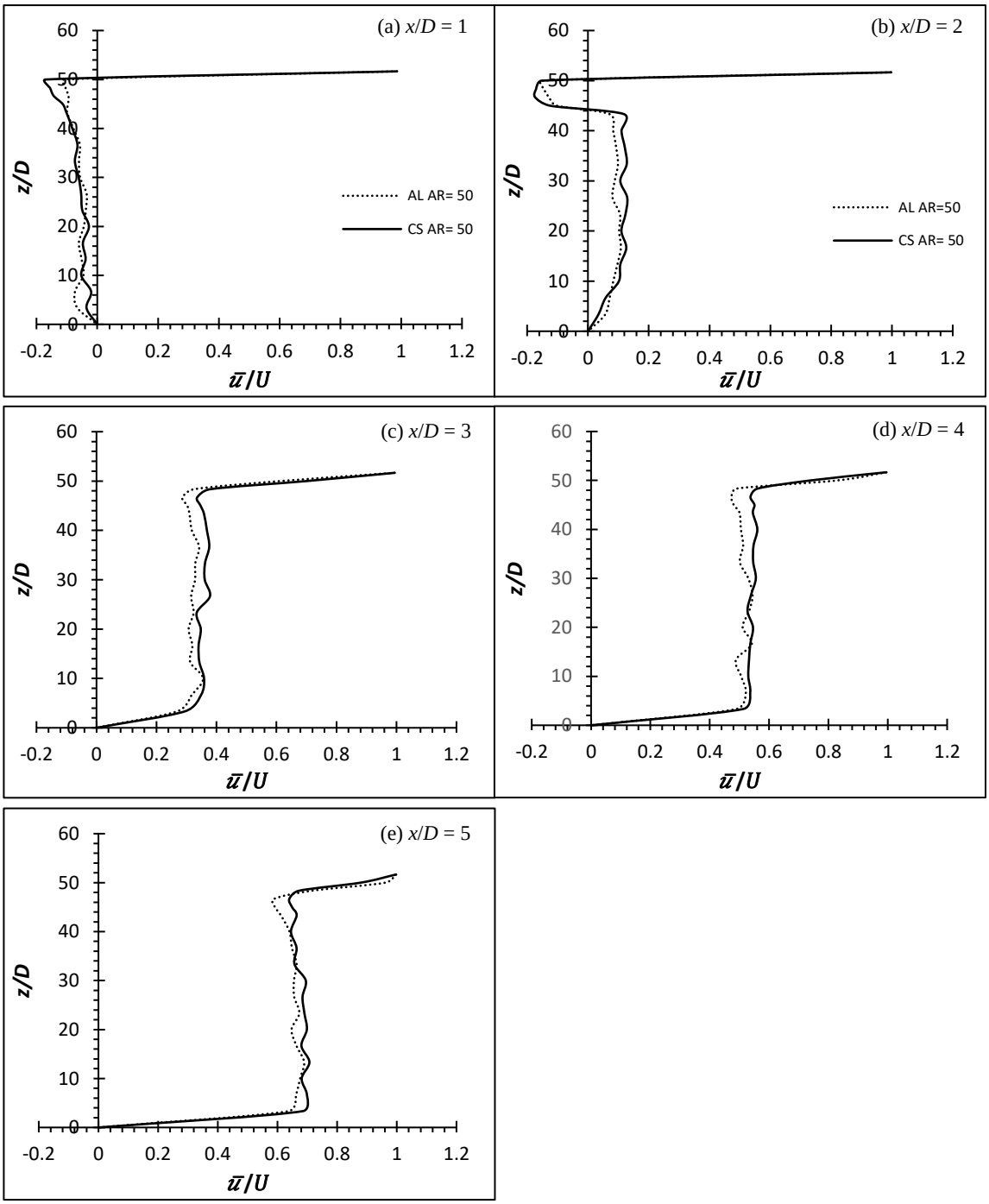

Figure 6.4: Time-average streamwise velocity profile of flexible finite cylinder (Aluminium and Carbon Steel) of *AR* = 50 at wake centreline (*y*/*D* = 0) for Re = 2500. Aluminium denotes *Al* while Carbon Steel denotes *CS*.

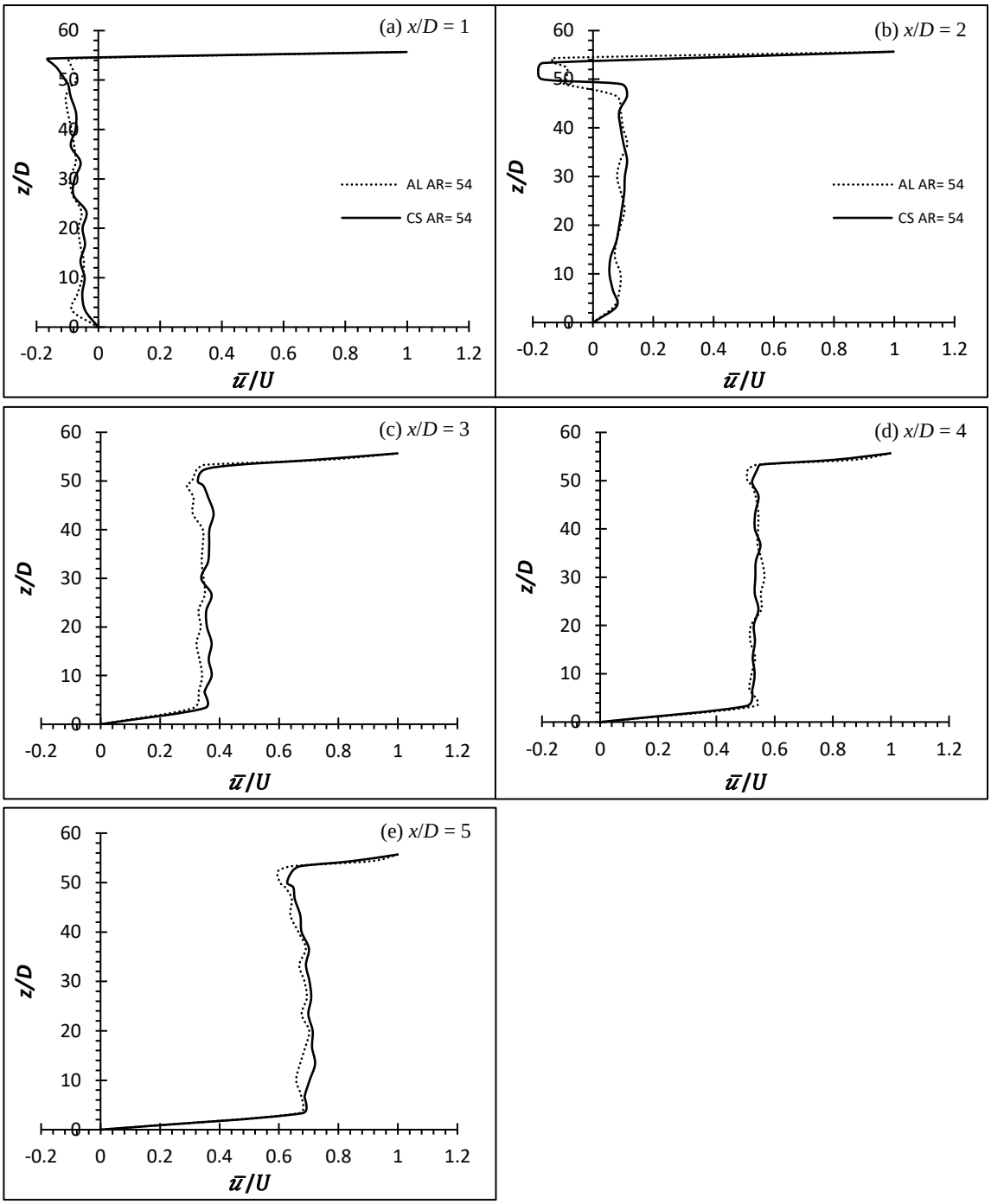

Figure 6.5: Time-average streamwise velocity profile of flexible finite cylinder (Aluminium and Carbon Steel) of *AR* = 54 at wake centreline (*y*/*D* = 0) for Re = 2500. Aluminium denotes *Al* while Carbon Steel denotes *CS*.

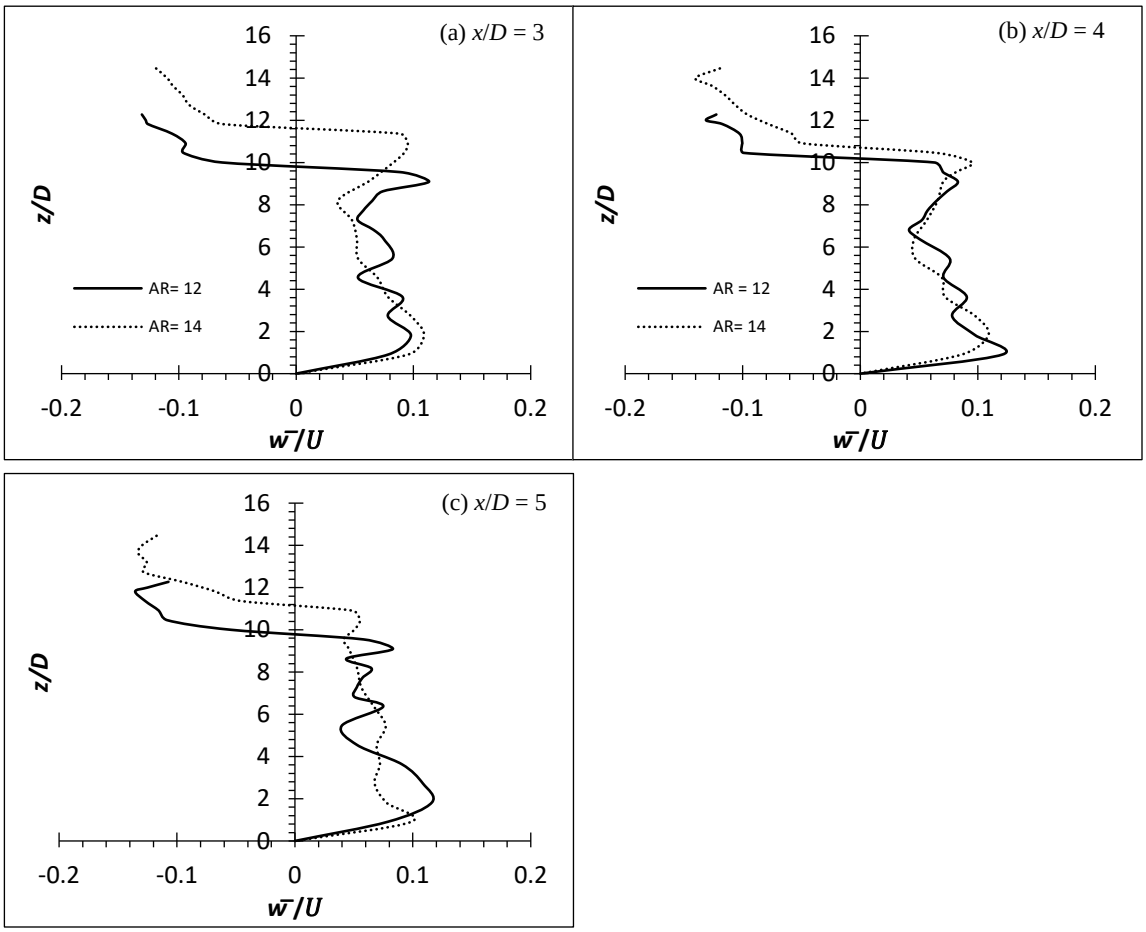

Figure 6.6: Time-average wall-normal velocity profile of flexible finite cylinder of *AR* = 12 and 14 at wake centreline (*y*/*D* = 0) for Re = 4000

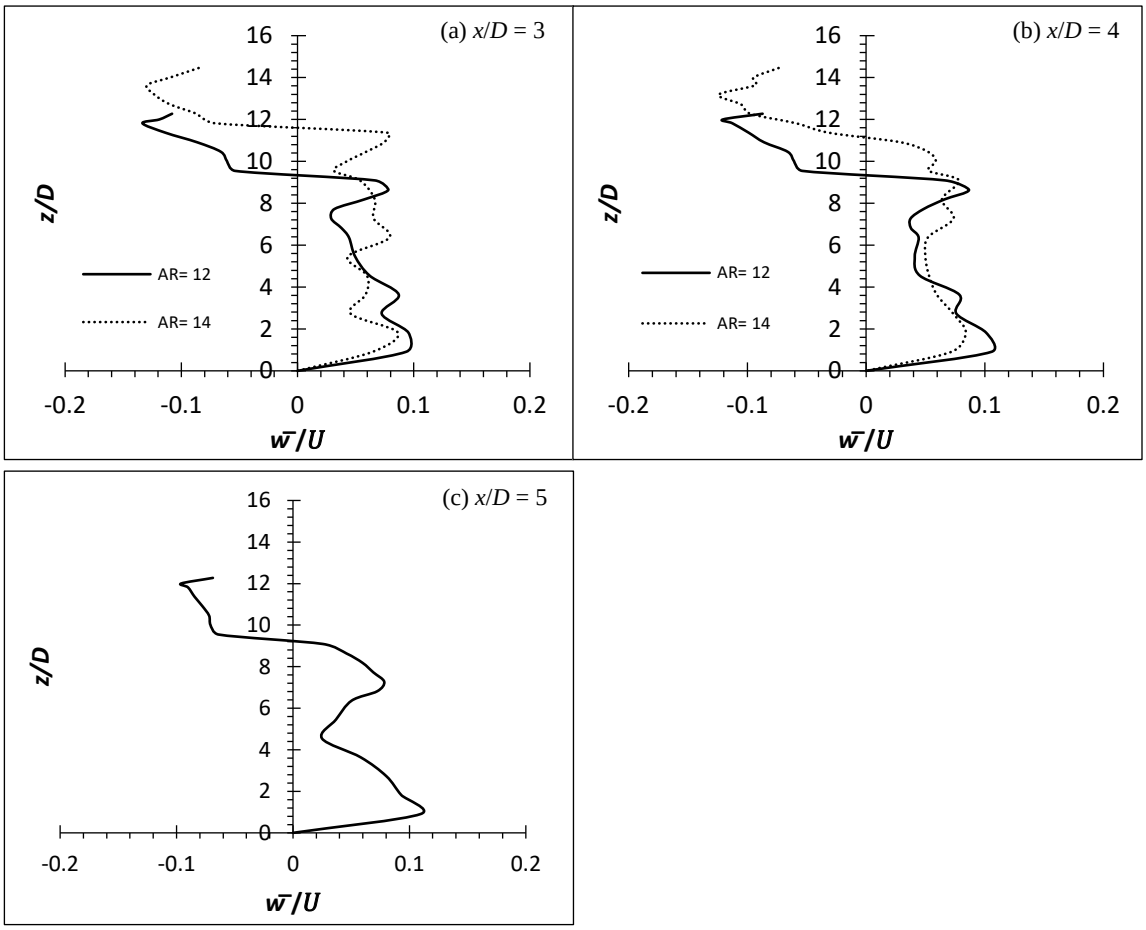

Figure 6.7: Time-average wall-normal velocity profile of flexible finite cylinder of *AR* = 12 and 14 at wake centreline (*y*/*D* = 0) for Re = 6000

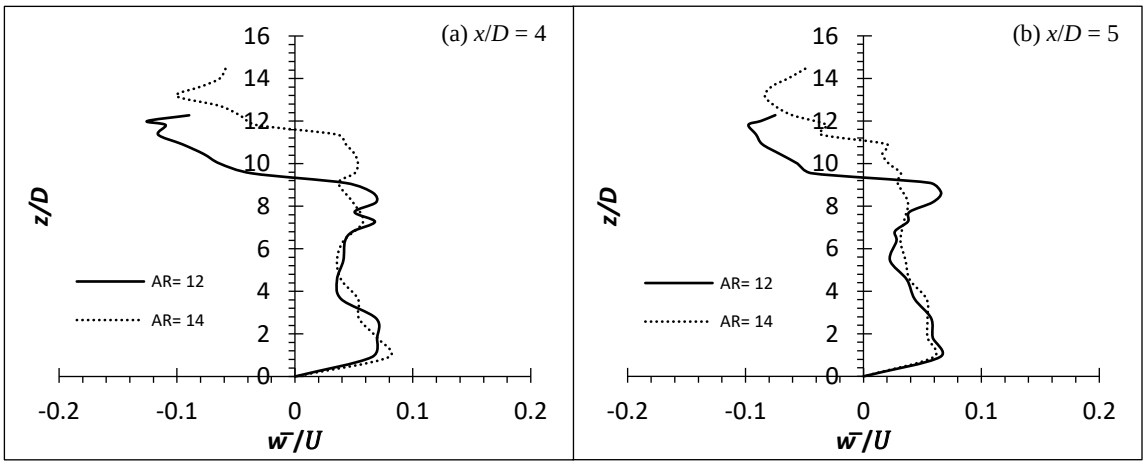

Figure 6.8: Time-average wall-normal velocity profile of flexible finite cylinder of *AR* = 12 and 14 at wake centreline (*y*/*D* = 0) for Re = 8000

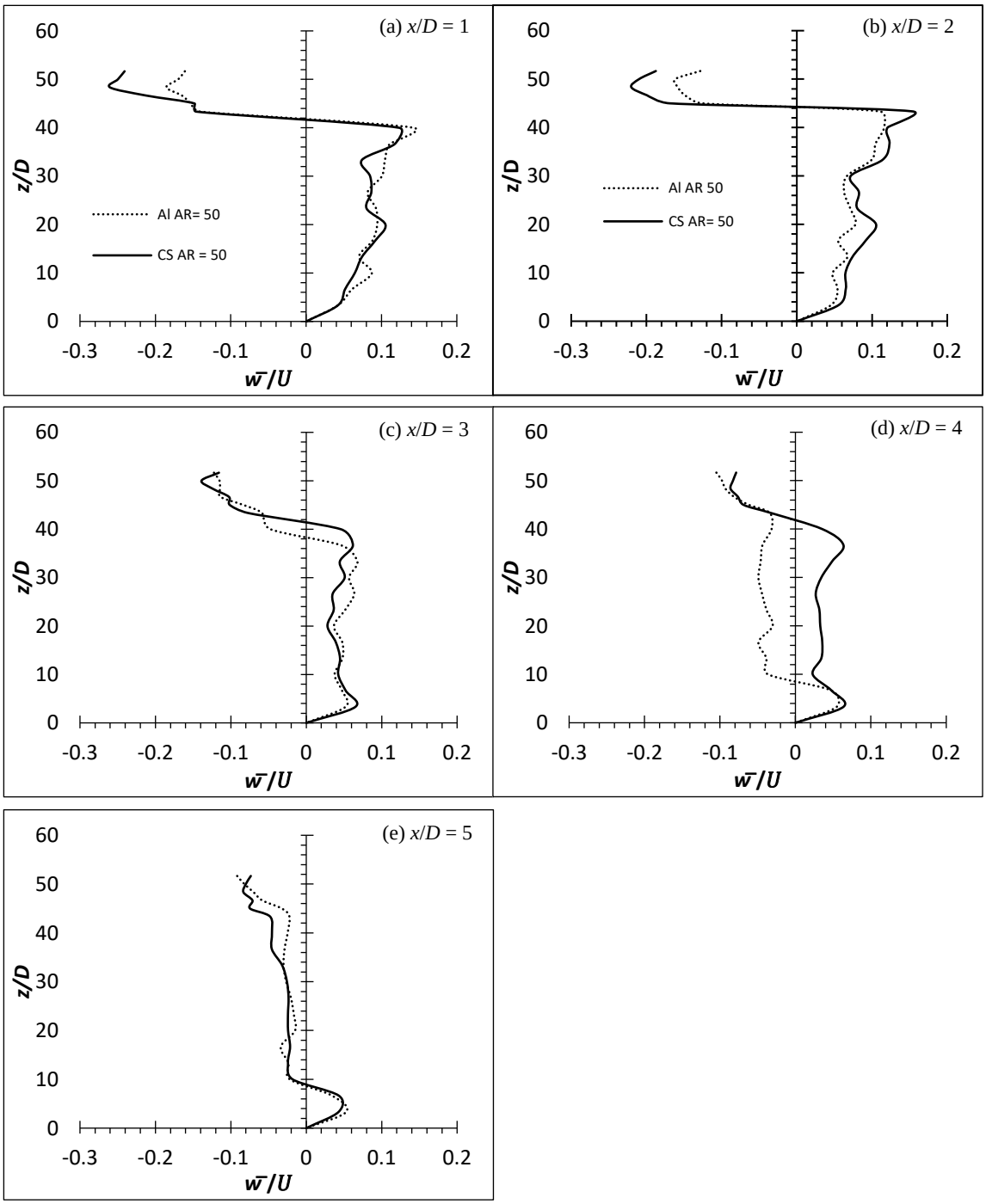

Figure 6.9: Time-average wall-normal velocity profile of flexible finite cylinder (Aluminium and Carbon Steel) of *AR* = 50 at wake centreline (*y*/*D* = 0) for Re = 2500. Aluminium denotes *Al* while Carbon Steel denotes *CS*.

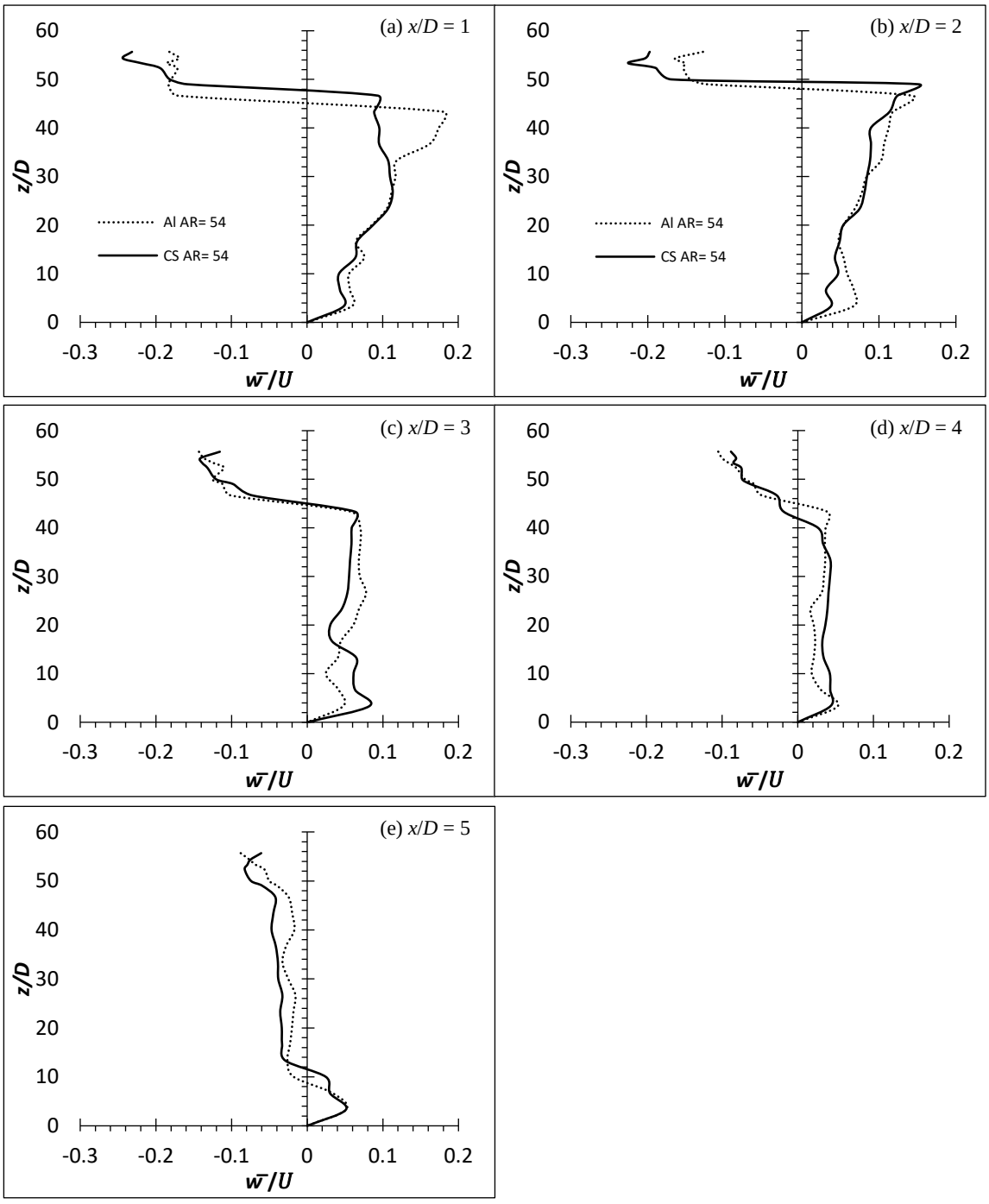

Figure 6.10: Time-average wall-normal velocity profile of flexible finite cylinder (Aluminium and Carbon Steel) of *AR* = 54 at wake centreline (*y*/*D* = 0) for Re = 2500. Aluminium denotes *Al* while Carbon Steel denotes *CS*.

Table 6.1: The average wake region (in approximation) behind the rigid and flexible cylinders at different conditions

Average wake region			
Material	AR	RE	Average Wake Region
EVA	12	4000	~ 10.45 D
		6000	~ 11.30 D
		8000	~ 10.90 D
	14	4000	~ 12.27 D
		6000	~ 12.27 D
		8000	~ 12.72 D
Aluminium	50	2500	~ 46.67 D
	54		~ 51.30 D
Carbon Steel	50		~ 46.67 D
	54		~ 50.00 D

6.2. Turbulence Intensity

6.2.1. Turbulence intensity distribution of EVA flexible cylinders

The distributions of the streamwise turbulence intensity (u'/U) and the wall-normal turbulence intensity (w'/U) of cylinders of AR = 12 and 14 at Re = 4000, 6000 and 8000 in the wake centreline (y/D = 0) are shown in Figure 6.11 to Figure 6.16. Though both the EVA cylinders are of the same material but the AR is different, therefore, affecting the stiffness of the cylinders; hence, it is suspected that there will be differences in the magnitude of the (u'/U).

In general, all of the cylinders have experienced an increment over the rigid cylinder of AR = 10 at Re = 4000, which is (u'_{max}/U) ≈ 26.14 %. They show an elevated region at near $z/D = AR$ - 3, corresponding to the region where the cylinder oscillates most. In spite of that, the magnitude of (u'_{max}/U) is very different for each cylinder. AR = 12 has a localized (u'_{max}/U) ≈ 42.14 %, 48.44 % and 41.66 % at increasing Re. On the other hand, AR = 14 has a localized (u'_{max}/U) ≈ 52.39 %, 64.48 % and 43.64 % at increasing Re.

It is observed that the localized (u'_{max}/U) of AR = 12 and 14 at Re = 8000 suffer from huge increment. It is therefore clear that the increment of the (u'/U) does not depend

directly on the *AR* or Re; instead it is the oscillating motion that is subjected to different *AR* or Re as it affects the structural stiffness. Mittal and Kumar (2001) concluded that the motion of the cylinder alters the flow field significantly in their simulation in an attempt to investigate the VIV of a light circular cylinder in a uniform flow.

The (w'/U) shows a decrease in magnitude for all deflected flexible cylinders of *AR* = 12 and 14 compared to the rigid cylinders. The local maximum turbulence intensity of *AR* = 12 at 4000, 6000 and 8000 are (w'_{max}/U) ≈ 30.27 %, 27.27 % and 23.63 %, which is slightly higher than *AR* = 14 at (w'_{max}/U) ≈ 23.76%, 21.53 %, 21.31% respectively. It can be seen that the more the deflection is for the cylinder, the lesser of the (w'_{max}/U) get. This could be due to the diminishing of downwash that leads the flow flowing downstream instead of downwards; thus it is not active in the w'.

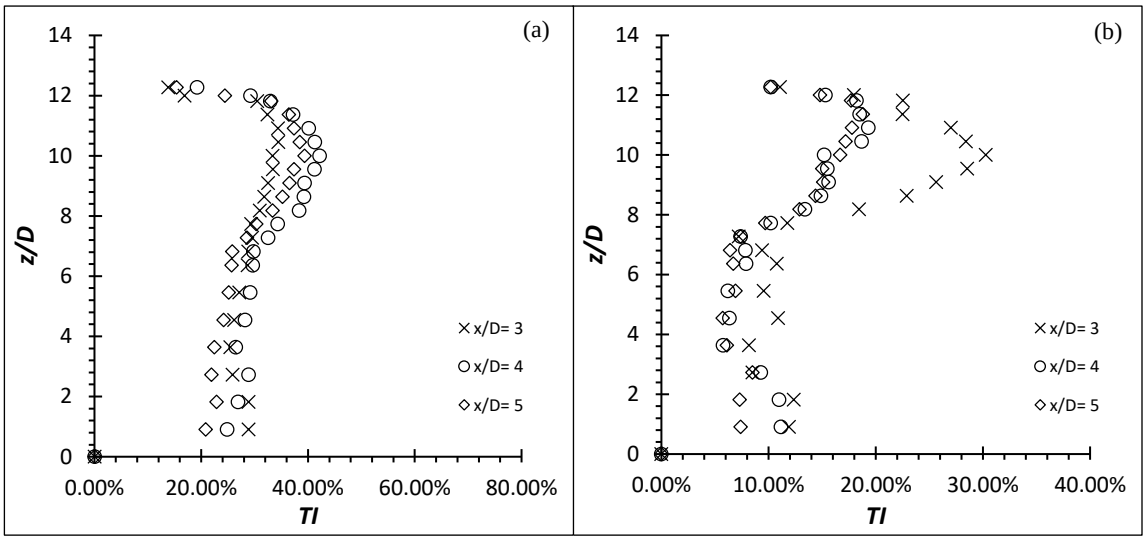

Figure 6.11: Turbulence intensity distribution for *AR* = 12 at Re = 4000: (a) Streamwise turbulence intensity (b) wall-normal turbulence intensity

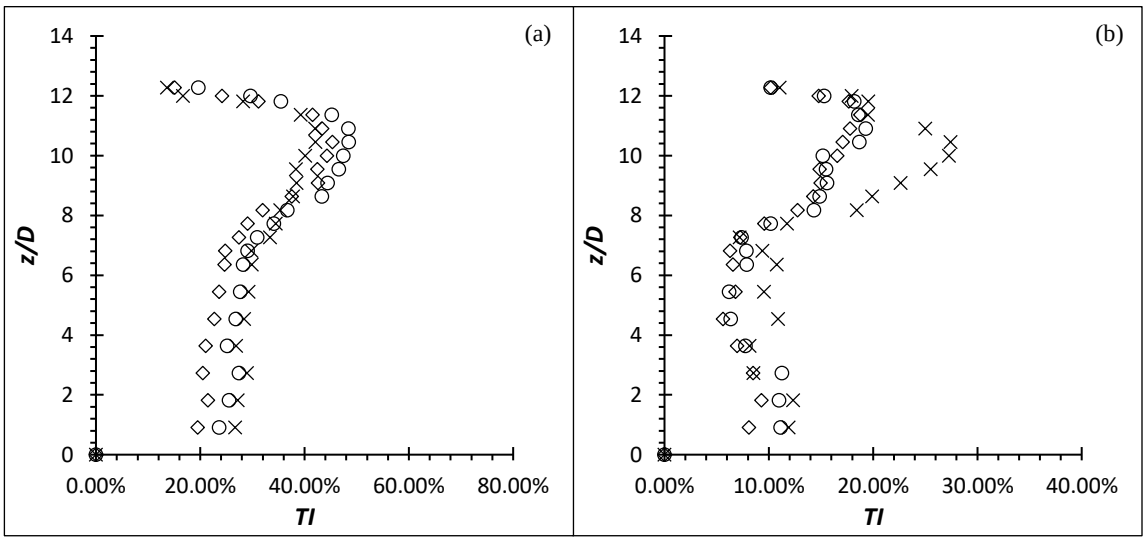

Figure 6.12: Turbulence intensity distribution for *AR* = 12 at Re = 6000: (a) Streamwise turbulence intensity (b) wall-normal turbulence intensity

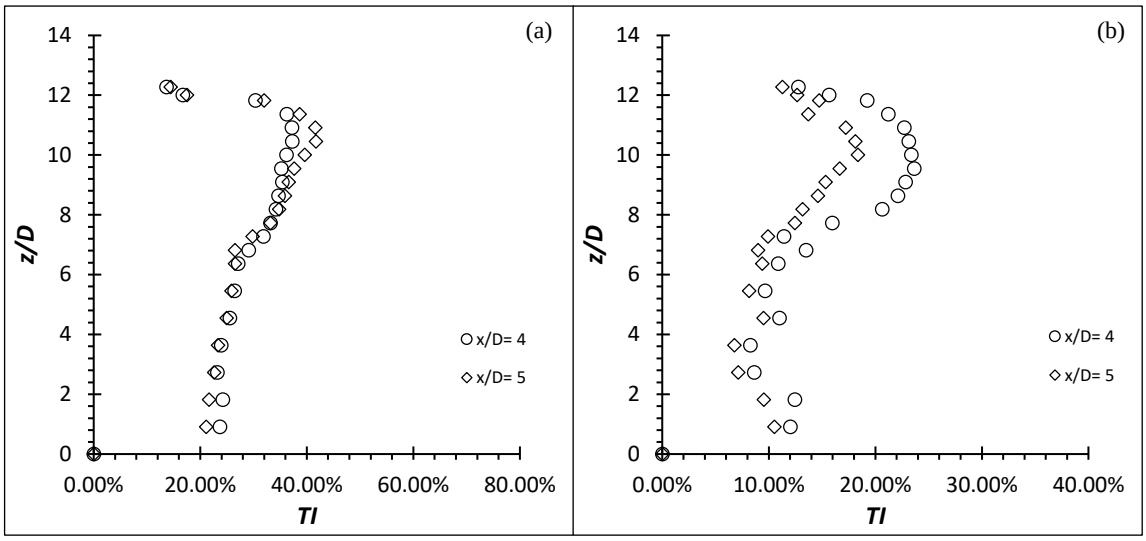

Figure 6.13: Turbulence intensity distribution for *AR* = 12 at Re = 8000: (a) Streamwise turbulence intensity (b) wall-normal turbulence intensity

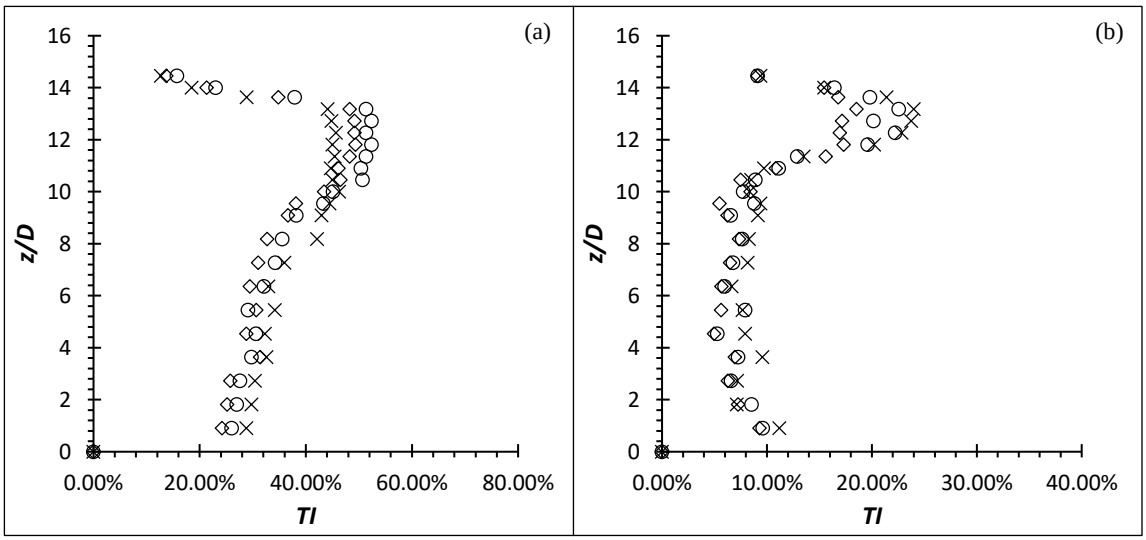

Figure 6.14: Turbulence intensity distribution for *AR* = 14 at Re = 4000: (a) Streamwise turbulence intensity (b) wall-normal turbulence intensity

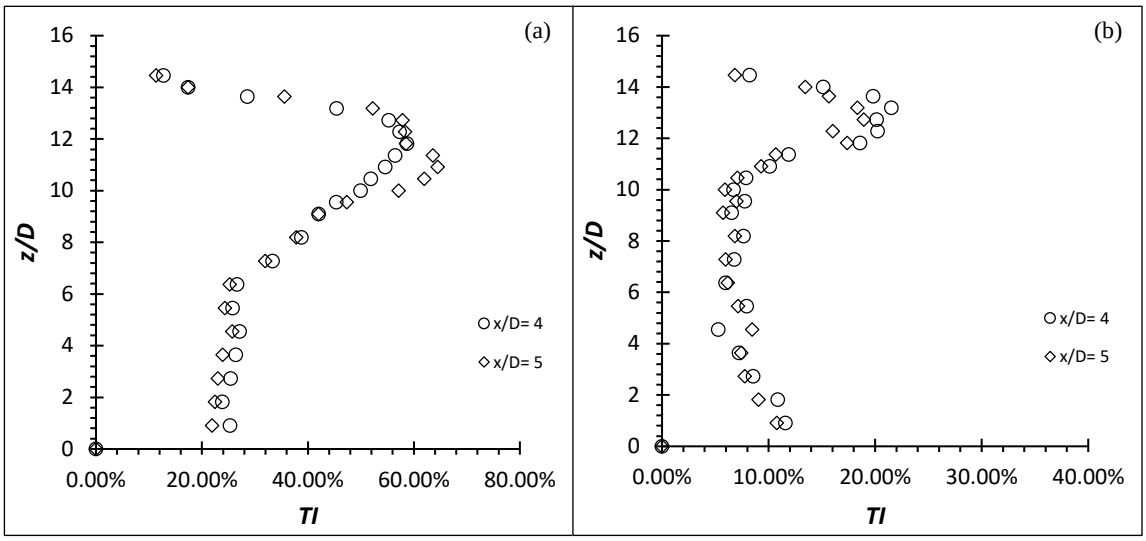

Figure 6.15: Turbulence intensity distribution for *AR* = 14 at Re = 6000: (a) Streamwise turbulence intensity (b) wall-normal turbulence intensity

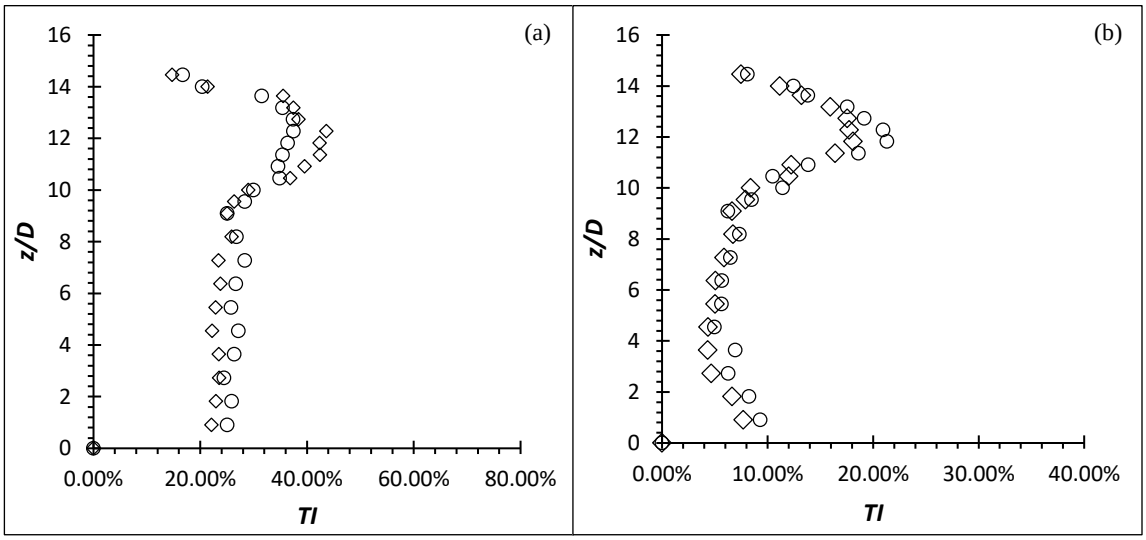

Figure 6.16: Turbulence intensity distribution for *AR* = 14 at Re = 8000: (a) Streamwise turbulence intensity (b) wall-normal turbulence intensity

6.2.2. Turbulence intensity distribution of metal group flexible cylinders

The distributions of the streamwise turbulence intensity (u'/U) and the wall-normal turbulence intensity (w'/U) of aluminium and carbon steel cylinders of AR = 50 and 54 at Re = 2500 in the wake centreline (y/D = 0) are shown in Figure 6.17 to Figure 6.20.

It is noticeable that the localized (u'_{max}/U) of the metal group flexible cylinders is at approximately 5D from the free end at x/D = 2, unlike the EVA flexible cylinders. Beyond x/D = 2, the (u'/U) quickly subsides. This suggest that the downwash phenomenon due to no deflection of the metal group flexible cylinders; has direct most of the vortical activities downward as the vortical activities follow the flow.

According to Figure 6.17 and Figure 6.18 of aluminium cylinder, the localized (u'_{max}/U) is scattered around 1/3 of the cylinder's span near the free end at $z/D \approx 33D$ to the free end. In contrast to that, the localized (u'_{max}/U) produced by the carbon steel cylinder (see Figure 6.19 and 6.20) is seen to concentrate only at the region from the free end to $z/D \approx AR - 10D$; a smaller area of elevated turbulence intensity compared to the aluminium cylinder. The reason of the smaller area of augmented turbulence intensity could be due to the carbon steel cylinders that behaved exactly as the rigid cylinder. Despite not having a x-deflection for the aluminium cylinder, it did vibrate at a comparatively high oscillating frequency (see Figure C4 and C5). As the vibration takes place greatest at the free end and subside along the span (its local stiffness is the least stiff at the free end and slowly increasing along the span towards the fixed end – in accordance to Equation 2.5), the region where the vibration takes place have augmented the turbulence intensity; hence the larger area of elevated turbulence intensity for aluminium cylinder. This finding is also in agreement with the findings from Thulukkanam (2013) where VIV (vibration of cylinder caused by the vortices shed) has the ability to increase the strength of the vortices shed.

Since the carbon steel flexible cylinder is behaving similarly as the rigid cylinder. Therefore, it is expected that it will have a similar performance as the rigid cylinder. The local (u'_{max}/U) of the carbon steel of AR = 50 and 54 are (u'_{max}/U) ≈ 23.0 % and 24.2 % respectively, slightly lesser than the (u'_{max}/U) produced by rigid cylinder of AR = 10 and

16 at Re = 4000. The local (u'_{max}/U) of the aluminium flexible cylinder of *AR* = 50 and 54 are (u'_{max}/U) ≈ 52.9 % and 57.8 %.

The (*w*'/U) shows increase magnitude compare to the (*w*'/U) of the EVA cylinders that is deflected. As the downwash phenomenon is more apparent in the metal group flexible cylinders, the *w*' is more active.

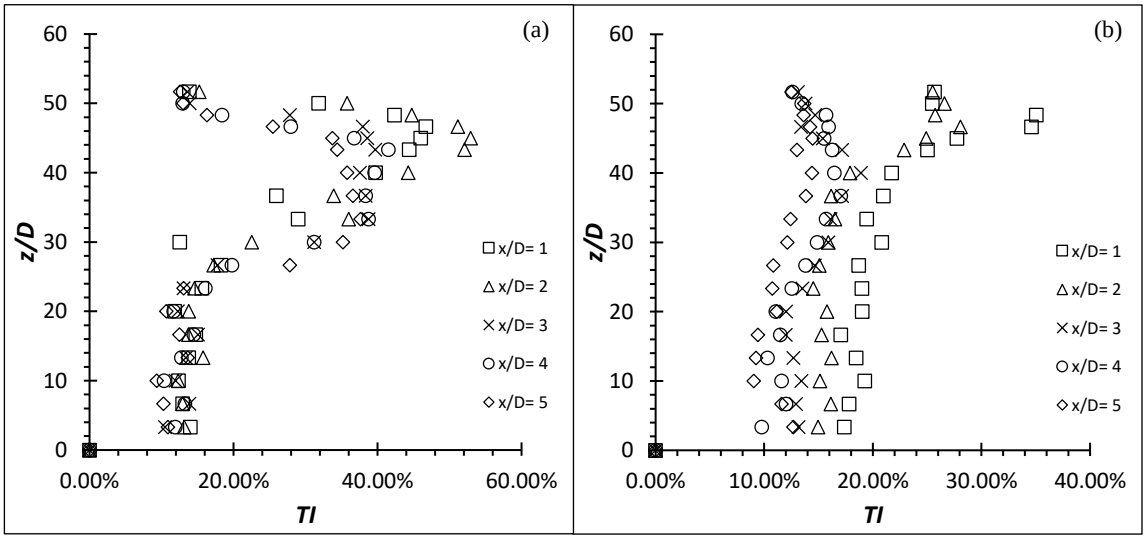

Figure 6.17: Turbulence intensity distribution for aluminium cylinder of *AR* = 50 at Re = 2500: (a) Streamwise turbulence intensity (b) wall-normal turbulence intensity

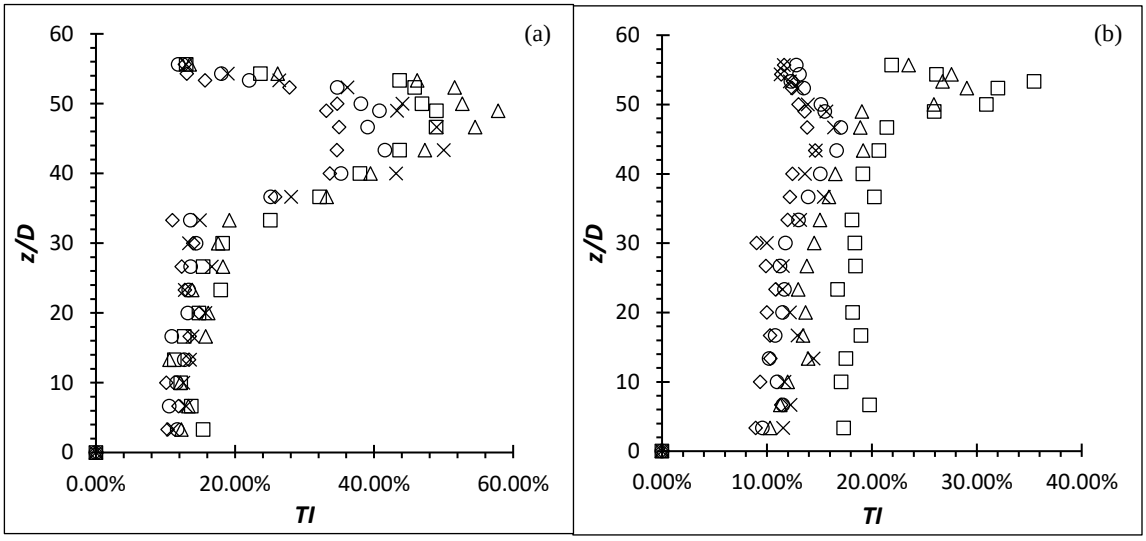

Figure 6.18: Turbulence intensity distribution for aluminium cylinder of *AR* = 54 at Re = 2500: (a) Streamwise turbulence intensity (b) wall-normal turbulence intensity

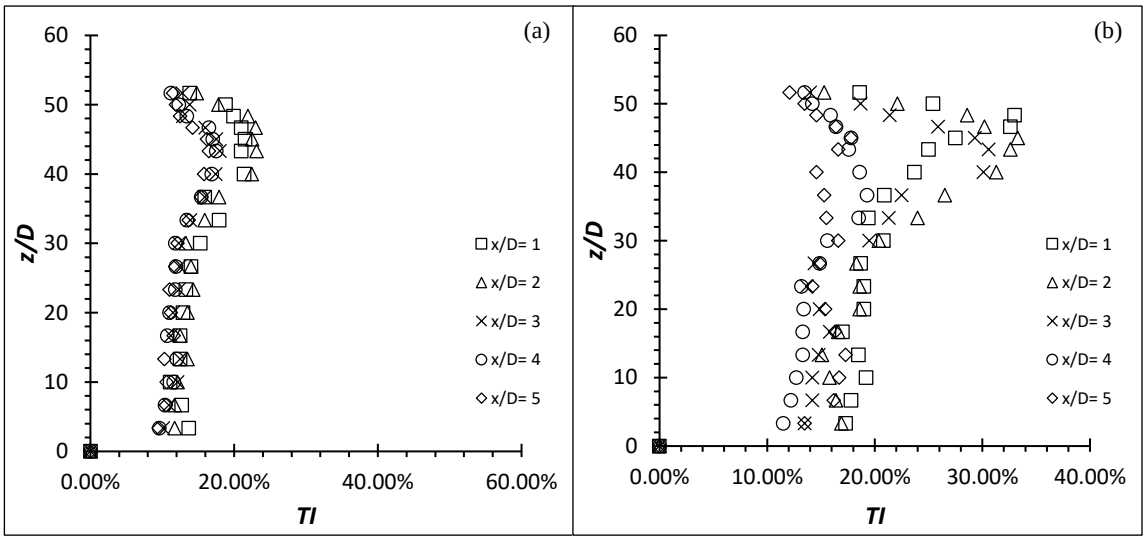

Figure 6.19: Turbulence intensity distribution for carbon steel cylinder of *AR* = 50 at Re = 2500: (a) Streamwise turbulence intensity (b) wall-normal turbulence intensity

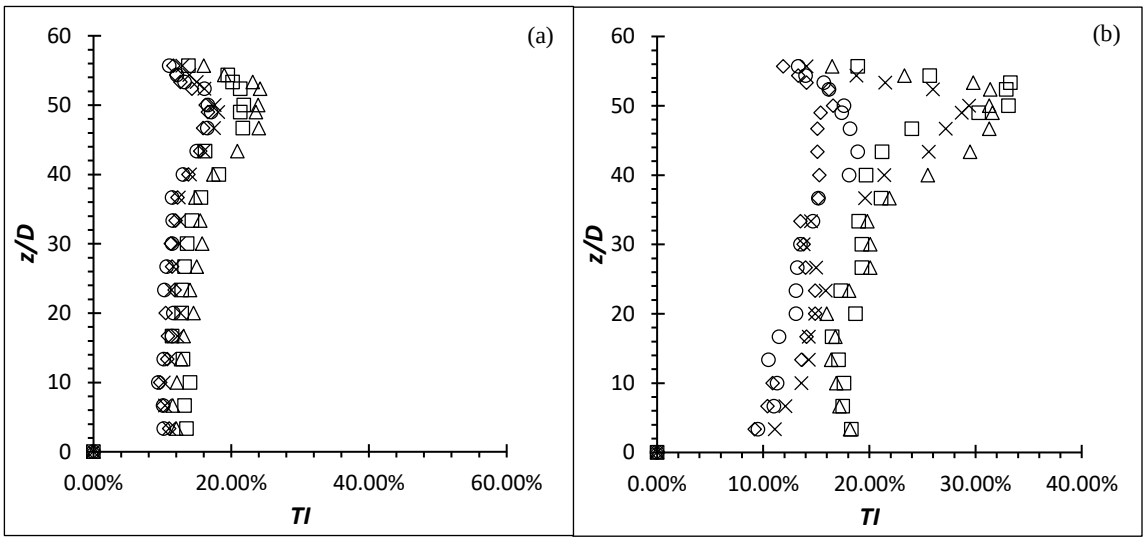

Figure 6.20: Turbulence intensity distribution for carbon steel cylinder of *AR* = 54 at Re = 2500: (a) Streamwise turbulence intensity (b) wall-normal turbulence intensity

6.3. Turbulent Kinetic Energy

6.3.1. Turbulent kinetic energy of EVA flexible cylinders

The normalized ($k/(U^2)$) graph downstream of the flexible cylinders of *AR* = 12 and 14 at Re = 4000, 6000 and 8000 are presented in Figure 6.21 and Figure 6.22. Both the flexible of *AR* = 12 and 14 have generated increased turbulent kinetic energy. Similar to flexible of *AR* = 14 and 16, the localized k_{max} occurs in the vicinity of the free end where the shear layer instability is the strongest.

It can be observed that the increment of *k* terms by the flexible cylinders of *AR* = 12 and 14 at all Re happen at a different magnitude. The localized k_{max} of *AR* = 12 are approximately 0.112, 0.135 and 0.095 at Re = 4000, 6000 and 8000 respectively. On the other hand, the localized k_{max} of *AR* = 14 have spotted to be at circa 0.154, 0.184 and 0.125 at increasing Re. The magnitude of increment is the same as the turbulence intensity whereby it is always higher turbulent kinetic energy associated with larger *AR* or higher Re.

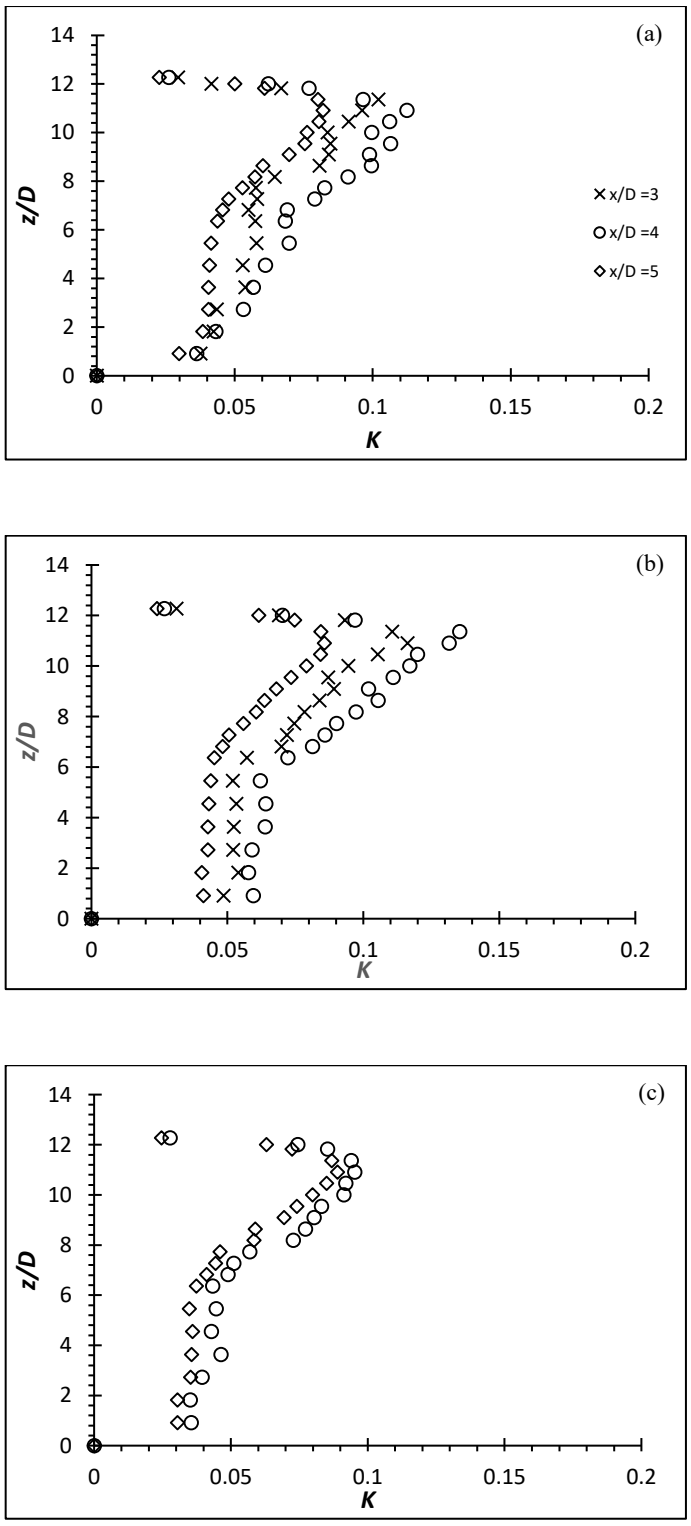

Figure 6.21: Turbulent kinetic energy, *k* for flexible cylinder of *AR* = 12 at (a) Re = 4000 (b) Re = 6000 (c) Re = 8000

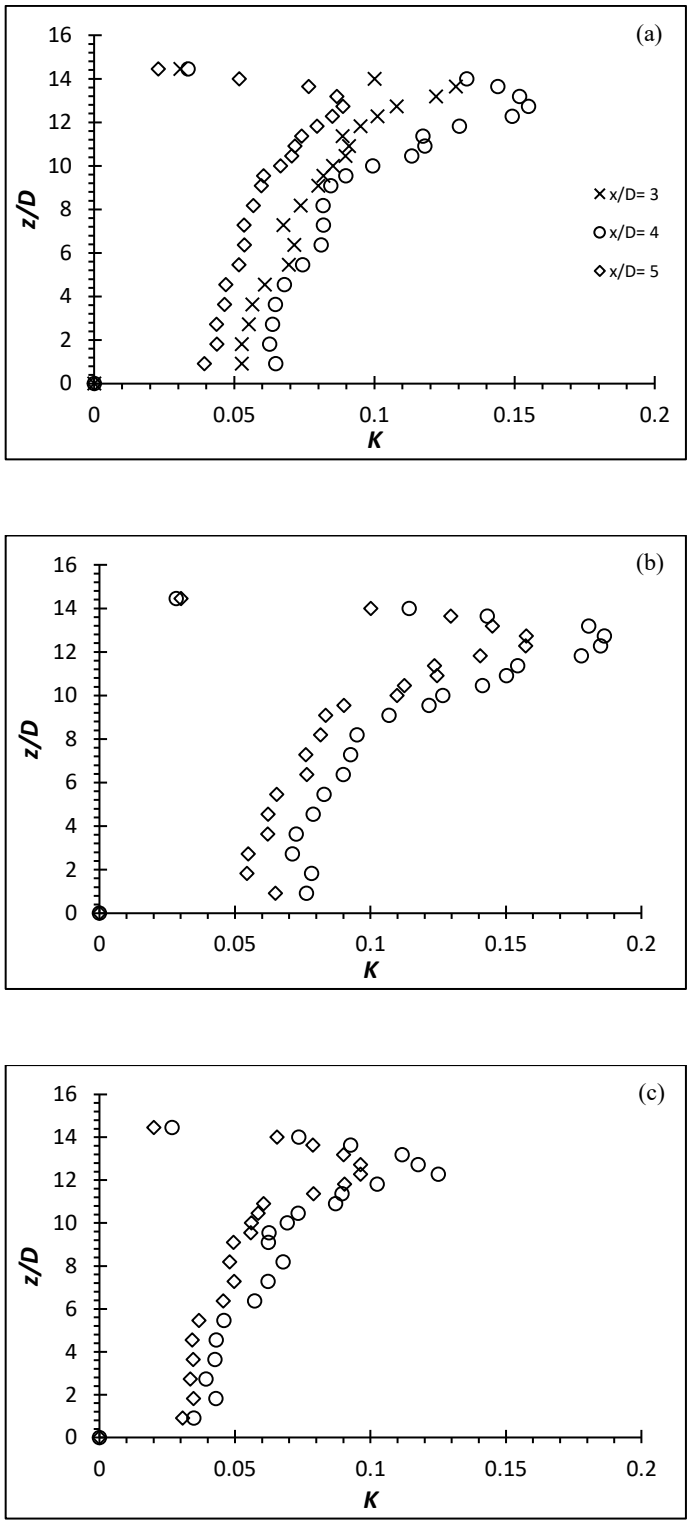

Figure 6.22: Turbulent kinetic energy, *k* for flexible cylinder of *AR* = 16 at (a) Re = 4000 (b) Re = 6000 (c) Re = 8000

6.3.2. Turbulent kinetic energy of metal group flexible cylinders

Figure 6.23 and Figure 6.24 show the normalized k graph by the metal group flexible cylinder – aluminium and carbon steel of AR = 50 and 54 at Re = 2500.

There is a similar phenomenon whereby the localized k_{max} occurs in the vicinity of the free end for both aluminium and carbon steel cylinders at both AR. This behaviour is very similar to that of rigid cylinders where the localized k drops considerably below the free end after x/D = 2 in the wake region. This dividing streamline region is the boundary which separates downward dominant flow and downstream dominant flow.

Increment of the k term by the aluminium cylinder of AR = 50 and 54 that oscillates can be seen from the graphs. The aluminium cylinder of AR = 54 has a slightly higher localized k_{max} at circa 0.122 as opposed to circa 0.108 of AR = 50.

The k term of carbon steel cylinder remains at a lower magnitude than the aluminium cylinder. This is due to the reason that the carbon steel cylinder is behaving like a rigid cylinder due its high structural stiffness. The localized k_{max} generated by the carbon steel is approximately 0.075 and 0.070 for AR = 50 and 54 at Re = 2500.

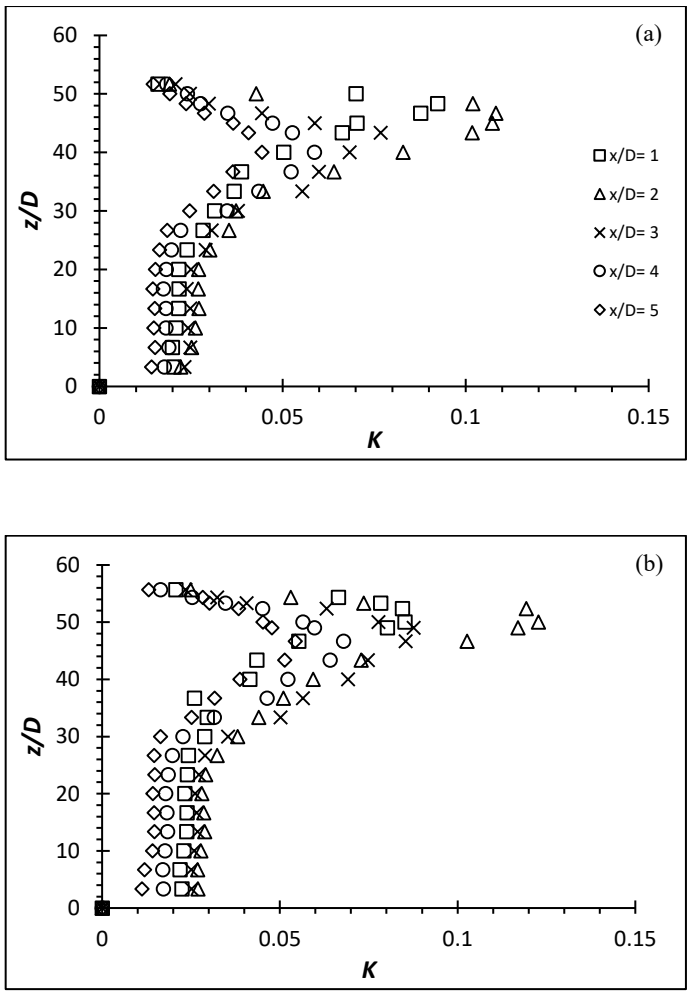

Figure 6.23: Turbulent kinetic energy, *k* for flexible aluminium cylinder of (a) *AR* = 50 and (b) *AR* = 54 at Re = 2500

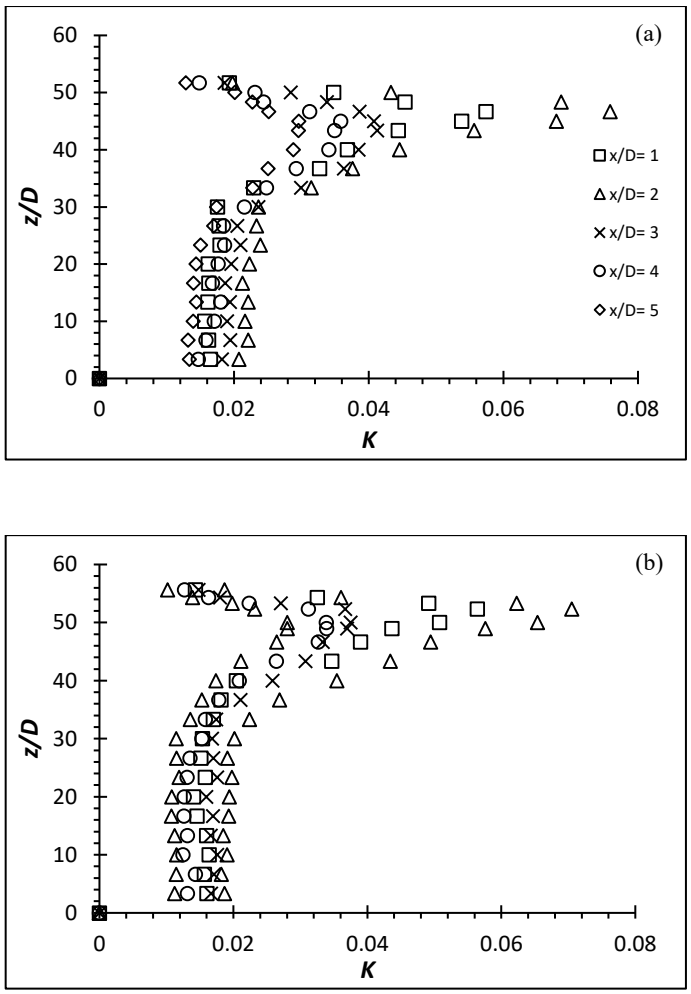

Figure 6.24: Turbulent kinetic energy, *k* for flexible carbon steel cylinder of (a) *AR* = 50 and (b) *AR* = 54 at Re = 2500

6.4. Turbulence Kinetic Energy Budget

6.4.1. Production term of EVA flexible cylinders

The normalized ($\boldsymbol{P}/(U^3/D)$) graph downstream of the flexible cylinders of AR = 12 and 14 at Re = 4000, 6000 and 8000 are presented in Figure 6.25 and Figure 6.26. As expected from the earlier results in Chapter 5, the flexible cylinder has the ability to enhance the turbulence generation; therefore, it can be seen that the normalized $\boldsymbol{P}$ term generated by the flexible cylinders of AR =12 and 14 at all Re have increased with reference to the rigid cylinder. Similarly, the localized $\boldsymbol{P}_{max}$ occurs in the vicinity of the free end where the shear layer instability is the strongest.

It can be observed that the increment of $\boldsymbol{P}$ terms by the flexible cylinders of AR = 12 and 14 at all Re happen at a different magnitude. The localized $\boldsymbol{P}_{max}$ of AR = 12 are approximately 0.048, 0.060 and 0.045 at Re = 4000, 6000 and 8000 respectively. On the other hand, the localized $\boldsymbol{P}_{max}$ of AR = 14 have spotted to be at circa 0.065, 0.072 and 0.054 at increasing Re. Indeed, it is evident that the $\boldsymbol{P}$ term values do not scale with the AR alone (though the values do indeed vary with the AR); instead, it is the different structural motion generated by the flexible cylinders at different AR which result in a different structural stiffness.

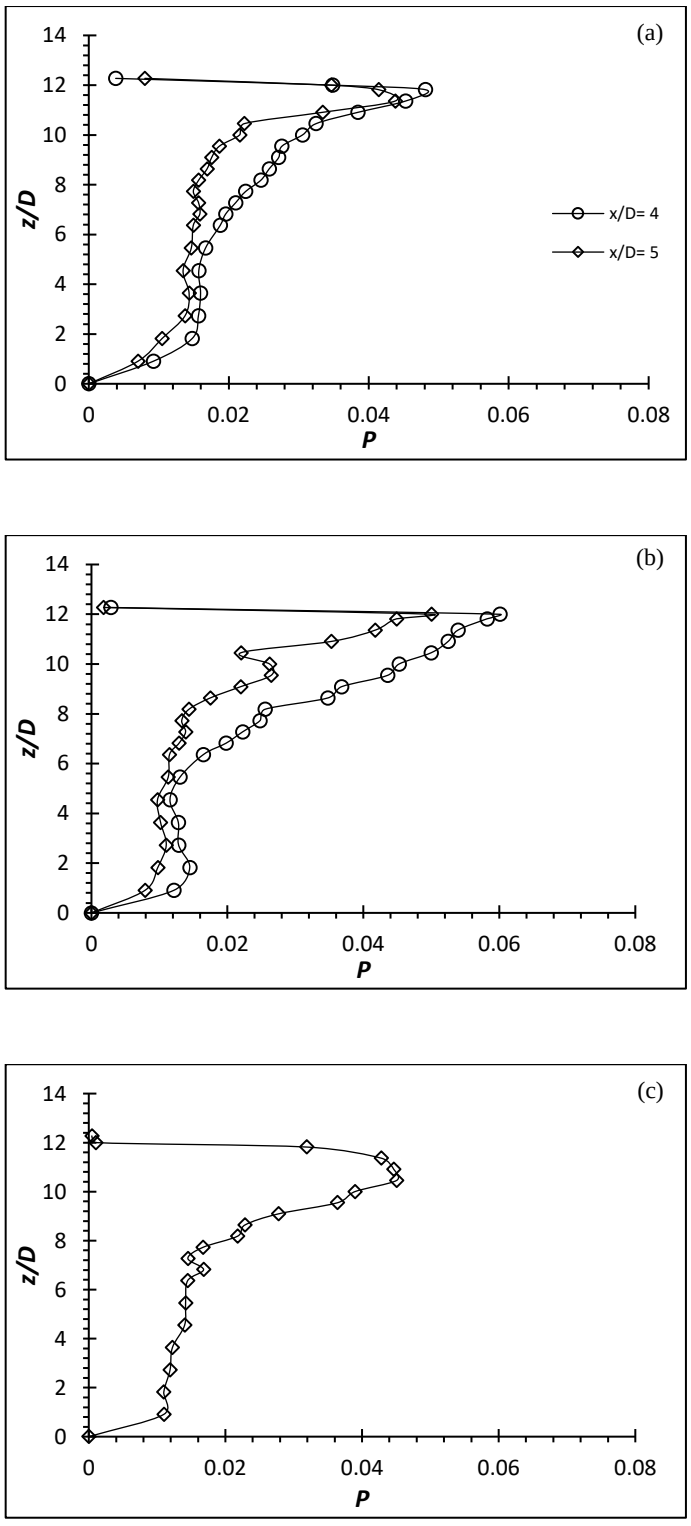

Figure 6.25: Production term, $-\overline{u_i' u_j'} \frac{\partial U_i}{\partial x_j}$ for flexible cylinder of AR = 12 at (a) Re = 4000 (b) Re = 6000 (c) Re = 8000

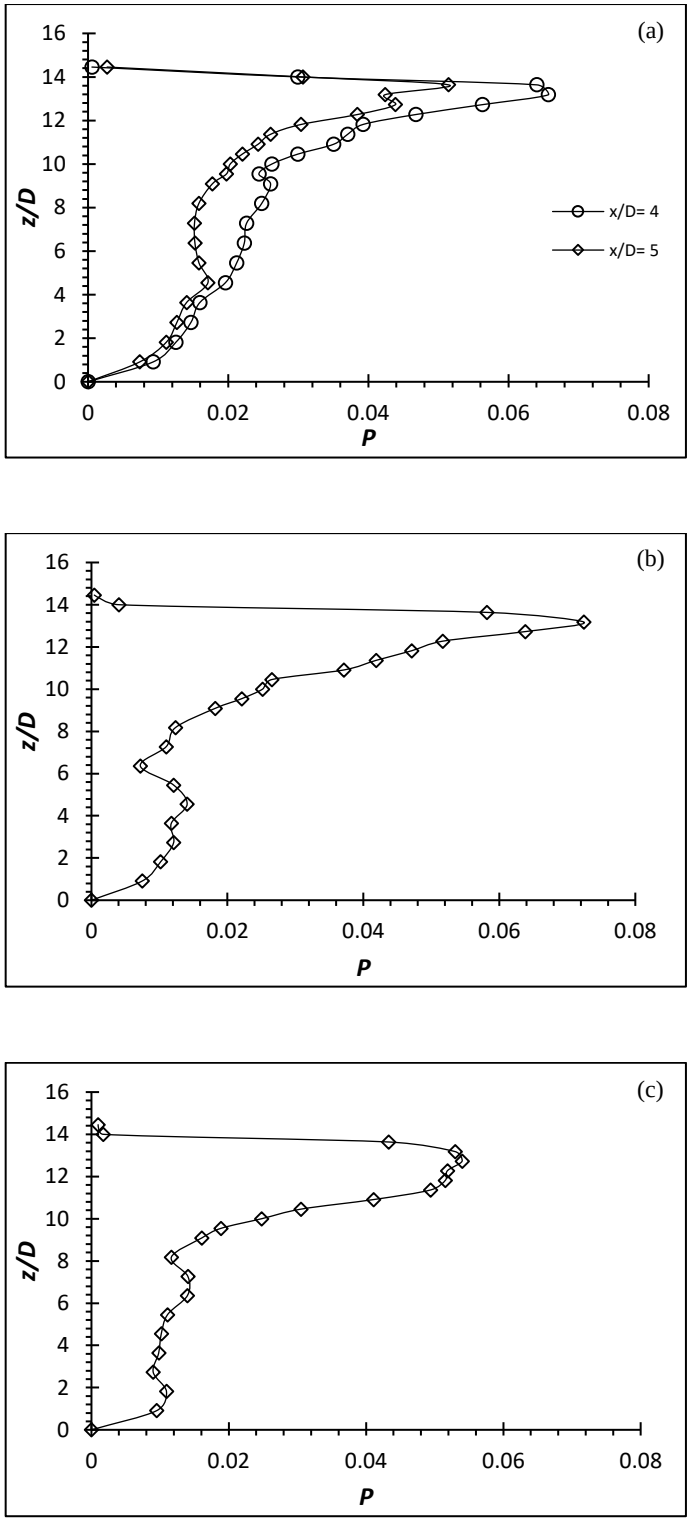

Figure 6.26: Production term, $-\overline{u_i' u_j'} \frac{\partial U_i}{\partial x_j}$ for flexible cylinder of AR = 14 at (a) Re = 4000 (b) Re = 6000 (c) Re = 8000

6.4.2. Production term of metal group flexible cylinder

Figure 6.27 and Figure 6.28 show the normalized $\boldsymbol{P}$ graph by the metal group flexible cylinder – aluminium and carbon steel of AR = 50 and 54 at Re = 2500.

Similarly, the localized $\boldsymbol{P}_{\max}$ occurs in the vicinity of the free end for both aluminium and carbon steel cylinders at both AR. Besides, it can be seen that the localized $\boldsymbol{P}_{\max}$ occurs at x/D = 2 in the wake region where the region is approximately close to the dividing streamline of the flow as indicated by the negative ($\bar{u}/\mathrm{U}$) at x/D = 2 and positive ($\bar{u}/\mathrm{U}$) at x/D = 3 of the velocity profile in Figure 6.4 and Figure 6.5. A dividing streamline is the boundary which separates downward dominant flow and downstream dominant flow (For better illustration, readers can refer to Figure 4 of journal paper by Rostamy *et al.*(2012)). Beyond x/D = 2, the $\boldsymbol{P}$ term quickly subside as the flow are less chaotic due to the downwash that directs most of the vertical activities downwards instead of downstream.

The $\boldsymbol{P}$ term of carbon steel cylinder remain at a lower magnitude than the aluminium cylinder. As mentioned, the carbon steel cylinder is behaving like a rigid cylinder due its high structural stiffness; therefore, it is can serve as a reference/benchmark to the increment of the aluminium cylinder that oscillates. The localized $\boldsymbol{P}_{\max}$ generated by the carbon steel is approximately 0.034 and 0.032 for AR = 50 and 54 at Re = 2500.

Increment of the $\boldsymbol{P}$ term by the aluminium cylinder of AR = 50 and 54 that oscillates can be seen from the graphs. They both have a rather similar pattern in terms of the evolution of turbulence production. Nevertheless, the aluminium cylinder of AR = 54 has a slightly higher localized $\boldsymbol{P}_{\max}$ at circa 0.057 as opposed to circa 0.052 of AR = 50. The contributor of this increment is suspected to be the higher oscillating amplitude (see Figure C4 and C5) by AR = 54 as its structural stiffness is slightly lower than that of AR = 50.

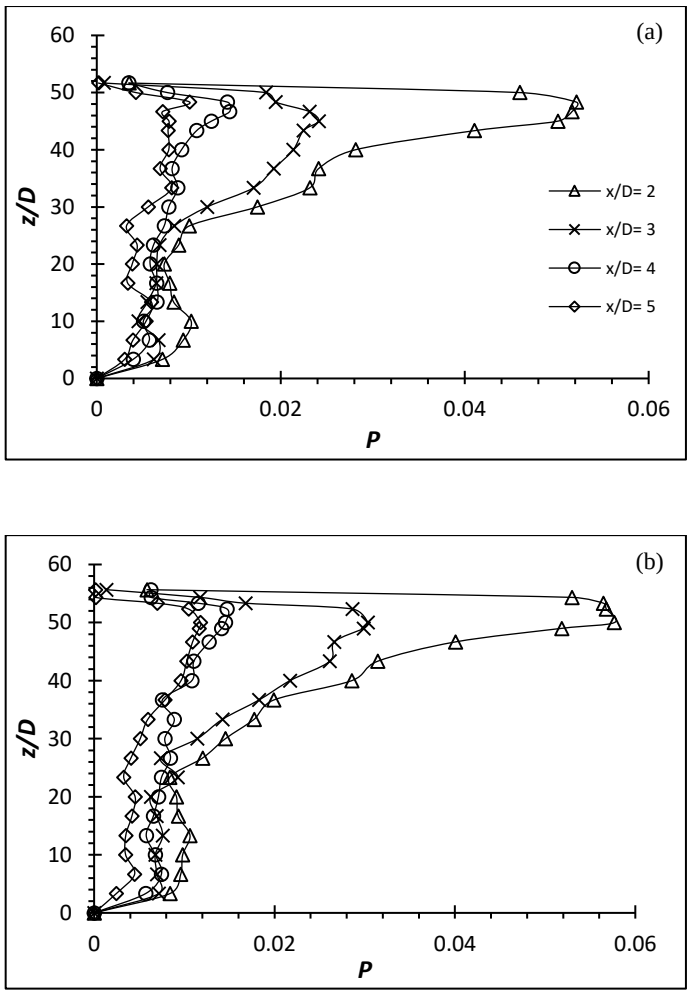

Figure 6.27: Production term, $-\overline{u_i' u_j'} \frac{\partial U_i}{\partial x_j}$ for flexible aluminium cylinder of (a) AR = 50 and (b) AR = 54 at Re = 2500

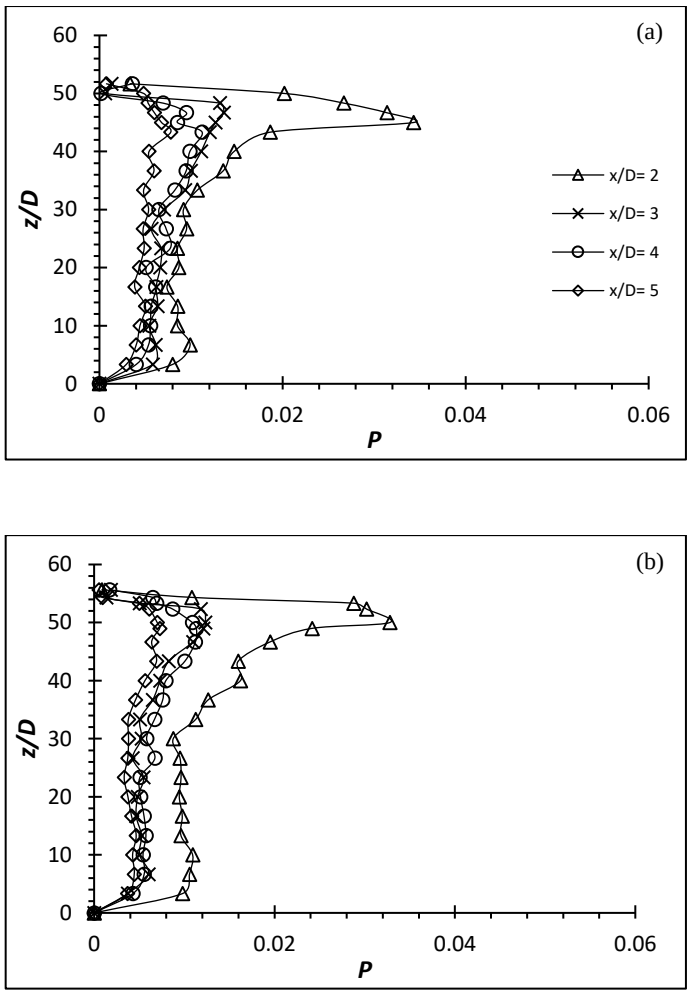

Figure 6.28: Production term, $-\overline{u_i' u_j'} \frac{\partial U_i}{\partial x_j}$ for flexible carbon steel cylinder of (a) AR = 50 and (b) AR = 54 at Re = 2500

6.5. Reynolds Stresses

6.5.1. Reynolds averaged statistics of EVA flexible cylinders

The Reynolds stresses for the flexible cylinders has seen a major increase over the rigid cylinders in the Chapter 5. The increment ranged from approximately 4.5 % for flexible cylinder of *AR* = 10 at Re = 8000 to over 150.0 % for flexible cylinder of *AR* = 16 at Re = 6000 under similar condition case basis. Also, as demonstrated by the (*u*'/U) and the ***P*** term generated by the EVA cylinders of *AR* = 12 and 14, it is expected that the $\frac{\overline{u'^2}}{U^2}$, $\frac{\overline{w'^2}}{U^2}$ and $\frac{\overline{u'w'}}{U^2}$ will gain as well. The Reynolds stresses, $\frac{\overline{u'^2}}{U^2}$, $\frac{\overline{w'^2}}{U^2}$ and $\frac{\overline{u'w'}}{U^2}$ of the EVA flexible cylinder of *AR* = 12 and 14 at Re = 4000, 6000 and 8000 are presented in Figure 6.29 to Figure 6.34 to provide insight on the turbulent fluctuations in the flow.

As anticipated, the $\frac{\overline{u'w'}}{U^2}$ of *AR* = 12 and 14 at all Re show increment. The $\frac{\overline{u'w'}}{U^2}$ is also consistent to the ***P*** term where the peak intensity coincides with each other near the free end, and is also evident in the high shear rate (high velocity gradient) of the mean flow. It shows good agreement that the energy from the mean flow is being passed on to the fluctuating components by the mechanism of shear.

Likewise, the $\frac{\overline{u'^2}}{U^2}$ shows a peak intensity in the regions of strong velocity gradient and it can be imagined that it is where the separated shear layer is. The localized $\frac{\overline{u'w'}}{U^2}_{\max}$ is located near the free end where the tip vortices are generated. The *u*' in the near wake are more energetic than the *w*', hence the magnitude of $\frac{\overline{u'^2}}{U^2}$ component is much larger than the $\frac{\overline{w'^2}}{U^2}$ component. The evaluated Reynolds shear stress can be said to stem from the $\frac{\overline{u'^2}}{U^2}$ since the $\frac{\overline{u'^2}}{U^2}$ are more energetic than the $\frac{\overline{w'^2}}{U^2}$ in that region.

The ***P*** term shows that the increment of turbulence production does not strictly follow the *AR* or Re pattern – increase in turbulent production as the *AR* or Re increase. Same phenomenon can also be seen throughout the $\frac{\overline{u'w'}}{U^2}$ of the cylinders. The localized

$\frac{\overline{u'w'}}{U^2}_{max}$ of *AR* = 12 is circa -0.049, -0.056 and -0.048 at increasing Re. On the other hand, the localized $\frac{\overline{u'w'}}{U^2}_{max}$ of *AR* = 14 is circa -0.061, -0.078, -0.051.

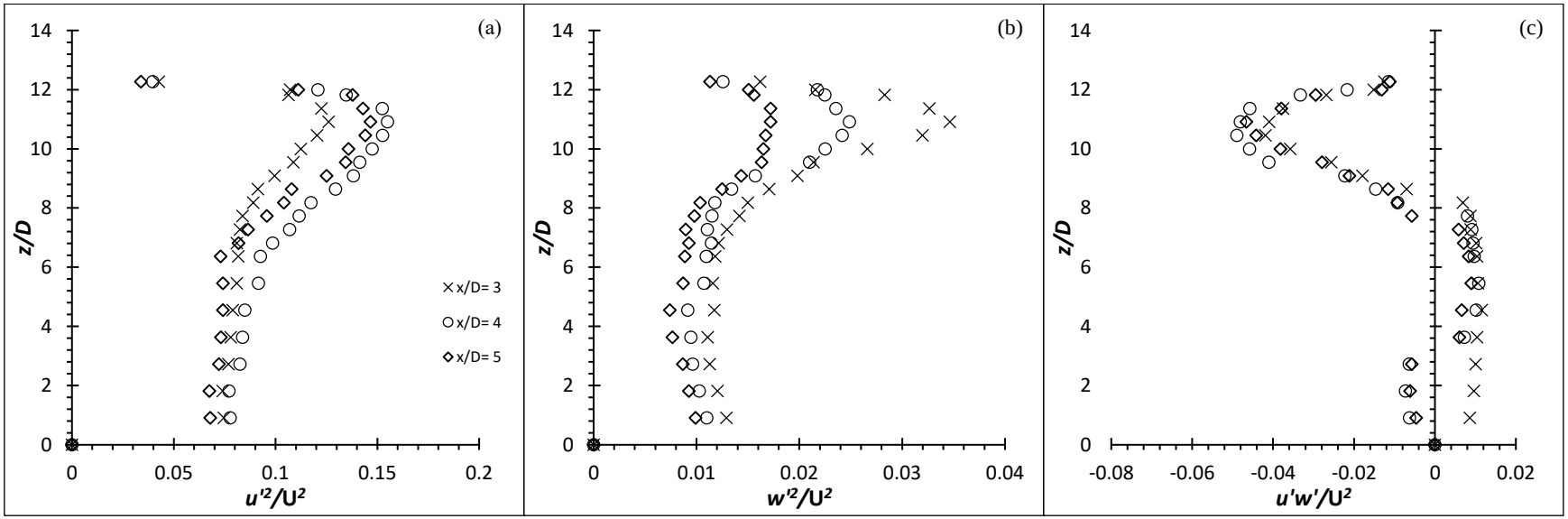

Figure 6.29: Reynolds stress profiles for cylinder of *AR* = 12 at Re = 4000: (a) $\frac{\overline{u'^2}}{U^2}$ (b) $\frac{\overline{w'^2}}{U^2}$ (c) $\frac{\overline{u'w'}}{U^2}$

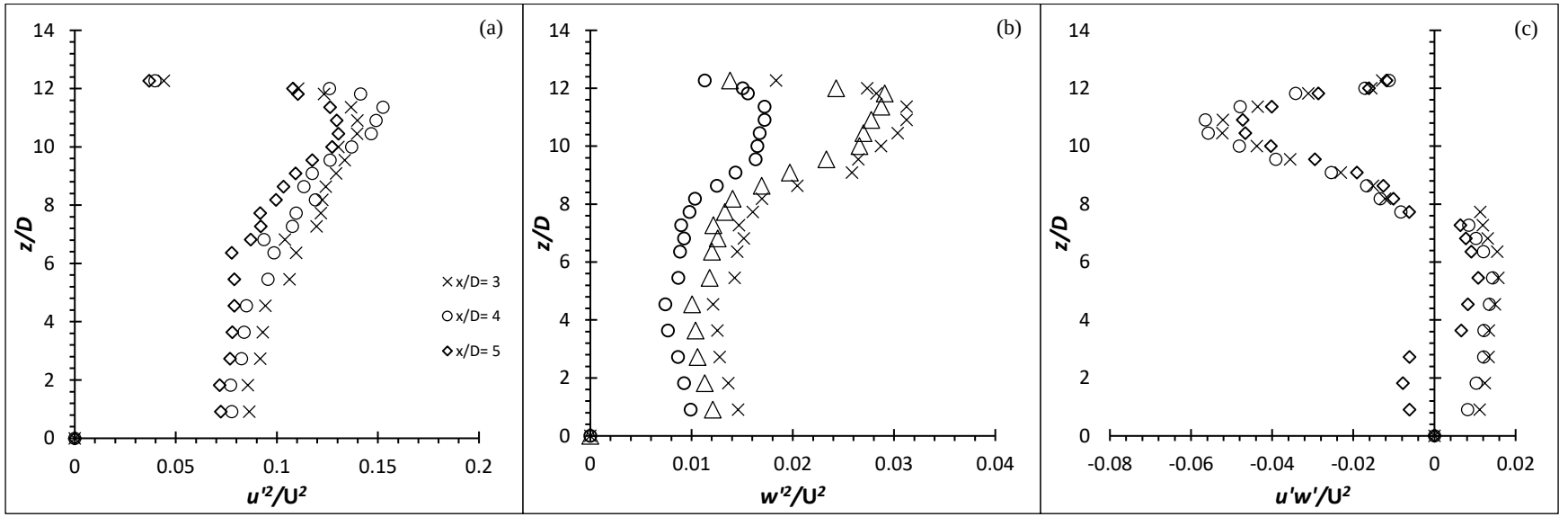

Figure 6.30: Reynolds stress profiles for cylinder of *AR* = 12 at Re = 6000: (a) $\frac{\overline{u'^2}}{U^2}$ (b) $\frac{\overline{w'^2}}{U^2}$ (c) $\frac{\overline{u'w'}}{U^2}$

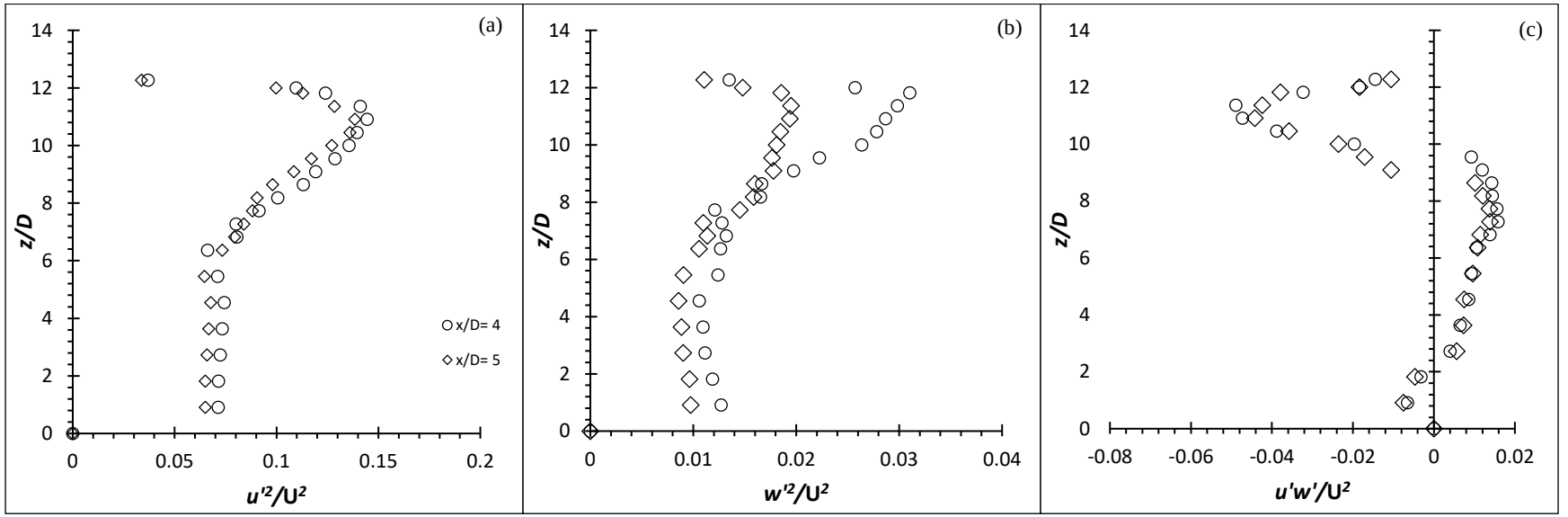

Figure 6.31: Reynolds stress profiles for cylinder of *AR* = 12 at Re = 8000: (a) $\frac{\overline{u'^2}}{U^2}$ (b) $\frac{\overline{w'^2}}{U^2}$ (c) $\frac{\overline{u'w'}}{U^2}$

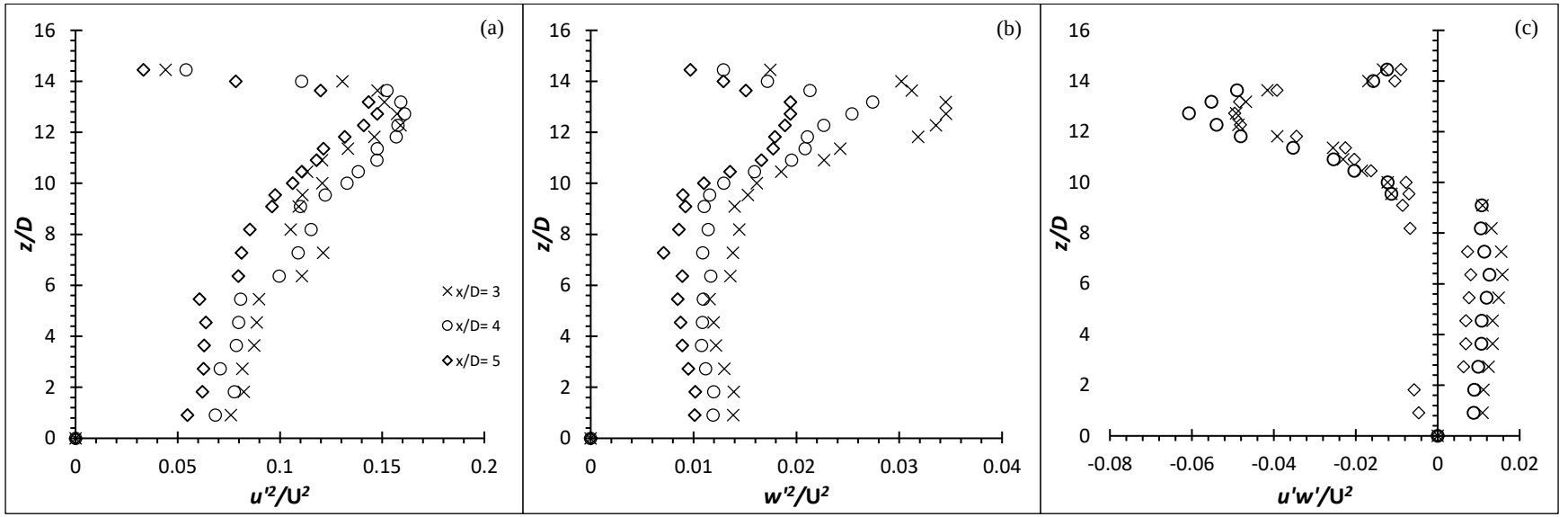

Figure 6.32: Reynolds stress profiles for cylinder of *AR* = 14 at Re = 4000: (a) $\frac{\overline{u'^2}}{U^2}$ (b) $\frac{\overline{w'^2}}{U^2}$ (c) $\frac{\overline{u'w'}}{U^2}$

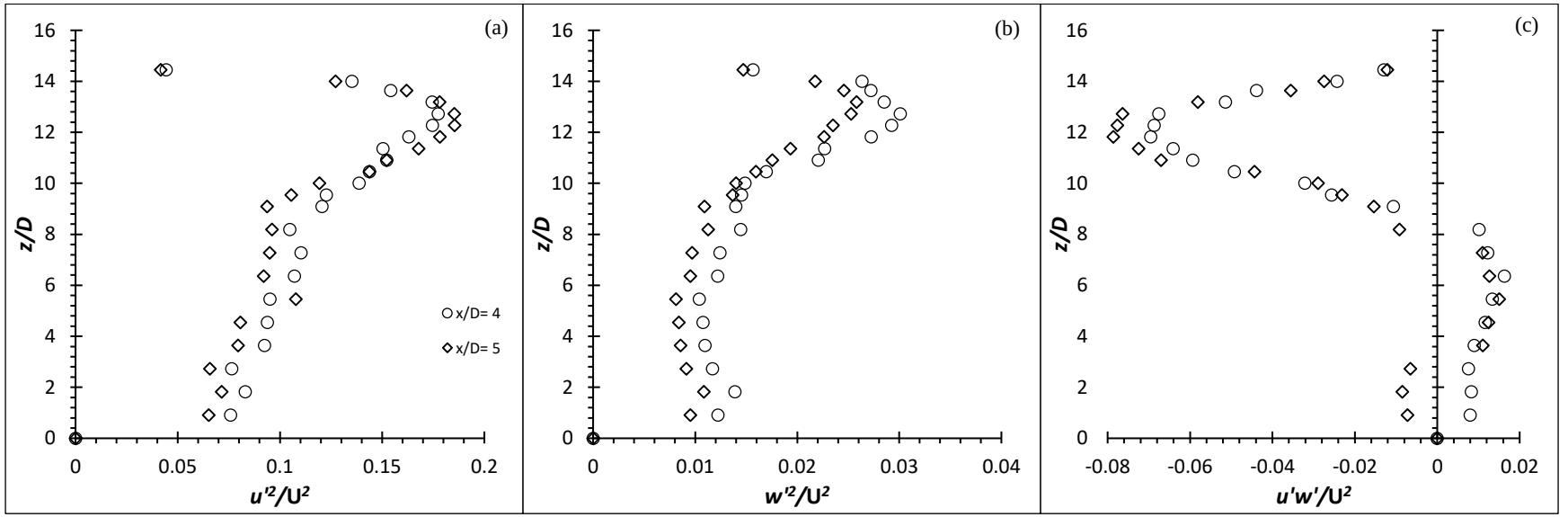

Figure 6.33: Reynolds stress profiles for cylinder of *AR* = 14 at Re = 6000: (a) $\frac{\overline{u'^2}}{U^2}$ (b) $\frac{\overline{w'^2}}{U^2}$ (c) $\frac{\overline{u'w'}}{U^2}$

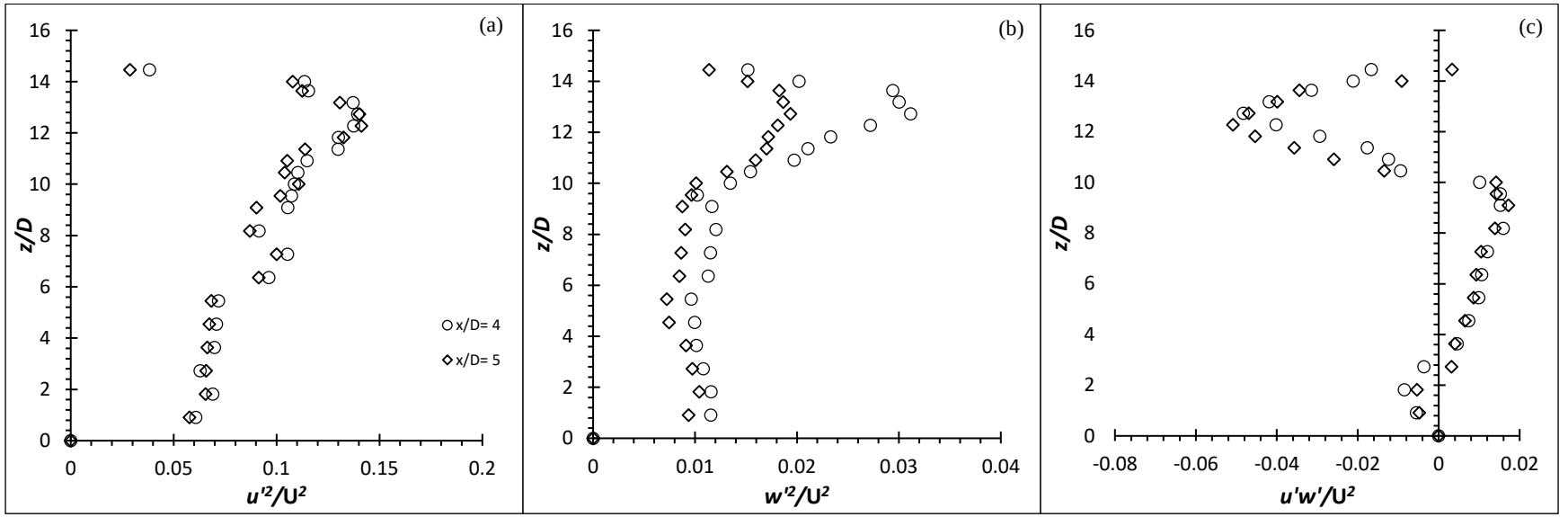

Figure 6.34: Reynolds stress profiles for cylinder of *AR* = 14 at Re = 8000: (a) $\frac{\overline{u'^2}}{U^2}$ (b) $\frac{\overline{w'^2}}{U^2}$ (c) $\frac{\overline{u'w'}}{U^2}$

6.5.2. Reynolds averaged statistics of metal group flexible cylinders

The Reynolds stresses, $\frac{\overline{u'^2}}{U^2}$, $\frac{\overline{w'^2}}{U^2}$and $\frac{\overline{u'w'}}{U^2}$ along the span of the aluminium and carbon steel cylinder of *AR* = 50 and 54 at Re = 2500 at the wake centreline (*y*/*D* = 0) are presented in Figure 6.35 to Figure 6.38.

The local peak Reynolds shear stress of the aluminium cylinder of *AR* = 50 and 54 near the free end shows $\frac{\overline{u'w'}}{U^2}_{max} \approx 0.048$ and 0.051 respectively; an approximate 128 % and 131 % increment for *AR* = 50 and 54 over the carbon steel flexible cylinder which behave the same as rigid cylinder. Their increment over the rigid cylinder of *AR* = 10 at Re = 4000 is approximately 14 % and 26 % for *AR* = 50 and 54, which shows a great deal of increment considering it is operating at Re = 2500. Apart from that, the region of the peak $\frac{\overline{u'w'}}{U^2}$ of the aluminium cylinder is bigger than that of the carbon steel cylinder where it only concentrates at the free end to *z*/*D* ≈ *AR* - 10 as opposed to *z*/*D* ≈ *AR* - 20 for aluminium cylinder. The enlargement in the region can also be seen from the (*u*'/U) and ***P*** graphs.

The local peak $\frac{\overline{u'w'}}{U^2}$ for the carbon steel cylinder of *AR* = 50 and 54 however, suffer from any increment as they behaved exactly like the rigid cylinder throughout the experiments. The local peak $\frac{\overline{u'w'}}{U^2}$ of *AR* = 50 and 54 are circa 0.021 and 0.022 respectively, approximately 47 % lower than the rigid cylinder of *AR* = 10 at Re = 4000.

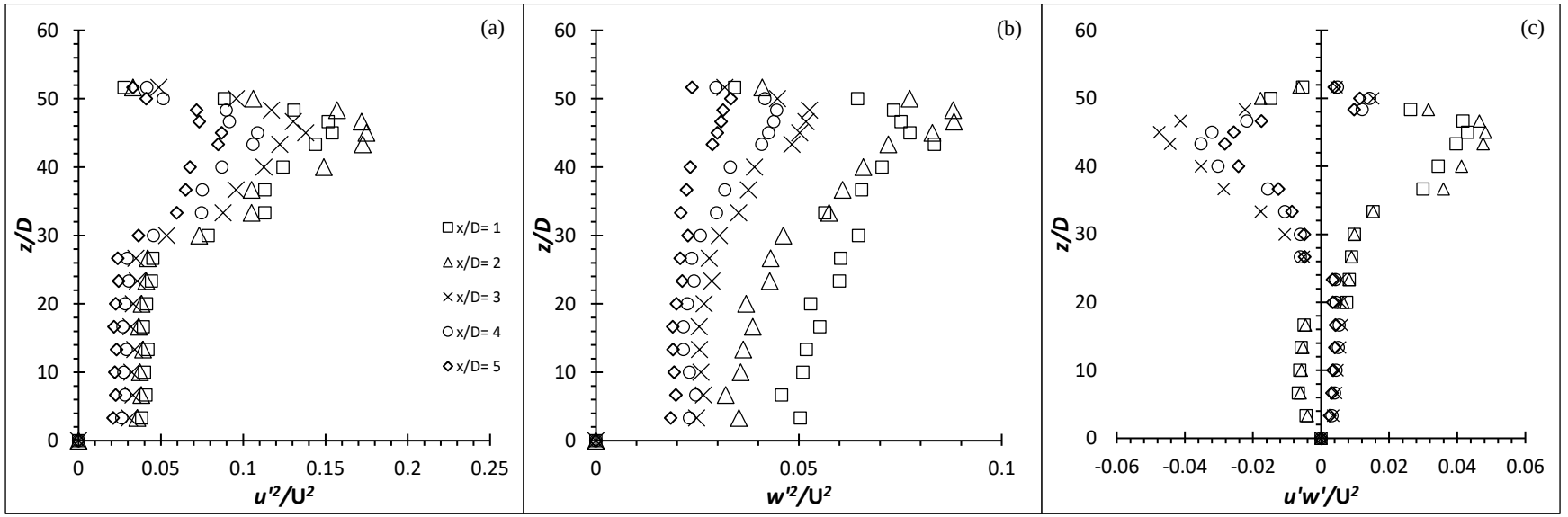

Figure 6.35: Reynolds stress profiles for Aluminium flexible cylinder of *AR* = 50 at Re = 2500: (a) $\frac{\overline{u'^2}}{U^2}$ (b) $\frac{\overline{w'^2}}{U^2}$ (c) $\frac{\overline{u'w'}}{U^2}$

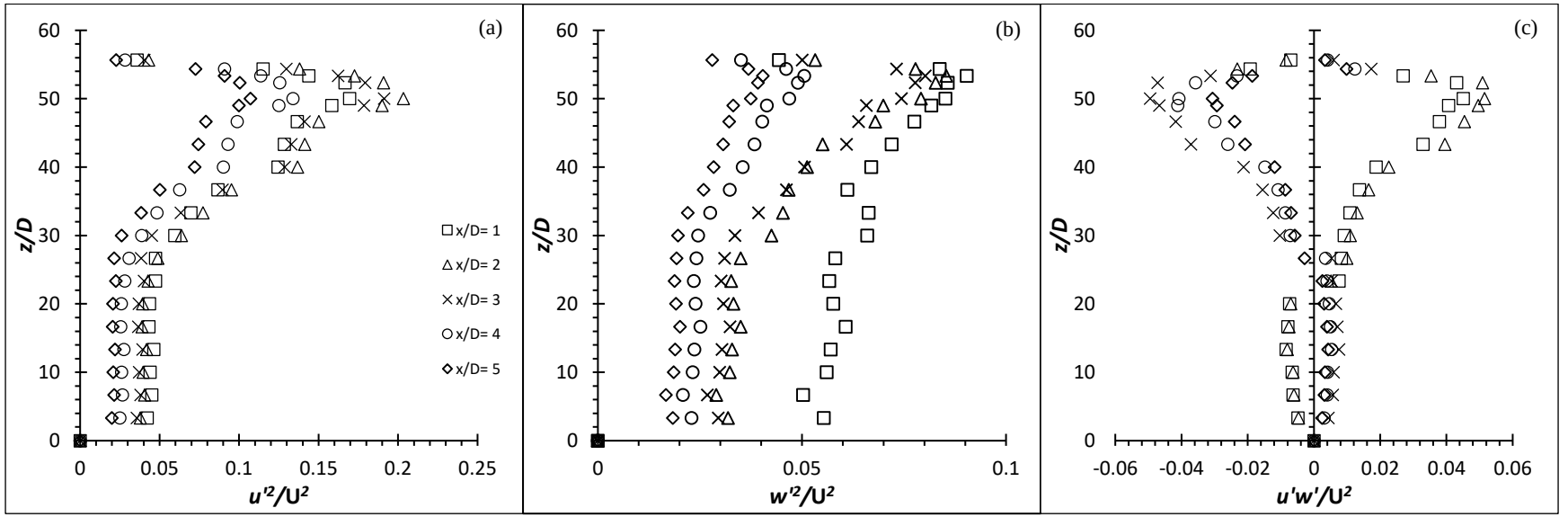

Figure 6.36: Reynolds stress profiles for Aluminium flexible cylinder of *AR* = 54 at Re = 2500: (a) $\frac{\overline{u'^2}}{U^2}$ (b) $\frac{\overline{w'^2}}{U^2}$ (c) $\frac{\overline{u'w'}}{U^2}$

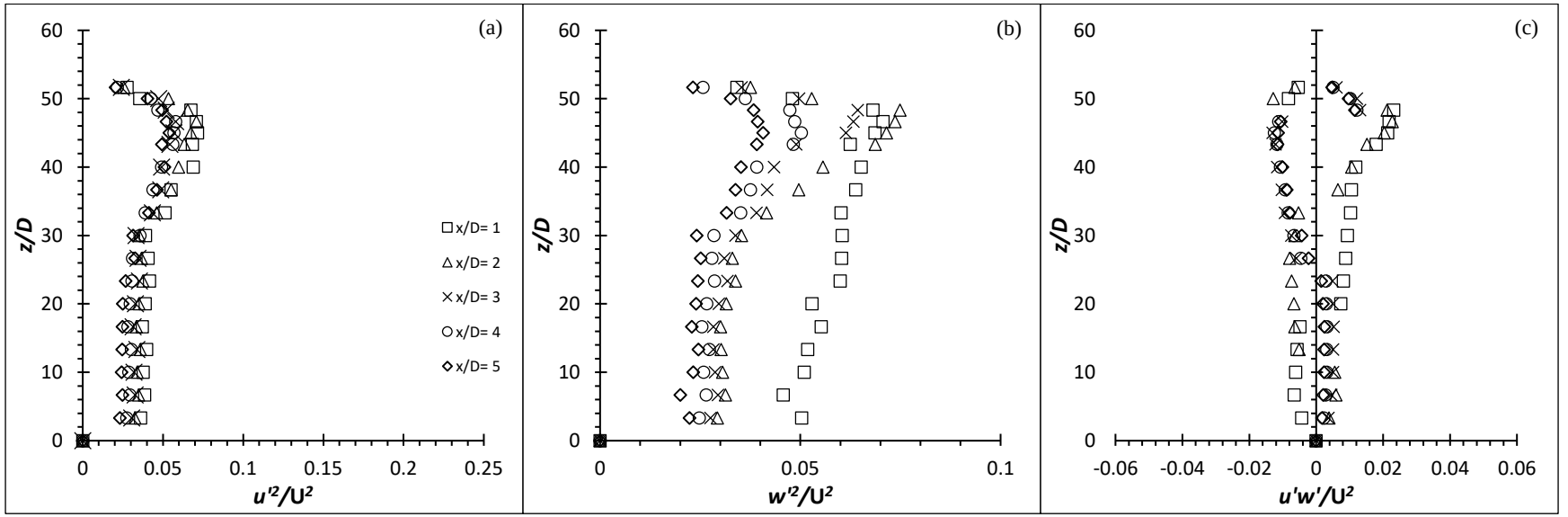

Figure 6.37: Reynolds stress profiles for Carbon Steel flexible cylinder of *AR* = 50 at Re = 2500: (a) $\frac{\overline{u'^2}}{U^2}$ (b) $\frac{\overline{w'^2}}{U^2}$ (c) $\frac{\overline{u'w'}}{U^2}$

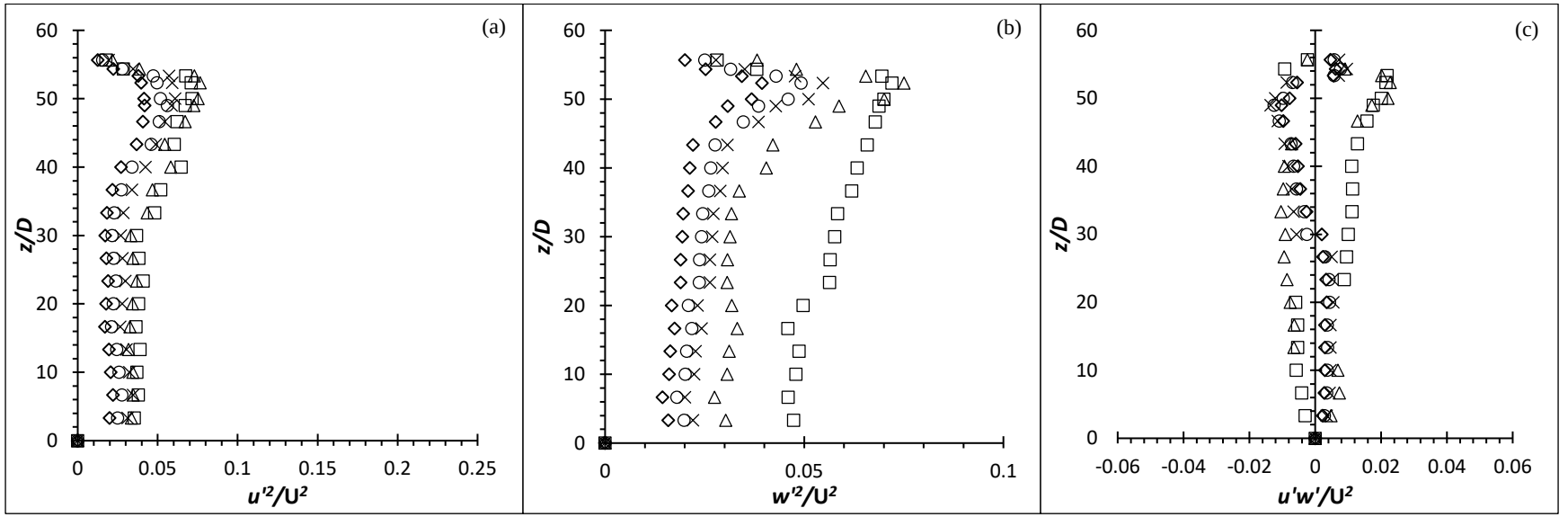

Figure 6.38: Reynolds stress profiles for Carbon Steel flexible cylinder of *AR* = 54 at Re = 2500: (a) $\frac{\overline{u'^2}}{U^2}$ (b) $\frac{\overline{w'^2}}{U^2}$ (c) $\frac{\overline{u'w'}}{U^2}$

6.5.3. Roles of oscillation of the flexible cylinder on the turbulence enhancement

The results have clearly shown that the turbulence production of the flexible cylinder is greater than the rigid cylinder. The turbulence intensity, production term from the Turbulence Kinetic Energy budget equations and the Reynolds stresses have revealed that the turbulence enhancement depends on the structural dynamics or the motion of the oscillating cylinder rather than the *AR* or Re itself. As a means to understand how the motion affects the turbulence enhancement, this sub-chapter aims to link the normalized amplitude response graphs, (y/D) to the flow dynamics of the vibrating cylinder. The (y/D) graphs are presented in Appendix D.

With reference to the ***P*** term of the EVA cylinder of AR = 12 and 14, the increment gained by the cylinder at Re = 8000 is the least. A look at the (y/D) of AR = 12 and 14 at Re = 8000 show that the cross-flow oscillations/motions are disorganized. Furthermore, both exist an abrupt change of amplitude and vortex shedding which latch on to a certain cycle. The abruptness of the cross-flow oscillations suggests that there could be a possibility of mode-change between two or more modes of vortex shedding. From the Literature Review Chapter, it has been established by William and Roshko (1988) regarding the vortex pattern in response to the oscillating motion of the vibrating cylinder. Apart from that, Mittal and Kumar (2001) also confirmed the existence of mode-change of vortex shedding in relation to the cylinder's motion mentioned above. They discovered the large amplitude of cross-flow oscillations correspond to anti-symmetric shedding. Despite that, no associated turbulence characteristics have been reported. Thus, the results generated in these experiments also serve to provide insights into the turbulence characteristics by the different oscillating motion of the flexible cylinders. Besides the above-mentioned features, it is also observed that the oscillations of AR = 16 at Re = 8000 are off-axis from the (y/D) graph. The same phenomenon was noticed by Behr (1992) and Mittal and Kumar (2001) in their results at high Re which the wake is bias towards a particular side, away from the centre line. This is also evident by the fact that the cylinder is oscillating in favour of one side. It is suggested that the disorganized cross-flow oscillations which happen at Re = 8000 is due to the relatively low structural stiffness against the relatively strong fluid force (U = 0.65 m/s); thus the flow becomes more complex.

Next, through the examination of *AR* = 12, 14 and 16 at Re = 6000, which coincidentally have the highest turbulence enhancement amongst each *AR* respectively, one can notice that the cross-flow oscillations are fairly organized. In other words, the oscillations have a fairly consistent frequency and amplitude.

The (*y*/*D*) of *AR* = 12, 14 and 16 at Re = 4000 show fairly organized cross-flow oscillations as well except their oscillating amplitude is lower than their respective *AR* operating at higher Re. The frequency of *AR* = 12 and 14 is close to regular and is in a more temporally periodic state. *AR* = 16 shows an occasion of higher amplitude in a certain cycle which could be due to the different mode-change. It is believed that the cross-flow oscillations/motions of *AR* = 12 and 14 behave in this manner because its structural stiffness is relatively high in comparison to the relatively weak fluid force (U = 0.33 m/s) and hence the cross-flow oscillations are more predictable but lower amplitude. Therefore, the flow field is quite similar to that of a rigid/stationary cylinder (Mittal & Kumar, 2001). Nevertheless, despite the similarity, the vibration of cylinder has proven to enhance the turbulence production.

Through the analysis above, it can be concluded that the vibration/oscillation/motion of the cylinder can alters the fluid flow significantly. The oscillation of the cylinder very much depends on the structural stiffness of the cylinder and the Re or fluid force more specifically. At a relatively high structural stiffness against relatively weak fluid force, the oscillations are fairly organized but the amplitudes are small. Turbulence enhancement is noticeable at this stage though not as significant. On the contrary, in the opposite condition, the flow becomes more complex and the cylinder undergoes fairly large amplitude but disorganized oscillation. Turbulence enhancement is also noticeable but at a low efficiency. The (*y*/*D*) graphs suggest the possibility of mode-change of vortex shedding. Mittal & Kumar (2001) observed that under chaotic flow condition, a large number of small vortices are seen shed alongside the large vortex and the flow field is very different from the rigid cylinder. It is at a suitable range of the structural stiffness and the fluid force only will the oscillations become fairly organized and at a high amplitude. The turbulence enhancement associated to this oscillation is significant.

Therefore, the results suggest that an organized oscillation with consistently high amplitude and frequency is important in enhancing the turbulence production. The (*y*/*D*) of the aluminium cylinder further substantiate the postulation.

As a result, a consistent amplitude and frequency are very important in determining the turbulence production. Both the parameters are further analysed and presented as a single unit – velocity. The frequency and amplitude is multiplied by differentiating the (*y*/*D*) graph. Since it represents the velocity of the oscillation by the flexible cylinder, it is thereby called structural velocity, $U_{clinder\ (RMS)}/U$ in this context. The structural velocity graphs are all normalized by the freestream velocity so that the actual structural velocity by the cylinder against the freestream velocity is plain to see. The computed results can be found in Appendix C6 to C10.

Table 6.2 to Table 6.4 show the magnitude of the local peak Reynolds shear stress to the RMS structural velocity of its respective flexible cylinder. The flexible cylinder of *AR* = 10 is not included in this Table because the vibrating motion of the cylinder is too minute to be measured accurately. The different *AR* of cylinders are put into comparison with the same Re. This is done so because a higher Re (higher fluid force) will inevitably cause a higher $U_{clinder\ (RMS)}/U$ for the cylinder of the same *AR* due to the higher fluid force.

Indeed, it shows that the $\frac{\overline{u'w'}}{U^2}_{max}$ corresponds to the highest $U_{clinder\ (RMS)}/U$ under the same Re. However, it can be observed that the $U_{clinder\ (RMS)}/U$ at Re = 8000 is lower compared to the $U_{clinder\ (RMS)}/U$ of the same *AR* under lower Re. This is because the structural stiffness is too low for the fluid force. It causes the cylinder to oscillate at a disorganized motion. The frequent lower frequency and amplitude at certain cycles contribute to the lower $U_{clinder\ (RMS)}/U$.

Table 6.2: The normalized Reynolds shear stress associated to the RMS of the structural velocity of the flexible cylinder for Re = 4000

AR	Re	Reynolds Shear Stress, $\frac{\overline{u'w'}}{U^2}_{max}$	RMS of Structural Velocity, $U_{cylinder\ (RMS)}/U$
12	4000	-0.0489	± 0.1572
14	4000	-0.0607	± 0.4396
16	4000	-0.0901	± 0.5905

Table 6.3: The normalized Reynolds shear stress associated to the RMS of the structural velocity of the flexible cylinder for Re = 6000

AR	Re	Reynolds Shear Stress, $\frac{\overline{u'w'}}{U^2}_{max}$	RMS of Structural Velocity, $U_{cylinder\ (RMS)}$/U
12	6000	-0.0564	± 0.2010
14	6000	-0.0785	± 0.3812
16	6000	-0.1132	± 1.1750

Table 6.4: The normalized Reynolds shear stress associated to the RMS of the structural velocity of the flexible cylinder for Re = 8000

AR	Re	Reynolds Shear Stress, $\frac{\overline{u'w'}}{U^2}_{max}$	RMS of Structural Velocity, $U_{cylinder\ (RMS)}$/U
12	8000	-0.0482	± 0.1698
14	8000	-0.0508	± 0.2221
16	8000	-0.0710	± 0.6291

Table 6.5 shows the magnitude of the local peak Reynolds shear stress to the RMS structural velocity of the flexible aluminium cylinder. It is clear to see that the $\frac{\overline{u'w'}}{U^2}_{max}$ of *AR* = 54 is higher than *AR* = 50 because the $U_{clinder\ (RMS)}$/U of *AR* = 54 is higher than that of *AR* = 50. Furthermore, the efficiency of the turbulence enhancement is also at a higher range, as is EVA cylinders at Re = 6000 due to the relatively organized cross-flow oscillations. In contrast to that, the $\frac{\overline{u'w'}}{U^2}_{max}$ generated by the EVA cylinders at Re = 8000 is at a disappointing range.

Table 6.5: The normalized Reynolds shear stress associated to the RMS of the structural velocity of the flexible aluminium cylinder for Re = 2500

AR	Re	Reynolds Shear Stress, $\frac{\overline{u'w'}}{U^2}_{max}$	RMS of Structural Velocity, $U_{cylinder\ (RMS)}$/U
50	2500	0.0483	± 0.2201
54	2500	0.0515	± 0.2966

Since the vortex pattern depends heavily on the oscillation, it is suspected that the energy feeding process to the vortex must have been altered – it no longer follows the normal condition (classic Kármán vortex) where the vortex only sheds off when it has

received sufficient energy as described in Chapter 2.2. The mode-change competition by the flexible cylinder could have interrupted the normal vortex formation for better or worse. Based on the performance of the turbulence enhancement by cylinders at Re = 8000, it can be confirmed that the alteration to the normal vortex formation at this Re is less than ideal as the improvement in $\frac{\overline{u'w'}}{U^2}_{max}$ is quite low. It is recommended that the relationship between the motion of the cylinder and the vortex shedding mode to be further studied or refined to further explore the effects of shedding mode on the vortex strength. Fortunately, regardless of the performance of the turbulence enhancement, the adoption of flexible cylinder still proves to have a higher turbulence production than the rigid cylinder.

6.6. Summary of Chapter

The results in this chapter has further demonstrated that the flexible cylinder is capable of generating a greater turbulence through the examination of turbulence intensity, ***P*** term and Reynolds stress. Since it was mentioned in the last chapter that the increment of turbulence production by the flexible cylinder is speculated to be oscillation, this chapter investigates the validity of the speculation through manipulating the structural stiffness of the flexible cylinder by employing different materials. All the flexible cylinders that oscillate show increment in turbulence production but at a different percentage. The cylinders studied in this chapter ranged from the least structural stiffness (EVA), moderate (aluminium) to the highest structural stiffness (carbon steel). Through studying the normalized amplitude responses graph of the flexible cylinder, it is identified that the oscillating motion does indeed contribute to increment. A further investigation into the graph, it is found that the factor which governs the increment is the structural velocity instead of just oscillating motion alone. This chapter marks the end of discussion on the improvement of turbulence characteristics achieved by the flexible cylinder.

CHAPTER 7

CONCLUSIONS AND RECOMMENDATIONS

This chapter gives the conclusions of the key findings on the wake region modification by the flexible cylinder and the turbulence characteristics improved by the flexible cylinder over the rigid cylinder. This chapter also discusses on the recommendations for future work in this research area.

7.1. Conclusions

The streamwise, *u* and wall-normal, *w* components flow behind the rigid and flexible finite cantilevers were investigated experimentally using UVP at Re = 2500, 4000, 6000 and 8000 with the goal to identify the turbulence characteristics in the flow field caused by the flexible cantilevers. Each cylinder was mounted normal to a ground plane and was partially immersed in a turbulent boundary layer. The aspect ratio of the rigid cylinder investigated was AR = 10 and 16. On the other hand, the flexible EVA cylinder and flexible metal based cylinder was AR = 10, 12, 14 and 16 and AR = 50 and 54 respectively. The velocity profiles at 5D behind the cylinders were studied to provide information on the wake region while turbulence characteristics such as turbulence intensity, production term and Reynolds stresses were studied to quantify the turbulence level in the wake. The main results can be summarized as follow:

The Wake Region Behind a Flexible Cylinder

The wake region always happens behind an object when flow past through it. A bluff body object usually has a bigger wake region compared to an object that is streamline. The flow velocity within the wake region greatly reduce (otherwise known as velocity defect) and it is where the turbulence activities occur. A greater wake region translates to an increase region of where turbulence activities take place.

Wake Region

In general, it is seen that the wake region behind the flexible cylinder (all of EVA cylinder excluding the aluminium and carbon steel flexible cylinder) is greater than the rigid cylinder. It is important to note that both the rigid and flexible cylinders are put into the same exact flow condition. The maximum wake height increment of the flexible cylinder is 11.10% over the rigid cylinder. An increase in the wake region indicates that the effective region of the turbulence activities is increased; thus, leading to an improvement of the turbulence generation. This indicates that the flexible cylinder can indeed improve in the turbulence generation through expanding the effective turbulent region.

The metal based flexible cylinder namely aluminium and carbon steel cylinder did not experience the similar increment found in the EVA cylinder; instead, it's wake region is approximately the same as the rigid cylinder. Through the analysis of the structural behaviour, it is found that the cause of the increment in wake region is due to the diminishing of the downwash that is presented in all cantilever cylinder (as discussed in Literature Review). The reason of the disappearance is because the EVA flexible cylinder is deflected to the *x*-direction due to the fluid force. As the metal based vibrating cylinders have a relatively higher stiffness property, it did not succumb to the bending; hence no deflection and thereby, the wake region remain the same as rigid cylinder. In conclusion, a greater deflection can greatly weaken the influence of downwash.

Turbulence Characteristics Behind a Flexible Cylinder

The turbulence intensity (u'/U) is investigated to examine the turbulence generated in the flow. Turbulence intensity describes how vigorously the fluctuating component deviates from the mean flow. Besides, the ***P*** term from the Turbulent Kinetic Budget energy equations is calculated to determine the energy level transferred from the mean flow to turbulent flow. The Reynolds stresses is also investigated. As Bernard *et al.* (1993) put it – the Reynolds stresses production is inseparable from the dynamics of organized coherent vortical structures. A higher Reynolds stress indicates a better transport of momentum; thereby improving the mixing of fluid in the flow.

Turbulence intensity

The turbulence intensity produced by the all the EVA and aluminium flexible cylinder experienced an increment over the rigid cylinder. The rigid cylinder of *AR* = 10 at Re = 4000 has produced a localized (u'_{max}/U) ≈ 26 %. The turbulence intensity produced by another rigid cylinder at different *AR* and Re do not deviate much from 26 %. In contrast to that, the increment of the localized (u'_{max}/U) produced by the flexible cylinder ranged from 36 % to 99 %. The carbon steel flexible cylinder however, did not experience any gain in value of the turbulence intensity as they behaved exactly like a rigid cylinder.

Based on the results, it is concluded that the cause of the augmented turbulence intensity produced by the flexible cylinder is due to the oscillation of the flexible cylinder. Three oscillating parameters namely oscillating amplitude, oscillating frequency and oscillating motion are identified to have altered the turbulence intensity.

Production term

Based on the previous simple analysis through the turbulence intensity, it indicates that the turbulence intensity does indeed increase when the flexible cylinder is employed. This suggest that more energy should be transferred to the fluctuating component. The results show that the ***P*** term generated by the flexible cylinder is higher than that of rigid cylinder. The maximum localized ***P*** term increased 203% against its rigid counterpart of *AR* = 16 of the same Re.

Reynolds stresses

Similarly, the Reynolds shear stress have produced a similar pattern of results. The Reynolds shear stress is seen gained massively through the employment of flexible cylinder. However, the increment of the Reynolds shear stress does not strictly follow the *AR* or Re pattern. This suggest that the turbulence enhancement is neither influenced by the geometry factor (*AR*) nor the Re. Instead, it is closely linked to the structural dynamics of the cylinder that is governed by the *AR* and Re.

Through the analysis of Reynolds stress and the (*y*/*D*) graph, it can be seen that the oscillating motion that is organized produced the highest increment of turbulence enhancement while the opposite produced the lowest turbulence enhancement. This is due

to the different structural stiffness against the fluid flow, which can complicate the flow field through different mode-change of vortex shedding. A further analysis of (y/D) graph provides insight that the turbulence enhancement is greater with a greater structural velocity within the same Re.

The results have concluded that the flexible cylinder is a better turbulence generator than the rigid cylinder, thus improving the mixing of fluid through augmented turbulent flow.

7.2. Recommendations for Future Work

While much of this research work has provided useful insights of the turbulence characteristics of flow around the fully three-dimensional flexible cantilever, much comprehensive work is still needed. Oftentimes during research, the outcome of one test will give birth to an idea of future testing. Likewise, the tests conducted during this research work have spurred ideas for future testing.

Experiments can always be improved by using better equipment or better experimental conditions. Due to the limitations of the available facilities and also the complex nature of the flow around the vibrating cantilever, some inputs of recommendations could greatly improve the quality of work in future. Though UVP is capable in measuring three velocity components, the experiments conducted in this research work only acquired two velocity components due to the number limitation of UVP probe. In addition, the combination of two or three probes in measuring three velocity components could potentially increase the precision error as no indicator or laser guideline to ensure the ultrasound signals from the various probes are perfectly intersected. Therefore, there is a need for further study with instruments such as PIV that has a very fine spatial resolution and high degree of accuracy. Parameters such as Reynolds stress tensor, turbulence production and turbulent kinetic energy distributions can then be determined to picture the flow and turbulence characteristics at a very fine spatial resolution. Each individual vortex strength can be calculated to pinpoint the evolution of energy dissipation. Besides, pressure taps can be installed along the cylinder

for the monitoring of pressure distribution around the cylinder to further confirm the speculated relationship of downwash to pressure drop but under the condition that it will not alter the structural stiffness of the flexible cylinder. In addition, CFD simulation should be employed to understand the turbulent modulation better.

It is seen how the flexible cylinder can alter the wake height. However, this study only studies the wake structure in *z*-position perspective. Future work on the wake structure of the flexible cylinder from *x* and *y* perspective should also be studied to better understand the turbulent modulation associated with it.

Although it is true that the turbulence enhancement increases with the structural velocity within a constant Re, the relationship does not extend to the different Re. This is due to the complicated relationship between the structural stiffness and the fluid force which can induce different vortex shedding mode during the VIV process. This will inevitably affect the turbulence enhancement as seen in Chapter 6.4.3. It also signifies that the turbulence enhancement can be optimized if the relationship between the motion of the cylinder and the vortex shedding mode is clear and the effects of shedding mode on the vortex strength is also known.

The current study is purely based on one protruding surface. The multiple numbers and position configurations are not known. In order for this idea to be incorporated in the industry, a system with multiple protruding surface should be considered. A future work that includes the turbulence generation of multiple flexible protruding surface, the interaction between the flexible protruding surface and the optimization of the protruding surface arranged in different positions should be studied. Besides, a guideline which suggest the appropriate structural stiffness in relation to the flow speed should be recorded so that an optimum oscillating motion can be attained.

This work shows promising turbulence enhancement where the use of flexible cylinder could potentially bring enhanced mixing of fluids or generating better turbulence for energy harvesting. It can be installed in the passageway where food industry needed different fluid to mix homogeneously.

REFERENCES

Adaramola, M. S. (2008). The wake of an exhaust stack in a crossflow. Ph.D. Thseis, Department of Mechanical Engineering, University of Saskatchewan, Saskatoon, Canada. Retrieved from https://ecommons.usask.ca/bitstream/handle/10388/etd-04212008-124717/MAdaramola.pdf

Afgan, I., Moulinec, C., & Laurence, D. (2006). Large eddy simulation of flow over a vertically mounted finite cylinder on a flat plate. *In Conference on Modelling Fluid Flow (CMFF 2006). The 13th International Conference on Fluid Flow Technologies, Budapest, Hungary*.

Afgan, I., Moulinec, C., Prosser, R., & Laurence, D. (2007). Large eddy simulation of turbulent flow for wall mounted cantilever cylinders of aspect ratio 6 and 10. *International Journal of Heat and Fluid Flow*, *28*(4), 561-574.

Agui, J. H., & Andreopoulos, J. (1992). Experimental Investigation of a Three-Dimensional Boundary Layer Flow in the Vicinity of an Upright Wall Mounted Cylinder (Data Bank Contribution). *Journal of fluids engineering*, 114(4), 566-576.

Anderson Jr, J. D. (1985). Fundamentals of aerodynamics. Tata McGraw-Hill Education.

Apelt, C., & Fox, T. (1992). Fluctuating Loads On Cantilevered Cylinders In Uniform Flow.

Aris, M. S., Owen, I., & Sutcliffe, C. J. (2007). The application of shape memory alloy as longitudinal vortex generators for enhanced convective heat transfer. *In Proceedings of the 10th UK National Heat Transfer Conference*.

Aris, M. S., Owen, I., & Sutcliffe, C. J. (2011). The development of active vortex generators from shape memory alloys for the convective cooling of heated surfaces. *International Journal of Heat and Mass Transfer*, *54*(15), 3566-3574.

Assessment of the Vortex-Induced-Vibration Prevention Efficiency of a Wave-Energy-Device (Accessed 12 April 2017)
https://sites.google.com/site/wecvivstudy/

Aubin, J., Kresta, S. M., Bertrand, J., Xuereb, C., & Fletcher, D. F. (2006). Alternate operating methods for improving the performance of continuous stirred tank reactors. *Chemical Engineering Research and Design*, *84*(7), 569-582.

Bai, Y., & Bai, Q. (Eds.). (2005). Subsea Pipelines and Risers: *Vortex-induced Vibrations (VIV) and Fatigue*. Elsevier.

Bailey, S. C. C., Kopp, G. A., & Martinuzzi, R. J. (2002). Vortex shedding from a square cylinder near a wall. *Journal of Turbulence*, 3(3), 1-18.

Bearman, P. W., & Obasaju, E. D. (1982). An experimental study of pressure fluctuations on fixed and oscillating square-section cylinders. *Journal of Fluid Mechanics, 119*, 297-321.

Bearman, P. W. (1984). Vortex shedding from oscillating bluff bodies. *Annual review of fluid mechanics, 16*(1), 195-222.

Bernard, P. S., Thomas, J. M., & Handler, R. A. (1993). Vortex dynamics and the production of Reynolds stress. *Journal of Fluid Mechanics, 253*, 385-419.

Bernitsas, M. M., Raghavan, K., Ben-Simon, Y., & Garcia, E. M. (2008). VIVACE (Vortex Induced Vibration Aquatic Clean Energy): A new concept in generation of clean and renewable energy from fluid flow. *Journal of Offshore Mechanics and Arctic Engineering*, 130(4), 041101.

Blackburn, H., & Henderson, R. (1996). Lock-in behaviour in simulated vortex-induced vibration. *Experimental Thermal and Fluid Science*, *12*(2), 184-189.

Budair, M., Ayoub, A., & Karamcheti, K. (1991). Frequency measurements in a finite cylinder wake at a subcritical Reynolds number. *AIAA journal*, *29*(12), 2163-2168.

Chan, H.B., Yong, T.H., Kumar, P., Wee, S.K., & Dol. S.S. (2016). The numerical investigation on the effects of aspect ratio and cross-sectional shape on the wake structure behind a cantilever. *ARPN Journal of Engineering and Applied Sciences*. *11*(16), 9926-9932.

Campbell, M. (2002). *U.S. Patent No. 6,427,948*. Washington, DC: U.S. Patent and Trademark Office.

Cantwell, B., & Coles, D. (1983). An experimental study of entrainment and transport in the turbulent near wake of a circular cylinder. *Journal of fluid mechanics*, *136*, 321-374.

Carletti, M. J., Rogers, C. B., & Parekh, D. E. (1996). Parametric study of jet mixing enhancement by vortex generators, tabs, and deflector plates. *ASME-PUBLICATIONS-FED*, 237, 303-312.

Chapter 9. Drag and lift. (Accessed 23 November 2015) http://www.mech.pk.edu.pl/~m52/pdf/fm/R_09.pdf

Chen, S. S. (1987). Flow-induced vibration of circular cylindrical structures.

Coleman, H.W., Steele, W.G., 1999. *Experimentation and Uncertainty Analysis for Engineers*. 2nd Edition, Wiley, New York.

Dahl, J. M., Hover, F. S., & Triantafyllou, M. S. (2006). Two-degree-of-freedom vortex-induced vibrations using a force assisted apparatus. *Journal of Fluids and Structures*, *22*(6), 807-818.

Dol, S. S., Kopp, G. A., & Martinuzzi, R. J. (2008). The suppression of periodic vortex shedding from a rotating circular cylinder. *Journal of Wind Engineering and Industrial Aerodynamics*, 96(6), 1164-1184.

Donnert, G. D., Kappler, M., & Rodi, W. (2007). Measurement of tracer concentration in the flow around finite-height cylinders. *Journal of Turbulence*, (8), N33.

Drescher, H. (1956). Messung der auf querangeströmte Zylinder ausgeübten zeitlich veränderten Drücke. Verlag Friedr. Vieweg & Sohn.

Etzold, F., & Fiedler, H. (1976). The near-wake structure of a cantilevered cylinder in a cross-flow. *Zeitschrift fur Flugwissenschaften*, 24, 77-82.

Faltinsen, O. (1993). *Sea loads on ships and offshore structures* (Vol. 1). Cambridge university press.Gabbai, R. D., & Benaroya, H. (2005). An overview of modeling and experiments of vortex-induced vibration of circular cylinders. *Journal of Sound and Vibration*, 282(3), 575-616.

Farivar, D. J. (1981). Turbulent uniform flow around cylinders of finite length. *AIAA journal*, *19*(3), 275-281.

Ford, D.N. (1994). Ferrybridge cooling towers. When technology fails: Significant technological disasters, accidents, and failures of the twentieth century. Gale Group.

Fox, T. A., & West, G. S. (1993). Fluid-induced loading of cantilevered circular cylinders in a low-turbulence uniform flow. Part 1: mean loading with aspect ratios in the range 4 to 30. *Journal of Fluids and Structures*, *7*(1), 1-14.

Fox, T. A., & West, G. S. (1993). Fluid-Induced loading of cantilevered circular cylinders in a Low-Turbulence uniform flow. part 2: Fluctuating loads on a cantilever of aspect ratio 30. *Journal of Fluids and Structures*, *7*(1), 15-28.

Fox, T. A., & Apelt, C. J. (1993). Fluid-induced loading of cantilevered circular cylinders in a low-turbulence uniform flow. Part 3: Fluctuating loads with aspect ratios 4 to 25. *Journal of fluids and structures*, *7*(4), 375-386.

Fröhlich, J., & Rodi, W. (2004). LES of the flow around a circular cylinder of finite height. *International journal of heat and fluid flow*, *25*(3), 537-548.

Fujarra, A. L. C., Pesce, C. P., Flemming, F., & Williamson, C. H. K. (2001). Vortex-induced vibration of a flexible cantilever. *Journal of Fluids and Structures, 15*(3), 651-658.

Govardhan, R., & Williamson, C. H. K. (2000). Modes of vortex formation and frequency response of a freely vibrating cylinder. *Journal of Fluid Mechanics, 420*, 85-130.

Govardhan, R., & Williamson, C. H. K. (2001). Mean and fluctuating velocity fields in the wake of a freely-vibrating cylinder. *Journal of Fluids and Structures, 15*(3), 489-501.

Graf W.H. and B. Yulistiyanto (1998): "Experiments on Flow around a cylinder; the velocity and vorticity fields", ", *J. Hydraulic Research*, Vol. 36, pp. 637-653.

Griffin, O. M. (1971). The unsteady wake of an oscillating cylinder at low Reynolds number. *Journal of Applied Mechanics*, *38*(4), 729-738.

Gupta, A., & Uniyal, M. (2012). Review of heat transfer augmentation through different passive intensifier methods. *IOSR Journal of Mechanical and Civil Engineering (IOSRJMCE) ISSN*, *2278-1684*

Haase, W., Braza, M., & Revell, A. (Eds.). (2009). *DESider–A European Effort on Hybrid RANS-LES Modelling: Results of the European-Union Funded Project, 2004-2007* (Vol. 103). Springer Science & Business Media.

Hain, R., Kähler, C. J., & Michaelis, D. (2008). Tomographic and time resolved PIV measurements on a finite cylinder mounted on a flat plate. *Experiments in fluids*, *45*(4), 715-724.

Heseltine, J. L. (2003). Flow around a circular cylinder with a free end (Master Thesis, University of Saskatchewan, Saskatchewan, Canada). Retrieved from https://ecommons.usask.ca/handle/10388/etd-07252011-090143

Hu, H., Saga, T., Kobayashi, T., & Taniguchi, N. (2002). Mixing process in a lobed jet flow. *AIAA journal*, *40*(7), 1339-1345.

Ihara, T., Kikura, H., & Takeda, Y. (2013). Ultrasonic velocity profiler for very low velocity field. *Flow Measurement and Instrumentation*, *34*, 127-133.

Inoue, Y., Yamashita, S., & Kondo, K. (1999). Experiments in an Initial Region of a Circular Free Jet. *Proc. 4th ISUD, Sapporo, Japan*.

Jauvtis, N., & Williamson, C. H. K. (2004). The effect of two degrees of freedom on vortex-induced vibration at low mass and damping. *Journal of Fluid Mechanics*, 509, 23-62.

Jeon, D., & Gharib, M. (2001). On circular cylinders undergoing two-degree-of-freedom forced motions. *Journal of Fluids and Structures*, *15*(3), 533-541.

Jeon, D., & Gharib, M. (2004). On the relationship between the vortex formation process and cylinder wake vortex patterns. *Journal of Fluid Mechanics*, *519*, 161-181.

Johnston, C.R., Clavelle, E.J., Wilson, D.J. & Peck, B.J. (1998). Investigation of the vorticity generated by flow around a finite cylinder. *In Proceedings of the 6th Conference of the CFD Society of Canada (CFD'98),* Quebec City, Canada, June 7-9, 1998.

Kang, Z., & Jia, L. (2013). An experiment study of a cylinder's two degree of freedom VIV trajectories. *Ocean Engineering*, *70*, 129-140.

Kantoush, S. A., De Cesare, G., Boillat, J. L., & Schleiss, A. J. (2008). Flow field investigation in a rectangular shallow reservoir using UVP, LSPIV and numerical modelling. *Flow measurement and Instrumentation*, *19*(3), 139-144.

Kawamura, T., Hiwada, M., Hibino, T., Mabuchi, I., & Kumada, M. (1984). Flow around a Finite Circular Cylinder on a Flat Plate: Cylinder height greater than turbulent boundary layer thickness. *Bulletin of JSME*, *27*(232), 2142-2151.

Keles, R. (2002). Active control of vortex shedding in the far wake of a cylinder. *In 15th ASCE Engineering Conference*, June (pp. 2-5).

Khalak, A., & Williamson, C. H. K. (1997). Fluid forces and dynamics of a hydroelastic structure with very low mass and damping. *Journal of Fluids and Structures*, *11*(8), 973-982.

Khalak, A., & Williamson, C. H. K. (1999). Motions, forces and mode transitions in vortex-induced vibrations at low mass-damping. *Journal of fluids and Structures*, *13*(7), 813-851.

King, R. (1974) Vortex-excited structural oscillations of a circular cylinder in flowing water. Ph.D. dissertation, Loughborough University of Technology, Loughborough, U.K.

King, R., & Johns, D. J. (1976). Wake interaction experiments with two flexible circular cylinders in flowing water. *Journal of Sound and Vibration*, 45(2), 259-283.

Kitagawa, T., Fujino, Y., Kimura, K., & Mizuno, Y. (2002). Wind pressures measurement on end-cell-induced vibration of a cantilevered circular cylinder. *Journal of Wind Engineering and Industrial Aerodynamics*, *90*(4), 395-405.

Klamo, J. T. (2007). Effects of damping and Reynolds number on vortex-induced vibrations. Doctoral dissertation, California Institute of Technology.

Knoblauch, H., Klasinc, R., Geisler, T., & Breitenstein, S. (2002). Ultrasonic velocity profile measurements in pipes and flumes in a hydraulic laboratory. *Third International Symponisum on Ultrasonic Doppler Methods for Fluid Mechanics and Fluid Engineering, EPFL*, 31-36.

Koughan, J. (1996). The collapse of the Tacoma Narrows Bridge, evaluation of competing theories of its demise, and the effects of the disaster of succeeding bridge designs. The University of Texas at Austin.

Lam, K. M., Liu, P., & Hu, J. C. (2010). Combined action of transverse oscillations and uniform cross-flow on vortex formation and pattern of a circular cylinder. *Journal of Fluids and Structures*, *26*(5), 703-721.

Leal, J. B., Fernandes, J. N., & Cardoso, A. H. (2010). Ultrasound velocity profile (UVP) measurements in shallow open-channel flows. IAHR.

Lee, J. H., & Bernitsas, M. M. (2011). High-damping, high-Reynolds VIV tests for energy harnessing using the VIVACE converter. Ocean Engineering, 38(16), 1697-1712.

Lee, L., & Wang, Y. (1987). Aerodynamics of a circular cylinder of finite length in cross flow. In *Forum on Turbulent Flows- 1987, Cincinnati, OH* (pp. 61-65).

Lin, J. C. (2002). Review of research on low-profile vortex generators to control boundary-layer separation. *Progress in Aerospace Sciences*, *38*(4), 389-420.

Liu, Y., So, R. M. C., & Cui, Z. X. (2005). A finite cantilevered cylinder in a cross-flow. *Journal of fluids and structures*, *20*(4), 589-609.

Lögdberg, O. (2006). *Vortex generators and turbulent boundary layer separation control*. KTH,.

Luo, S. C. (1993, January). Flow past a finite length circular cylinder. In *The Third International Offshore and Polar Engineering Conference*. International Society of Offshore and Polar Engineers.

Mittal, S., & Kumar, V. (2001). Flow-induced vibrations of a light circular cylinder at Reynolds numbers 10^3 to 10^4. *Journal of Sound and Vibration*,*245*(5), 923-946.

Mohan, N. D., Greenblatt, D., Nayeri, C. N., Paschereit, C. O., & Panchapakesan, N. R. (2015). Vortex-enhanced mixing through active and passive flow control methods. *Experiments in Fluids*, *56*(3), 1-16.

Morse, T. L., Govardhan, R. N., & Williamson, C. H. K. (2008). The effect of end conditions on the vortex-induced vibration of cylinders. *Journal of Fluids and Structures*, 24(8), 1227-1239.

Nakamura, T., Kaneko, S., Inada, F., Kato, M., Ishihara, K., Nishihara, T., & Langthjem, M. A. (Eds.). (2013). *Flow-induced vibrations: Classifications and lessons from practical experiences*. Butterworth-Heinemann.

Okamoto, S. (1991). Flow Past Circular-Cylinder Of Finite Length Placed On Ground Plane. *Transactions of the Japan Society for Aeronautical and Space Sciences*, *33*(102), 234-246.

Okamoto, S., & Sunabashiri, Y. (1992). Vortex shedding from a circular cylinder of finite length placed on a ground plane. *Journal of Fluids Engineering*,114(4), 512-521.

Ohkubo, T., Kashiwaguma, N., Yokoyama, K., Takeda, Y., & Ouchi, K. (2004) Vector Measurement of Environmental Flow Field by UVP.

Okamoto, T., & Yagita, M. (1973). The experimental investigation on the flow past a circular cylinder of finite length placed normal to the plane surface in a uniform stream. *Bulletin of JSME*, 16(95), 805-814.

Palau-Salvador, G., Stoesser, T., Fröhlich, J., Kappler, M., & Rodi, W. (2010). Large eddy simulations and experiments of flow around finite-height cylinders. *Flow, turbulence and combustion*, *84*(2), 239-275.

Park, C. W., & Lee, S. J. (2000). Free end effects on the near wake flow structure behind a finite circular cylinder. *Journal of Wind Engineering and Industrial Aerodynamics*, 88(2), 231-246.

Park, C. W., & Lee, S. J. (2002). Flow structure around a finite circular cylinder embedded in various atmospheric boundary layers. *Fluid Dynamics Research*,*30*(4), 197-215.

Park, C. W., & Lee, S. J. (2004). Effects of free-end corner shape on flow structure around a finite cylinder. *Journal of Fluids and Structures*, *19*(2), 141-158.

Paterson, R. W. (1984). Turbofan mixer nozzle flow field—A benchmark experimental study. *Journal of Engineering for Gas Turbines and Power*,*106*(3), 692-698.

Pattenden, R. J., Turnock, S. R., & Zhang, X. (2005). Measurements of the flow over a low-aspect-ratio cylinder mounted on a ground plane. *Experiments in Fluids*, 39(1), 10-21.

Pesce, C. P., & Fujarra, A. L. C. (2000). Vortex-induced vibrations and jump phenomenon: experiments with a clamped flexible cylinder in water. *International Journal of Offshore and Polar Engineering*, *10*(01).

Porteous, R., Moreau, D. J., Doolan, C. J., & Prime, Z. (2014). Wake Dynamics of Circular Finite Wall-mounted Cylinders in Different Boundary Layers.

Prastianto, R. W., Otsuka, K., & Ikeda, Y. (2009). Vortex-induced Vibration of a Flexible Free-hanging Circular Cantilever. *Journal of Engineering and Technological Sciences*, 41(2), 111-125.

Qiu, Y. J. (1992). A Study of Streamwise Vortex Enhanced Mixing in Lobed Mixer Devices.

Quackenbush, T., McKillip, R., & Whitehouse, G. (2010, June). Development and testing of deployable vortex generators using sma actuation. In*Proceedings of the 28th AIAA Applied Aeroacoustics Conference, Chicago, IL* (pp. 1-16).

Raghavan, K., & Bernitsas, M. M. (2011). Experimental investigation of Reynolds number effect on vortex induced vibration of rigid circular cylinder on elastic supports. *Ocean Engineering*, *38*(5), 719-731.

Roh, S., & Park, S. (2003). Vortical flow over the free end surface of a finite circular cylinder mounted on a flat plate. *Experiments in fluids*, 34(1), 63-67.

Rostamy, N., Sumner, D., Bergstrom, D. J., & Bugg, J. D. (2012). Local flow field of a surface-mounted finite circular cylinder. *Journal of Fluids and Structures*, 34, 105-122.

Rostamy, N. (2012) Fundamental studies of the wake structure for surface-mounted finite-height cylinders and prisms. (Ph.D. Thesis, University of Saskatchewan, Saskatchewan, Canada). Retrieved from https://ecommons.usask.ca/handle/10388/ETD-2012-09-644?show=full

Rödiger, T., Knauss, H., Gaisbauer, U., & Kraemer, E. (2007). Pressure and heat flux measurements on the surface of a low-aspect-ratio circular cylinder mounted on a ground plate. *In New Results in Numerical and Experimental Fluid Mechanics VI* (pp. 121-128). Springer Berlin Heidelberg.

Sakamoto, H., & Arie, M. (1983). Vortex shedding from a rectangular prism and a circular cylinder placed vertically in a turbulent boundary layer. *Journal of Fluid Mechanics, 126,* 147-165.

Singh, S. P., & Chatterjee, D. (2014). Impact of transverse shear on vortex induced vibrations of a circular cylinder at low Reynolds numbers. Computers & Fluids, 93, 61-73.

SNAJ. (1986). Directory of ship hydrodynamics research laboratories in Japan; 2nd edition. Japan Towing Tank Committee. The Society of Naval Architects of Japan.

So, R. M., Wang, X. Q., Xie, W. C., & Zhu, J. (2008). Free-stream turbulence effects on vortex-induced vibration and flow-induced force of an elastic cylinder. Journal of Fluids and Structures, 24(4), 481-495.

Song, K. W., & Wang, L. B. (2013). The effectiveness of secondary flow produced by vortex generators mounted on both surfaces of the fin to enhance heat transfer in a flat tube bank fin heat exchanger. *Journal of Heat Transfer, 135*(4), 041902.

Stansby, P. K. (1974). The effects of end plates on the base pressure coefficient of a circular cylinder. *Aeronautical Journal*, 78, 36.

Sumner, D. (2013). Flow above the free end of a surface-mounted finite-height circular cylinder: a review. *Journal of Fluids and Structures*, *43*, 41-63.

Sumner, D., Heseltine, J. L., & Dansereau, O. J. P. (2004). Wake structure of a finite circular cylinder of small aspect ratio. *Experiments in Fluids*, 37(5), 720-730.

Swan, C. (2011, March 16) Thermopedia. Shear Layer (Accessed April 8, 2016) http://www.thermopedia.com/content/1118/

Taniguchi, S., Sakamoto, H., & Arie, M. (1981). Flow around circular cylinders of finite height placed vertically in turbulent boundary layers. *Bulletin of JSME*, 24(187), 37-44.

Takeda, Y. (1995). Velocity profile measurement by ultrasonic Doppler method. *Experimental thermal and fluid science*, 10(4), 444-453.

Tanaka, S., & Murata, S. (1999). An Investigation of the Wake Structure and Aerodynamic Characteristics of a Finite Circular Cylinder. Time-Averaged Wake

Structures behind Circular Cylinders with Various Aspect Ratios.*JSME International Journal Series B, 42*(2), 178-187.

Turbulence Handbook for Experimental Fluid Mechanics Professionals. Skovlunde, Denmark: Dantec Dynamics. (Accessed 4 August 2016) http://www.it.cas.cz/~uruba/docs/Aero/Turbulence_Uruba_EN_42_9.pdf

Thulukkanam, K. (2013). *Heat exchanger design handbook*. CRC Press.

Vandiver, J. K., & Jong, J. Y. (1987). The relationship between in-line and cross-flow vortex-induced vibration of cylinders. *Journal of Fluids and Structures, 1*(4), 381-399.

Vickery, B. J. & Watkins, R. D. (1964) Flow-induced vibrations of cylindrical structures. *In Proceedings of the First Australian Conference on Hydraulics and Fluid Mechanics* (ed. R. Silvester), pp. 213-241, New York: Pergamon Press.

Vortex Bladeless. Wind Turbine Without Blade (Accessed October 30, 2015) http://www.vortexbladeless.com/

Waitz, I. A., Qiu, Y. J., Manning, T. A., Fung, A. K. S., Elliot, J. K., Kerwin, J. M., ... & Marble, F. E. (1997). Enhanced mixing with streamwise vorticity. *Progress in Aerospace Sciences, 33*(5), 323-351.

Warsop, C. (2004). *Active flow control using MEMS*. BAE SYSTEMS BRISTOL (UNITED KINGDOM) ADVANCED TECHNOLOGY CENTRE.

West, G. S., & Apelt, C. J. (1982). The effects of tunnel blockage and aspect ratio on the mean flow past a circular cylinder with Reynolds numbers between 10^4 and 10^5. *Journal of Fluid Mechanics, 114*, 361-377.

Williamson, C. H. (1996). Vortex dynamics in the cylinder wake. *Annual review of fluid mechanics*, 28(1), 477-539.

Williamson, C. H. K., & Govardhan, R. (2004). Vortex-induced vibrations. *Annu. Rev. Fluid Mech., 36*, 413-455.

Yokoyama, K., Kashiwaguma, N., Okubo, T., & Takeda, Y. (2004). Flow measurement in an open channel by UVP. *Proceedings, ISUD, 4*, 204-210.

APPENDIX A

Experimental Setup

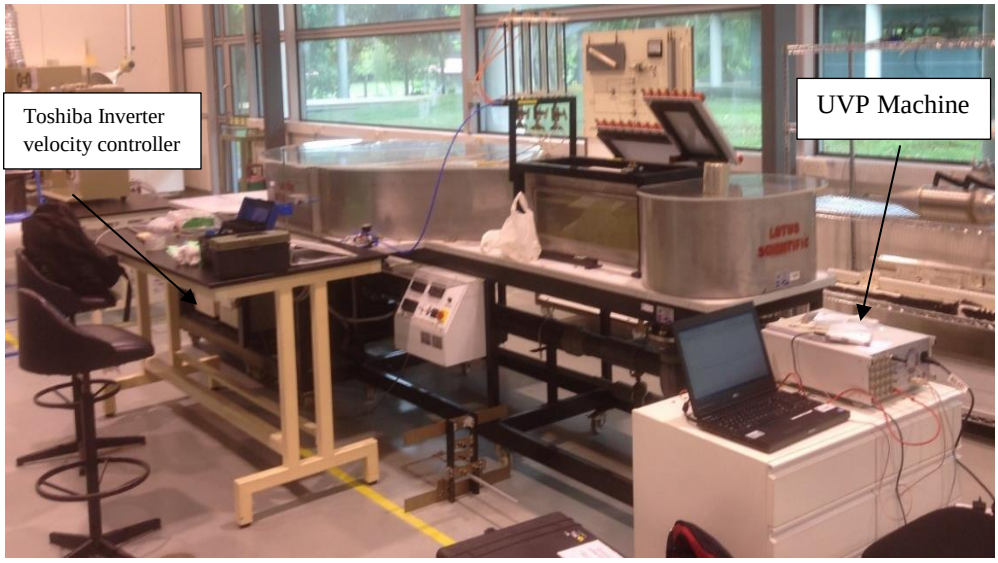

Figure A0.1: Side view of the water tunnel with the test section made of Plexiglas for visualization purpose

Figure A0.2: The endplate used in the experiment that has a sharp-edged leading edge of 30°

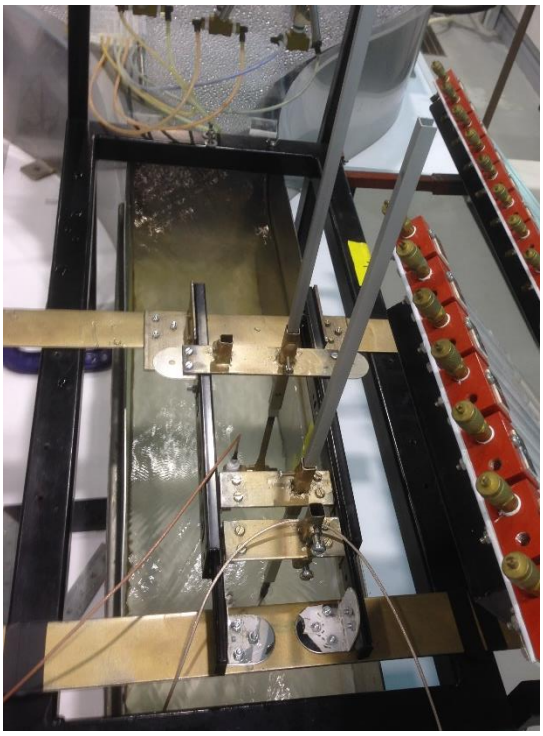

Figure A0.3: Traverse with probe holder during experimental measurements

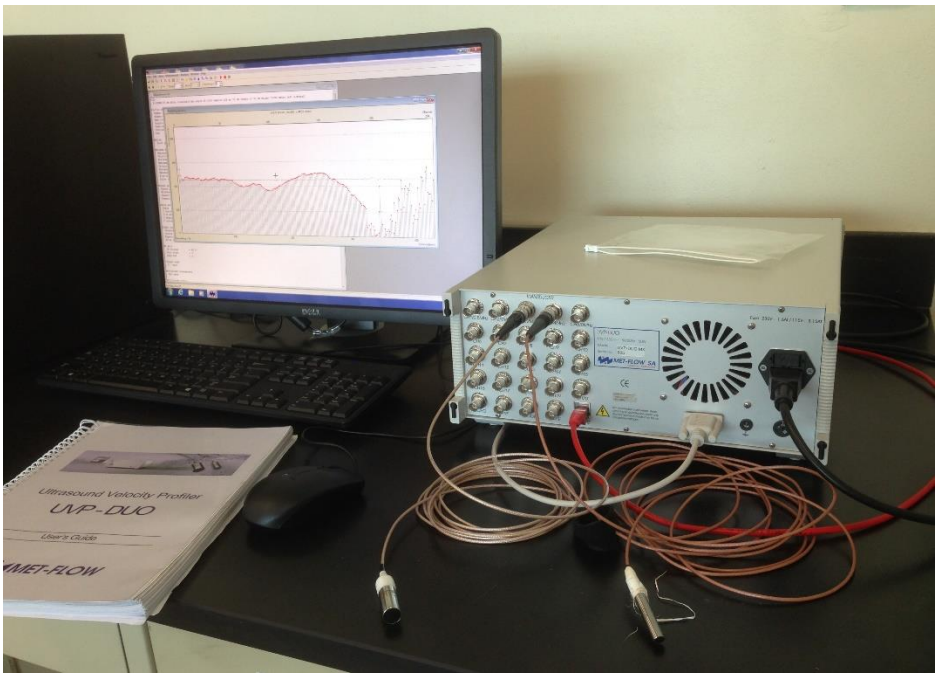

Figure A0.4: UVP machine from MET-FLOW employed in this research work

APPENDIX B

Experimental Results: Visualization

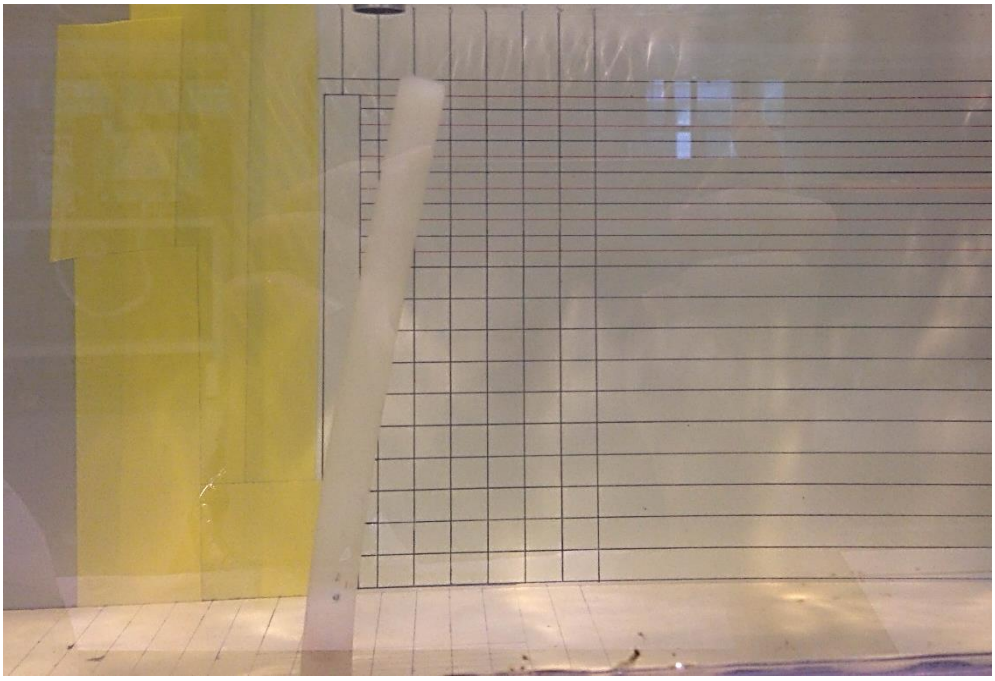

Figure B0.1: The flexible cylinder of AR = 16 shows evidence of bending to $x/D \approx 2$ by the oncoming fluid force for Re = 4000

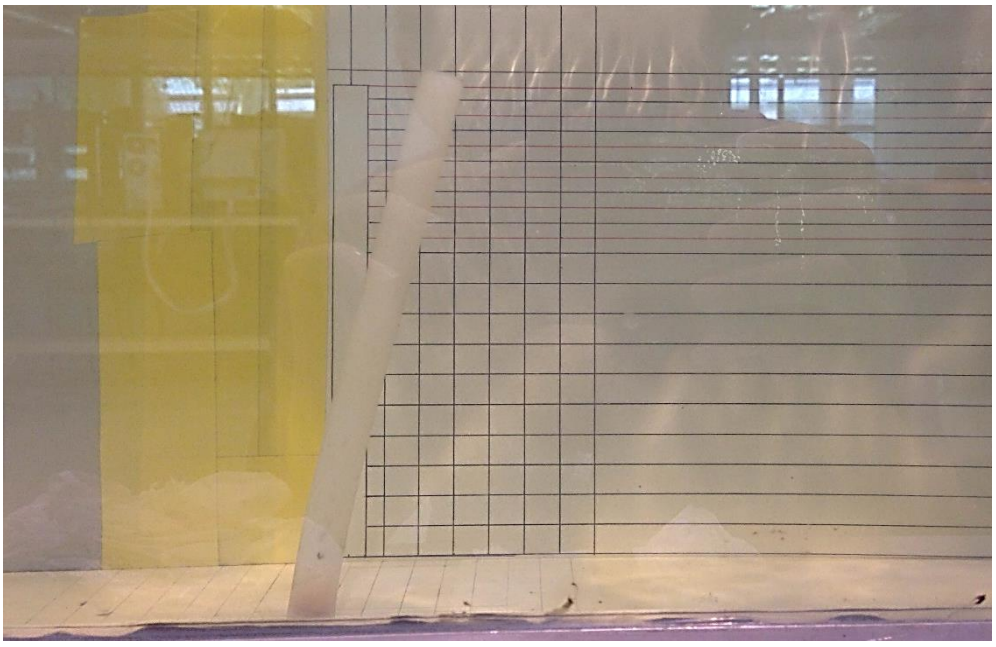

Figure B0.2: The flexible cylinder of AR = 16 shows evidence of bending to $x/D \approx 3$ by the oncoming fluid force for Re = 6000 and 8000

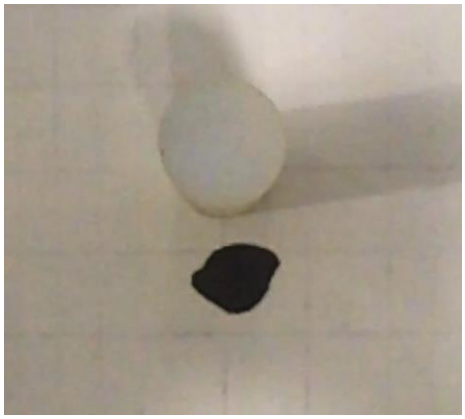

Figure B0.3: The flexible cylinder of *AR* = 10 at Re = 4000 shows no sign of deflection and vibration when viewed from top

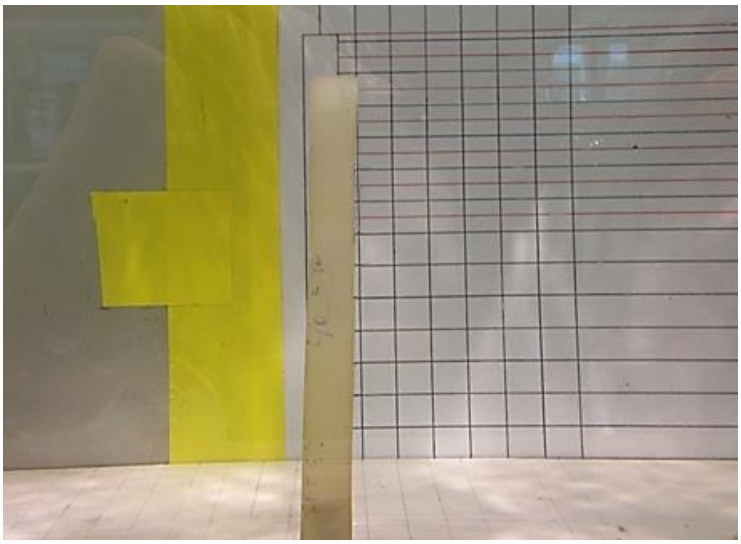

Figure B0.4: The flexible cylinder of *AR* = 10 shows evidence of slight bending to $x/D < 1$ by the oncoming fluid force for Re = 6000

Figure B0.5: The flexible cylinder of *AR* = 10 shows evidence of slight bending to $x/D < 2$ by the oncoming fluid force for Re = 8000

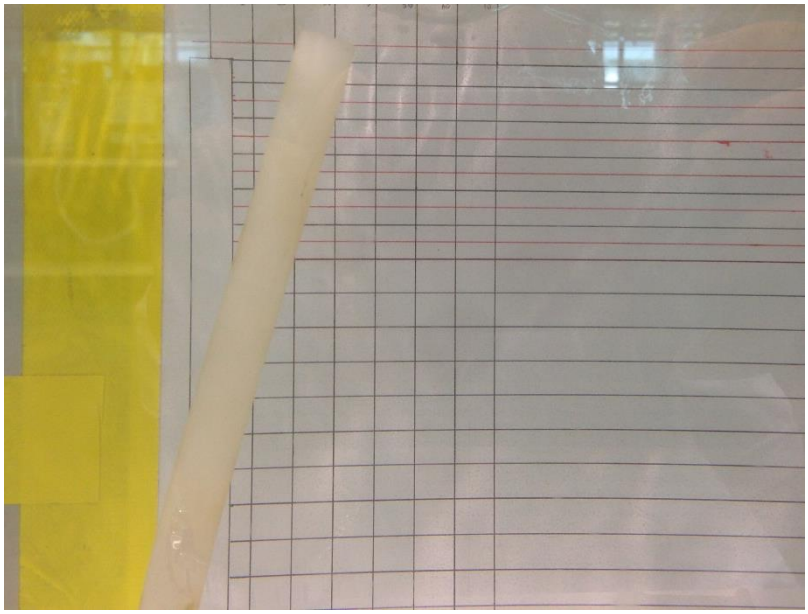

Figure B0.6: The flexible cylinder of *AR* = 14 shows evidence of bending to $x/D \leq 3$ by the oncoming fluid force for Re = 6000

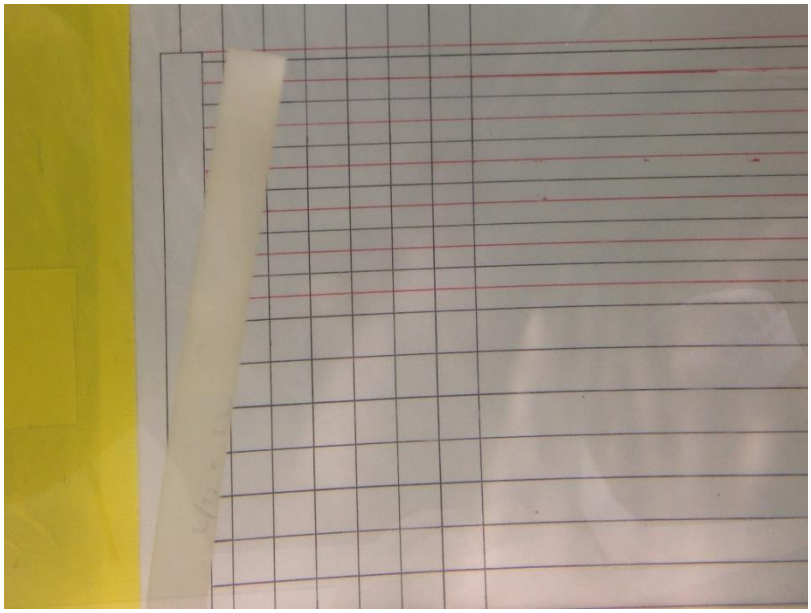

Figure B0.7: The flexible cylinder of *AR* = 12 shows evidence of bending to $x/D \leq 2$ by the oncoming fluid force for Re = 6000

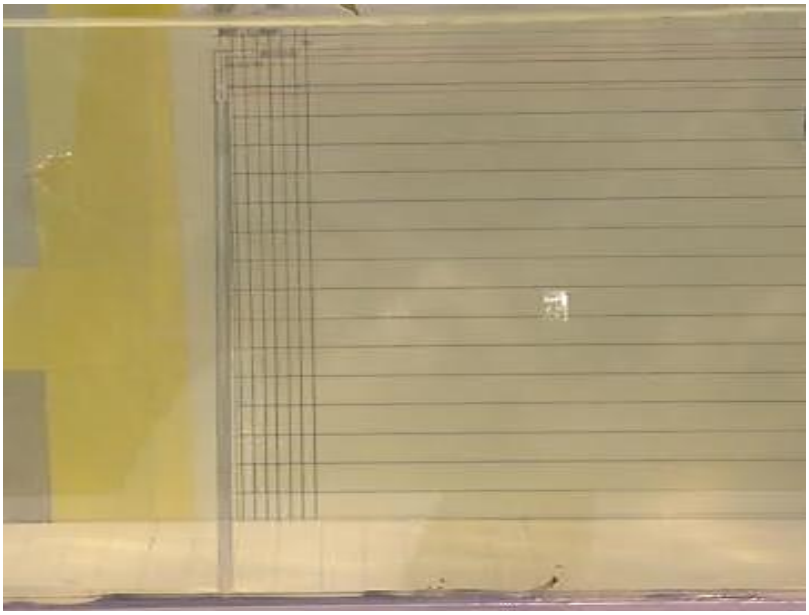

Figure B0.8: The Aluminium flexible cylinder of *AR* = 50 show evidence of no deflection at Re = 2500. Same phenomenon is also seen for Aluminium flexible cylinder of *AR* = 54 and Carbon Steel flexible cylinder of both *AR* at Re = 2500

APPENDIX C

Normalized Amplitude Responses Graph in *y*-direction

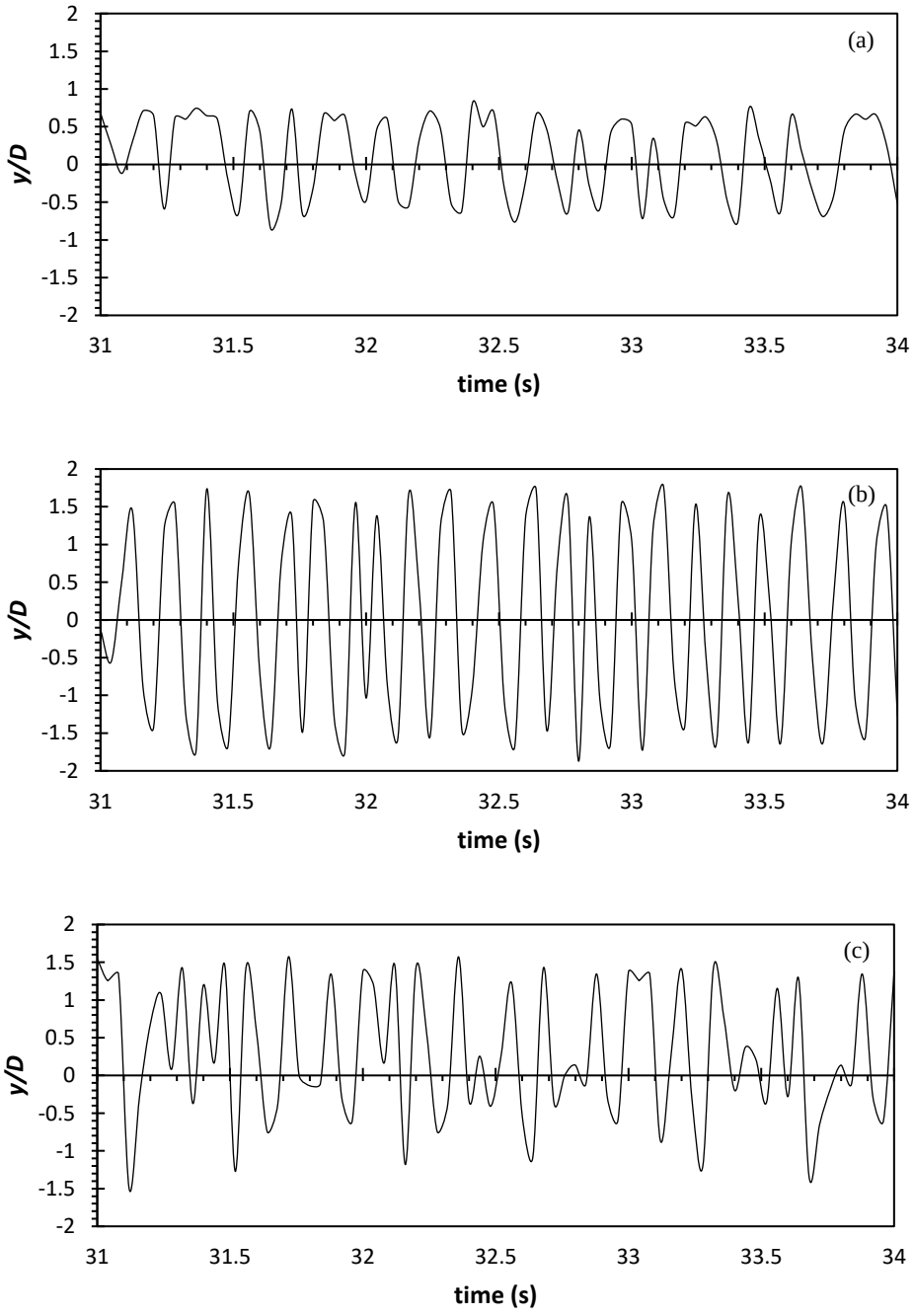

Figure C0.1: Oscillation of flexible cylinder of *AR* = 16. (a) Re = 4000 (b) Re = 6000 (c) Re = 8000

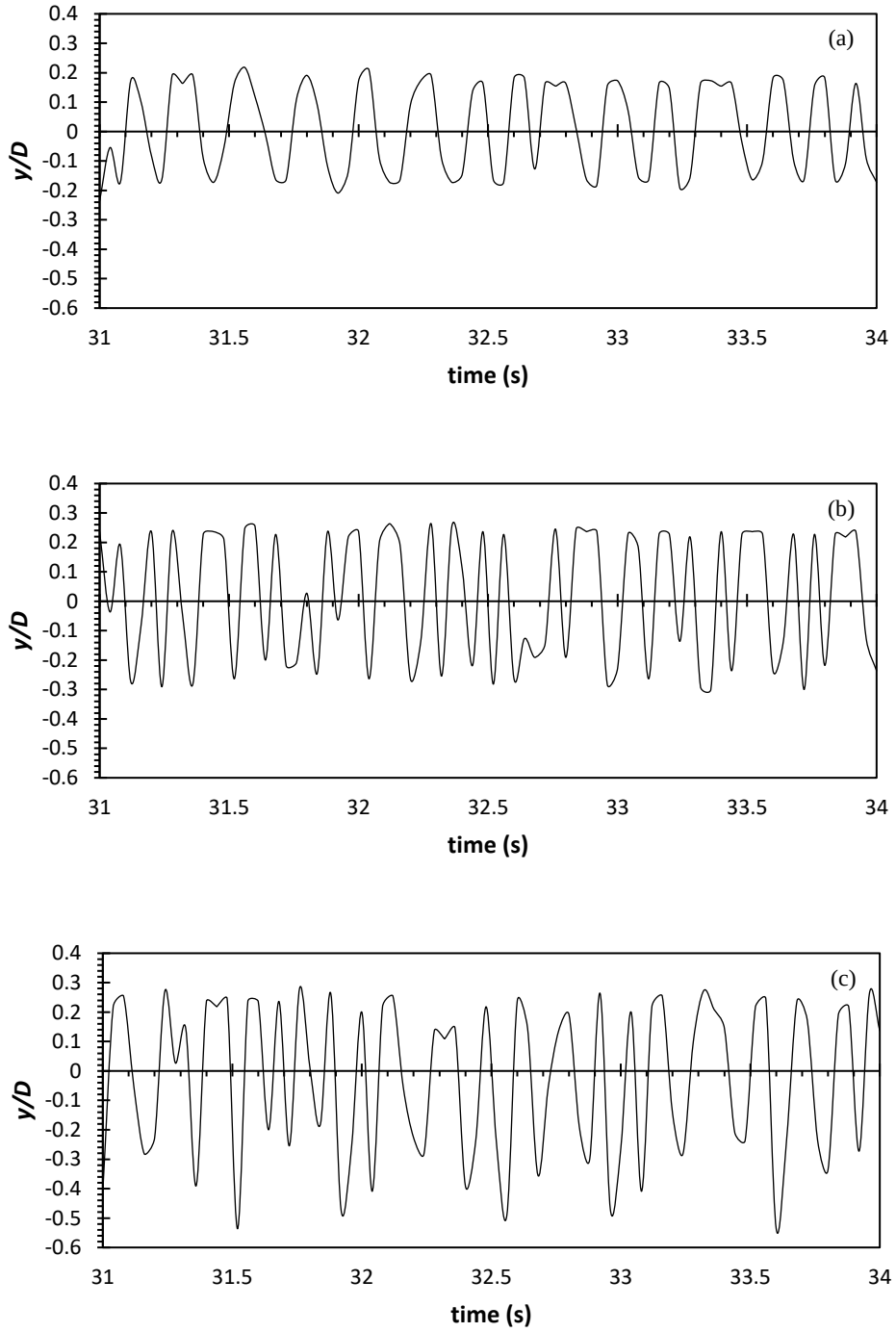

Figure C0.2: Oscillation of flexible cylinder of *AR* = 12. (a) Re = 4000 (b) Re = 6000 (c) Re = 8000

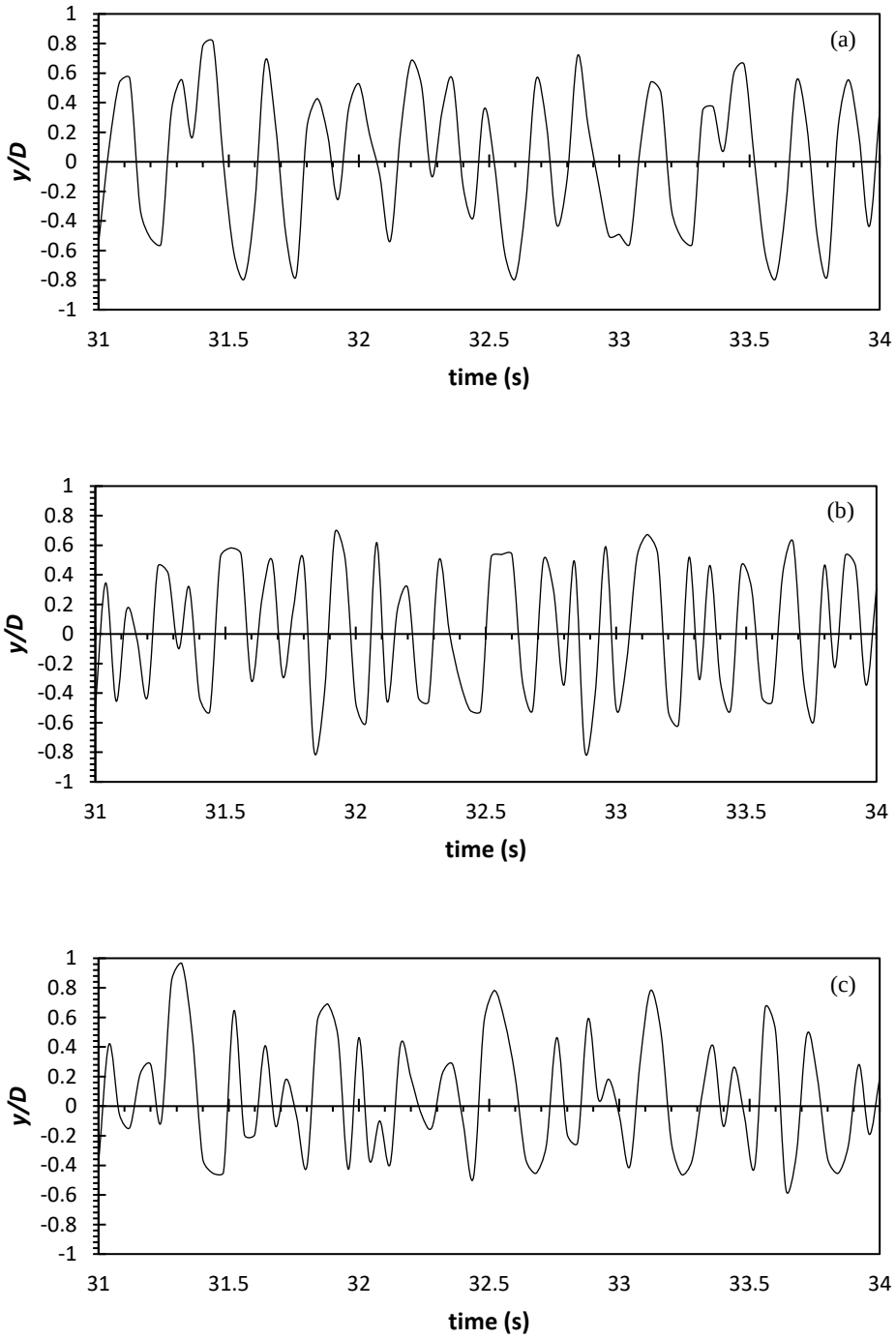

Figure C0.3: Oscillation of flexible cylinder of *AR* = 14. (a) Re = 4000 (b) Re = 6000 (c) Re = 8000

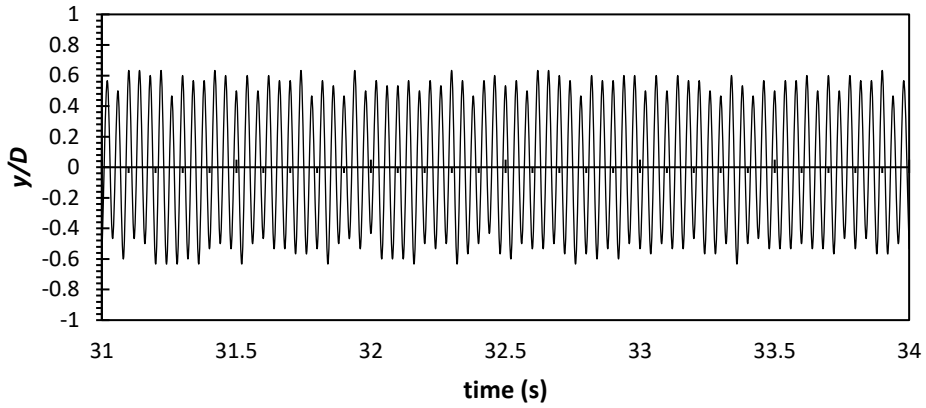

Figure C0.4: Oscillation of aluminium flexible cylinder of AR = 50 at Re = 2500

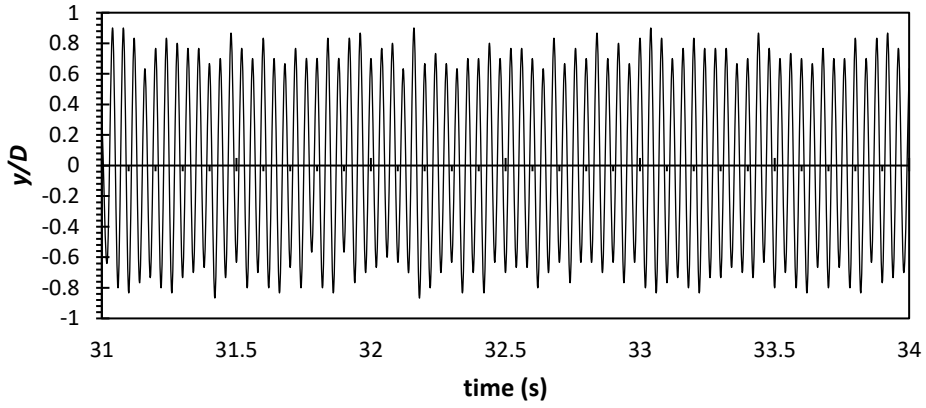

Figure C0.5: Oscillation of aluminium flexible cylinder of *AR* = 54 at Re = 2500

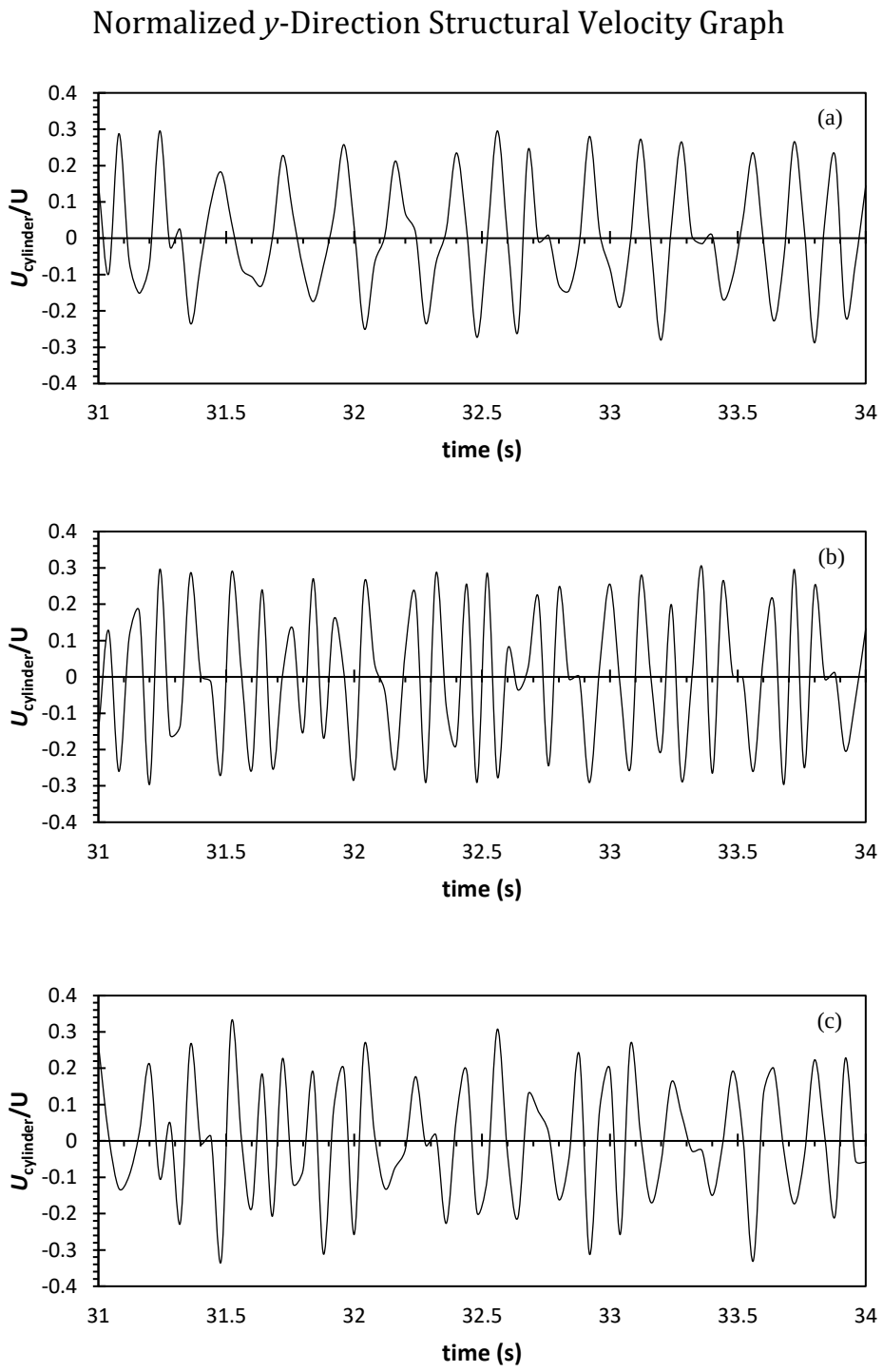

Figure C0.6: The normalized structural velocity of flexible cylinder *AR* = 12 in the *y*-direction. (a) Re = 4000 (b) Re = 6000 (c) Re = 8000

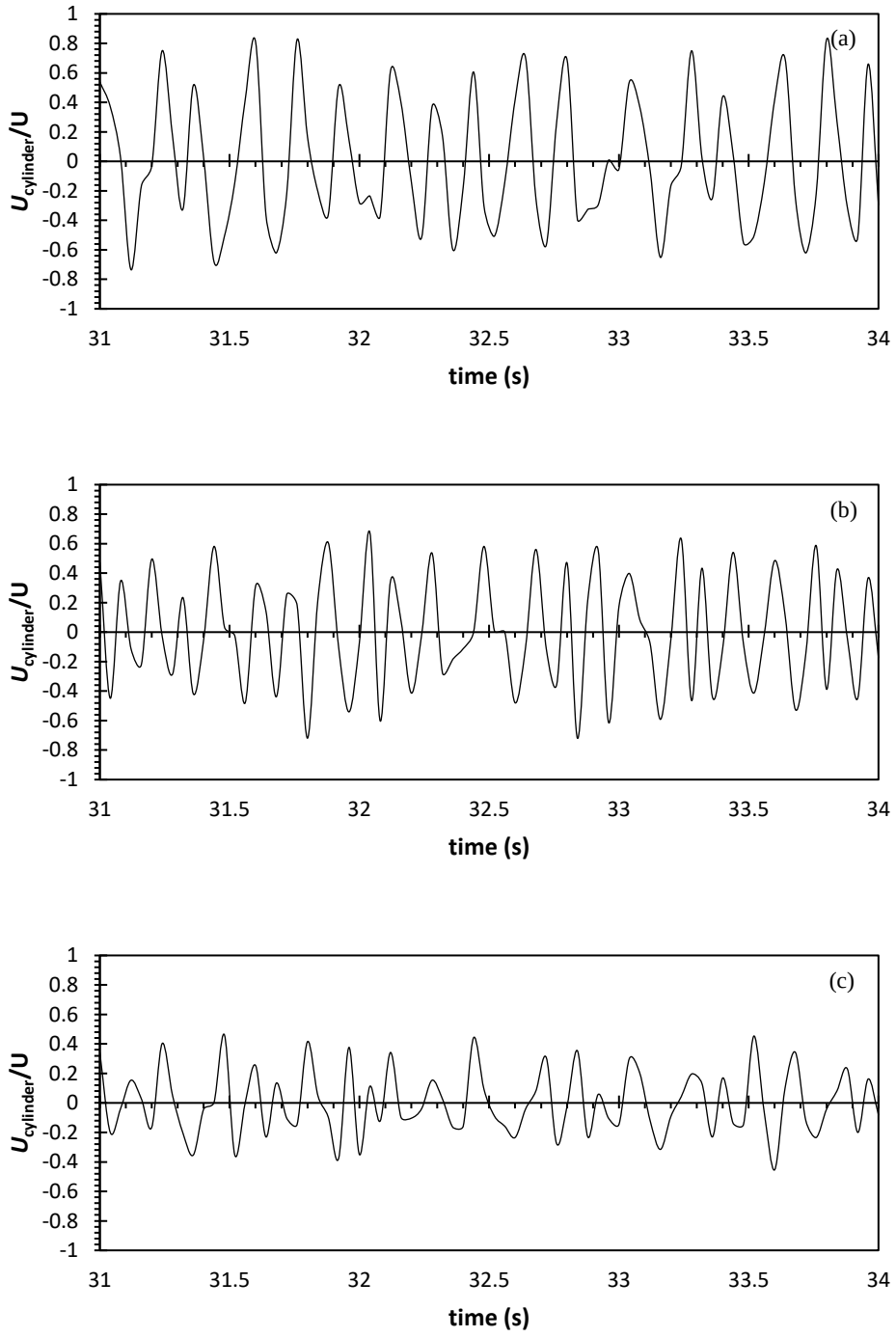

Figure C0.7: The normalized structural velocity of flexible cylinder *AR* = 14 in the *y*-direction. (a) Re = 4000 (b) Re = 6000 (c) Re = 8000

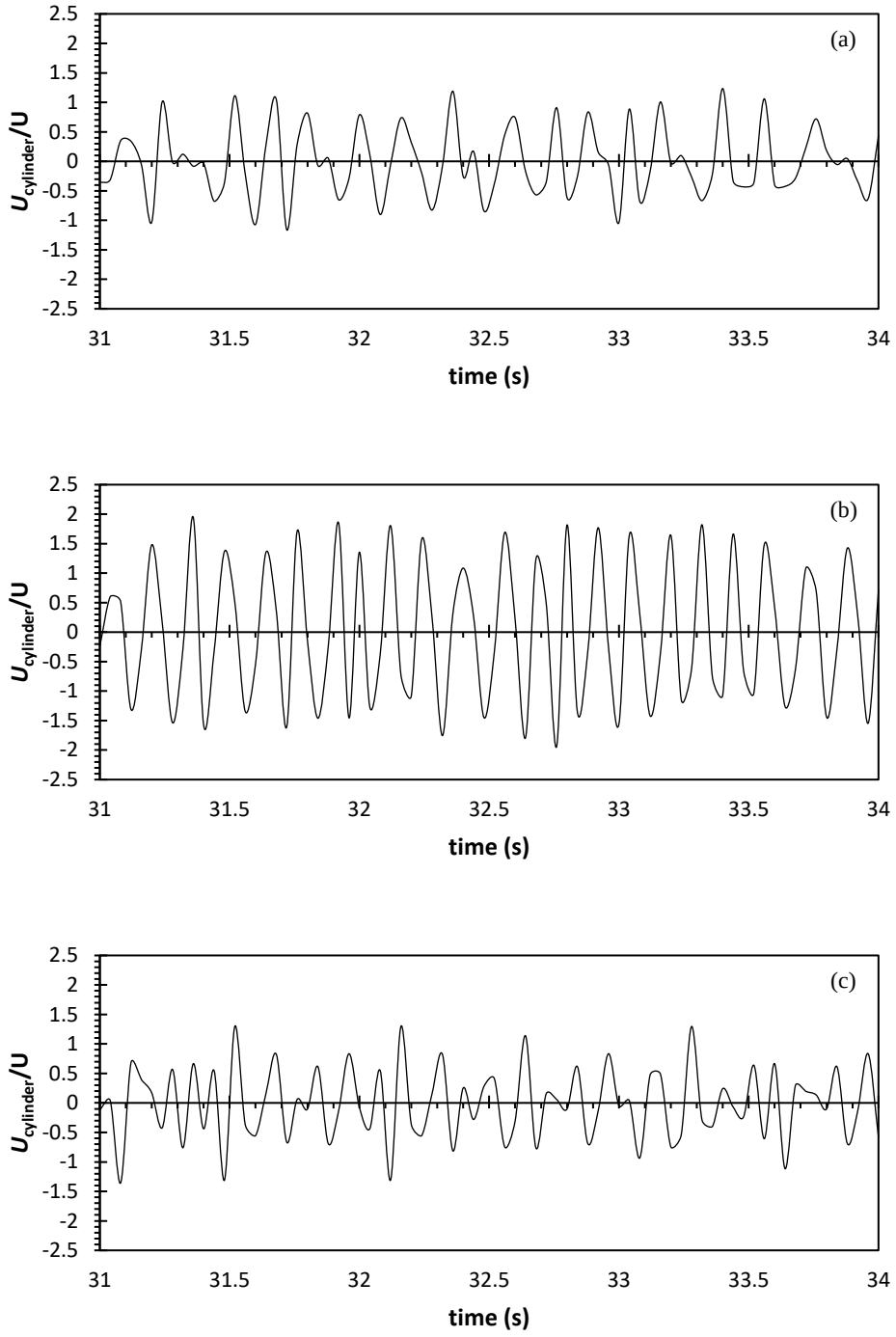

Figure C0.8: The normalized structural velocity of flexible cylinder *AR* = 16 in the *y*-direction. (a) Re = 4000 (b) Re = 6000 (c) Re = 8000

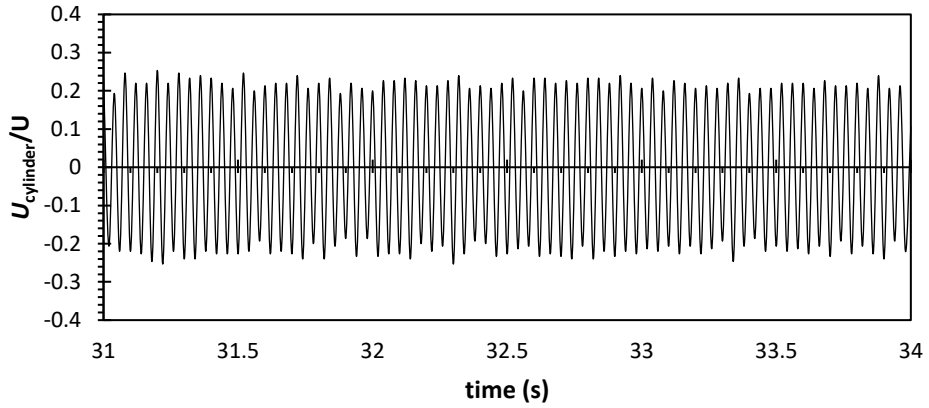

Figure C0.9: The normalized structural velocity of aluminium flexible cylinder *AR* = 50 at Re = 2500 in the *y*-direction

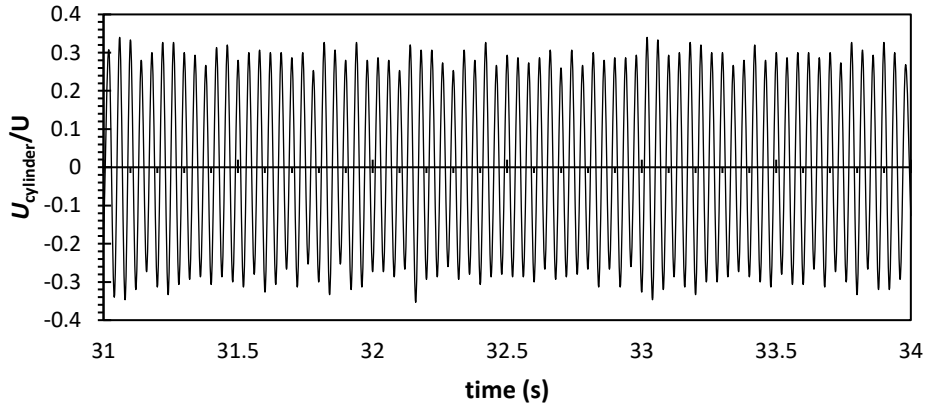

Figure C0.10: The normalized structural velocity of aluminium flexible cylinder *AR* = 54 at Re = 2500 in the *y*-direction